

Improvement of Ion-Beam Energy Resolution in a Solenoid-based Radioactive Nuclear Beam Facility

by
Hao Jiang

A dissertation submitted in partial fulfillment
of the requirements for the degree of
Doctor of Philosophy
(Nuclear Engineering and Radiological Sciences)
in The University of Michigan
2010

Doctoral Committee:

Professor Frederick Becchetti Jr., Co-Chair
Professor Kimberlee Kearfott, Co-Chair
Professor Ron Fleming
Professor Henry Griffin

❖澹泊明志宁静致远❖

To my parents and my wife

ACKNOWLEDGEMENTS

Many thanks to my advisor **Professor Frederick D. Becchetti Jr.**, for his many years of great mentoring, endless support and for the opportunities he gave me throughout this study. I would also like to thank the co-chair of the committee, **Professor Kimberlee Kearfott** for her patience, generosity and superb mentoring. My sincere gratitude to the members of the committee, **Professor Ron Flemming** and **Professor Henry Griffin** for being on my thesis committee, giving advice, and sharing instruments in collaborated projects.

I would also like to acknowledge the contributions of **Dr. R. Raymond** and **Mr. Ramon Torres-Isea** for guidance in experiments and prudent advice to improve my understanding of many scientific concepts.

I also wish to thank our collaborators at University of Notre Dame, **Professor James Kolata, Jim Kaiser, Dr. Larry Lamm, Dr. Hanan Amro, Dr. Anthony Villano** and **Amy Roberts** for their help, especially during the experiments at UND.

Finally I wish to thank **Dr. Mitaire Ojaruega** and **Dr. Yu Chen** for their constant hands-on assistance with my experimental work, for their consistent partnership through all these years.

TABLE OF CONTENTS

DEDICATION	ii
ACKNOWLEDGEMENTS	iii
LIST OF TABLES	vi
LIST OF FIGURES	vii
LIST OF APPENDICES	xiv
CHAPTER	
I. Introduction	1
1.1 Radioactive Nuclear Beams	1
1.2 UM-UND <i>TwinSol</i> Apparatus	3
1.3 Limitations in <i>TwinSol</i> RNB Reaction Studies	5
1.3.1 Energy spread in <i>TwinSol</i>	5
1.3.2 ^8Li inelastic scattering	6
1.4 Main Goals	7
II. Energy-spread Compensation In A Solenoid-based Secondary Radioactive Beam Apparatus	9
2.1 Introduction	9
2.2 Apparatus Layout	10
2.3 Energy Compensation Test	11
2.4 In-beam Energy-compensation Absorber Tests	12
2.5 Limits Due to Energy Profile and Production Reaction	17
III. Time-of-flight(ToF) Measurement Using Intrinsic Beam Bunching	21
3.1 Introduction	21
3.2 Intrinsic Primary Beam Bunching	21
3.3 Ray-trace Calculations	23
3.4 ToF Experiment with Beam Bunching	24
3.5 Conclusion	26
IV. Time-of-Flight(ToF) Measurement Using A Micro-channel Plate Detector 31	
4.1 Introduction	31
4.2 Time-of-flight Ray Trace Calculations Using an MCP	33
4.3 MCP Information	35
4.3.1 Specification of BURLE MCP	35

4.3.2	Design of the MCP holder and HV resistor chain	37
4.3.3	Simulation of secondary electron trajectories in a magnetic field . . .	38
4.4	^{244}Cm α Source MCP Tests	39
4.4.1	Vacuum chamber setup	39
4.4.2	α source test setup	40
4.4.3	α test result	43
4.5	^8Li RNB in-beam Test at <i>TwinSol</i>	44
4.5.1	In-beam test of MCP at ToF chamber	45
4.5.2	In-beam test of MCP at cross-over chamber	47
4.6	Conclusion	49
V. ^8Li + gold Coulomb Excitation Measurements Using ToF		51
5.1	Introduction	51
5.2	Experimental Setup and Data Acquisition	52
5.3	Experimental Results for Inelastic Scattering (Coulomb Excitation) of ^8Li .	61
5.4	DWBA Analysis	63
VI. Low-Energy and Secondary (Radioactive) Ion-Beam Profile Measurements and Optimization using Modified Gafchromic[®] EBT Film		68
6.1	Introduction	68
6.2	Film Characteristics	72
6.3	Film Imaging Measurements	74
6.3.1	Measurements with a ^{244}Cm α -source	74
6.3.2	In-beam <i>TwinSol</i> RNB measurements	75
6.3.3	Primary RNB film images	78
6.3.4	Use in a typical ^8B and ^7Be low-energy RNB experiment	86
6.4	Special Aspects of RNB Imaging	88
6.5	Conclusions	88
VII. Conclusions		91
7.1	Achievement of Project Goals	91
7.2	Future of <i>TwinSol</i> ToF	92
APPENDICES		95
BIBLIOGRAPHY		204

LIST OF TABLES

Table

3.1	Kinematic calculation of ${}^8\text{Li}$ energy for production angles from 1° to 6°	24
3.2	Specific solenoid settings.	24
3.3	List of detectors.	25
3.4	α decay activities for the ${}^{228}\text{Th}$ source.	25
3.5	Detector calibration results ($E = E_0 + E_1 \times CH$ MeV).	25
4.1	Specification of MCP from Burle, Inc.	35
4.2	Detectors list and angles using MCP in ToF chamber.	48
5.1	List of detectors used in CoulEx experiment.	53
5.2	Measurements of all distances noted in Figure 5.2 for all detectors and corresponding calculated solid angles.	54
5.3	<i>TwinSol</i> parameters.	54
5.4	Optical model parameters	66
5.5	CoulEx results	67

LIST OF FIGURES

Figure

1.1	Nucleonic-transfer reaction producing secondary short-lived radioactive nuclear beams in a production chamber on a ^3He gas cell.	2
1.2	Layout of UND nuclear structure laboratory.	3
1.3	The layout of original <i>TwinSol</i> apparatus.	4
1.4	Two operation modes of <i>TwinSol</i> . Top: Cross-over mode. Bottom: Parallel mode.	5
1.5	^{16}O energy states from the reaction $^{12}\text{C}(^7\text{Be},^3\text{He})^{16}\text{O}$. Several excited states cannot be separated due to poor energy resolution [Amr07].	6
1.6	Data showing ^8Li RNB scattered from a Pb target at $E=30.5$ MeV, $\theta=38^\circ$ [Mu02]. A fraction of the incident ^8Li RNB is scattered inelastically into its first excited state. Due to the poor energy resolution one can only see a tail extended from the ground state peak.	7
2.1	Schematic of a dipole-based fragment separator. The first section runs from the production target to the wedge energy-loss absorber and momentum slits, which set the momentum acceptance. The fragments selected in magnetic rigidity are then refocused on the wedge selection slits by the second section. Finally, an optional third section provides an additional selection by using a velocity filter before the fragments are sent to a detection system, a reaction target or further beamline. [Baz02].	10
2.2	Absorber (polyester) thickness vs. 34 MeV ^7Be RNB trajectory angle.	11
2.3	<i>TwinSol</i> layout with energy compensating absorber.	12
2.4	Print of absorber plate. Cocentric ring of holes are covered by radially symmetric absorbers with a radius-dependent thickness.	14
2.5	Print of modified ISO-250 plate with LEMO feed through. A CAJON fitting is placed at the center of this plate.	15
2.6	Ray trace calculation for ^7Be beam through <i>TwinSol</i> . The position of absorber plate in the beam is marked and the radius of each ray at the absorber position is calculated.	16
2.7	Top: Kinematic prediction and energy scan. Bottom: Yield vs. angle of ^7Be beam.	19
2.8	^7Be beam imaging on a 25 mm \times 25 mm PSD in back chamber.	20

3.1	Layout of <i>TwinSol</i> apparatus with extended beam line and new time-of-flight vacuum chamber.	22
3.2	Picture of new ToF chamber constructed as part of this thesis project.	27
3.3	Ray trace calculation of 28 MeV ^8Li from 1° to 6° through <i>TwinSol</i>	28
3.4	Silicon detector array	28
3.5	Schematic illustration of the electronic setup	28
3.6	Time of flight vs. total energy histogram at zero degree(80 keV/ch for energy and 0.5 nsec/ch for ToF).	29
3.7	Projected ^8Li energy spectrum ($\theta = 30^\circ$).	30
4.1	Schematic construction of an MCP and operation of electron amplification. [Kum88]	32
4.2	Ray trace calculation for ToF of 6 m flight path (Figure 3.1). Each ray is at an emission angle (^8Li) of $\theta=1^\circ, \dots, 6^\circ$ with each ray's ToF indicated (ca. 277 nsec). . .	34
4.3	Burle MCP dimensions.	36
4.4	MCP holder with resistor chain.	37
4.5	Secondary electron trajectories from a foil in a realistic magnetic field at the <i>TwinSol</i> cross over using Monte-Carlo calculations.	40
4.6	MCP alpha test vacuum chamber setup	41
4.7	MCP α test setup	42
4.8	MCP α test electronics setup	42
4.9	MCP Signal	43
4.10	MCP α test 2D histogram (50 psec/ch).	44
4.11	Projection onto time (see Figure 4.10; 50 psec/ch).	45
4.12	Microchannel Plate installed inside ToF chamber in front of target holder.	46
4.13	Two-dimensional Time-of-flight vs. Energy histogram ($\theta=0^\circ$) when using MCP in ToF chamber (80 keV/ch for energy and 0.5 nsec/ch for ToF).	47
4.14	Histogram projection showing ^8Li ground state and excited $^8\text{Li}^*$ from MCP foil and Si detector excitation.	48
4.15	Time of flight from MCP to detector D vs. energy histogram taken at 22.5° (80 keV/ch for energy and 0.5 nsec/ch for ToF).	49
4.16	ToF vs. E histogram with MCP at cross-over position (80 keV/ch for energy and 0.5 nsec/ch for ToF).	50

4.17	Comparison of timing resolution for MCP and beam buncher ToF.	50
5.1	Levels in ^8Li decay mode = beta to ^8Be , $T_{\frac{1}{2}}=842$ ms [NDE].	52
5.2	The geometry of detectors with collimators according to the target position for calculating solid angles.	53
5.3	ToF vs. E histogram ($\theta=0^\circ$) shows the identification of different particle groups (80 keV/channel in E and 0.5 nsec/channel in ToF.)	56
5.4	Detector array placed on the rotational table inside the ToF chamber. The detectors were placed at 30° , 45° , 60° and 75° lab angle with respect to the target. The picture shows the back of the detector array.	57
5.5	The geometry of primary beam, target and detector array.	57
5.6	As shown here, the target foils are typically sandwiched between two target frames and attached to the target ladder.	58
5.7	A schematic of the electronic data-acquisition hardware.	59
5.8	A schematic of the electronic data-acquisition hardware for the PSD.	60
5.9	Total energy profile of low-intensity ^8Li secondary beam ($\theta=0^\circ$) measured on a Si detector at the target position in the back chamber.	62
5.10	An example of data for a single data collection period (8 hours) for one detector (45°) ($^8\text{Li} + \text{nat. Au}$ thin target). The fitted peaks to the data shown were used to extract the inelastic reaction probability $P(\theta)$	63
5.11	ToF vs. total energy histogram taken at 30° with empty target frame shows almost no scattering ions from primary beam into ^8Li group.	64
5.12	Experimental data and DWBA calculation for inelastic excitation (CoulEx) of a ^8Li RNB incident upon a $475 \mu\text{g}/\text{cm}^2$ and a $2.025 \text{ mg}/\text{cm}^2$ nat. Au target at 28 MeV. Previous data for a 30.5 MeV ^8Li on a ^{208}Pb target also is shown [Mu02].	66
6.1	Top: A schematic layout of the <i>TwinSol</i> RNB system showing the extended beam line and new ToF chamber. The location of chambers used to obtain film images described in the text are indicated with the labels A, B, C and D. Bottom: Ray-tracing calculations for the ^8Li RNB used for in-beam tests (note scales). The trajectories of ^8Li 3+ ions produced at initial angles 2 to 6 degrees (spanning the <i>TwinSol</i> entrance aperture) are indicated.	70
6.2	Cross section of the modified EBT film used in the present ion-beam measurements (adapted from material provided by ISP [Rol88]).	74
6.3	Top: Gray-scale pixel image (relative intensity profile) of a thick ^{244}Cm alpha source located a few cm (in vacuum) from modified EBT film. (The original colored images have been converted to grayscale for publication.) Bottom: A cross-sectional profile for the section AA indicated in the ^{244}Cm film image is shown. (Same distance scale at top also applies to the bottom profile with ca. 40 units/cm)	76

6.4	A photograph of a film paddle with modified EBT film mounted for use in an ISO-250 chamber.	78
6.5	Images of RNBs with background ions obtained at chamber A indicated in Figure 6.1. Top: Image obtained on front film. Bottom: Image obtained on a film piece located after first film (top) where the latter acts as a ca. 137 micron plastic absorber (see text). The images of the off-focus background beams are overexposed in these films as the exposure times were set to optimize images of the less intense ^8Li ions. (The original colored images have been converted to grayscale for publication.)	80
6.6	Image of RNBs, background ions, and radiation obtained at the cross-over chamber (B; Figure 6.1). The ions focused at the center of the image are the $^8\text{Li } q=3^+$ RNB and its analog ions. (The original colored images have been converted to grayscale for publication.)	81
6.7	Off-focus image (top) and profiles (bottom) for cross sections indicated of the ^8Li RNB and background ions observed in the small chamber (C in Figure 6.1) upstream of the ToF chamber. The distance is relative to the film edge and corresponds to about 100 units/cm as indicated by the scale. (The original colored images have been converted to grayscale for publication.)	84
6.8	^8Li RNB beam images (including contaminant ions) obtained in the new ToF chamber (D in Figure 6.1). Top: Image at entrance to the chamber. Middle: Image at the target location (center of chamber). Bottom: Image at exit of the chamber. (The original colored images have been converted to grayscale for publication.)	87
6.9	^8B , ^7Be (analog) ions and background ions off focus (top) at the entrance to chamber C and on focus (bottom) at the target location in chamber C (Figure 6.1). Part of a low-energy ^8B and ^7Be RNB experiment to determine optimal collimation for that specific experiment. (The original colored images have been converted to grayscale for publication.)	89
7.1	Fringe field calculation at the cross-over location when applying the magnetic shield.	93
7.2	Schematic depiction of using two MCP detectors for ToF measurements.	94
A.1	Windows <i>TwinSol+</i> GUI.	97
A.2	<i>TwinSol+</i> menus and toolbars	97
A.3	<i>TwinSol+</i> preference property page	98
A.4	“Particle” tab of <i>TwinSol+</i>	99
A.5	“Energy” tab of <i>TwinSol+</i>	100
A.6	“Magnet” tab of <i>TwinSol+</i>	101
A.7	Geometry for the on-axis magnetic field calculation from a solenoid current sheet approximation.	102
A.8	“Absorber” tab of <i>TwinSol+</i>	103
A.9	“Path length” tab of <i>TwinSol+</i>	104

A.10	Ray-trace calculation of 34 MeV ^7Be beam in <i>TwinSol</i> with a short flight path (5.5 m).	105
A.11	Ray-trace calculation of a 28 MeV ^8Li beam in <i>TwinSol</i> with a long flight path (8 m).	105
A.12	Ray-trace calculation of 34 MeV ^7Be in parallel mode (8 m flight path).	106
B.1	Assembly layout of the new ToF chamber.	118
B.2	ISO-250 side plate dimension for the ToF chamber.	119
B.3	ToF chamber frame 3D model.	120
B.4	Top adapter ring print.	120
B.5	The bottom plate for the ToF chamber.	121
B.6	Print of top lid for <i>TwinSol</i> ToF chamber.	122
B.7	The current configuration of the ToF chamber.	123
B.8	Print of the ToF chamber target ladder.	124
B.9	Tof chamber rotating detector table.	126
B.10	Print of hub between the rotating table and the bottom plate of the ToF chamber.	127
B.11	The 3D model of the ToF chamber supporting frame.	128
C.1	CMC100 FastCamac USB Crate Controller [CMC100]	133
C.2	CANBERRA GX4018 germanium detector positions relative to the ^{228}Th source.	134
C.3	NIM electronic setup for gamma-gamma coincidence measurements.	135
C.4	Data block from ORTEC 811 ADC (5 bytes each).	136
C.5	Typical gamma-gamma coincidence measurements with Kmax GUI.	138
C.6	Typical coincidence-gated gamma spectrum obtained from the CAMAC-Kmax DAQ system.	139
C.7	Pulse-shape discrimination by applying two different time gates on anode PMT QDC signals (10 nsec/ch).	140
C.8	Neutron detector data acquisition schematic [Mo09].	153
C.9	Top: 2-dimensional histogram obtained using the Kmax DAQ system showing the PSD between neutrons and γ s [Mo09]. Bottom: Projected neutron spectrum after gating on the neutron group in the 2D PSD histogram.	154
D.1	Program Layout of Compact plus	158

D.2	Scheme of the program Analyze is using to get the net and the error.	160
D.3	The chance coincidence of E1 obtained by gating on the first channel of E1 histogram using the program ‘Projection’.	164
D.4	The E1 histogram obtained by gating a 129 keV peak on E2 using the program ‘Projection’.	165
D.5	Summary of γ - γ coincidence relationships. An asterisk denotes only seen in coincidence experiments [Dal87].	166
E.1	Print for ISO 250 to ISO 160 adapter plate (material: aluminum).	180
E.2	Print of brass rod for holding MCP support plate.	181
E.3	Print of center tube (material: aluminum).	182
E.4	Print of collar (material: aluminum).	183
E.5	Print of custom ISO 100 plate (material: aluminum).	184
E.6	Print of EBT film paddle (material: aluminum).	185
E.7	Print of modified ISO 100 plate with vacuum and LEMO feedthroughs (material: aluminum).	186
E.8	Print of modified ISO 100 plate with compression fitting (material: aluminum). . .	187
E.9	Print of ISO 100 to Dependex plate adapter (material: aluminum).	188
E.10	Print of modified ISO 100 plate (material: aluminum).	189
E.11	Print of ISO 160 to Dependex plate adapter (material: aluminum).	190
E.12	Print of ISO 250 to ISO 160 adapter (material: aluminum).	191
E.13	Print of Lexan MCP holder.	192
E.14	Print of magnetic field shielding box for MCP (material: steel).	193
E.15	Print of mid chamber supporting plate (material: aluminum).	194
E.16	Print of ISO 100 Lexan viewing plate.	195
E.17	Print of detector holder (material: aluminum).	196
E.18	Print of target frame for <i>TwinSol</i> ToF chamber.	197
E.19	Print of ToF chamber frame top piece (material: aluminum).	198
E.20	Print of ToF chamber frame bottom piece (material: aluminum).	199
E.21	Print of ToF chamber frame side piece (material: aluminum).	200

E.22	Print of leveling block for ToF chamber frame (material: aluminum).	201
F.1	Film poster presented in SORMA west conference.	203

LIST OF APPENDICES

Appendix

A.	Twinsol+ Program	96
A.1	Introduction	96
A.2	<i>TwinSol+</i> Usage	97
A.3	Sampled Calculations	100
A.4	Code for <i>Twinsol+</i> Program	103
A.5	Code for <i>Electron Trajectory</i> Program	112
B.	Time-of-Flight Chamber Design and Construction	116
B.1	Time-of-Flight Chamber Design	116
B.2	Leak Testing and Vacuum Tests of the ToF Chamber	117
B.3	Construction of Other Components	117
C.	Kmax CAMAC Data Acquisition System	129
C.1	Introduction	129
C.2	Kmax-CAMAC System Developed for γ - γ Coincident Measurements	130
C.2.1	CMC100 controller	130
C.2.2	NIM electronics setup	131
C.2.3	Data process in CAMAC	136
C.2.4	Kmax user interface	137
C.3	System for γ -neutron Pulse Shape Discrimination (PSD) Measurements	138
C.3.1	γ neutron PSD	138
C.3.2	C ₆ D ₆ neutron detector data acquisition	140
C.3.3	Kmax program for neutron-gamma PSD experiment	140
C.4	Kmax Code Listings	142
C.4.1	Gamma-gamma coincidence measurement Kmax Java code	142
C.4.2	Neutron-gamma PSD experiment Kmax Java code	147
D.	Tutorial: KMAX Program for Gamma-gamma Coincidence Experiments	155
D.1	Several Utilities Developed for γ - γ Coincidence Analysis	155
D.1.1	Data acquisition software Kmax and its limitations	155
D.1.2	Binary data compressing program - Compact	157
D.1.3	2D-array generating program - Transfer	158
D.1.4	Program for histogram projection - Projection	159
D.1.5	Calculation of coincidence intensity - Analyze	160
D.1.6	Matlab subroutine - Readnet	161
D.2	Data Analysis and Results	162
D.3	Code Lists	164
D.3.1	Compact code	164

	D.3.2	Transfer code	172
	D.3.3	Projection code	173
	D.3.4	Analyze code	175
	D.3.5	ReadNet Matlab code	178
E.		Other Prints for <i>TwinSol</i> Project	179
F.		Poster SORMA-WEST 2008	202

CHAPTER I

Introduction

1.1 Radioactive Nuclear Beams

The production and use of radioactive nuclear beams (RNB) are of great interest in nuclear astrophysics. For example, in big bang nucleosynthesis (BBN), the nuclei which are “stable” for a fraction of second are critically involved in production of elements. Several nuclear reaction rates involving unstable nuclei such as ${}^6\text{He}$, ${}^8\text{Li}$, ${}^7\text{Be}$ etc. at low energies are essential for accurate modeling in astrophysics [Rol88, Sch98]. As an example, the production of ${}^7\text{Li}$ or ${}^6\text{Li}$ in BBN is of interest as the abundance of these nuclei in the Universe can help establish the precise amount of baryonic i.e. normal matter that was originally created [Rol88]. At present there is an anomaly in observed abundances of lithium isotopes relative to the amount of hydrogen in the Universe [Cyb03]. Reactions which produce lithium and other elements in BBN can involve short-lived nuclei such as ${}^8\text{Li}$, ${}^6\text{He}$, ${}^7\text{Be}$, ${}^8\text{B}$, and other specific RNBs at low (MeV to keV) energies. This requires measurement with these short-lived RNBs to fully understand BBN reaction rates. The RNBs also are important in expanding our basic understandings of the properties of nuclei, because these RNB which have $N \gg Z$ or $Z \gg N$ often exhibit behavior very different from ordinary, non-radioactive nuclei [Cas99].

In this work, the method for producing radioactive nuclear beams is referred to as the nucleonic-transfer method (or the in-flight transfer method) which is capable of producing short-lived secondary RNBs of a few Mev/u [Bec03]. In this method, a low-energy primary beam incident on a production target, with a selective high-cross-section nucleon-transfer or exchange process, produces secondary radioactive beams. As an example shown in Figure 1.1, the primary beam ${}^6\text{Li}$ goes into the production chamber, interacts with a ${}^3\text{He}$ gas target and produces the radioactive nuclear beam ${}^7\text{Be}$ ($T_{1/2} = 53$ days with decay mode electron capture to ${}^7\text{Li}$) at 34 MeV. This technique was developed by the nuclear physics group of the University of Michigan in collaboration with members of the nuclear structure lab of the University of Notre Dame (UND) .

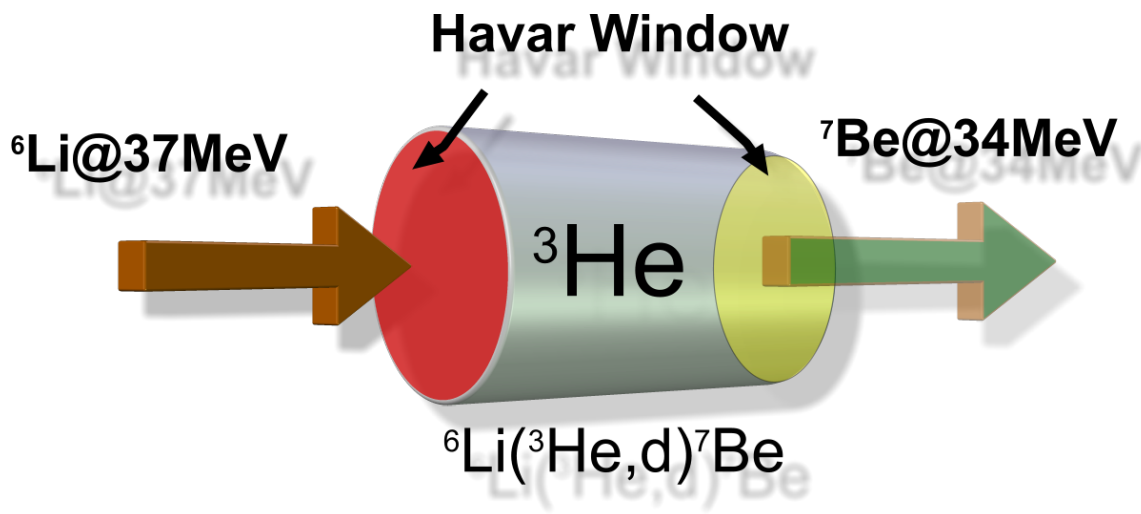


Figure 1.1: Nucleonic-transfer reaction producing secondary short-lived radioactive nuclear beams in a production chamber on a ${}^3\text{He}$ gas cell.

As part of this thesis work, intense exotic beams of ${}^7\text{Be}$ and ${}^8\text{Li}$ were created and studied with elastic scattering and inelastic scattering together with studies involving the determination of reaction rates at low energies for astrophysical purposes.

1.2 UM-UND *TwinSol* Apparatus

TwinSol is a unique apparatus designed and built as a joint enterprise of the nuclear physics research groups of the University of Michigan and the University of Notre Dame. This ion-optical apparatus is specifically designed to be coupled with the 10 megavolt tandem Van de Graaff accelerator (HVEC model FN tandem) located at the nuclear structure lab of the University of Notre Dame [Mu02]. Figure 1.2 shows the layout of the UND nuclear structure lab (NSL). *TwinSol* is located in the west target room at NSL along a dedicated beam line.

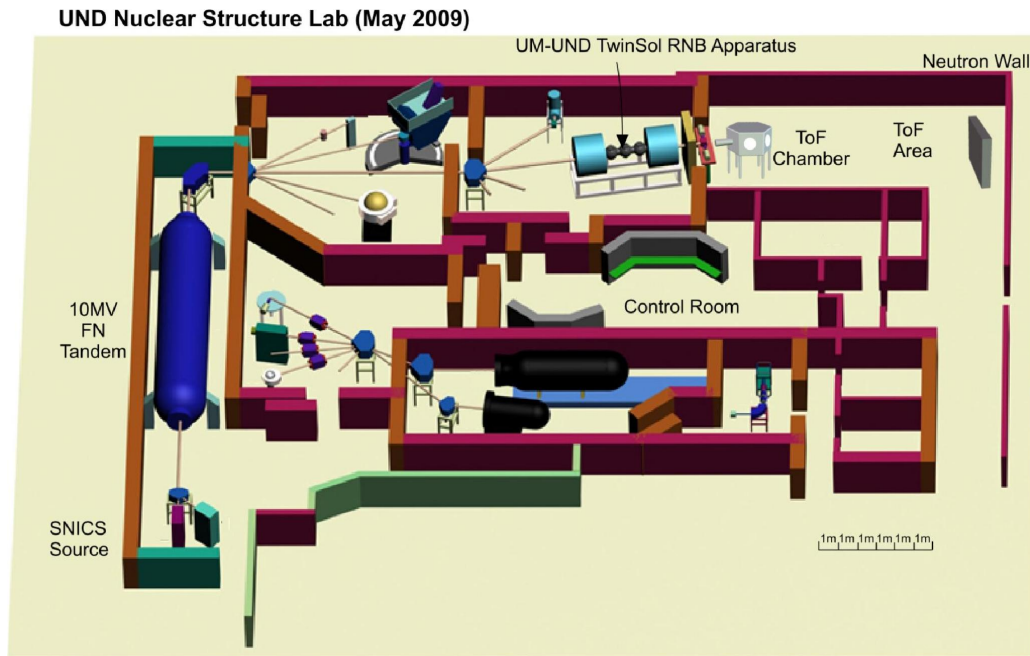


Figure 1.2: Layout of UND nuclear structure laboratory.

This device utilizes a pair of in-line, large bore (30 cm), air-core persistent-mode superconducting solenoids which have magnetic field strength up to 6 tesla. It is capable of producing, collecting, transporting and focusing low-energy secondary radioactive nuclear beams. Reactions induced by these secondary ions relevant to the production of energy and synthesis of elements in astrophysical processes are

studied using several particle-detection systems.

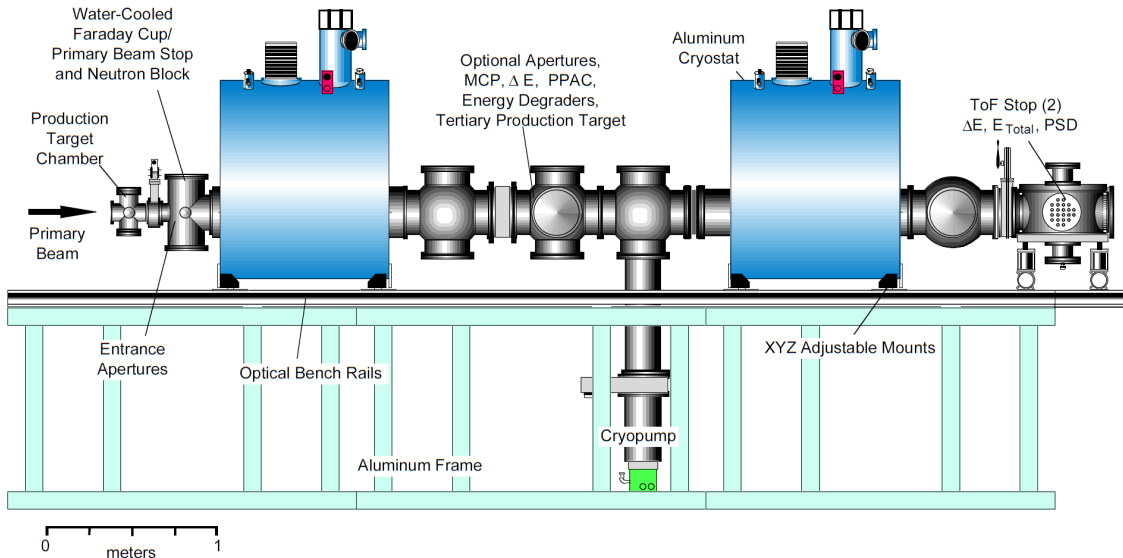


Figure 1.3: The layout of original *TwinSol* apparatus.

Figure 1.3 shows that the intensive primary beam is stopped in a carbon faraday cup attached to an extended tungsten-alloy beam stop, which also serves as a small angle γ and neutron block. The scattered primary beam ions produced at small angles (in the most intense charge state) normally are stopped in a small circular blocking element located at the downstream focus of these unwanted background ions [FDB03]. *TwinSol* can be operated in two different modes (Figure 1.4). One is called the cross-over mode. In this mode, the primary RNB ions of interest along with other ions with the same magnetic rigidity (analogs) are typically focused using the first solenoid, which acts as a large aperture magnetic ion-optical lens, through a small aperture at a cross-over point between the two magnets. These ions are then refocused onto reaction targets located in one of several secondary reaction chambers located downstream of the second solenoid. One also can operate *TwinSol* in parallel mode when the system can be operated without an intermediate cross-over

focus. The two magnets combine to form a thick lens system without an intermediate image. In this mode, *TwinSol* can be used as a single high $B\rho$ lens to bend higher magnetic-rigidity ions.

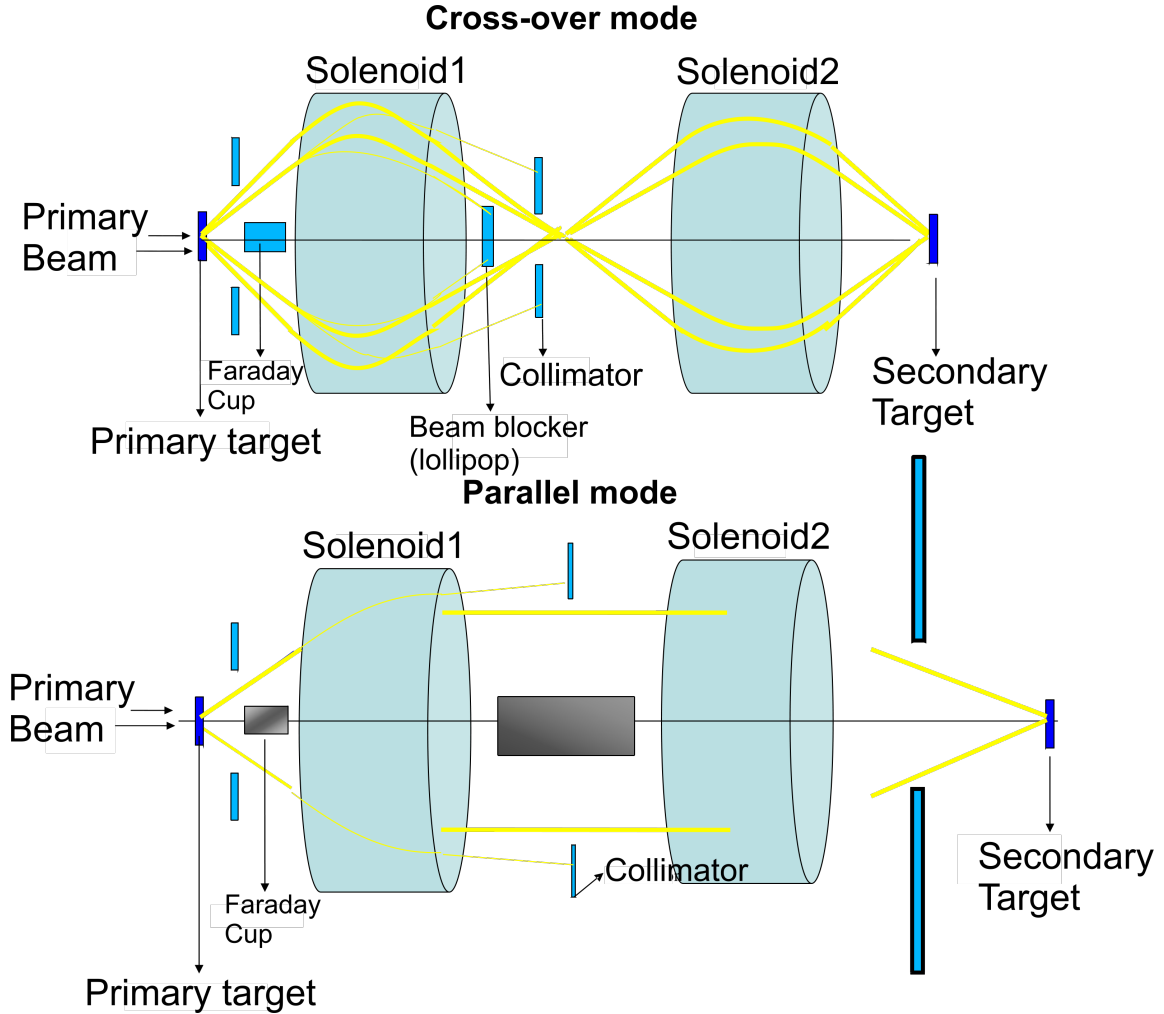


Figure 1.4: Two operation modes of *TwinSol*. Top: Cross-over mode. Bottom: Parallel mode.

1.3 Limitations in *TwinSol* RNB Reaction Studies

1.3.1 Energy spread in *TwinSol*

A common problem associated with the production of low-energy secondary radioactive nuclear beams is that there is a large energy spread introduced in the RNB by the thick production target often required, the energy spread created by gas-cell

windows, and the large kinematic energy shifts when using a light production target. The latter is a major limitation for a solenoid-based RNB apparatus (UM-UND *TwinSol* apparatus) which has a very large angular acceptance, typically about 2° - 6° [Hao07]. This leads to a large energy spread in the secondary RNB, e.g. 1 MeV in a 34 MeV ${}^7\text{Be}$ beam (Figure 1.5), and limits the type of experiment that can be done [Amr07].

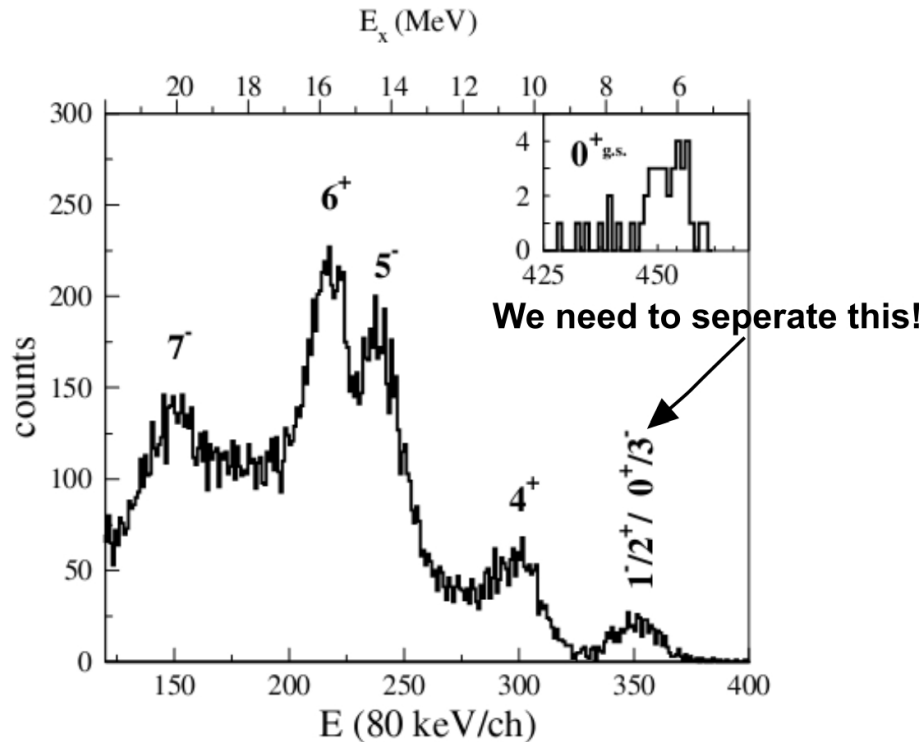


Figure 1.5: ${}^{16}\text{O}$ energy states from the reaction ${}^{12}\text{C}({}^7\text{Be}, {}^3\text{He}){}^{16}\text{O}$. Several excited states cannot be separated due to poor energy resolution [Amr07].

1.3.2 ${}^8\text{Li}$ inelastic scattering

In studies of elastic and inelastic ${}^8\text{Li}$ scattering near the Coulomb barrier on Ni and Pb, for example, a “ghost” peak in the ${}^8\text{Li}$ beam due to its 0.98 MeV excited state needs to be separated from its ground state to permit study of the Coulomb and nuclear excitation of ${}^8\text{Li}$ to this state and deduce the $B(E2)\uparrow$ value. (Figure 1.6; [Bro91], [Mu02]) We need to develop a method to compensate this kinematic energy

spread to separate this excited state from its ground state, and similarly for other RNB reactions (Figure 1.5).

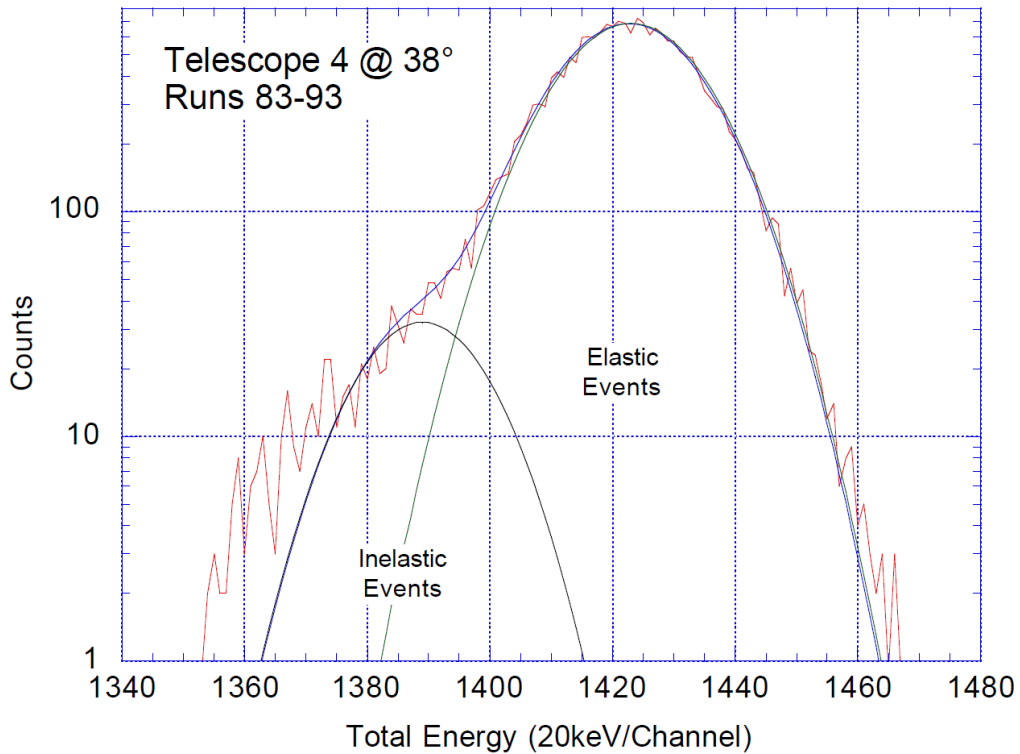


Figure 1.6: Data showing ${}^8\text{Li}$ RNB scattered from a Pb target at $E=30.5$ MeV, $\theta=38^\circ$ [Mu02]. A fraction of the incident ${}^8\text{Li}$ RNB is scattered inelastically into its first excited state. Due to the poor energy resolution one can only see a tail extended from the ground state peak.

1.4 Main Goals

The main goal of this thesis was to develop and test methods for reducing the energy spread in low-energy short-lived secondary radioactive nuclear beams produced in the *TwinSol* system and to reduce interference from spurious ions in the RNB. Two methods have been proposed to reduce the energy spread and were tested as part of this thesis. One method is to use a tapered energy-loss absorber placed off-focus to compensate the energy spread due to kinematic shifts. The other method is to use time-of-flight measurements utilizing both intrinsic beam bunching and cross-

over-detector event-by-event time-of-flight (ToF) measurements for energy-spread compensation.

As part of the latter we developed an oil-free ISO-250 test chamber setup to test various timing detectors (MCP and Si detectors) at UM. Related to this we also developed a CAMAC-based multi-dimensional USB2-based data acquisition and analysis system. (See Appendix C)

To further assist with the above goals, we also developed a method using a modified version of Gafchromic[®] EBT medical imaging film to image low-energy radioactive and other ion beams. It can be used to assist optimizing the collimation needed to minimize unwanted background ions, and to accurately determine the ion-optical alignment of RNB production and transport systems. Employing this film allows effective imaging of beam profiles and its relative intensities throughout the beam-transport system and especially at locations not readily accessible to electronic imaging detectors.

CHAPTER II

Energy-spread Compensation In A Solenoid-based Secondary Radioactive Beam Apparatus

2.1 Introduction

In dipole-based high-energy RNB systems [Baz02], one can compensate the energy spread in the secondary RNB to some extent by introducing a “wedge” shaped absorber at the dispersive focal plane between two dipole magnets (Figure 2.1). Alternatively, one can use dispersion matching where the energy spread of the RNB is canceled by a dipole spectrometer in an energy-loss mode.

Unfortunately, these highly effective dispersion-matching techniques [She99] cannot be readily applied to a solenoid-based system because conventional solenoids are always dispersive even if the direction of the magnetic field is reversed (See [Bec89] for an exception to this). Energy-spread compensation using a wedge absorber appears possible for a solenoid. Finally, energy compensation also can be achieved by fast beam pulsing ion time-of-flight (ToF) or ion-by-ion time-of-flight measurements using a timing detector over several meters at the few- or sub-nanosecond level. However, the ion-by-ion method is typically count-rate limited, about $10^5/s$ or less [Odo94]. Although dispersion matching is as yet not practical for solenoid-based RNB systems, both energy-loss absorbers and ToF methods for energy compensation should be achievable and were tested for this thesis.

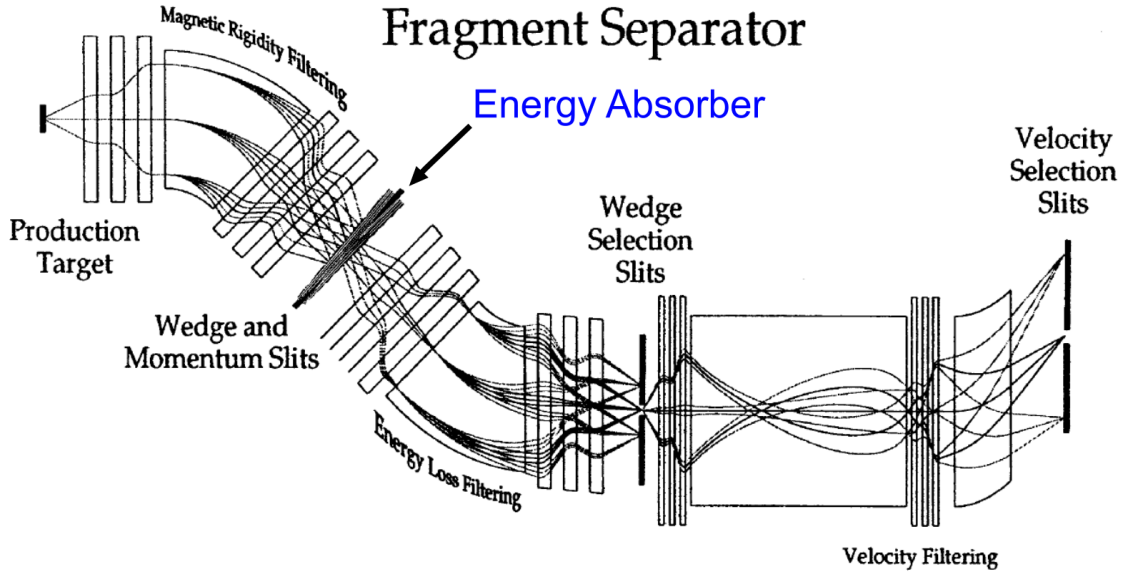


Figure 2.1: Schematic of a dipole-based fragment separator. The first section runs from the production target to the wedge energy-loss absorber and momentum slits, which set the momentum acceptance. The fragments selected in magnetic rigidity are then refocused on the wedge selection slits by the second section. Finally, an optional third section provides an additional selection by using a velocity filter before the fragments are sent to a detection system, a reaction target or further beamline. [Baz02]

In particular, the absorber technique also should be applicable in the case of a twin-solenoid-based RNB system, where the “wedge” absorber is replaced with a radially symmetric absorber with a radius-dependent thickness (Fig. 2.2). We have done a first set of in-beam tests of such a system.

2.2 Apparatus Layout

In Fig. 2.3 we show a schematic layout of the *TwinSol* system together with a realistic set of ion-optical ray trace orbits with an optimum energy absorber inserted. The RNB used in this test experiment, which is a typical beam used in nuclear reaction experiments, is a 34 MeV ^7Be beam. This RNB is produced at a front ^3He gas-cell production target (Fig. 2.3) via the $^6\text{Li}(^3\text{He},d)^7\text{Be}$ reaction [Bas81] utilizing inverse kinematics with a 37 MeV primary ^6Li Beam.

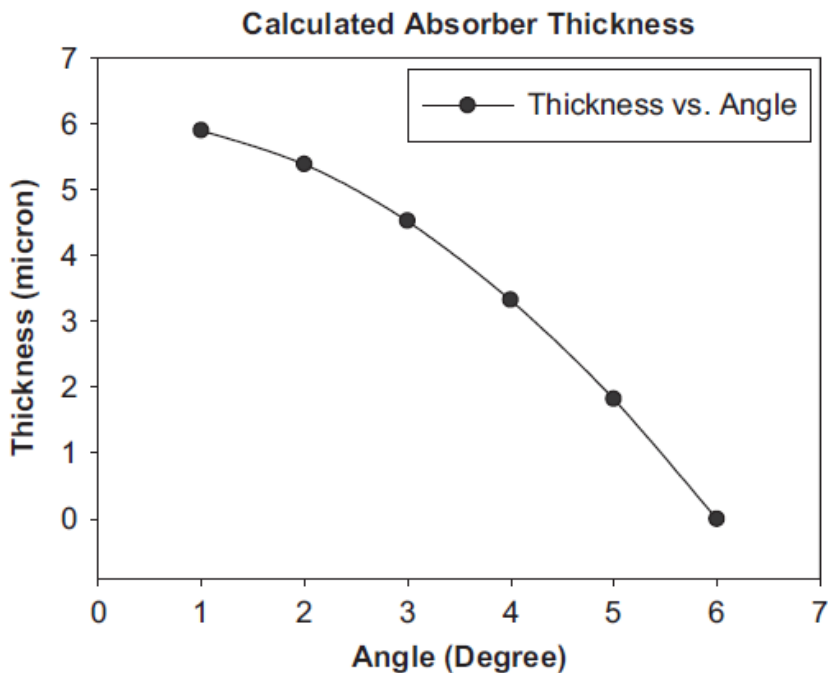


Figure 2.2: Absorber (polyester) thickness vs. 34 MeV ^7Be RNB trajectory angle.

2.3 Energy Compensation Test

While the use of inverse kinematics allows the use of a gas cell and in addition can increase the yield of ^7Be due to kinematic focusing, it also produces a large kinematic energy spread of the outgoing ^7Be beam, which is collected over a range of lab angles from 2° to 6° (Figures 2.2 and 2.3). This yields a fairly intense ^7Be beam with a fairly large energy spread (ca.1 MeV full width at half maximum [FWHM]), limiting the type of RNB reactions one can study. Reduction of the RNB energy spread to a few hundred keV without loss of beam intensity would be highly advantageous. Unfortunately, the ion-by-ion ToF method which is likely to give the best energy-spread compensation (see below), requires the reduction of the RNB intensity by $\times 10$ or more. Therefore, we examined the use of a tapered energy absorber located off-focus (Figure 2.3) to provide energy compensation without a reduction in beam

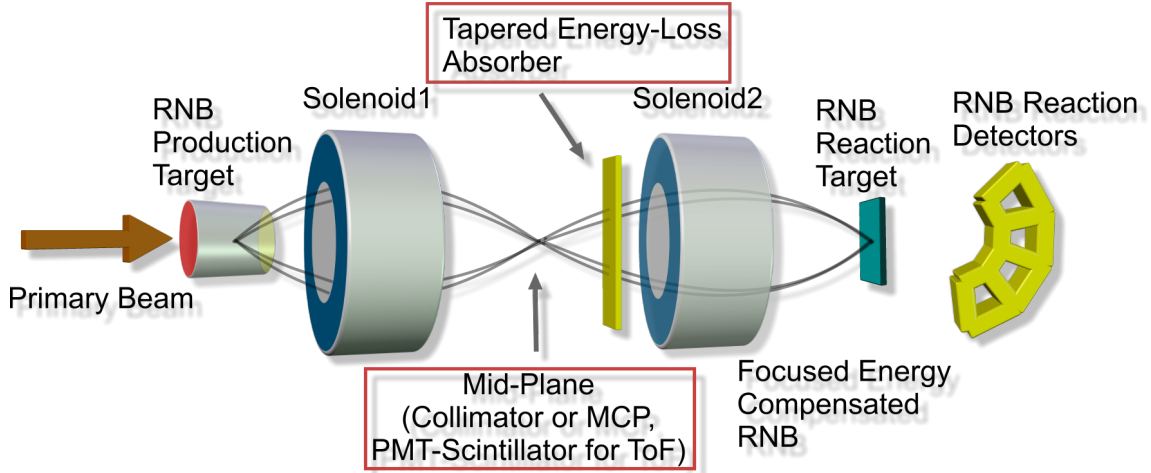


Figure 2.3: *TwinSol* layout with energy compensating absorber.

intensity.

An existing ion-optical ray-tracing code [Mu02] was modified to allow the insertion of radially tapered energy-loss absorber at various points along the RNB trajectories to compensate for ca. 1 MeV kinematic shift *vs.* emission angle at the production target. Using an optimal absorber made up of 1.5 μm polyester layers and located at a suitable off-focus location just beyond the cross-over point (Fig. 2.3) enables in theory a large degree of energy compensation (Figure 2.2). However, this would be an ideal situation since it neglects the energy spread arising from the gas cell due to its 2.4 μm titanium windows (about 50 - 100 keV each). Nonetheless, it appeared worthwhile to pursue a first set of in-beam tests in order to determine the feasibility of this method.

2.4 In-beam Energy-compensation Absorber Tests

During a nuclear-reaction experiment utilizing the ^7Be beam noted above, we did several tests using an absorber as shown in Figure 2.2. Instead of using a continuous absorber, we opted, for practical considerations, to use a set of thin, fixed-thickness

absorbers (see above), overlaid as needed, covering a radial set of holes in an absorber aperture (Figure 2.4) located after the cross-over collimator as indicated in Figure 2.3. The holes were spaced at radii corresponding to a particular RNB production angle suitable for a certain thickness of available absorber, based on the ray-tracing calculations and the kinematic shift of ${}^7\text{Be}$ (Figure 2.6).

There exist two sets of absorber rings on the absorber plate, enabling the insertion of two different absorbers into the beamline without breaking the vacuum. In the middle of the absorber plate, we also placed a silicon-surface-barrier detector to measure the energy and profile of the ${}^7\text{Be}$ beam.

In addition, we also modified a standard ISO-250 plate (Figure 2.5) to accommodate several LEMO feed-throughs and a bore-press hole for a 1" CAJON fitting at the plate center. A supporting shaft attached to the absorber plate, together with an extension ISO-250 tube, can slide through this vacuum fitting. With this setup, we were capable of changing the absorbers and moving the silicon detector to different positions in the beam.

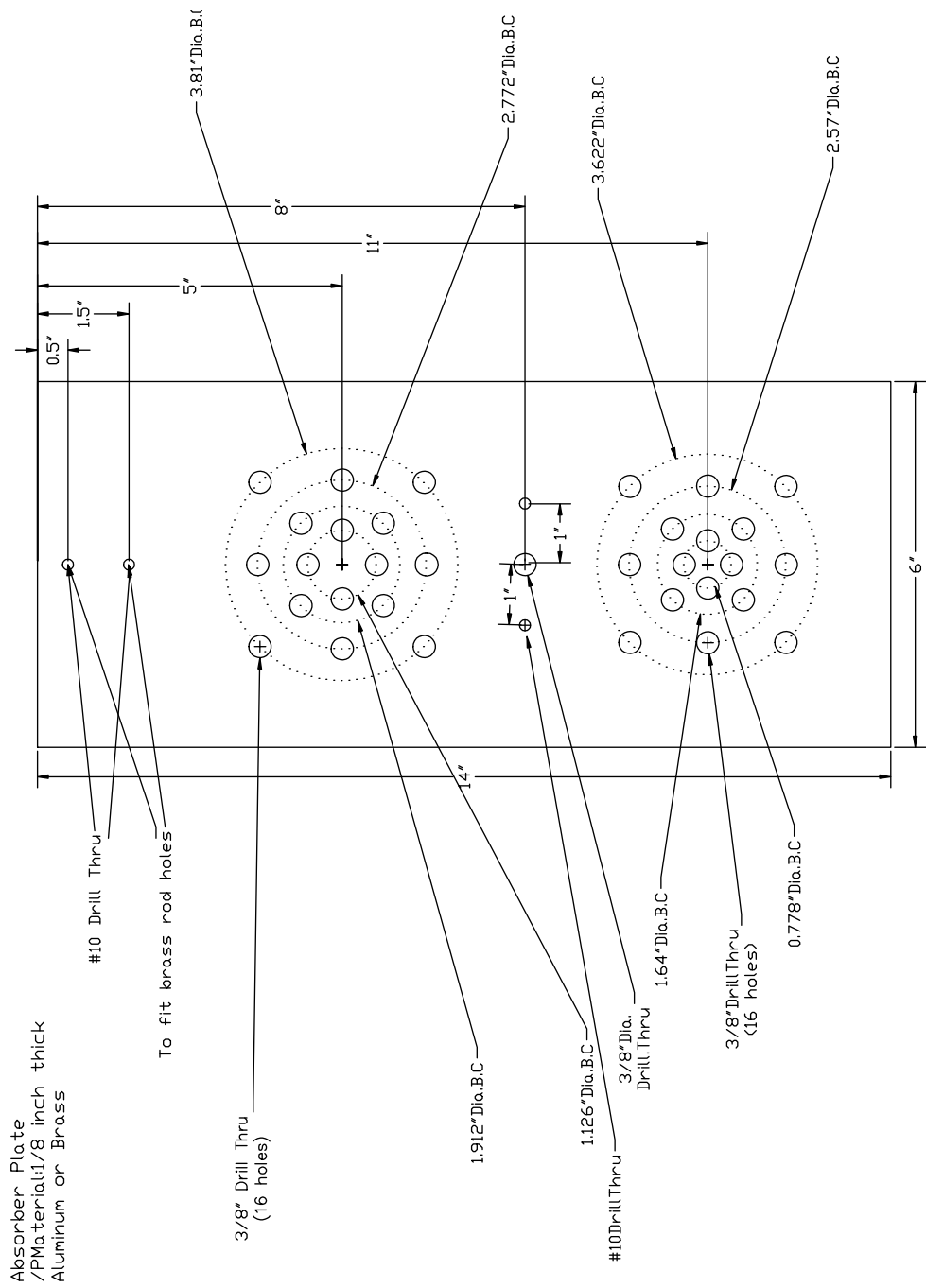


Figure 2.4: Print of absorber plate. Cocentric ring of holes are covered by radially symmetric absorbers with a radius-dependent thickness.

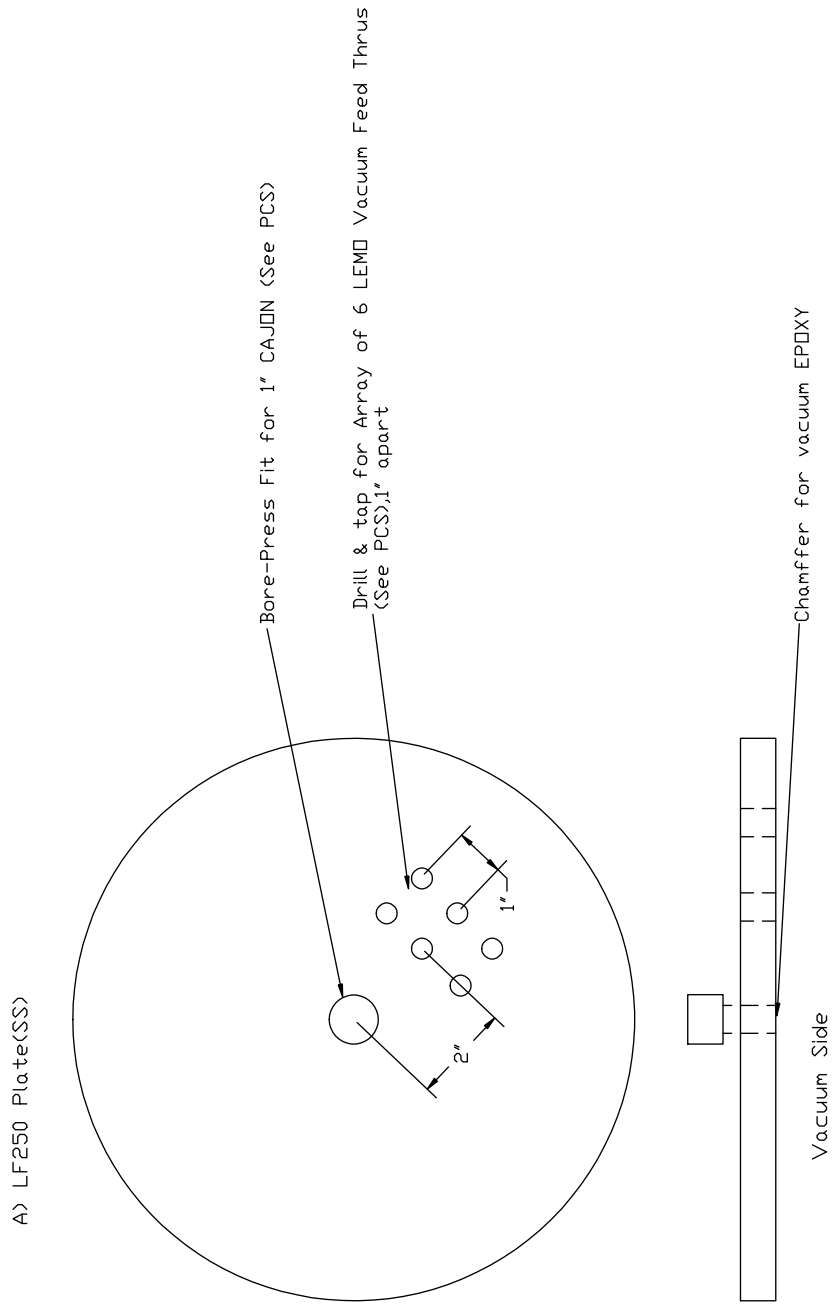


Figure 2.5: Print of modified ISO-250 plate with LEMO feed through. A CAJON fitting is placed at the center of this plate.

34 MeV ^7Be ToF Ray Tracing

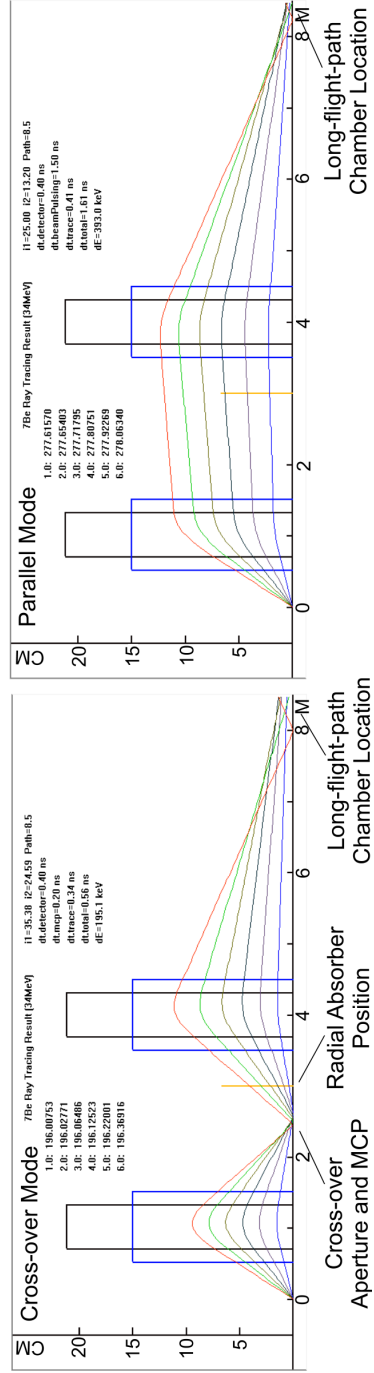


Figure 2.6: Ray trace calculation for ^7Be beam through *TwinsSol*. The position of absorber plate in the beam is marked and the radius of each ray at the absorber position is calculated.

The focus and energy distribution of the ^7Be RNB at the back focus were measured by a ΔE -E-PSD (position-sensitive detector) silicon detector telescope [Mu02]. It provided ion identification, ion energy and XY position information. An image of ^7Be ions is shown in Figure 2.8 together with the corresponding energy distribution for a run with a cross-over aperture in place (1.5 cm diameter) but without energy-loss absorber. A “shadow” of the faraday-cup support [Mu02, Mu99] also is seen. However, such an absorber, at least a thin one, does not produce any significant distortion in the beam image. (It was feared, based on our previous calculations, that multiple scattering in the absorbers combined with the high axial field of the solenoid would produce a poorly focused RNB image.) Despite the good focus, little if any improvement in the RNB ion-beam energy spread is observed, even if the absorber is slightly displaced to adjust for the misalignment of optical and magnetic axes. We will discuss the reasons for this later, since it can impact the decision on the optimum method to produce a specific type of RNB for a given experiment using solenoids.

2.5 Limits Due to Energy Profile and Production Reaction

Our assumption was that the main source of energy spread was caused by the kinematic shift of ^7Be energy with an angle. In order to verify this, we did an energy scan using a small ΔE -E telescope Si detector of the out-of-focus ^7Be beam vs. radial position (angle) at the absorber position (Figure 2.3). The results shown in Figure 2.7 indicate that it is only correct at the largest angle. However, the energy profile of the beam also involves the yield of the RNB production with angle. Thus there is a significant contribution to the ^7Be beam from small angle production, exhibiting anomalously lower energy than expected. In this case, it is not appropriate to use

the absorber based only on the calculated kinematic shift.

A scan of ${}^7\text{Be}$ beam intensity vs. angle at the absorber position, as discussed earlier, indicates a slight misalignment (ca. 5 mm) of the solenoid's optical and magnetic axes at the absorber position. Hence, the set of measurements shown in Fig. 2.7 were done with the absorber slightly offset. Nonetheless, the anomalous energy distribution of the ${}^7\text{Be}$ beam limited the effect of the absorber on the energy spread. Future in-beam tests are planned to better understand the origin of the anomalous ${}^7\text{Be}$ energy and/or to eliminate the ${}^7\text{Be}$ yield from small angles or large angles, as appropriate, using a collimator.

The reaction chosen to produce ${}^7\text{Be}$ was the ${}^3\text{He}({}^6\text{Li}, {}^7\text{Be})\text{d}$ reaction, i.e. (${}^3\text{He}, \text{d}$) done in inverse kinematics. This reaction has a large cross-section and was expected, based on empirical extrapolation to small angles of measured cross-sections [Bas81], to have significant yield over the entire range of ${}^7\text{Be}$ production angles (2° - 6°). Since this did not appear to be the case (Fig. 2.7), we investigated more carefully, using DWBA calculations to estimate the forward-angle ${}^7\text{Be}$ yield better. The calculations indicated that the empirical extrapolations were not correct, and this combined with the center-of-mass (c.m.) to lab angle conversion for inverse kinematics basically can explain the yield observed (Figure 2.7). It suggests that implementation of energy-loss absorbers for energy compensation requires more accurate calculations and detailed measurement of the RNB production yields at small angles, together with consideration of any misalignment of the optical and magnetic axes [Hao07]. In order to facilitate the latter and also reduce spurious background ions in the designed RNBs, we developed a new, unique method using a new type of medical x-ray imaging film to image low-intensity RNBs. The details of this will be investigated in Chapter VI.

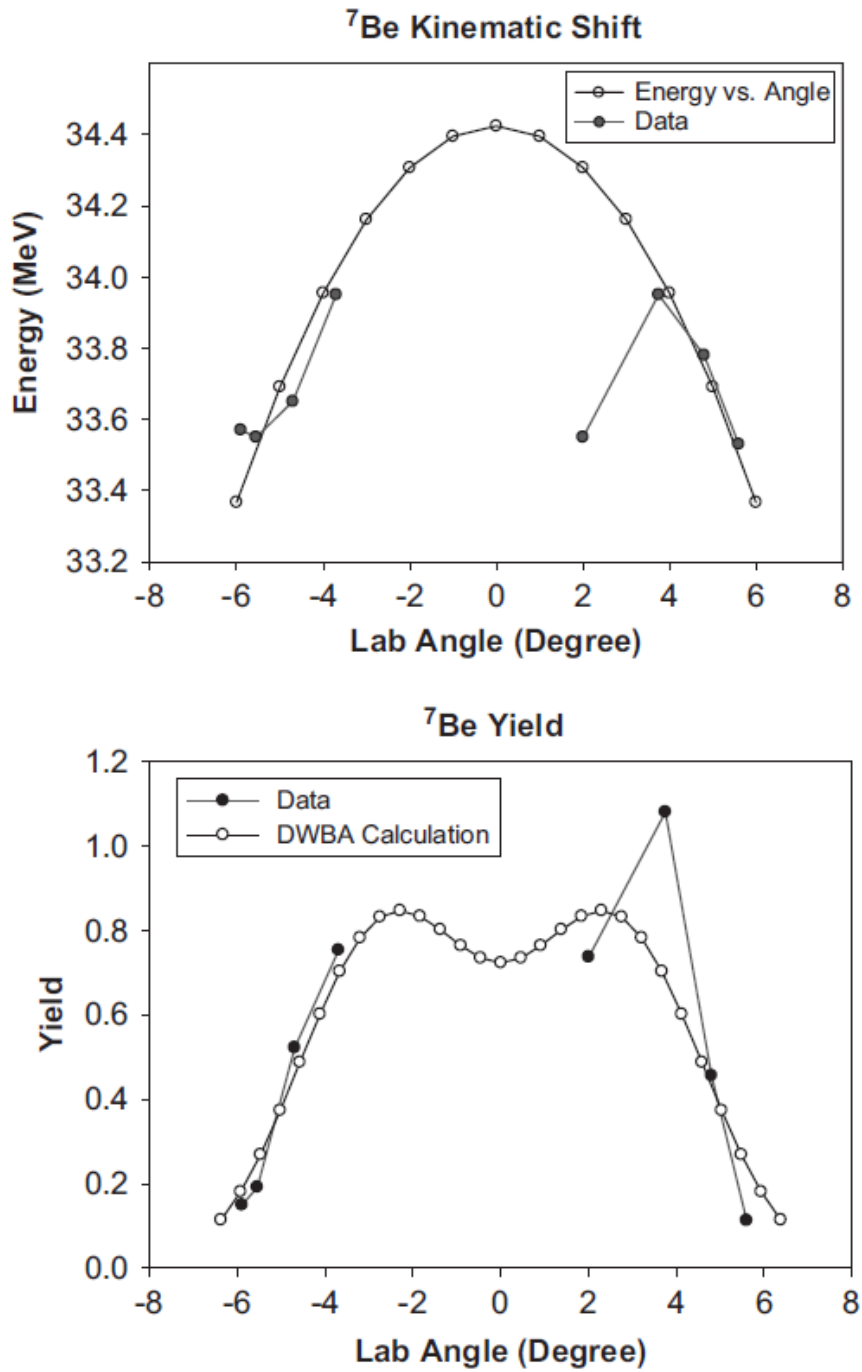


Figure 2.7: Top: Kinematic prediction and energy scan. Bottom: Yield vs. angle of ^7Be beam.

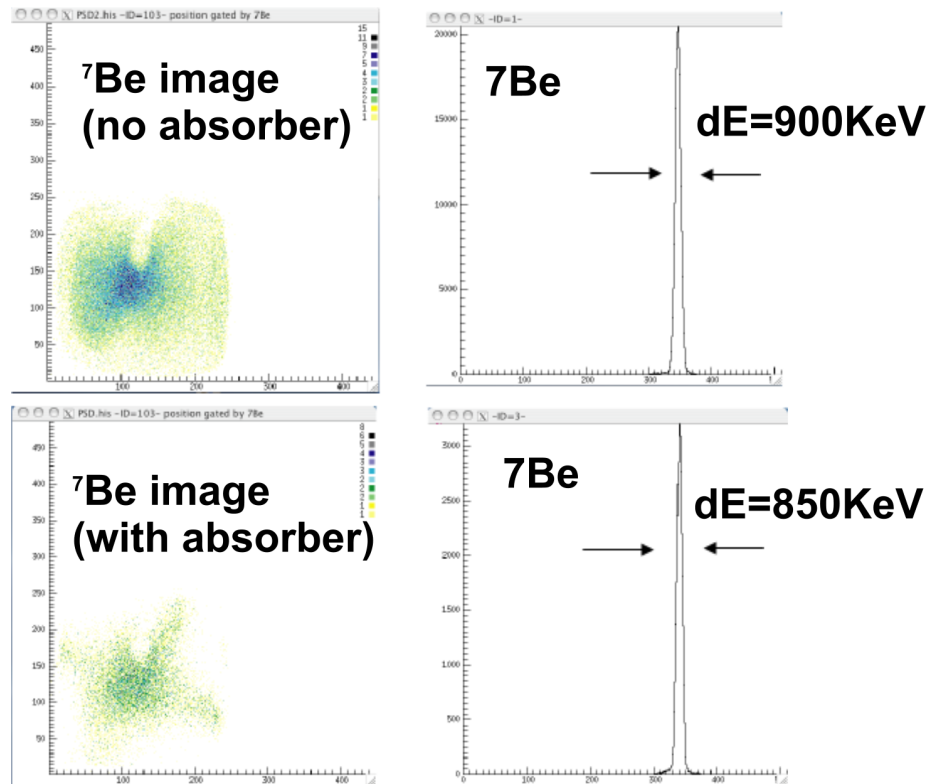


Figure 2.8: ^7Be beam imaging on a $25\text{ mm} \times 25\text{ mm}$ PSD in back chamber.

CHAPTER III

Time-of-flight(ToF) Measurement Using Intrinsic Beam Bunching

3.1 Introduction

Besides the absorber energy-compensation method, another method to improve the energy resolution for the *TwinSol* RNB system is the measurement of time of flight of particles going through the apparatus to achieve energy of the RNB particles event by event. The first set of measurements using this method was done using intrinsic primary beam bunching.

3.2 Intrinsic Primary Beam Bunching

As part of the earlier UM-UND RNB project, the FN-Tandem accelerator was upgraded to deliver pulsed beams in ca. 2 nanosecond-wide bunches separated by ca.100 nsec. We employed this intrinsic beam bunching to perform a first set of time-of-flight measurements. The radio frequency (RF) signal of the beam-buncher is used as a timing start (or stop) signal, while timing signals from detectors in several vacuum chambers along the beam line are used as stop (or start). However there is an inherent uncertainty spread of at least 1.5 nsec between the RF and the actual time of the primary beam bunch. Therefore, the best timing resolution using beam bunching is determined by:

$$(3.1) \quad \Delta t_{intrinsic} = \sqrt{\Delta t_{buncher}^2 + \Delta t_{detector}^2}$$

$\Delta t_{buncher}$ is the timing uncertainty of the RF buncher (1.5 to 2 nsec), and $\Delta t_{detector}$ is the timing resolution of the detectors as (typically <2 nsec).

To further improving the timing resolution using the intrinsic beam bunching, we designed, built, and installed a new 32" ISO-250 based aluminum vacuum chamber behind a neutron shielding wall with an extended beam line about 8 m away from the production target as shown in Figures 3.1 and 3.2. It provides about 2.5 m more time-of-flight path than the original target chamber which was 5.5 m from the production target (Figure 1.3). This upgrade was a major part of this thesis project.

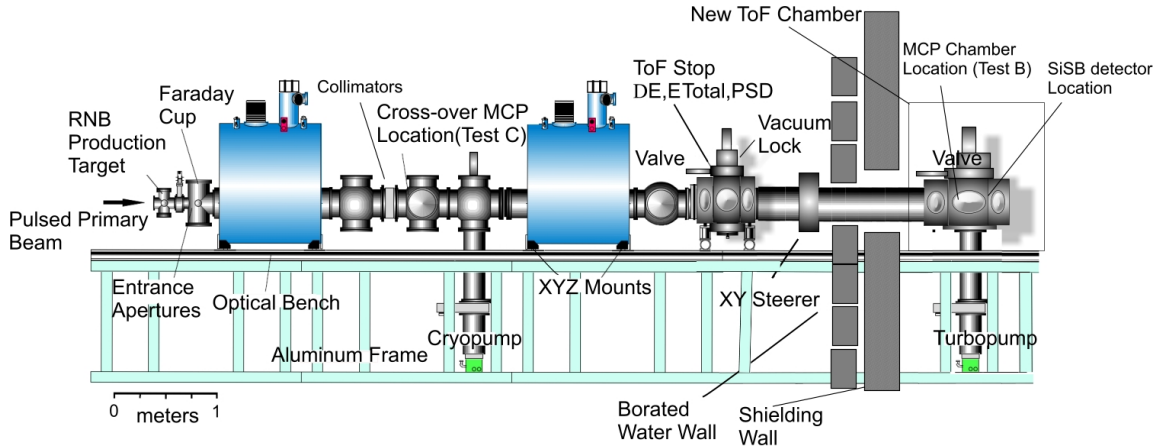


Figure 3.1: Layout of *TwinSol* apparatus with extended beam line and new time-of-flight vacuum chamber.

The time-averaged pulsed beam has an intensity of about 30% to 50% compared to that of an unbunched beam. We have used such a bunched beam in previous experiments, for example, the break-up of ^8B on a nickel target [GUI00]. ^7Be , one of the contaminant beams created during the production process of ^8B , also is the residual nucleus from the breakup of ^8B . In order to distinguish breakup events from contaminant events, we measured the time difference between the arrival of a ^7Be

upon detectors and the FN tandem's bunched beam. Because ${}^7\text{Be}$ and ${}^8\text{B}$ arise from production events with different velocities, ${}^7\text{Be}$ produced from ${}^8\text{B}$ breakup events has a time signature matching the ${}^8\text{B}$ RNB and not the contaminant ${}^7\text{Be}$. In this way, we can effectively eliminate the unwanted ${}^7\text{Be}$ events.

During the ${}^8\text{Li}$ Coulomb excitation experiment we will discuss in Chapter 5, the 0.98 MeV excited state of ${}^8\text{Li}$ from the ${}^8\text{Li}$ production reaction needs to be separated from the same excitation energy state generated from Coulomb excitation of ${}^8\text{Li}$ on a gold target. Since the ground state (2+) of ${}^8\text{Li}$ and its first excited state (1+) have 0.98 MeV energy difference, the velocities, hence the time of arrival at detectors, are slightly different from the production target. However the excited state ${}^8\text{Li}$ originating from Coulomb excitation on the gold target shares the same time of flight with its ground state. In this case, we are able to use intrinsic time-of-flight method or event-by-event ToF to distinguish both particles because of their different flight time.

3.3 Ray-trace Calculations

We developed a program to calculate particle rays through the *TwinSol* apparatus and to calculate time of flight and the corresponding achievable energy resolution.

The ${}^8\text{Li}$ production reaction we chose is ${}^7\text{Li}({}^9\text{Be}, {}^8\text{Be}){}^8\text{Li}$ with a 30 MeV ${}^7\text{Li}$ primary beam. The corresponding kinematics calculation for angles from 1° to 6° is shown in Table 3.1. Ray traces of ${}^8\text{Li}$ from 1° to 6° with the new long (8m) flight path for a ${}^8\text{Li}$ beam of average energy of 28 MeV produced from the production reaction of ${}^7\text{Li}({}^9\text{Be}, {}^8\text{Be}){}^8\text{Li}$ with 30 MeV primary ${}^7\text{Li}$ beam are shown in Figure 3.3.

Assuming the spread of the beam buncher at 1.5 nsec and an optimal time resolution of silicon detectors at 0.4 nsec, the program shows that the best energy resolution

Angle	^8Li Energy (MeV)
1°	28.289
2°	28.263
3°	28.219
4°	28.157
5°	28.078
6°	27.982

Table 3.1: Kinematic calculation of ^8Li energy for production angles from 1° to 6°.

that can be achieved is 339 keV. This program also calculates time of flight of ^8Li particles at each angle and lists them in the output. Additional calculations and a listing of the code are given in Appendix A.

3.4 ToF Experiment with Beam Bunching

The new *TwinSol* beamline configuration (Figure 3.1) was used and the two solenoids were operated in cross-over mode. A suitable collimator was put at the cross-over position to further purify the beam after the second solenoid.

Since a percentage of the ^8Li secondary beam is produced in its first excited state, the first solenoid is tuned so that primarily ^8Li in its ground state is focused at the cross-over point. Specific information of the solenoids setting is listed in Table 3.2. The negative sign in the second solenoid field setting means the fields of the two solenoids are reversed.

	Sol 1	Sol 2
Current	46.80 A	32.75 A
Field	2.685 kG	-1.956 kG

Table 3.2: Specific solenoid settings.

Four detectors were used in this experiment. Specific information about each detector is shown in Table 3.3. The configuration of all detectors is shown in Figure 3.4.

Prior to the in-beam experiment, the detectors were illuminated with a ^{228}Th α

Detectors mounted	ID	Area (mm ²)	Thickness (um)	Voltage (V)	Leakage current (uA)
Detector A	36-235D	450	1000	295	1.36
Detector B	31-485A	450	1000	200	0.69
Detector C	40-183B	450	1000	110	0.61
Detector D	31-184J	450	1000	500	1.36

Table 3.3: List of detectors.

source. Table 3.4 shows the source information. The data from this test was used to calibrate the detectors' signal response vs. particle energy.

Parent	Energy (MeV)	(%) ²²⁸ Th Activity	Activity (μ Ci)
²²⁴ Ra	5.685	92%	1.78
²²⁰ Rn	6.288	94%	1.82
²¹⁶ Po	6.778	93%	1.80
²¹² Bi	6.051	32%	0.62
²¹² Po	8.785	60%	1.16

Table 3.4: α decay activities for the ²²⁸Th source.

The detectors' calibration information is listed in Table 3.5. Detector C was used as the major detector to monitor the secondary ⁸Li beam at zero degrees with the beam reduced. A schematic illustration of the electronic setup for obtaining energy vs. ToF histogram is shown in Figure 3.5. The start and stop are signals inverted to avoid invalid ToF signals without an ion in the Si detectors.

Detector	E0	E1
A	-0.6076	0.00867
B	-0.8592	0.00892
C	-0.78642	0.00823
D	-1.00455	0.00905

Table 3.5: Detector calibration results ($E = E0 + E1 \times CH$ MeV).

The secondary beam consists of both the ground state and the first excited states of ⁸Li beams, and other analog ions at the same magnetic rigidity. Those ions are determined by

$$(3.2) \quad E = kq^2/A$$

where k is a constant, q is the atomic charge and A is the atomic mass for a particular ion. By constructing the histogram of two-dimensional ToF versus energy, we are able to identify different particles with distinct energy and time signatures as shown in Figure 3.6.

The longer flight path improved the ToF resolution, such that the excited state ^8Li group is clearly separated from its ground state. Figure 3.7 shows the projected ^8Li energy spectrum from Coulomb excitation on a $475 \mu\text{g}/\text{cm}^2$ gold target at $\theta=30^\circ$ with gaussian fits of ground and first excited states (see Chapter V).

3.5 Conclusion

Although the intrinsic primary and hence RNB beam pulsing is limited to 1.5 nsec at best, with a suitably long-flight path, as feasible with a solenoid system [Odo94] including the *TwinSol* system, a useful improvement in effective RNB energy resolution is possible. This has the advantage that no event-by-event ion “start” detector (MCP-foil, PPAC or PMT-scintillator) and their count rate limits (10^5 s^{-1} or so) are needed as only the low-rate (few per second) RNB reaction products are used as the initial ToF trigger.



Figure 3.2: Picture of new ToF chamber constructed as part of this thesis project.

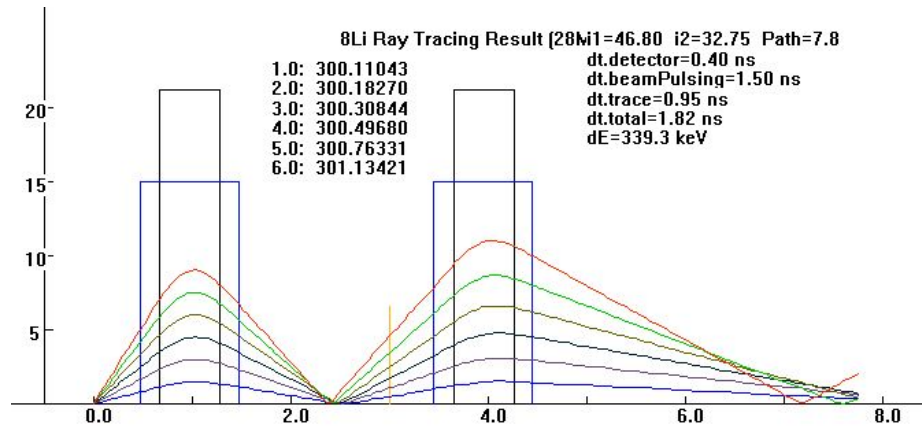


Figure 3.3: Ray trace calculation of 28 MeV ^8Li from 1° to 6° through *TwinSol*.

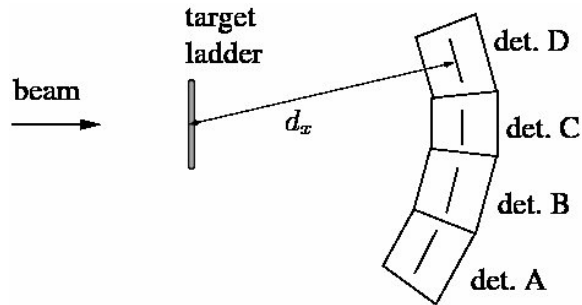


Figure 3.4: Silicon detector array

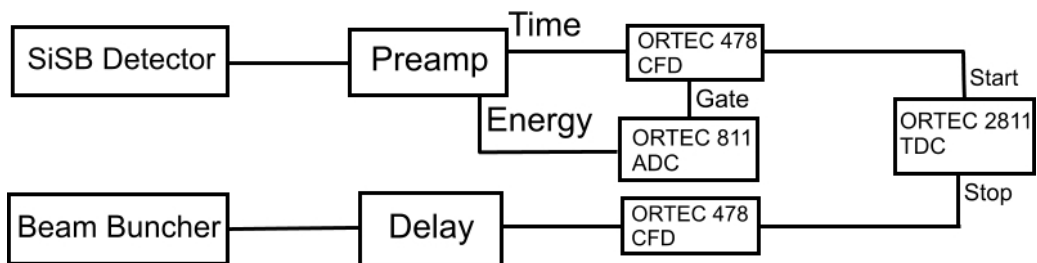


Figure 3.5: Schematic illustration of the electronic setup

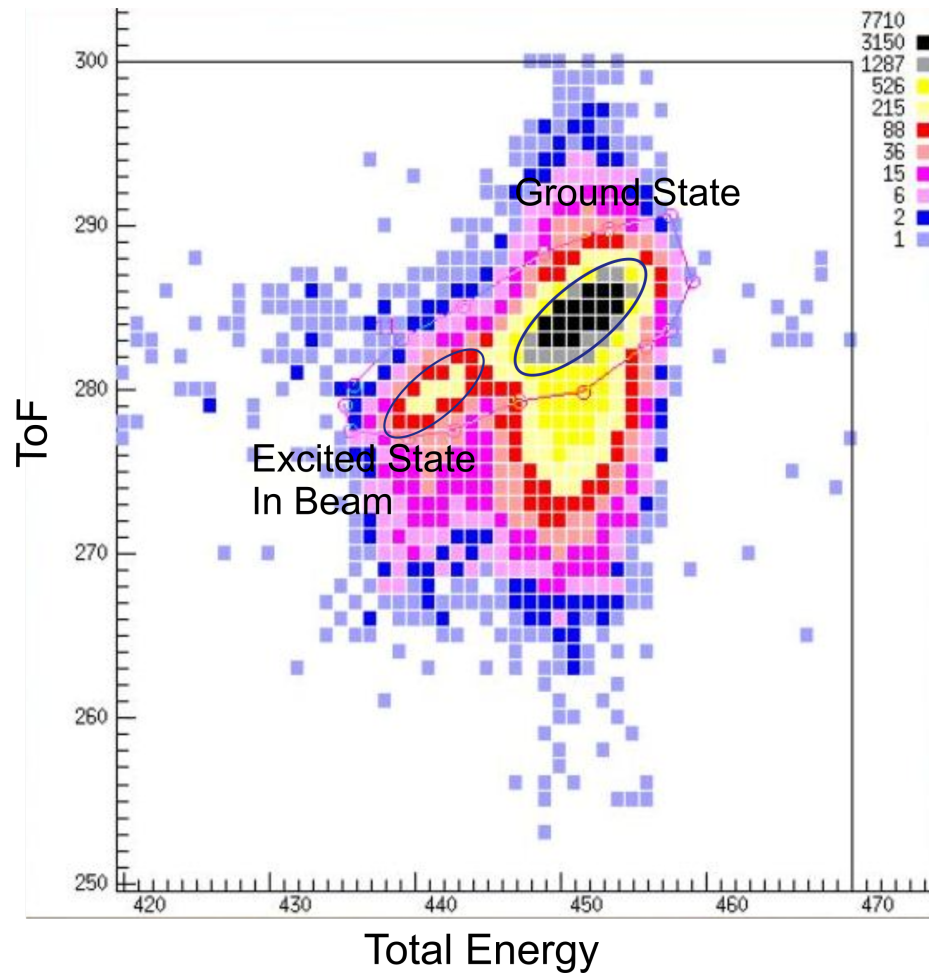


Figure 3.6: Time of flight vs. total energy histogram at zero degree (80 keV/ch for energy and 0.5 nsec/ch for ToF).

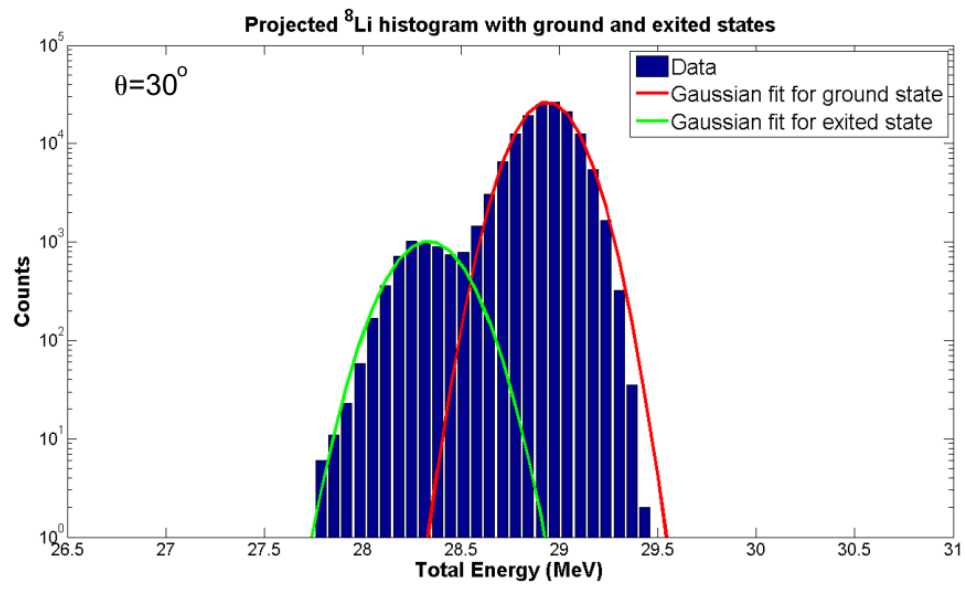


Figure 3.7: Projected ${}^8\text{Li}$ energy spectrum ($\theta = 30^\circ$).

CHAPTER IV

Time-of-Flight(ToF) Measurement Using A Micro-channel Plate Detector

4.1 Introduction

When a less intense radioactive nuclear beam can be utilized, it should be possible to use a precision sub-nanosecond ToF measurement from a suitable mid-plane cross-over timing detector to the ΔE -E Silicon detector array used for reaction-product detection in the back chamber. This then could be used to compensate event-by-event for the energy spread in the RNB (Fig. 1.6). One of the fastest timing detectors we can use for this is a micro-channel-plate detector (MCP) and a foil.

An MCP consists of an array of miniature electron multipliers and can be used for detection of particles and impinging radiations through secondary electron emission [Joe79]. It is coupled with a thin foil to produce secondary ions and can be used as a fast particle timing device. The sub-nanosecond timing resolution of an MCP makes it suitable for high resolution time-of-flight experiments if the MCP counting rate is below 10^6 particles per second [Gre75].

A typical MCP configuration shows electron multipliers oriented parallel to one another with channel diameters in the range 10-100 μm and length to diameter ratios between 40 and 100 (Fig 4.1). Channel axes typically are normal to, or biased at a small angle to the MCP input surface. The channel matrix is usually fabricated

from lead glass, treated in such a way as to optimize the secondary electron emission [Joe79].

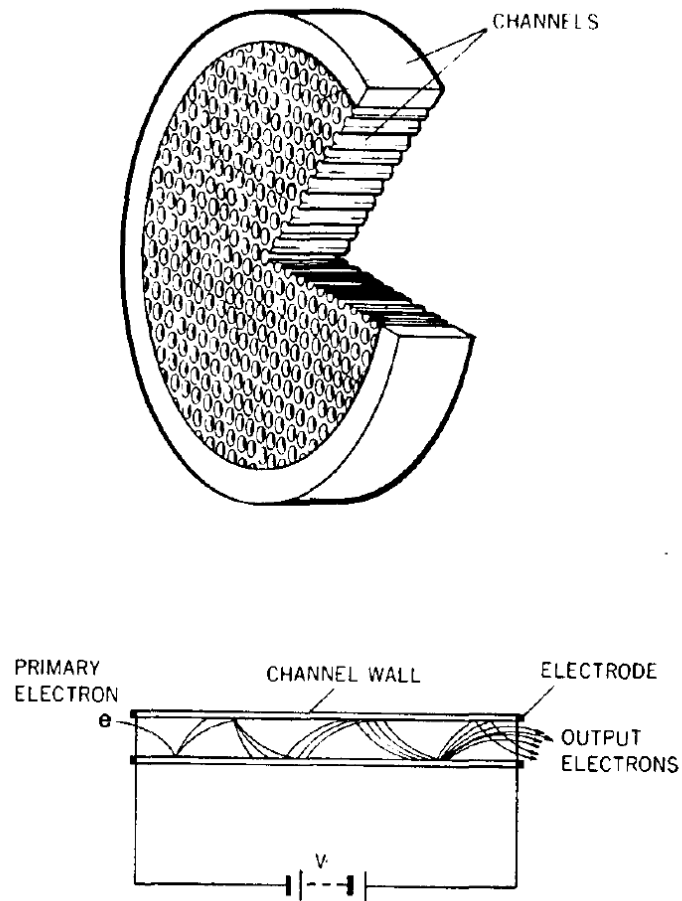


Figure 4.1: Schematic construction of an MCP and operation of electron amplification. [Kum88]

Most modern MCP detectors consist of two micro-channel plates with angled channels rotated 180° from each other producing a chevron (v-like) shape. Electrons exiting the first plate in a chevron MCP start the cascade in the next plate. The advantage of the chevron MCP over the straight channel MCP is significantly more gain at a given voltage and suppression of spurious background signals.

4.2 Time-of-flight Ray Trace Calculations Using an MCP

We have done ion-optical ray tracing assuming a fast (200 ps resolution) MCP-foil (or PMT-scintillator) time pick off at the cross-over and 400 ps resolution ΔE Si-detector timing at the back detector array. Calculated profiles of E vs. ToF profiles compensated by ToF suggests that at ca. 34 MeV, effective FWHM energy resolutions of about 332 keV (flight path = 3 m) and about 200 keV (long-flight path = 6m, Figure 4.2) should be possible. This would permit several RNB measurements now limited by the *TwinSol* energy resolution (ca. 1 MeV), provided the reaction cross-sections are large (e.g. elastic and inelastic scattering including Coulomb excitation). Additional calculations are shown in Appendix A.

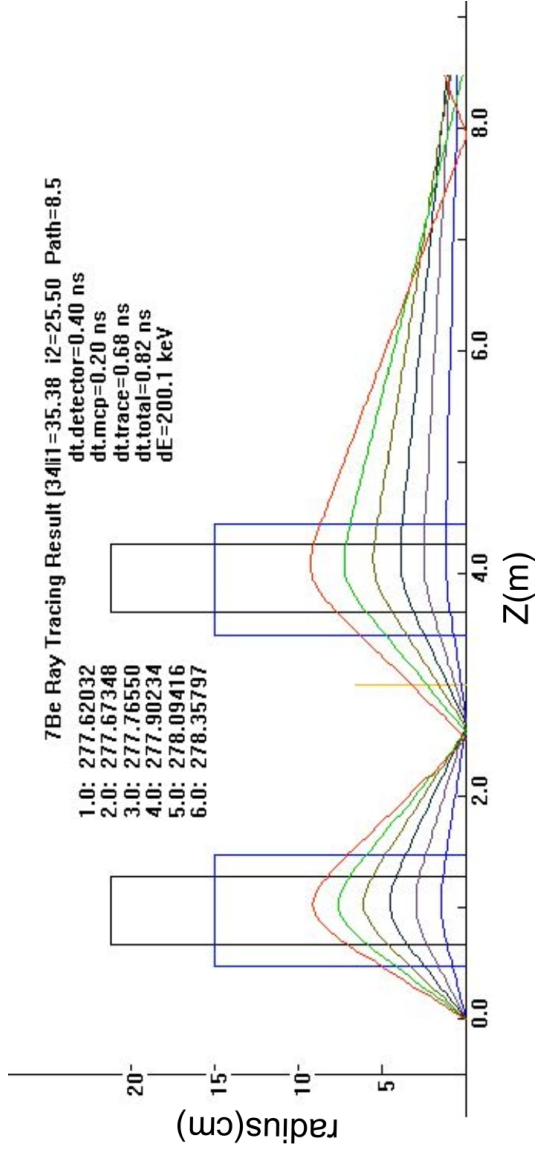


Figure 4.2: Ray trace calculation for ToF of 6 m flight path (Figure 3.1). Each ray is at an emission angle (^8Li) of $\theta=1^\circ, \dots, 6^\circ$ with each ray's ToF indicated (ca. 277 nsec).

4.3 MCP Information

4.3.1 Specification of BURLE MCP

The chevron MCP detector used was purchased from Burle Industries, Inc. (18 mm ultra-fast time-of-flight detector). The specification of the MCP is listed in Table 4.1 and its dimension shown in Figure 4.3.

<u>PHYSICAL CHARACTERISTICS of MCPS</u>	<u>SPECIFICATION</u>
MCP Quick-Fit® Replacement Cartridge:	30034
Microchannel Plate Type:	Extended Dynamic Range Long-Life™
Active Diameter:	18mm Minimum
Center-to-Center Spacing:	6μm Nominal
Pore Size:	5μm Nominal
Bias Angle:	12° ± 1°
Open Area Raio:	62% Minimum
Quality Level:	Detection
<u>PHYSICAL CHARACTERISTICS OF DETECTOR</u>	<u>SPECIFICATION</u>
Mechanical Dimension Defined by Drawing Number:	30035
Parallelism of Input MCP to Flange (Inside Surface):	±0.010" (Typical)
Vacuum Bake Specification (Not Operating):	Non-Bakeable
Operating Temperature Range:	-50° to 100°
Vacuum Flange:	None
Maximum DC Offset Voltage on Output Signal:	500 Volts
Input Grid:	90% Transmission (Typical)
<u>ELECTRICAL CHARACTERISTICS of DETECTOR</u>	<u>SPECIFICATION</u>
Operating Pressure (Maximum):	1.0 × 10 ⁻⁶ Torr
Maximum Specified Operating Voltage:	2400 Volts
Bias Current Range @ 2400 Volts:	6-36 microamps
Resistance (For Reference Only):	66-400 Megohms
Output Bias Resistor:	10 Megohms
Gain (Minimum):	1.0 × 10 ⁷ @ 2400 Volts Maximum
Linear Output Current Density (Microamps/cm ²):	Typically 10% of Bias Current Density
Dark Count (Maximum):	760 cts in 60 seconds
	5 cts/second/cm ²
Pulse Width:	750 psec FwHm (Typical)

Table 4.1: Specification of MCP from Burle, Inc.

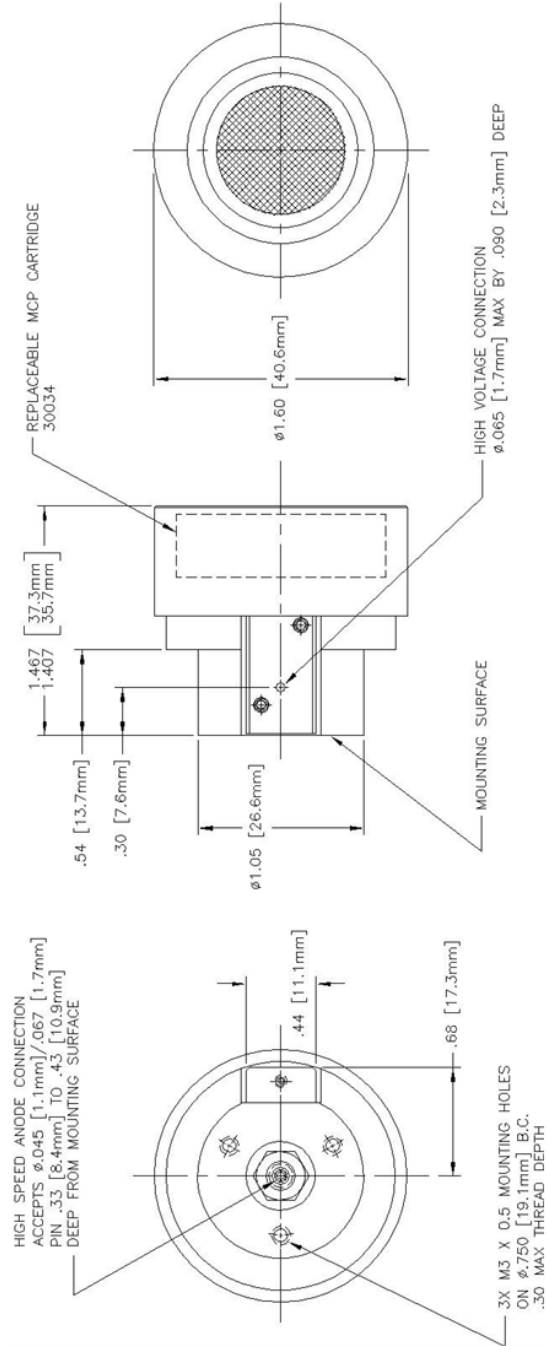


Figure 4.3: Burtle MCP dimensions.

4.3.2 Design of the MCP holder and HV resistor chain

We designed and built a MCP holder together with peripheral voltage-divider resistor chains (Figure 4.4) to hold the MCP in vacuum for the purpose of insertion of the MCP into the beamline and using it as a ToF detector. The resistor chain produces the needed electric field drawing secondary electrons from the foil and onto the MCP surface. This design implemented a $450 \mu\text{g}/\text{cm}^2$ thick aluminum-mylar foil producing secondary electrons at an angle of 45° from the beamline and two 85% transmission grids used to accelerate secondary electrons through the electric field. The holder is made of Lexan and the supporting plate is aluminum so it is safe to put into a high magnetic field. The resistor chain was made from $12 \text{ M}\Omega$ and $18 \text{ M}\Omega$ resistors as shown. The design for MCP-foil systems can be found in [Bus80, Sha00].

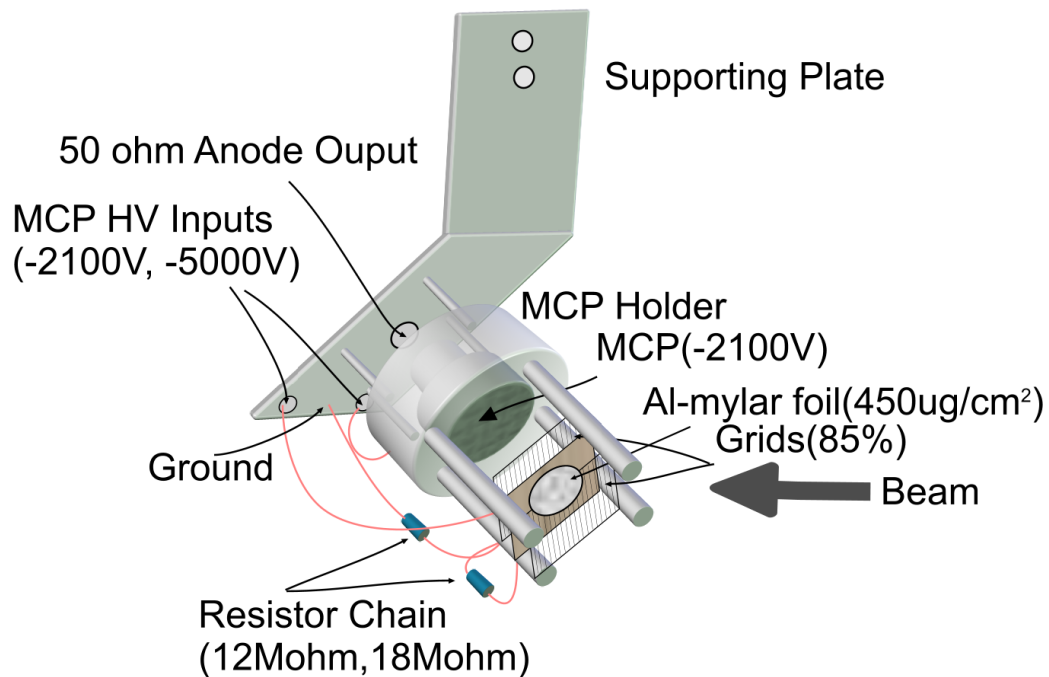


Figure 4.4: MCP holder with resistor chain.

When used in the experiment, the foil is biased at -5000V and the MCP surface is biased at -2100V , as provided by a model HK dual MWPC 5900 HV power supply

(10 KV max. HV, 1 ma. max.) which have a fast current trigger to prevent damage. Also, the MCPs need oil-free high vacuum (ca. 10^{-6} torr) for operation. The resistor chain is designed that the voltage drop between the foil and the grid will be twice the voltage drop between the grid and MCP surface. When charged particles hit the aluminum-mylar foil, secondary electrons will be emitted and accelerated towards the MCP due to the electric field. A few electrons hitting the MCP surface generates the anode signal via electron multiplication ($\times 10^5$ or above).

4.3.3 Simulation of secondary electron trajectories in a magnetic field

Secondary electron emission from the foil and the electron movements inside the subsequent magnetic and electric fields determines the MCP signal strength. The distribution of secondary electrons with kinetic energies T can be calculated by [Ros52]

$$(4.1) \quad \frac{d^2 N}{dT dx} = \frac{1}{2} K z^2 \frac{Z}{A} \frac{1}{\beta^2} \frac{F(T)}{T^2}$$

for $I \ll T \ll T_{max}$, where T_{max} is given by

$$(4.2) \quad T_{max} = \frac{2m_e c^2 \beta^2 \gamma^2}{1 + 2\gamma m_e / M + (m_e / M)^2}$$

and $F(T)$ is

$$(4.3) \quad F(T) = (1 - \beta^2 T / T_{max})$$

Here β is the velocity of the primary incident particle. Z is the atomic number and A is the atomic mass of the foil material, and $m_e c^2$ is the electron rest mass (0.511 MeV). An electron with kinetic energy T_e and corresponding momentum p_e is produced at an angle θ given by

$$(4.4) \quad \cos(\theta) = (T_e/p_e)(p_{max}/T_{max})$$

where p_{max} is the momentum of an electron with the maximum possible energy transfer T_{max} .

With this distribution known, the corresponding energy and direction of each electron ray can be calculated. We developed a Monte-Carlo code calculating secondary-electron trajectories in practical magnetic and electric fields. Although we decided to put the MCP at the cross-over position in *TwinSol* so that magnetic fields from both solenoids cancel for the most part, they are not negligible and need to be carefully considered. Realistic magnetic fields at the cross-over point for a 28 MeV ^8Li beam with solenoids settings showing in Table 3.2 were calculated, and then secondary electron trajectories were simulated with energies and outgoing angles from the distribution based on these magnetic field settings (Figure 4.5).

This simulation result showed that with 3000 V voltage gap between the Al-mylar foil and MCP surface, we should be able to observe sufficient fast timing signal from the MCP even with some signal degradation due to the magnetic field (about 50 gauss) present.

4.4 ^{244}Cm α Source MCP Tests

4.4.1 Vacuum chamber setup

For the purpose of adapting the MCP setup into the *TwinSol* beamline, we tested the MCP+foil setup in an ISO-250 oil-free vacuum chamber at UM similar to the one installed at the cross-over point in *TwinSol*. We modified an ISO-250 flange to include a 1" compression fitting for the MCP holder support shaft, an ISO-40 adapter for a high voltage SHV feedthrough and added several LEMO feedthroughs

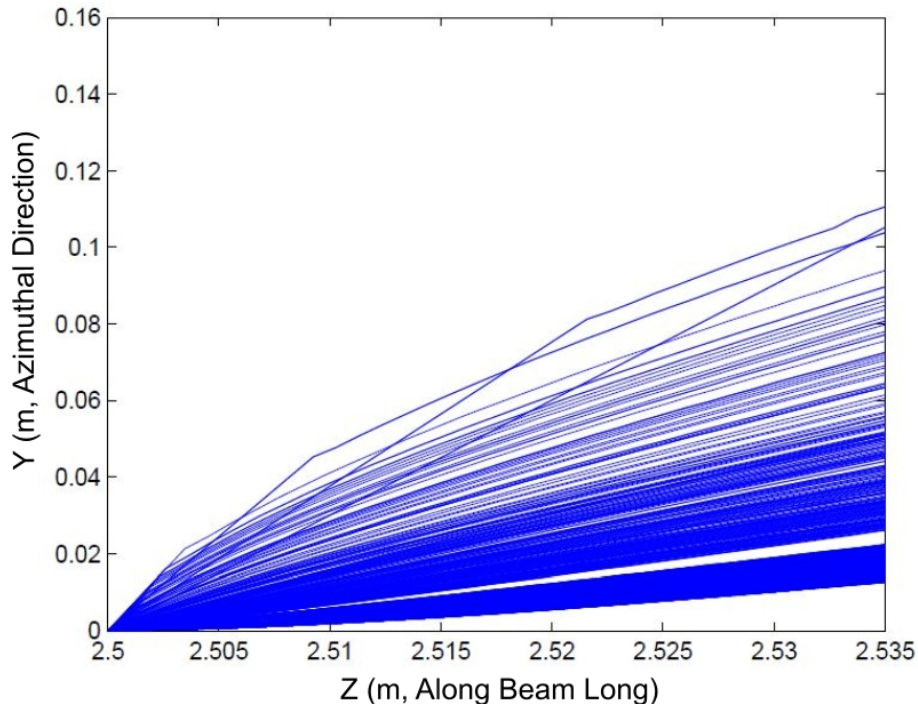


Figure 4.5: Secondary electron trajectories from a foil in a realistic magnetic field at the *TwinSol* cross over using Monte-Carlo calculations.

for the MCP and Si detector anode signal outputs (similar to Figure 2.5).

Figure 4.6 shows the experimental setup for the vacuum chamber with all SHV and BNC cables connected to a separate NIM bin holding the electronics and HV MCP supplies. We also installed a Lexan ISO-250 viewing plate on the side to check the alignment for MCP, foil and Si detector. The Si detector was ORTEC model TD-060-450-75. The chamber was pumped to a vacuum $\leq 5 \times 10^{-6}$ torr using an Alcatel oil-free pump. Once this vacuum was reached (about 2 hours), both MCP and Si detectors was biased.

4.4.2 α source test setup

The alpha source used was a 1 mCi ^{244}Cm source with α particle energy at about 5.5 MeV with 0.5 MeV FWHM. Being a thick source, α particles with a range of different energies are emitted because of energy loss in the α -source volume. To get

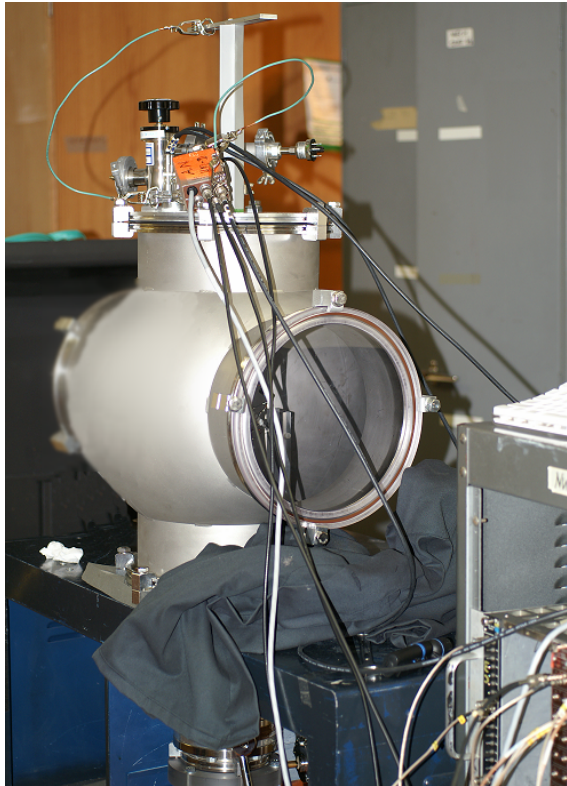
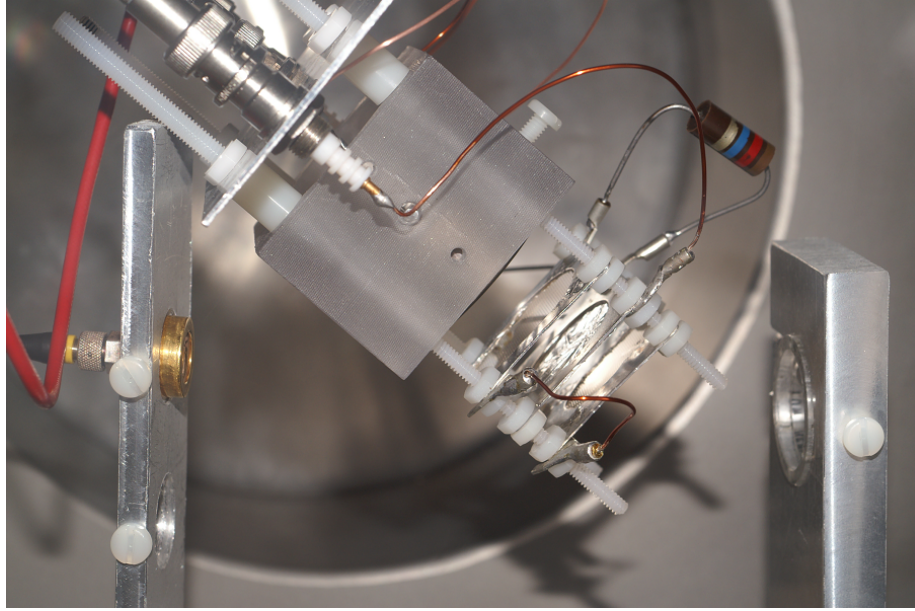


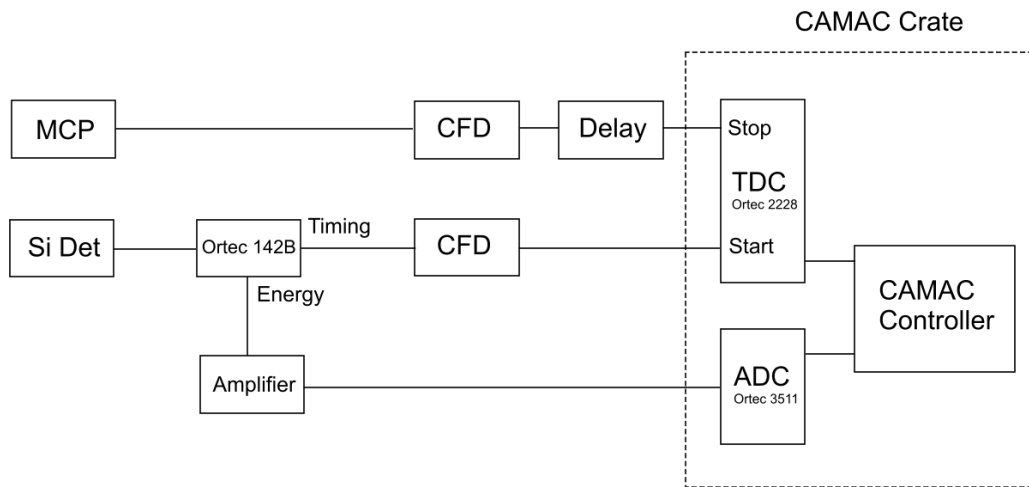
Figure 4.6: MCP alpha test vacuum chamber setup

the maximum α particle counting rate, we put the source as close as possible to the foil as shown in Figure 4.7 and aligned the source, the foil and the Si detector to be in line.

The aluminum-mylar foil together with MCP produced the start signal and the Si surface barrier detector was located on the other side in the test chamber as the stop detector. The α particles first hit the foil and generate secondary electrons detected by the MCP, then hit the Si detector producing the stop signal. The timing signal from MCP anode is first delayed, then sent into one ORTEC 478 constant fractional discriminator (CFD), the output signal of the CFD was then sent to the stop of the time-to-digital converter (TDC, Ortec 2228). The timing signal from the Si detector was sent directly into the other ORTEC 478 CFD and then brought to the start of the TDC to trigger time conversion. The energy signal from the Si detector was

Figure 4.7: MCP α test setup

amplified and then sent into an ORTEC 811 CAMAC analog-to-digital converter (ADC) as shown in Figure 4.8.

Figure 4.8: MCP α test electronics setup

The TDC was only triggered by the timing signal from the Si detector since there were α particles always hitting the MCP foil but not always hitting the Si detector. These will not give the right time-of-flight information and hence were not of interest. Due to the energy registration in the Si detector and coincidence with the ToF timing

signal, a two dimensional histogram of energy vs. ToF was achieved. Together with the information of a valid data register and total number of particles hitting the Si detector, the MCP system efficiency also could be deduced.

4.4.3 α test result

A fast NIM pulser (Model Ortec 480) was first used for time calibration of the data acquisition system. Using varying delays, the timing calibration showed that the ultimate time resolution was 50 picosecond per channel. A typical timing signal from the MCP is shown in Figure 4.9 and shows the expected fast nanosecond-level rise time. Typically with a good signal-to-noise ratio one can obtain a ToF resolution of about 10% of the rise time (so here about 200 psec).

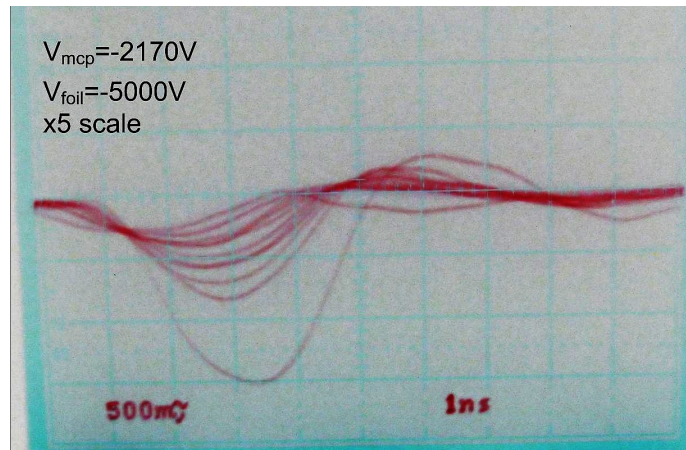


Figure 4.9: MCP Signal

A two-dimensional histogram of energy vs. ToF is shown in Figure 4.10. The tilted shape is expected due to the correlation in α energy and velocity. After we put a tight energy cut on this 2D histogram, we can deduce the intrinsic timing resolution.

The timing resolution was deduced as 700 picosecond from Figure 4.11. Because the timing resolution of the MCP is superior to the silicon surface barrier detector

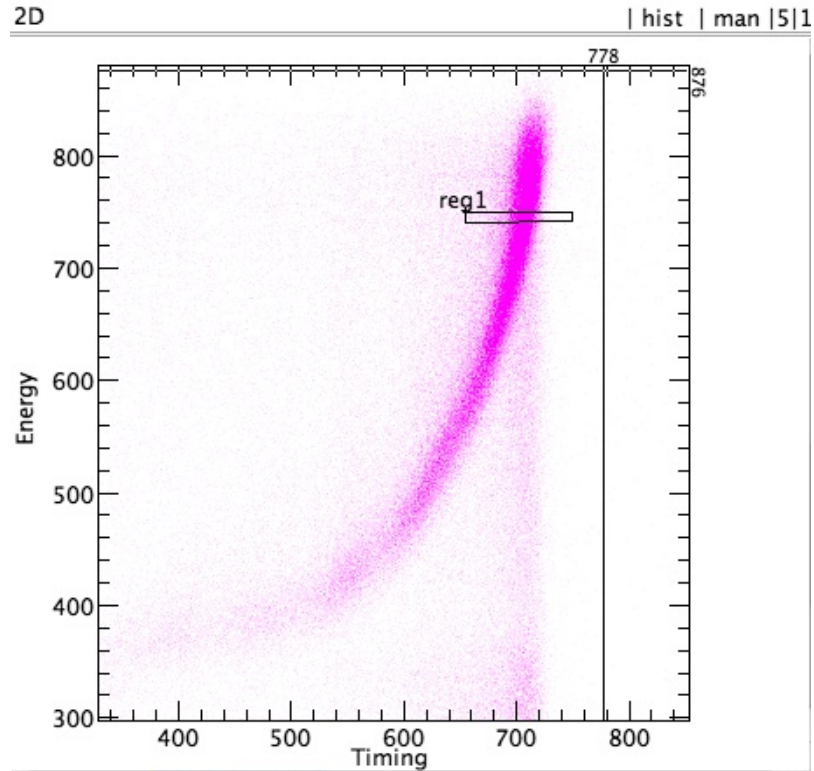


Figure 4.10: MCP α test 2D histogram (50 psec/ch).

in this case, the timing resolution is determined by the silicon detector.

In the data acquisition (DAQ) system, although we only recorded E and ToF signals from the silicon detector in coincidence with the MCP signals, we still counted every event in the silicon detector in order to deduce the efficiency for the whole system. The efficiency for this α test was about 50%, as expected [Sha00].

4.5 ^8Li RNB in-beam Test at *TwinSol*

After successfully testing the MCP+foil with an α source at UM, it was used for a radioactive nuclear beam experiment at UND. The RNB chosen was a ^8Li beam at 28 MeV and the ToF time resolution was measured at the focus point in the ToF chamber with a Si detector.

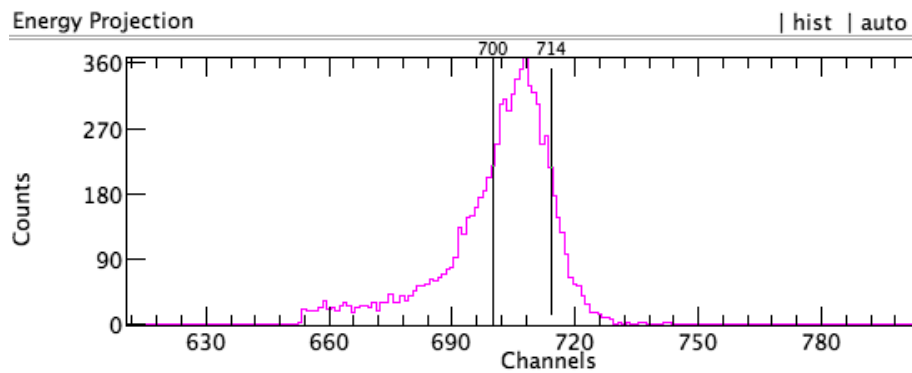


Figure 4.11: Projection onto time (see Figure 4.10; 50 psec/ch).

4.5.1 In-beam test of MCP at ToF chamber

Owing to the uncertainty in the effect of magnetic field on the MCP signals, the first in-beam MCP test was carried out inside the new ToF chamber (see Appendix B). The MCP was installed in front of the target holder and the time of flight from the MCP to the ΔE -E Si detectors in the chamber were indirectly measured (Figure 4.12). Since the ToF from the MCP to the Si detectors is fairly short, the measurement was done by measuring time of flight of both MCP and Si detectors from the beam buncher, and then calculating the difference of the two times.

A detailed electronic setup is shown in Figure 5.7 and 5.7 in Chapter V. Two NIM-standard constant fraction discriminators (CFD) are used to generate timing gates triggering a CAEN V775 TDC for time conversion an ORTEC 811 ADC used for energy signals.

A two-dimensional ToF vs. E histogram for detector C at 0° was constructed (Figure 4.13). Besides the ground and first excited states of ^8Li produced from the production reaction [$^9\text{Be}(^7\text{Li}, ^8\text{Li})^8\text{Be}$], also observed was excited $^8\text{Li}^*$ particles at the same ToF with its ^8Li ground state. Unlike previous beam-bunching experiments, an intense ^8Li beam was going through the thick MCP foil and hitting the silicon detector and hence we noticed some excited $^8\text{Li}^*$ particles from the MCP foil and

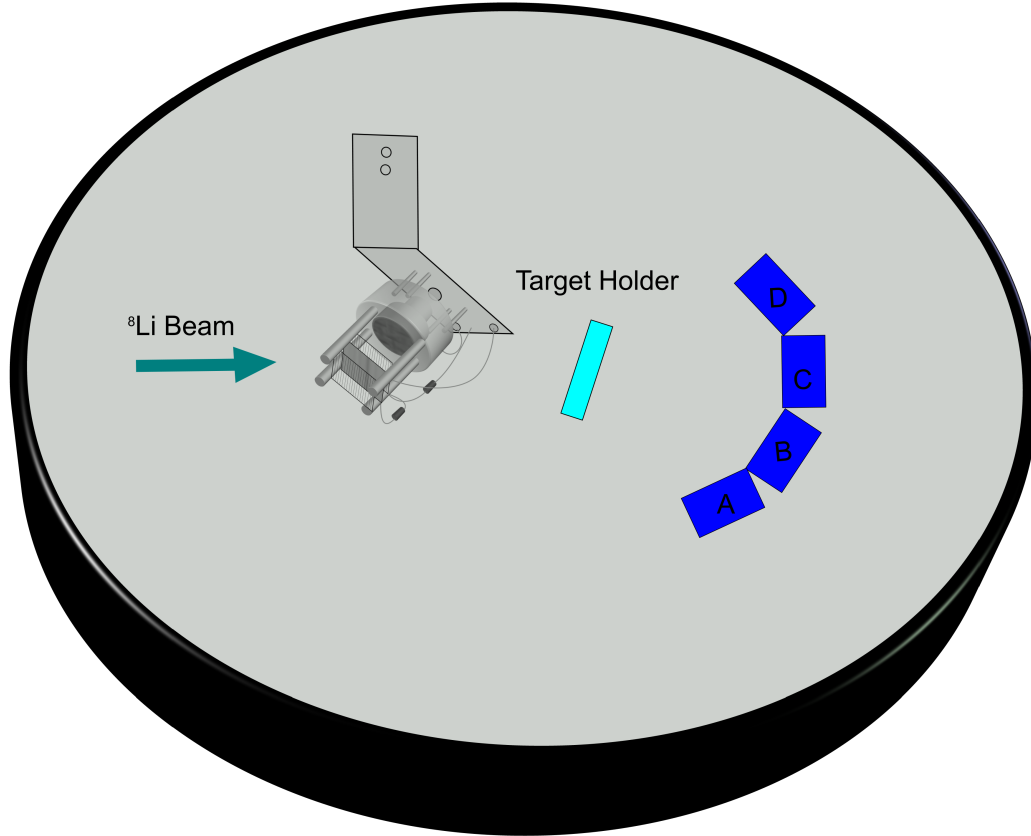


Figure 4.12: Microchannel Plate installed inside ToF chamber in front of target holder.

also excitation of Si nuclei in the detector. Those excitation particles (about 4% of the primary ^8Li beam) are showing in Figure 4.14 at the same ToF with the ground state ^8Li , but with less energy. They need to be considered in future experiments for improvement of energy resolution when using the MCP+foil (See Chapter VI).

With insertion of a nat. Au target, we looked for the Coulomb excitation (CoulEx) at non-zero angles when using the MCP+foil for ToF. The detectors used in this experiment with their positions are listed in Table 4.2. Figure 4.15 shows the MCP-Si ToF vs. E histogram taken with detector D at 22.5° . The results of the Coulomb excitation experiment will be further discussed in Chapter V.

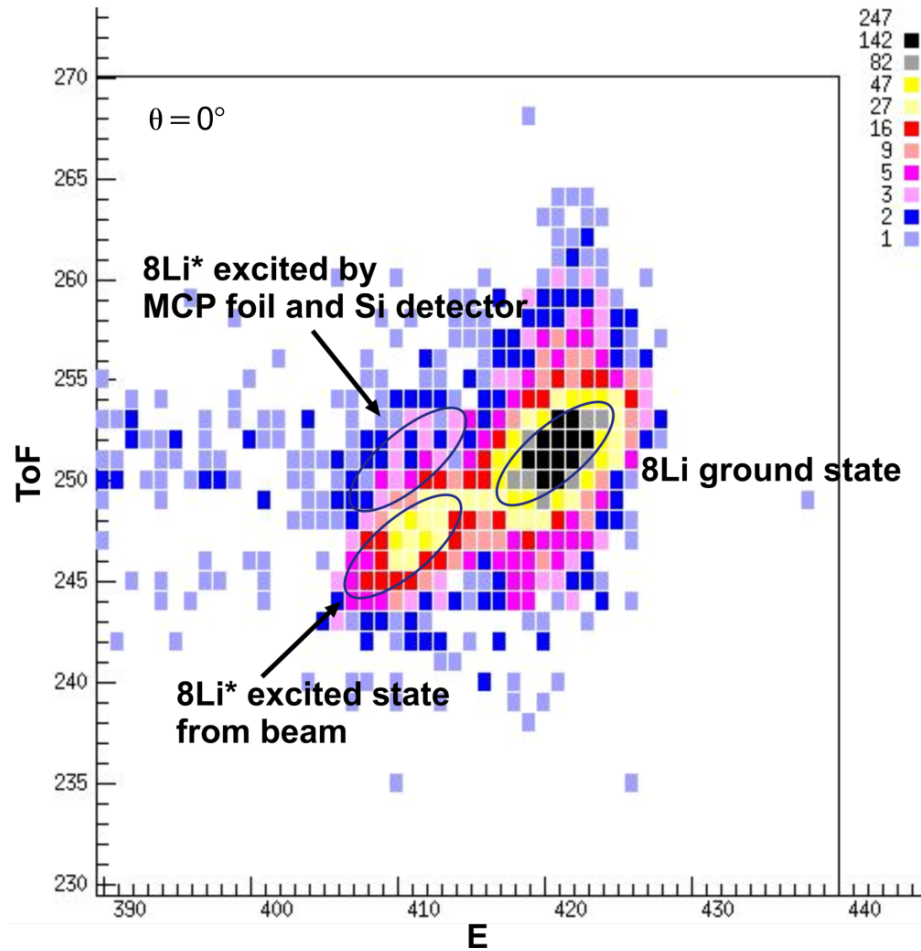


Figure 4.13: Two-dimensional Time-of-flight vs. Energy histogram ($\theta=0^\circ$) when using MCP in ToF chamber (80 keV/ch for energy and 0.5 nsec/ch for ToF).

4.5.2 In-beam test of MCP at cross-over chamber

Testing of the MCP+foil at the *TwinSol* cross-over chamber is more of a challenge because of the much stronger fringe magnetic field at the cross-over point (almost 50 gauss). The magnetic field bends secondary electrons out of their original trajectories towards the MCP surface, making much weaker signals coming out of the MCP anode. During the test experiment, we noticed that this weaker signal didn't meet the lowest threshold on our CFD, hence a fast linear amplifier (ORTEC FTA820A, $\times 10$) had to be introduced in our electronics, causing more complications in the ToF resolution measurements.

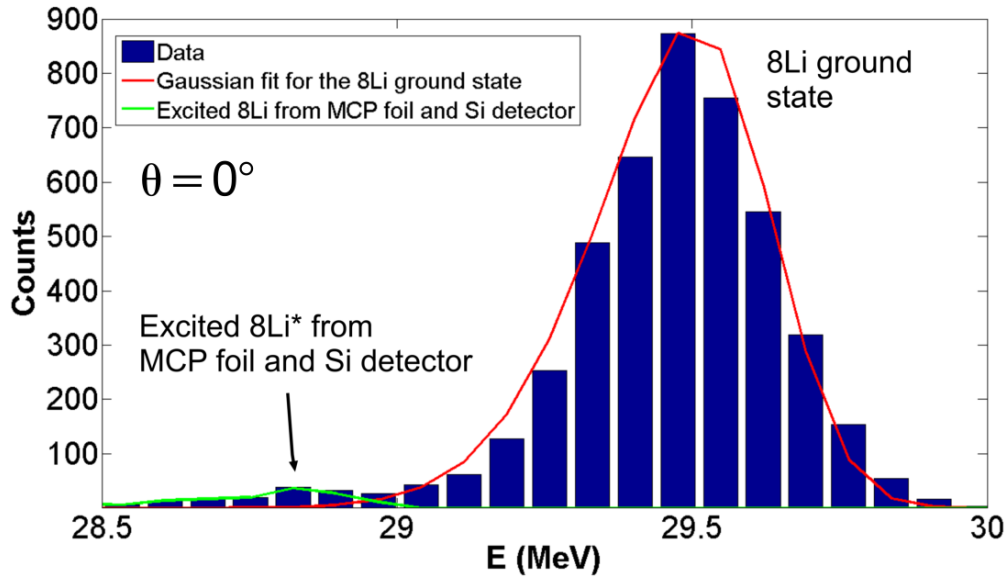


Figure 4.14: Histogram projection showing ^8Li ground state and excited $^8\text{Li}^*$ from MCP foil and Si detector excitation.

Detector	Angle ($^\circ$)	Serial	Voltage (V)	Leakage Current (μA)
Det. A	67.5	36-235D	273	1.82
Det. B	52.5	31-485A	200	1.02
Det. C	37.5	40-183B	110	0.74
Det. D	22.5	31-184J	300	2.32

Table 4.2: Detectors list and angles using MCP in ToF chamber.

Due to limited experimental time, only ToF from the cross-over to a 0° silicon detector was tested. Figure 4.16 shows the ToF vs. E histogram.

The timing resolution using the MCP and the intrinsic r.f. beam bunching (Chapter III) were compared (Figure 4.17). Due to its 1.4 nsec (FWHM) intrinsic uncertainty, the timing resolution when using the r.f. beam buncher was totally determined by the beam bunching. Therefore it is not surprising to see much better timing resolution (800 psec) even when using the MCP in the *TwinSol* fringe field. A steel box (shown in Chapter VI) was built for future use which could cancel the *TwinSol* fringe field.

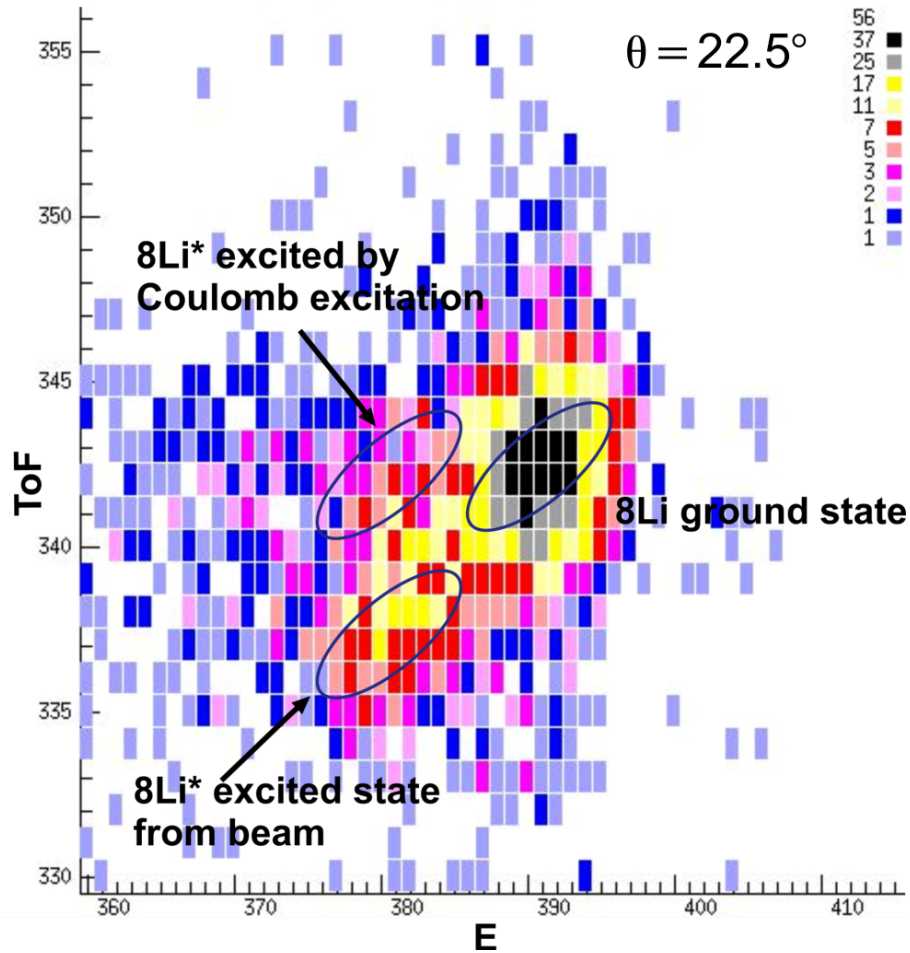


Figure 4.15: Time of flight from MCP to detector D vs. energy histogram taken at 22.5° (80 keV/ch for energy and 0.5 nsec/ch for ToF).

4.6 Conclusion

The MCP ToF tests were carried out both in the new ToF chamber and at the cross-over chamber. The comparison of ToF resolution shows superior resolution than intrinsic beam bunching ToF by $\times 2$ or more. However this method is count-rate limited and only can work when the count rate at the MCP is less than $10^6/s$. The use of other foils, to minimize energy spread of the RNBS in the foil (though should be < 0.1 MeV) and nuclear excitation, or the use of coated foils to increase the efficiency [Sha00] was not investigated and should be investigated in any future work.

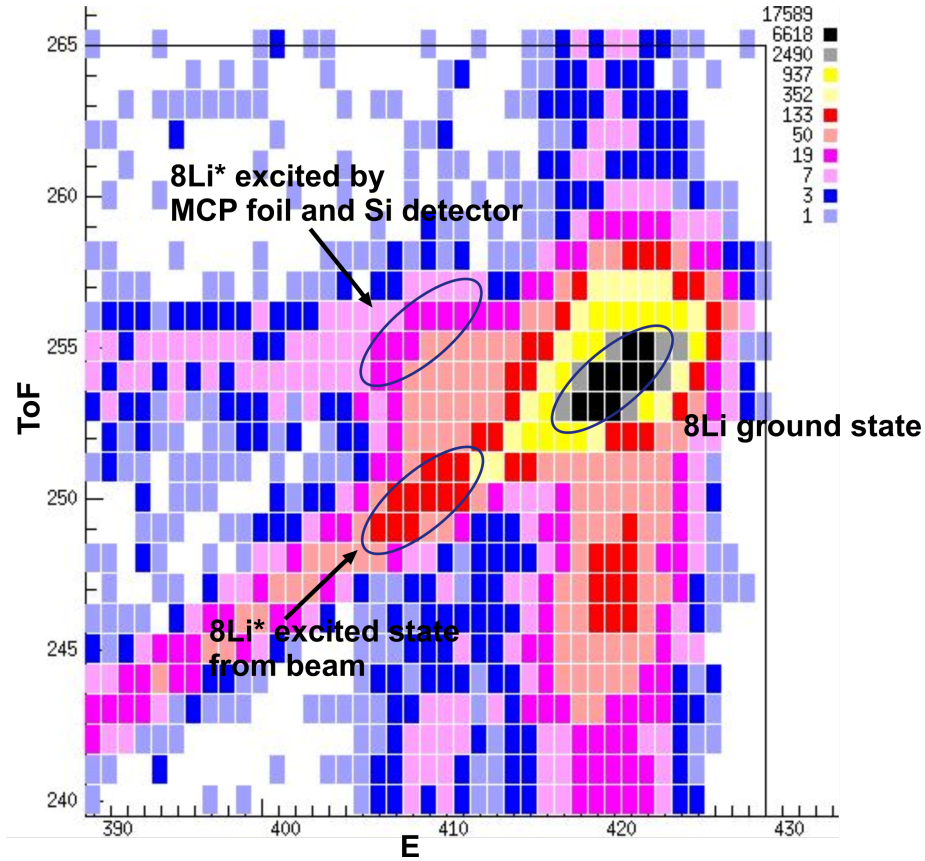


Figure 4.16: ToF vs. E histogram with MCP at cross-over position (80 keV/ch for energy and 0.5 nsec/ch for ToF).

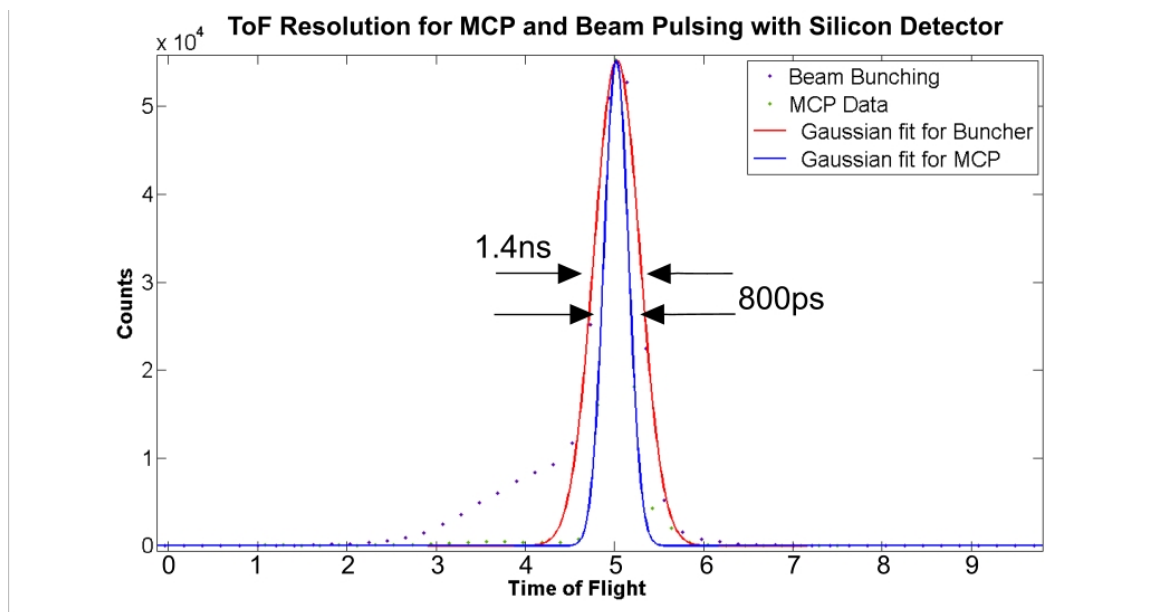


Figure 4.17: Comparison of timing resolution for MCP and beam buncher ToF.

CHAPTER V

^8Li + gold Coulomb Excitation Measurements Using ToF

5.1 Introduction

When heavy nuclei are bombarded with charged particles with an energy near or appreciably below the Coulomb barrier the short-range nuclear forces cannot operate. The collisions may, however, still give rise to nuclear excitations produced by the electric field of the impinging particles. Such reactions are called Coulomb excitation (Coulex) [Ald66]. It is a proven method for studying electromagnetic transition strengths in nuclei. Several earlier works using Coulex have been done by the UM+UND group in studying nuclear reactions with low-energy RNBs [Bec97, Bro91, Mu02].

In the previous Coulomb excitation experiments utilizing *TwinSol* [Bro91, Mu02], the Coulex of a 30.5 MeV ^8Li beam on Pb and Ni targets was investigated as well as 14.6 MeV ^8Li on Ni. However at that time, the long time-of-flight path was not available, and the measurements were done without ToF information by using $\Delta\text{E-E}$ telescopes for separating inelastic excitation ^8Li ($J_i^\pi = 2^+ \rightarrow J_f^\pi = 1^+$, $\text{Ex}=0.98$ MeV) from its ground state (Figure 5.1). The inelastic ^8Li group was thus partially contaminated by excited ^8Li coming from the production target. Hence the accuracy of the experimental results could be effected even though the contaminated excited

^8Li from the production target was measured and said to be accounted for.

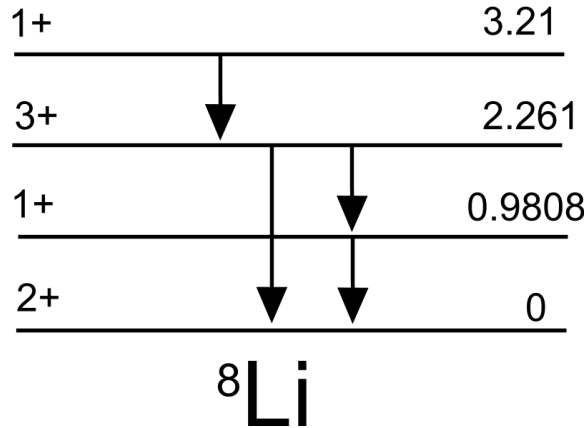


Figure 5.1: Levels in ^8Li , decay mode = beta to ^8Be , $T_{1/2}=842$ msec [NDE].

5.2 Experimental Setup and Data Acquisition

The new *TwinSol* ToF beamline configuration (Figure 2.3) was used. More specific information about the physical layout of the components is shown in Table 5.3. Four thick Si detectors (Table 5.1) were utilized in this experiment. Unlike the previous CoulEx experiments [Bro91, Mu02], thin Δ -E Si detectors were not used in order to achieve the best timing resolution. Thus only thick E detectors were used to stop all particles of interest and measure the total energies and ToF of these particles. The identification of different particle groups then was simply done by using ToF vs. total energy (Figure 5.3) which greatly simplified the setup. Prior to in-beam measurements, the detectors were illuminated with a ^{228}Th alpha source. The data from this was used to calibrate the detectors' signal response vs. particle energy (Table 3.5). All detectors together with their collimators were mounted on a rotating table in the ToF chamber on mounting holes (Appendix B). The geometry of detectors corresponding to the target position are shown in Figure 5.2. Corresponding solid angle for each detector were calculated and are listed in Table 5.2.

Detector	Angle	Serial number	area (450^2)	thickness (mm)	Voltage	Leakage Current
Det. D	30°	31-184J	1000	450	500 V	$2.23 \mu\text{A}$
Det. C	45°	40-183B	1000	450	110 V	$0.70 \mu\text{A}$
Det. B	60°	31-485A	1000	450	200 V	$0.99 \mu\text{A}$
Det. A	75°	36-235D	1000	450	295 V	$1.78 \mu\text{A}$

Table 5.1: List of detectors used in CoulEx experiment.

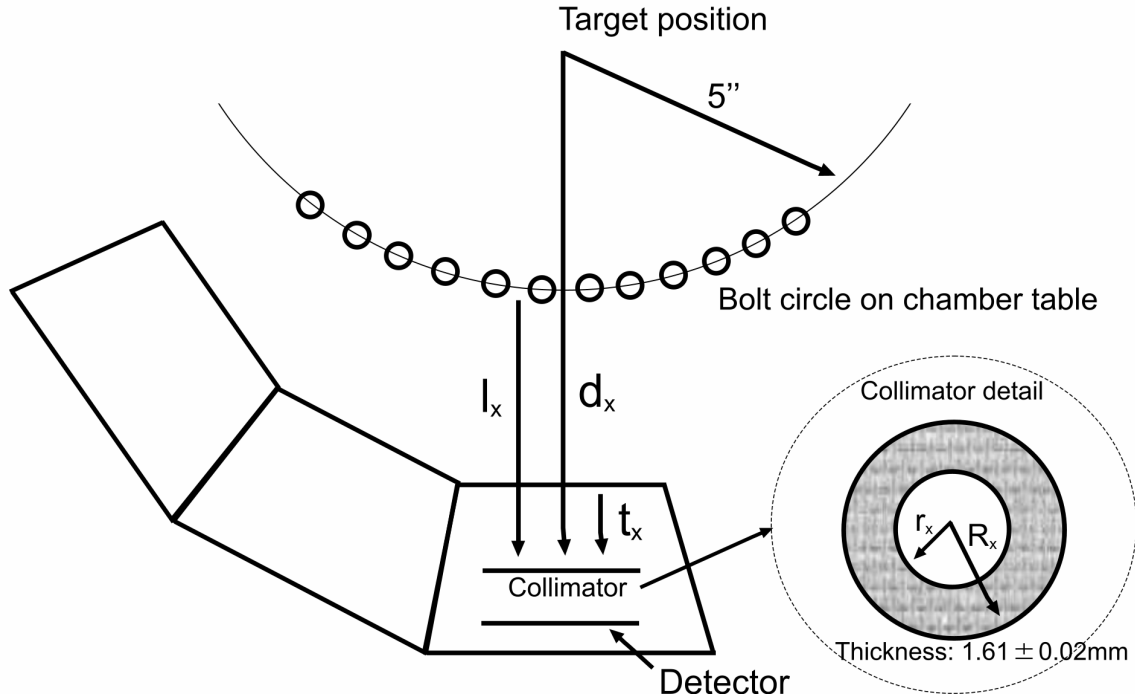


Figure 5.2: The geometry of detectors with collimators according to the target position for calculating solid angles.

All detectors were located on a rotational table (Figure B.9, 5.4, 5.5) installed in the ToF chamber. As noted earlier, development of the ToF chamber and its accessories was part of this thesis project and details can be found in Appendix B. At the *TwinSol* cross-over point, a beam collimator was installed. Since a percentage of the ^8Li secondary beam is produced in its excited state, the first solenoid is tuned so that only ^8Li primarily in its ground state is focused at the cross-over point. The excited state $^8\text{Li}^*$ secondary beam is lower in magnetic rigidity, $B\rho$, because part of its kinetic energy was been converted to internal energy (0.98 MeV). Therefore, it

Detector	d_x (mm)	r_x (mm)	R_x (mm)	l_x (mm)	t_x (mm)	$d\Omega$ (sr)
Det. D	176.64	18.55	39.85	49.635	27.39	0.0346
Det. C	178.015	18.53	39.80	51.015	28.95	0.034
Det. B	179.305	18.51	39.84	52.305	29.63	0.0335
Det. A	180.505	18.52	39.79	53.505	30.78	0.0331

Table 5.2: Measurements of all distances noted in Figure 5.2 for all detectors and corresponding calculated solid angles.

comes to a focus mostly at an earlier position along the beamline. Despite this, due to the thick RNB production target, there are still some $^8\text{Li}^*$ excited ions together with other background ions with close magnetic rigidity going through the second solenoid. The collimator can greatly improve the beam purity and block many of the problematic contaminant beams which have traversed through the first solenoid.

Production Target Material	^9Be
Target to Center of Cryostat 1	101.0 cm
Entrance Aperture	$\pm 5.7^\circ$
Center of Cryostat 1 to Midplane	147.5 cm
Midplane Collimator	0.5 cm dia.
Midplane to Center of Cryostat 2	151.0 cm
Center of Cryostat 2 to Reaction Target	146.9 cm
Reaction Target 1	nat. Au $475\mu\text{g}/\text{cm}^2$
Reaction Target 2	nat. Au $2.025\text{ mg}/\text{cm}^2$

Table 5.3: *TwinSol* parameters.

There are three reaction-target foils that can be mounted on a target ladder located at the *TwinSol* focal plane in the ToF chamber (Figure 5.6). The target foils are typically sandwiched between two target frames (made of plastic, stainless steel or tantalum) and attached to the target ladder. The ladder is mounted on a sliding shaft which can be adjusted in height to select one (or none) of three possible targets. The shaft also may be rotated to change the angle of incidence of the beam upon the target such that the target frame does not obstruct the outgoing reaction products. One detector (Detector C) was moved to the focal plane at $\theta=0^\circ$ before the actual Coulomb excitation measurements. A calibration run was conducted to measure the ratio of ^8Li secondary beam per incident primary beam and the $^8\text{Li}^*$

in the beam. During the actual experiment, the primary beam current is recorded event-by-event by the UND data acquisition software [ORNL].

A schematic illustration of the electronics setup is shown in Figures 5.7 and 5.8.

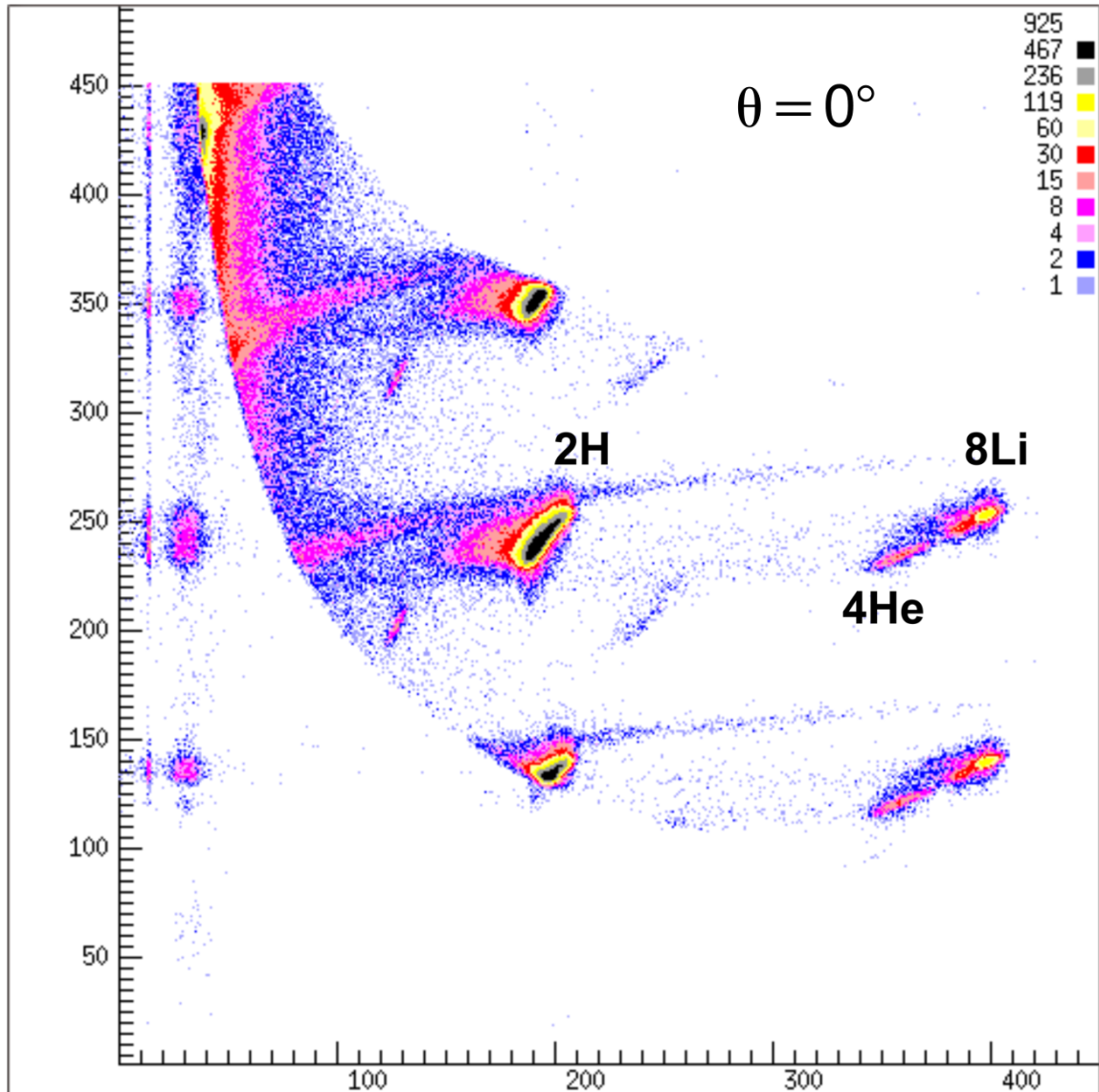


Figure 5.3: ToF vs. E histogram ($\theta=0^\circ$) shows the identification of different particle groups (80 keV/channel in E and 0.5 nsec/channel in ToF.)

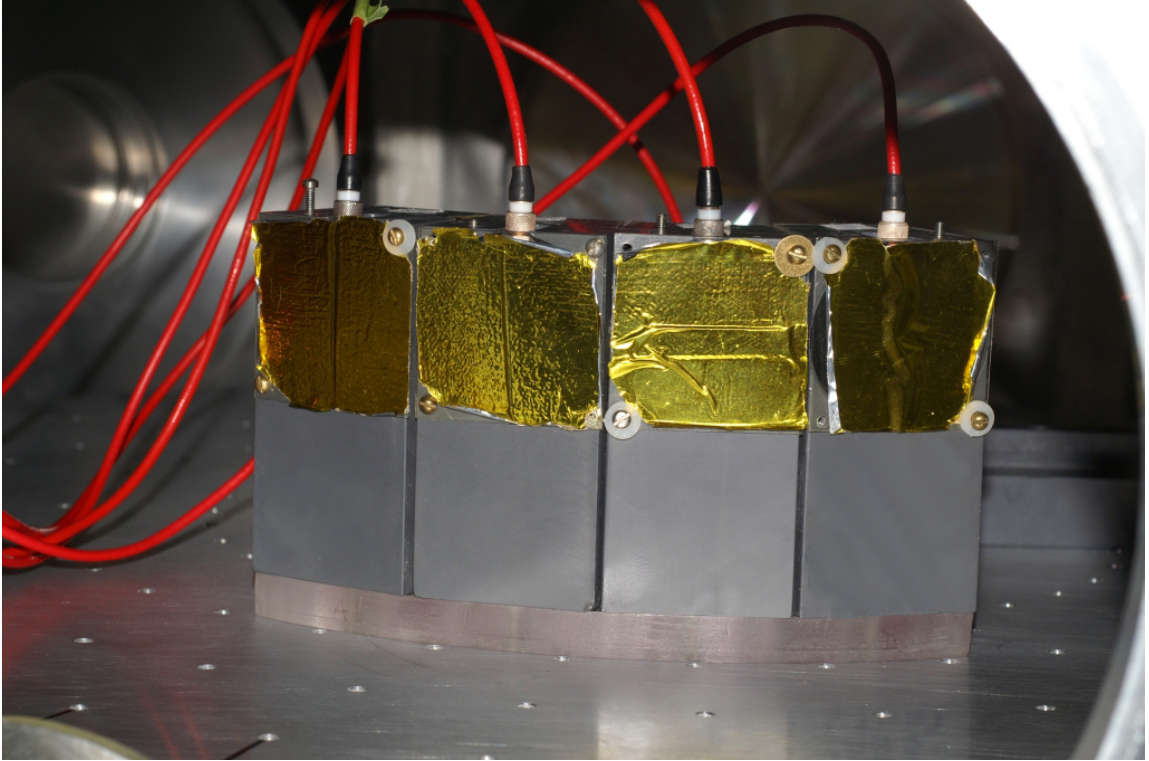


Figure 5.4: Detector array placed on the rotational table inside the ToF chamber. The detectors were placed at 30° , 45° , 60° and 75° lab angle with respect to the target. The picture shows the back of the detector array.

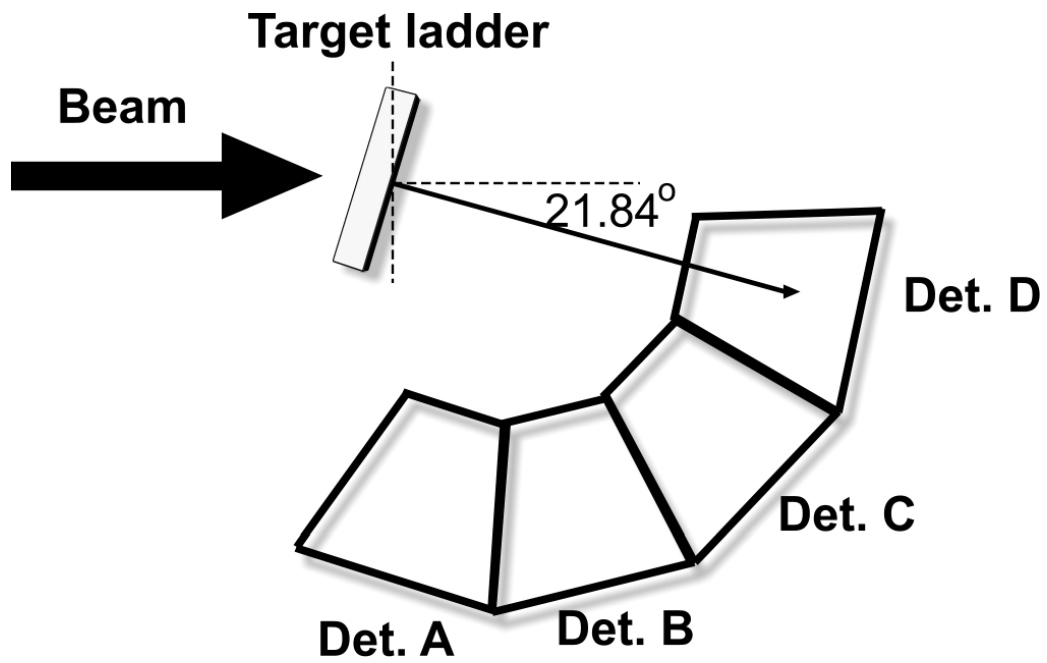


Figure 5.5: The geometry of primary beam, target and detector array.

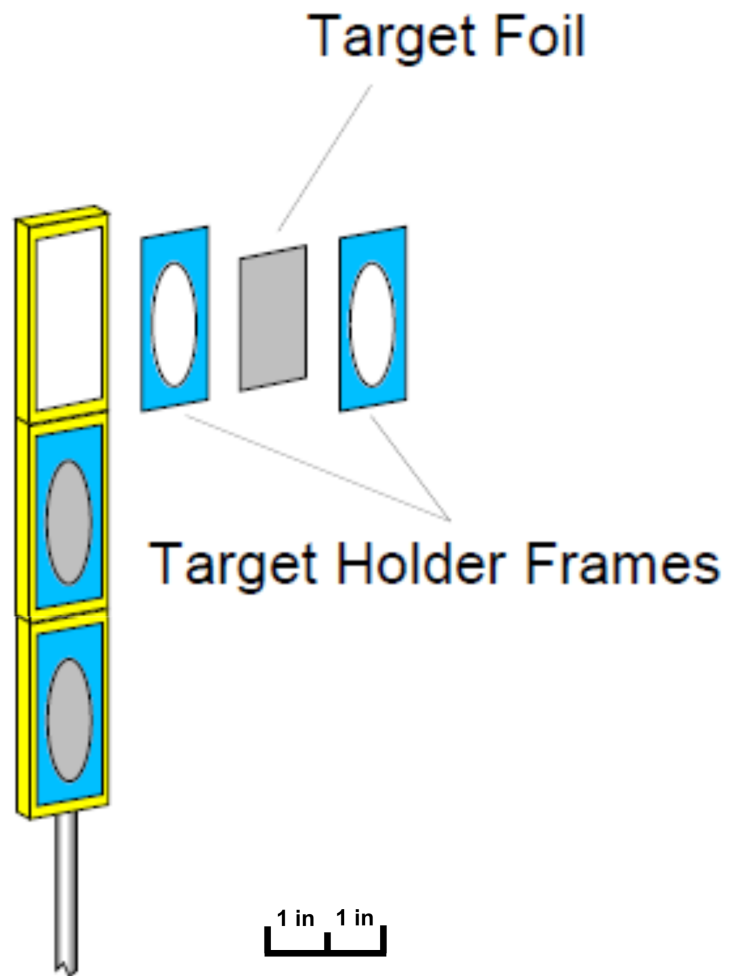


Figure 5.6: As shown here, the target foils are typically sandwiched between two target frames and attached to the target ladder.

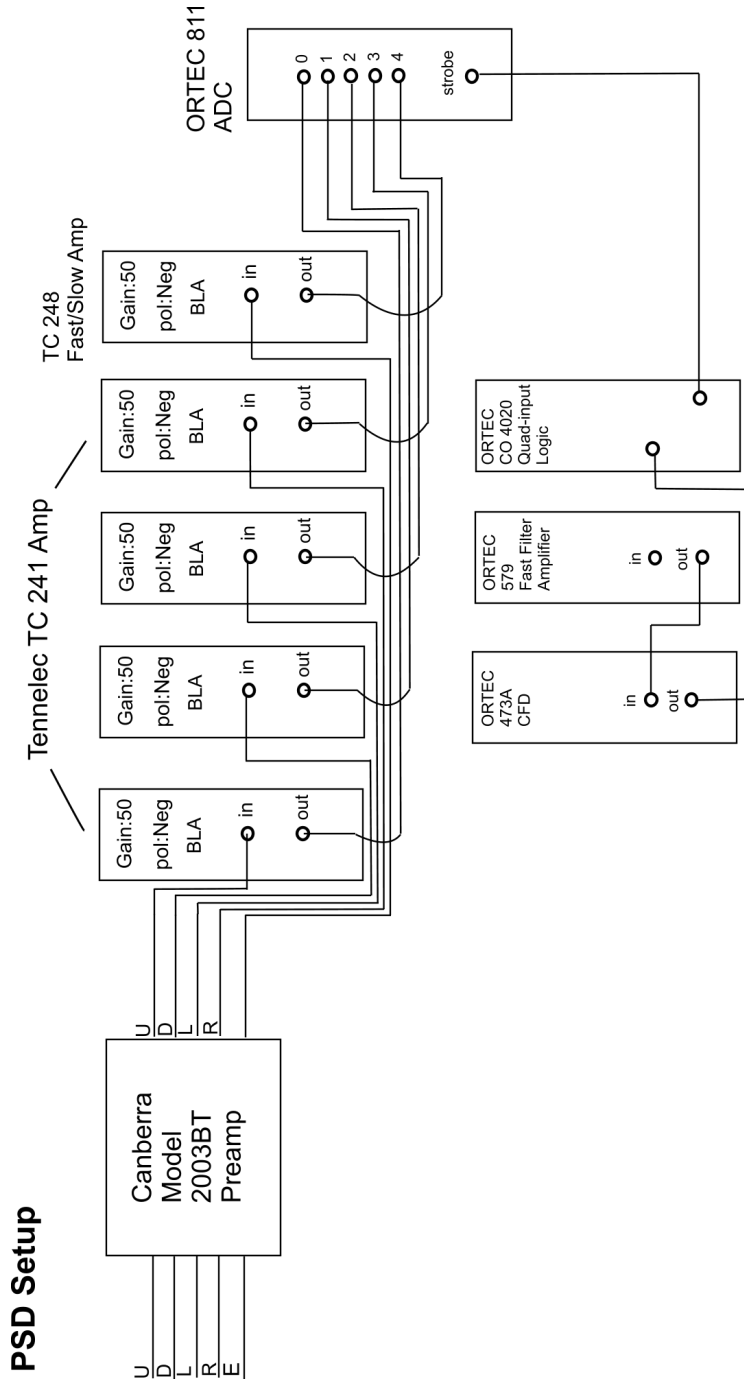


Figure 5.8: A schematic of the electronic data-acquisition hardware for the PSD.

5.3 Experimental Results for Inelastic Scattering (Coulomb Excitation) of ${}^8\text{Li}$

The basic measurement was to sum the inelastic and elastic ${}^8\text{Li}$ scattering events recorded with the detectors set at various angles. During some of the runs, the target foil was rotated at an angle (15°) with respect to the incident beam because at certain angular positions of the detectors, the target ladder itself could partially shield the detectors. Altering the angle of the target foil will of course change the number of target nuclei encountered by the RNB. However, measuring the ratio of the inelastic to elastic events provides a probability of excitation, $P(\theta)$, as a function of scattering angle that is independent of the target rotation angle, beam current, solid angles, etc.

Due to the production mechanism and beam optics, the ${}^8\text{Li}$ secondary beam arriving at the ToF chamber had a low-energy “tail”. A total energy spectrum of the beam at $\theta=0^\circ$ is shown in Figure 5.9. The tail is a problem in certain experiments, such as this one, because elastic scattering of these lower-energy ${}^8\text{Li}$ overlap with the inelastic scattering of the main ${}^8\text{Li}$ group. In the previous ${}^8\text{Li}$ Coulex experiment, the tail had to be estimated for each angle and subtracted from the measured yields of ${}^8\text{Li}^*$ when calculating $P(\theta)$ hence effecting the accuracy of the results. In this experiment, this tail can be very well separated from the ${}^8\text{Li}$ ground state by using the ToF information.

Data was recorded at detector angles ranging from 30° up to 75° (laboratory reference frame) for a thin ($475 \mu\text{g}/\text{cm}^2$) gold target and from 45° to 90° for a thick ($2.025 \text{ mg}/\text{cm}^2$) gold target. Analysis of the small angle (30°) data showed reactions which were dominated by elastic scattering from light-nuclei contaminants (e.g. oxygen and carbon). Because these contaminant nuclei are comparable in

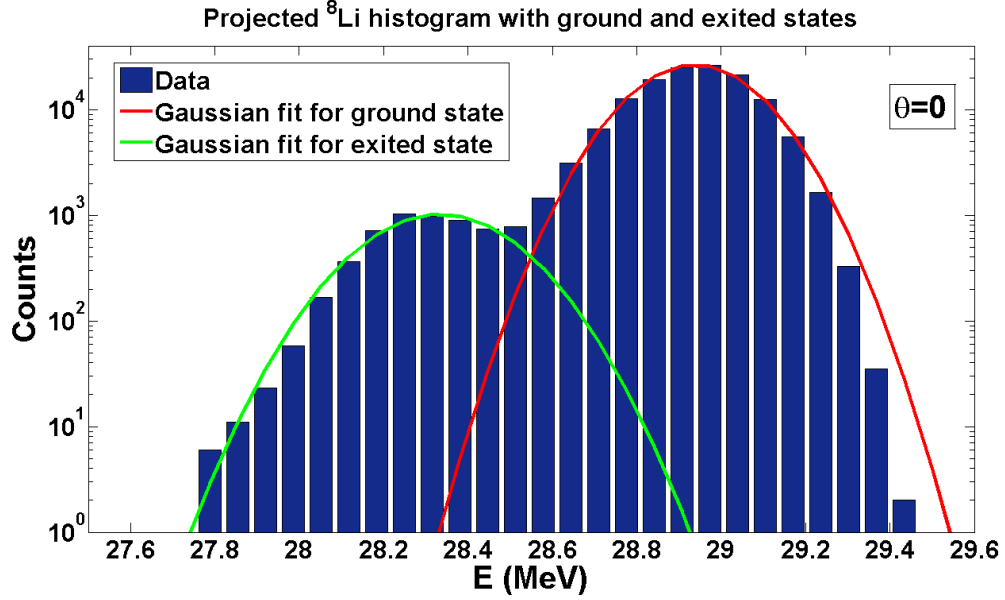


Figure 5.9: Total energy profile of low-intensity ${}^8\text{Li}$ secondary beam ($\theta=0^\circ$) measured on a Si detector at the target position in the back chamber.

mass to ${}^8\text{Li}$, the kinematic shift from such an elastic scattering is large enough to obscure the inelastic scattering from the target nuclei. These contaminant peaks are still visible for larger angles, however they are separated from the ${}^8\text{Li}^*$ Coulomb excitation group. An example of data from a typical run for one detector (45°) using the thin gold target is shown in Figure 5.10. The ${}^8\text{Li}$ ground state data was fitted using a skewed Gaussian peak shape:

$$(5.1) \quad f(x) = 2 \times \frac{1}{\sqrt{(2\pi)}} e^{-\frac{x^2}{2}} \times \frac{1}{2} \left[1 + \text{erf} \left(\frac{x}{\sqrt{(2)}} \right) \right]$$

The residual from this fitting includes the ${}^8\text{Li}^*$ excited state group together with several contamination groups from excitation of gold or other contaminant nuclei in the target. $P(\theta)$ was determined by the ratio of a Gaussian fit of the excited ${}^8\text{Li}$ group to the skewed Gaussian fit of the ground state ${}^8\text{Li}$ group. Plots of $P(\theta)$ are shown in the next section. In general, the data from the thin and thick gold targets

are in reasonable agreement.

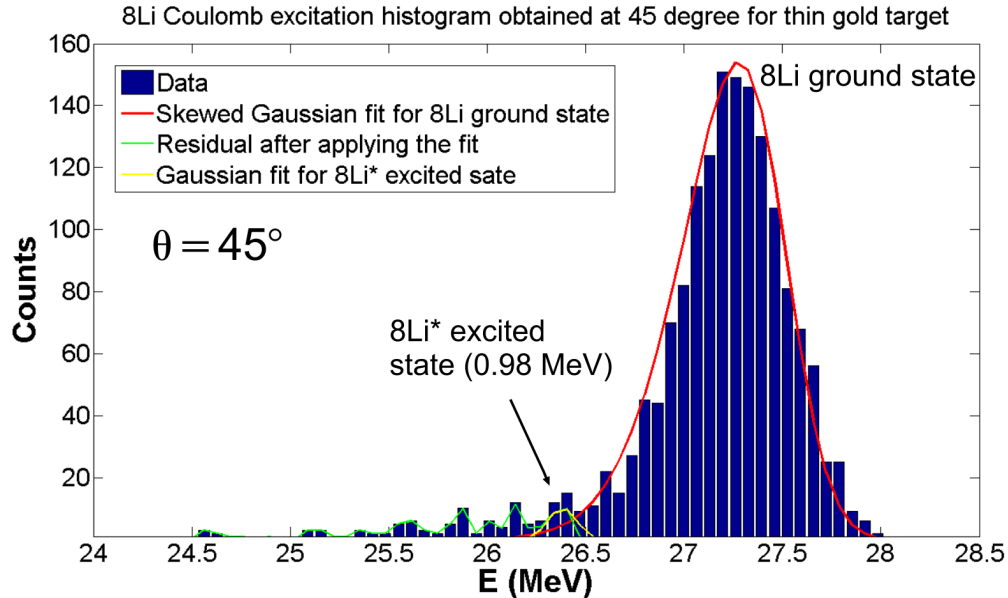


Figure 5.10: An example of data for a single data collection period (8 hours) for one detector (45°) ($^8\text{Li} + \text{nat. Au}$ thin target). The fitted peaks to the data shown were used to extract the inelastic reaction probability $P(\theta)$.

Between experimental runs of the ^8Li beam on the natural Au targets, several runs with empty target frames also were taken to investigate whether there was any primary beam hitting the target frame (which were made of plastic and aluminum) and creating contaminations contributing to the $^8\text{Li}^*$ excited group region. This investigation (Figure 5.11) shows almost no scattered ions from the primary beam were scattered from the target frame into the ^8Li group region at all angles studied.

5.4 DWBA Analysis

A detailed description of DWBA can be found in several references [Sat80, Ald66, Ald75]. The DWBA codes Dwuck4 [Kunz] and Ptolemy [Ptol] were used to perform the DWBA calculations. These codes can implement several hundred partial waves per calculation as specified by the user as needed for CoulEx.

There are many options for the reaction form factor of the perturbative potential

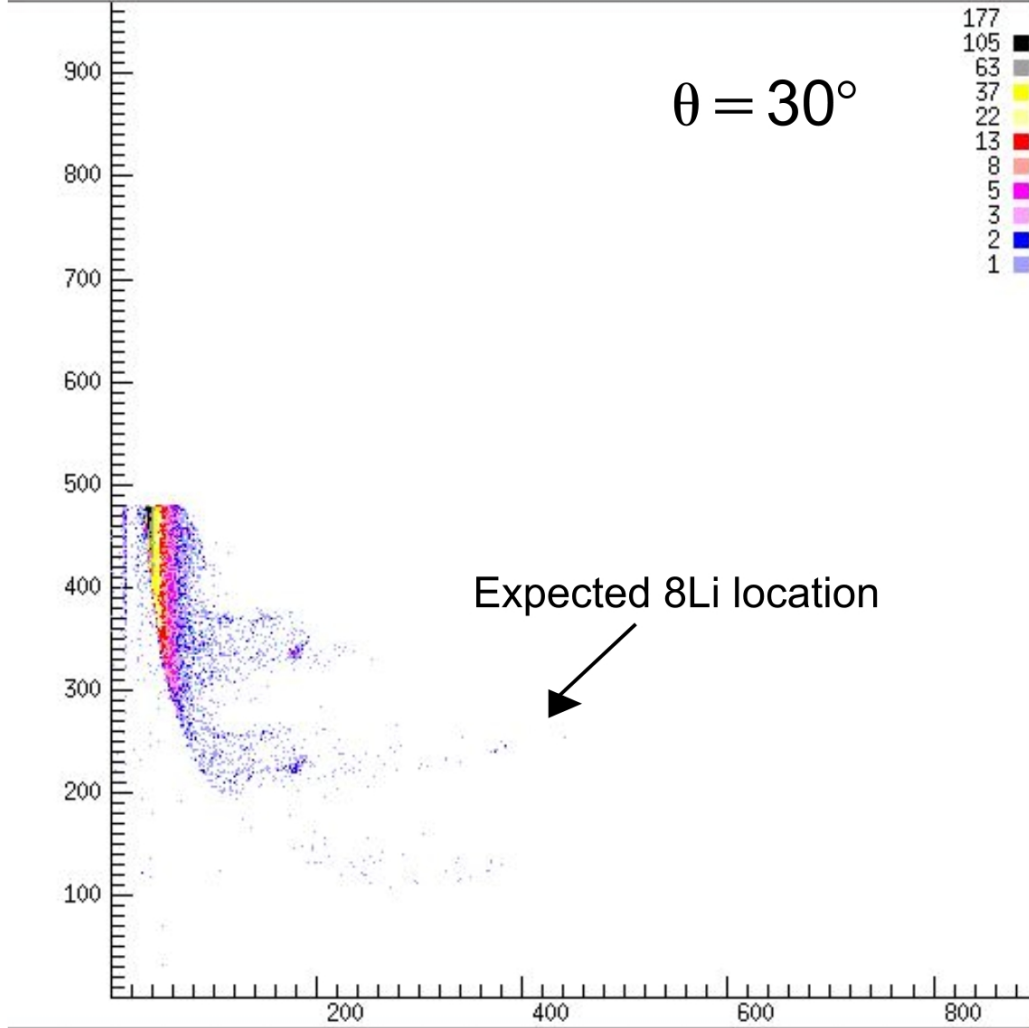


Figure 5.11: ToF vs. total energy histogram taken at 30° with empty target frame shows almost no scattering ions from primary beam into ^8Li group.

that may be used in DWBA. A suitable nuclear interaction potential for the L=2 inelastic excitation studied in this experiment, has a form factor which can be written in terms of phenomenological quadrupole deformation parameter β [Kunz; Sat80].

$$(5.2) \quad V'(r, \theta) = -\beta \frac{dV(r)}{dr} Y_2^0(\theta)$$

where $V(r)$ is the optical potential. $V(r)$ has both real and imaginary nuclear components and a Coulomb part $V_C(r)$, where the imaginary term accounts for the nuclear absorption of the incident beam:

$$(5.3) \quad V(r) = -V_R f(x_R) - iV_I f(x_I) + V_C(r)$$

$$(5.4) \quad f(x_i) = (1 + e^{x_i})^{-1}$$

$$(5.5) \quad x_i = (r - r_{0i} A_T^{1/3})/a_i = (r - R_i)/a_i$$

$$(5.6) \quad V_C(r) = \begin{cases} \frac{Z_P Z_T e^2}{2R_c} [3 - (r/R_c)^2] & r \leq R_c \\ \frac{Z_P Z_T e^2}{r} & r > R_c \end{cases}$$

The nuclear well depths (V_R and V_I) and the diffuseness (a_R and a_I) of the nuclear potentials as well as the characteristic radii (r_{0R} and r_{0I}) are the input parameters. $V_C(r)$ is the Coulomb potential from the finite size target charge. To process the DWBA calculation, we used the optical model (OM) parameters from an earlier ^8Li elastic scattering experiment done at somewhat lower energies (14.6 MeV) using the L'il Sol apparatus and a nickel target [Bec93]. Although this experiment was conducted at higher energies with gold targets, the earlier OM parameters should be reasonably acceptable for performing these calculations. Since the ^8Li beam energy is well below the Coulomb barrier, we verified that only Coulomb scattering dominates. One can then turn off the nuclear part of the OM parameters by setting V_R and V_I as 0 and keeping only $V_C(r)$. A list of the input parameters is given in Table 5.4.

In this experiment the nucleus is excited to a higher state and the transition is typically dominated by the electric quadrupole (E2) moment [Bro91]. As discussed earlier the excitation primarily is due to Coulomb excitation. The computer program generates an output of the calculated differential cross sections (not scattering amplitude) that must be scaled by a factor β^2 to fit the observed data (Figure 5.12).

Optical Model Parameters for ^8Li Inelastic Scattering		
Real Potential	V_R	0 MeV
Real Radius Parameter	r_{0R}	1.30 fm
Real Diffuseness	a_R	0.80 fm
Imaginary Potential	V_I	0 MeV
Imaginary Radius Parameter	r_{0I}	2.25 fm
Imaginary Diffuseness	a_I	0.80 fm
Coulomb Radius Parameter	r_{c0}	1.25 fm
$R_R = 1.3A_T^{1/3}\text{fm}$ $R_I = 2.25A_T^{1/3}\text{fm}$ $R_C = 1.25[A_p^{1/3} + A_t^{1/3}]\text{fm}$		

Table 5.4: Optical model parameters

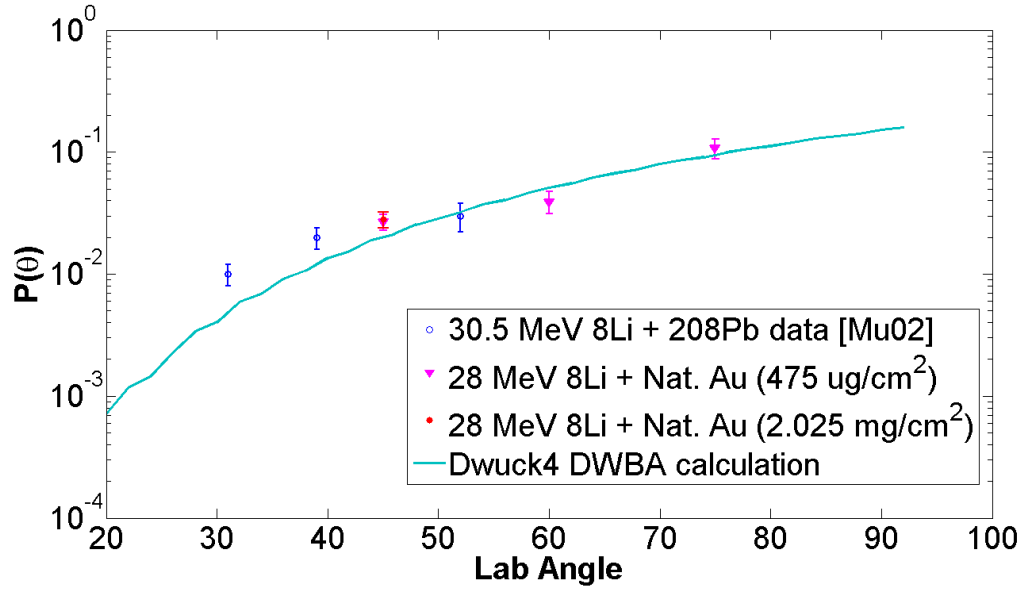


Figure 5.12: Experimental data and DWBA calculation for inelastic excitation (CoulEx) of a ^8Li RNB incident upon a $475 \mu\text{g}/\text{cm}^2$ and a $2.025 \text{mg}/\text{cm}^2$ nat. Au target at 28 MeV. Previous data for a 30.5 MeV ^8Li on a ^{208}Pb target also is shown [Mu02].

The reduced reaction probability $B(E2)\uparrow$ (measured in units of $e^2\text{fm}^4$) can be calculated as follows [Ptol]:

$$(5.7) \quad B(E2)\uparrow = \left(\frac{3Z_p}{4\pi}\beta_p R_p^2\right)^2$$

The transition in ^8Li from a non-spherical $J^\pi = 2^+$ ground state to a $J^\pi = 1^+$ excited state ($E_x = 0.98\text{MeV}$; Figure 5.1) is an L=2 transition, or E2 \uparrow transition in the case of Coulomb excitation. The Ptolemy or Dwuck4 codes can be used to

extract $B(E2)\uparrow$ directly. The results of the curve fitting shown in Figure 5.12 are found in Table 5.5. (The data at back angles for the thick gold target only provide upper limits due to the large target energy spread.)

8Li Energy (MeV)	Target	βR (fm)	$B(E2)\uparrow$ ($e^2\text{fm}^4$)
28	475 $\mu\text{g}/\text{cm}^2$ nat. Au	1.38 ± 0.14	55 ± 10
28	2.025 mg/cm^2 nat. Au	1.38 ± 0.14	(30-100)
30.5 [Mu02]	^{208}Pb	1.41 ± 0.14	100 ± 20
30.5 [Mu02] ^a	^{58}Ni	0.91 ± 0.10	22 ± 5
14.6 [Bro91]	^{58}Ni	1.36 ± 0.14	51 ± 10

Table 5.5: CoulEx results

^aMay include significant nuclear excitation.

This experiment reveals that the Coulomb excitation of ^8Li at 28 MeV from a gold target is similar to the Coulomb excitation from the previous study performed at 14.6 MeV on a nickel target [Bro91] and the thesis data reported by M. Lee for $^8\text{Li} + ^{208}\text{Pb}$ [Mu02], but in our case using ToF to clearly separate out the $^8\text{Li}^*$ in the ^8Li RNB. Both 28 MeV and 14.6 MeV represent ion-beam energy values below the nominal Coulomb barriers for a lithium beam incident upon gold and nickel targets respectively, and indicate an unusually large $B(E2)\uparrow$ for ^8Li compared to stable nuclei in this mass region [Bro91]. The new ToF techniques used here should permit improved nuclear reaction measurements at *TwinSol*.

CHAPTER VI

Low-Energy and Secondary (Radioactive) Ion-Beam Profile Measurements and Optimization using Modified Gafchromic[®] EBT Film¹

6.1 Introduction

Two of the most effective techniques for producing exotic ($N \ll Z$ or $Z \gg N$), short-lived (i.e. radioactive) nuclear beams (RNB) are via in-flight fragmentation or selective nuclear transfer reactions using an intense, stable primary beam [Mor98, Bec91, Kol89]. The secondary RNB ions made by these methods as noted are then separated and refocused to a secondary reaction target using magnetic dipole- or solenoid-based ion-optical systems [Mor98, Bec91, Kol89, DJM2, Mor03, Bec03]. The RNBs produced must be carefully collimated and refocused to avoid contamination of the desired RNB from the intense scattered primary beam, which may appear in various charge states, and from other sources of background ions which also may be present. This is particularly true of solenoid-based systems, which operate in-line at zero degrees with the primary beam and thus refocus the secondary RNBs produced close to zero degrees. This is the situation for the dual-superconducting solenoid system *TwinSol* (Figure 6.1). In *TwinSol* the secondary RNB is typically produced via a high-cross-section selective nucleon-transfer reaction using a ${}^7\text{Li}$ or ${}^6\text{Li}$ primary

¹Adapted from manuscript submitted to Nuclear Instrument and Methods written by the author and his thesis advisor.

beam ($E=20$ to 40 MeV) on a foil or a gas production target. This method produces reasonably intense ($10^4/s$ to $10^7/s$) secondary beams of low-energy ^8Li , ^6He , ^7Be , ^8B , and other specific RNBs collected over a range of 2° to 6° (or more) at the entrance of the first solenoid (Figure 6.1), depending on the particular entrance aperture. In addition to existing first- and second-generation RNB facilities such as *TwinSol* several new third-generation accelerator facilities for low-energy RNB work of this type are under construction or in the final planning stages [Hen08, Voc08, Lew08, Kra09].

In *TwinSol* the intense primary beam is stopped as noted in a carbon faraday cup backed by an extended tungsten-alloy beam stop, which also serves as a small-angle γ and neutron block. The primary RNB ions of interest along with other ions with the same magnetic rigidity (analogs) typically are focused using the first solenoid (which acts as a large aperture magnetic ion-optical lens) through a small aperture at a cross-over point between the two magnets(B; Figure 6.1). These ions are then refocused onto reaction targets located in one of several secondary reaction chambers located downstream of the second solenoid (e.g. C and D; Figure 6.1). Alternately, the system can be operated without an intermediate cross-over focus, where the two magnets combine to form a thick lens system without an intermediate image. In either mode, the alignment of the ion-optical and beam-line components (magnets, faraday cup, primary beam stop, vacuum beam pipe and chambers, beam blocks, apertures, etc.) is critical to minimizing unwanted background in the desired RNB. Unfortunately, manufacturing tolerances in the magnets, cryostats, beam-line components, and especially tolerances in large International Organization for Standards (ISO) components can result in misalignment of the mechanical, optical and ion-optical (i.e. magnetic) axes, which can, and often does, enhance the background in

certain RNB experiments.

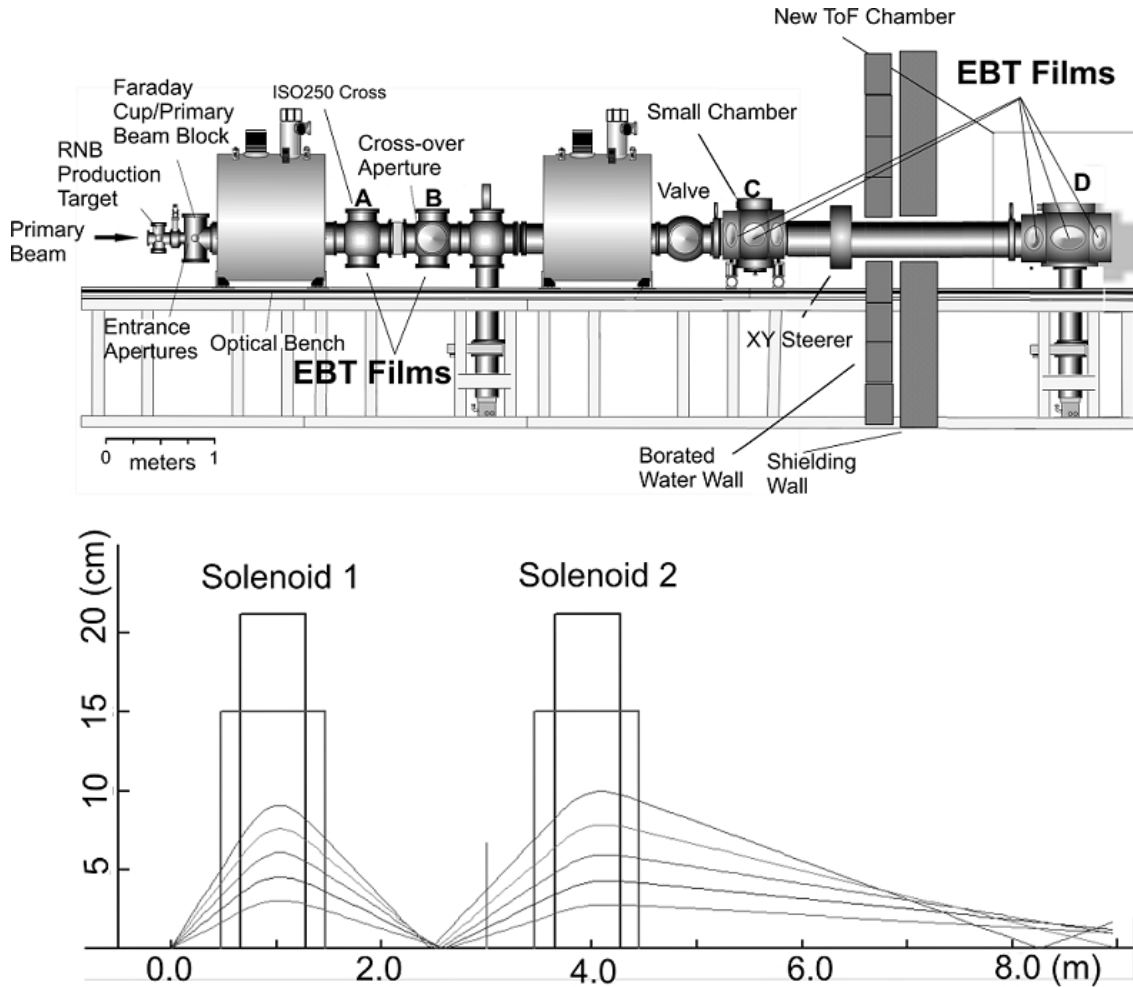


Figure 6.1: Top: A schematic layout of the *TwinSol* RNB system showing the extended beam line and new ToF chamber. The location of chambers used to obtain film images described in the text are indicated with the labels A, B, C and D. Bottom: Ray-tracing calculations for the ${}^8\text{Li}$ RNB used for in-beam tests (note scales). The trajectories of ${}^8\text{Li}^{3+}$ ions produced at initial angles 2 to 6 degrees (spanning the *TwinSol* entrance aperture) are indicated.

Although we have used electronic detectors such as position-sensitive silicon and gas detectors (e.g. PPACs) for RNB imaging, these require special mounts, electronics, vacuum feedthroughs, have limited dimensions, etc. Hence, they cannot easily be used in many of the locations in a typical multi-element ion-optical system where beam images (even if off focus, i.e. where the images are very large) would

be desirable. This also holds true for scintillators that must be viewed with a high-sensitivity camera. Unlike film images, geometrical linearity and accurate centering can be problematic with electronic detectors, often requiring extensive calibrations. In addition, silicon and gas imaging detectors are not always sensitive to the wide range of ions, electrons x-rays and γ radiation that nonetheless can produce background in the reaction-product detectors used in a specific experiment. In order to deal with the above issues and especially to optimize the design and location of precision collimators and blocks for specific RNB experiments, we have developed a method to quickly acquire accurate beam profiles for low-intensity, low-energy ions utilizing custom-made film based on a unique type of high-sensitivity radiochromatic medical imaging film (Gafchromic[®] EBT). This is particularly advantageous for the *TwinSol* system, which typically operates with the magnets running in persistent mode as the magnets have no steel yoke. In this mode the magnetic fields and hence the ion-optics are very stable over the long accelerator running times typically needed for RNB experiments (1-2 weeks) which permits the use of fixed, precision collimators at critical locations provided they can be optimally located. Once their locations have been determined using film imaging, these collimators can be positioned at the start of an RNB experiment to ensure optimal running conditions.

Most ions of interest, as well as any electrons or other radiation present usually will be imaged on the modified EBT film. While conventional silver-halide based photographic film can be used in some cases for RNB imaging, they require light-tight enclosures and external developing. Similar limitations apply to CR39 and other plastic track detectors [Hen08], which we previously have used, as these require chemical etching and scanning to reveal an image. Hence the EBT film is a more immediate, simple, and flexible solution for many low-energy ion beam imag-

ing applications. However, once images with the EBT film have first been obtained, some of these alternate imaging methods then can be used more effectively to obtain additional imaging data (e.g. ion identification).

Below, we present some recent results using the modified EBT film. The primary in-beam measurement described involves use of the film to check the ion-optical versus optical alignment of the *TwinSol* system in cross-over mode, including the alignment and ion optics into a new scattering chamber. It also included identifying sources of unwanted background and determining the collimation needed to improve future *TwinSol* RNB experiments. Although we describe beam imaging relevant for a particular RNB system, the techniques used and the images obtained would be typical of many other low-energy RNB or ion-beam systems.

6.2 Film Characteristics

As noted, the film used is a custom version of a high-sensitivity version of Gafchromic[®] EBT radiochromatic medical imaging film [ISP]. The general characteristics of the modified film are listed in Table 1. It is said to be tissue equivalent but that refers to x-rays and γ -rays where plastic (basically CH₂) and tissue (mostly H₂O) have similar absorption. Typically the film can be calibrated to provide x-ray and γ -ray dose profiles using gray-scale pixel values determined by scanning the exposed film using a high-quality flat-bed scanner [NIH]. This does not necessarily apply to charged particles where the relation between the scanned gray-scale pixel values and dose (or absolute intensity) will be a function of the ions' energy loss in the film layer (which may depend on angle of incidence although here the ions imaged are incident at angles less than 10 degrees) and other factors (ion type). In our measurements the primary beam profile (beam image) and its intensity relative to background ions

of similar mass and not their absolute intensities (fluence) were of primary interest.

Earlier, standard low-sensitivity versions of this type of film (e.g. MD-55) have been used to image electron and proton radio-therapy beams [Cyb03, Kra09], but as noted the thick laminate coating covering the active material on the stock film (97 microns for EBT film) is too thick for many applications involving imaging of low-energy ions. At our request special versions of EBT film, with only one side of the laminate present (Figure 6.2), were made by the film supplier (ISP, [ISP]) and used in the work described here. After suitable exposure, the film is scanned on a high-quality but conventional optical scanner where relative ion intensity profiles can be obtained. In our measurements we used a 300 dpi, 32 bit Epson®model 1260 flat-bed scanner to generate gray-scale pixel values from the exposed film. After scanning, any standard image analysis program (in our case we use variations of the public-domain program NIH Image [NIH]) can then be used to generate relative intensity profiles of gray values, and to analyze the images in detail.

Table 6.1: EBT film features relevant to ion-beam imaging^a

Sensitive to x-ray doses ranging from about 1cGy to 800cGy
Self developing and viewable in real time
Uniform and consistent
Energy-independent x-ray dose response from keV to MeV
Near tissue-equivalent for x-rays ^b
High spatial resolution
Insensitive to light
Water resistant - Usable in vacuum
Digitized with standard optical flat-bed scanners

^aAdopted from ISP literature [ISP]

^bDoes not necessary apply to particles (see Sec. 6.2)

As shown below, after the initial in-beam measurements demonstrated the advantages of beam imaging with the film ,the film is now being used in several *TwinSol* RNB experiments to design and locate suitable collimators for specific nuclear reaction studies.

6.3 Film Imaging Measurements

6.3.1 Measurements with a ^{244}Cm α -source

The first imaging measurements with the modified EBT film were done using a thick ca. 100 μCi ^{244}Cm α source. Owing to energy lost in the metal plating sealing the source, the mean α -particle energy was less than the α decay energy and was measured to be about 4.5 MeV. ^{244}Cm α source images were obtained both in vacuum and in air and an intensity profile for the source produced from a scanned image (Figure 6.3). Other than normal precautions of using gloves to handle the film, not touching the sensitive surface, and keeping the film when not in use in a light-tight protective envelope, no other special precautions were taken in handling the film.

The images obtained from the gray-scale pixel values reproduce the intensity profile expected for a uniform source assuming the film is not saturated, as appears to be the case. The gray scale values obtained varied only slightly (1-2%) depending on the orientation of the film when scanned. Likewise when the film was scanned 6 months after the initial scans (after being kept in a light tight envelope at room temperature) it reproduced the original gray-scale pixel values and image to within 5%.

If needed images from a source of known intensity (as above) could be used to

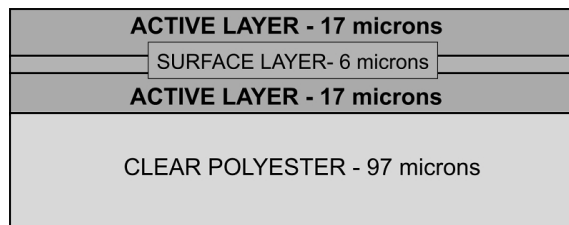


Figure 6.2: Cross section of the modified EBT film used in the present ion-beam measurements (adapted from material provided by ISP [Rol88]).

calibrate the film gray-scale pixel values (accounting for ion energy loss in the film) to obtain absolute ion-beam intensities for a low-energy ion similar to an alpha particle, but again we can obtain that information from silicon imaging detectors and did not pursue that possibility. Hence, it appears that this modified high-sensitivity EBT film can be used to determine the intensity and uniformity of low-energy radioactive sources. This especially may be useful for short-lived sources made in-beam by various methods.

Based on these initial results, a set of in-beam measurements at the UM-UND *TwinSol* RNB facility at UND were performed using a low-intensity secondary RNB. The α -source measurements then served as a guide to the exposure times needed to obtain good in-beam images.

6.3.2 In-beam *TwinSol* RNB measurements

The primary in-beam tests described here involved production of a standard short-lived (i.e. < 1 sec.) *TwinSol* RNB (^8Li) run in cross-over mode. This beam then was used to check the optical versus ion-optical alignment of the system at various key locations. This included images of the beam transported to a newly-installed large chamber on an extended time-of-flight (ToF) beam line (Figure 6.1). We were particularly interested in locating possible sources of unwanted contaminant ions and other sources of background, especially those due to mis-aligned collimators and beam blocks.

RNB production and transport

A 30 MeV ^7Li primary beam on a gas-cooled beryllium production target (Figure 6.1) produced a 28 MeV secondary ^8Li beam of ca. $10^6/\text{sec}$ per 100 electrical nanoamps of primary beam. A 2 to 6 degree aperture before the first solenoid lens

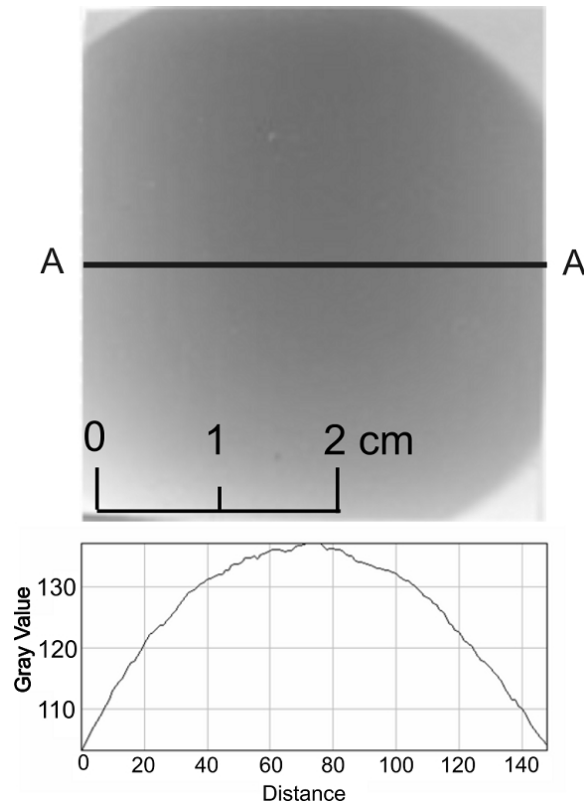


Figure 6.3: Top: Gray-scale pixel image (relative intensity profile) of a thick ^{244}Cm alpha source located a few cm (in vacuum) from modified EBT film. (The original colored images have been converted to grayscale for publication.) Bottom: A cross-sectional profile for the section AA indicated in the ^{244}Cm film image is shown. (Same distance scale at top also applies to the bottom profile with ca. 40 units/cm)

defined the ^8Li production angles and hence the initial beam divergence. The beam then passed through one ISO-250 chamber (A; Figure 6.1) and into a second ISO-250 chamber (B; Figure 6.1) where it was focused at a cross-over point near the middle of that chamber. Using the second solenoid magnet the ^8Li secondary beam, after passing through another set of ISO-250 chambers and a smaller chamber (C; Figure 6.1), was then steered and focused at the target location of the newly-constructed large scattering chamber (D; Figure 6.1). The ToF chamber, used in the RNB experiments utilizing ion time-of-flight to improve energy resolution, is located in a low-neutron-background area on an extended *TwinSol* beam line situated behind a large borated-water shielding wall (Figure 6.1). An electronic position-sensitive silicon-detector $\Delta\text{E-E}$ telescope located at the ToF chamber target position initially was used to identify, focus and steer the desired ^8Li RNB onto the target position and determine its intensity.

Film imaging locations

Since the EBT film does not require removal for developing or other special processing (and is not very sensitive to light), multiple film images can be obtained and viewed in situ along several different positions in the ion-optical system via the use of multi-position movable film holders. The film then can be viewed via standard or custom beam-line viewing ports. At one of the ISO-250 chamber locations (A; Figure 6.1) we used a thick aluminum sliding paddle with the EBT film attached (Figure 6.4) and a similar arrangement at the other locations. The optical center of each film is accurately located and noted using a standard alignment telescope which is aligned with the *TwinSol* beam-line optical axis. By using sliding and similar film paddles it is possible to obtain many film images at various locations (Figure 6.1) without

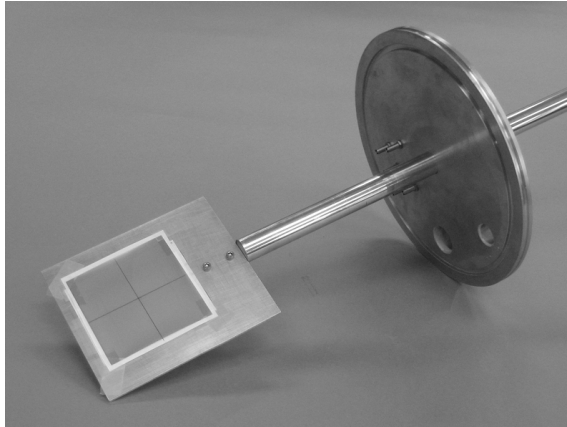


Figure 6.4: A photograph of a film paddle with modified EBT film mounted for use in an ISO-250 chamber.

breaking vacuum. Thus a uniform set of film images through the entire ion-optical system can be obtained in a minimal amount of in-beam time. The front side of our standard film paddle can hold two 2 in. \times 2 in. (50 mm \times 50 mm) or single 4 in. \times 4 in. (100 mm \times 100 mm) film pieces, while the backside can hold another set of film. The paddles, which can be moved via an o-ring vacuum shaft seal are 1/8 in. (3.2 mm) aluminum and can stop any of the expected spurious ions in the desired RNB. In general, γ -rays and neutrons will not be stopped and must be considered separately (see below). If more film is needed at a given location, larger paddles together with an ISO-250 extension piece can be utilized to provide 4 or more film pieces at a given location.

6.3.3 Primary RNB film images

Since the EBT film displays an image without development and can be used without any light-tight coverings, appropriate film exposure can be determined just by looking at the film in situ through viewports. We used large custom-made clear Lexan[®] viewports on the ISO-250 chambers (A and B; Figure 6.1) or on the new chamber (D; Figure 6.1) to view the film images during the in-beam exposures. This

is a significant advantage over other film-imaging methods. Even if the film cannot be viewed directly in place, as noted the needed exposure for a usable image can be estimated from exposures using a known alpha source (Sect 3.1). Although the EBT high-sensitivity film is linear with dose over a wide range of dose for photons [ISP], care must be taken not to overexpose the film if more quantitative measurements (e.g. relative gray scale profiles) are desired. Again, we note that since the film can be viewed in situ with the exposure observed in real time the exposure can be kept below saturation values.

RNB images for the above ^8Li RNB were obtained at several upstream locations (A,B,C; Figure 6.1), which includes the small chamber (C) after solenoid 2, just before the XY steering element (Figure 6.1) where the RNB of interest is off focus . Other images (Figs. 6.5 and 6.6) were obtained at the ISO-250 chambers (A and B) immediately after the first solenoid which are at or near the ^8Li RNB cross-over focus in chamber B. These chambers also are close to the production target and beam stop (Figure 6.1). Silicon detectors at the target position in the back ToF chamber(D) indicate that the RNB after the second solenoid is mostly made up of secondary ^8Li ions.

As discussed in more detail below, while the ^8Li beam images at the back ToF chamber(D) were basically as expected, the upstream images close after the first and second solenoids indicate some unexpected background sources where the film images proved particularly useful.

RNB film images: Chambers A and B

The images obtained in the upstream ISO-250 chamber (A) and at the adjacent cross-over location (B) between the solenoids (Figures 6.5 and 6.6) together with

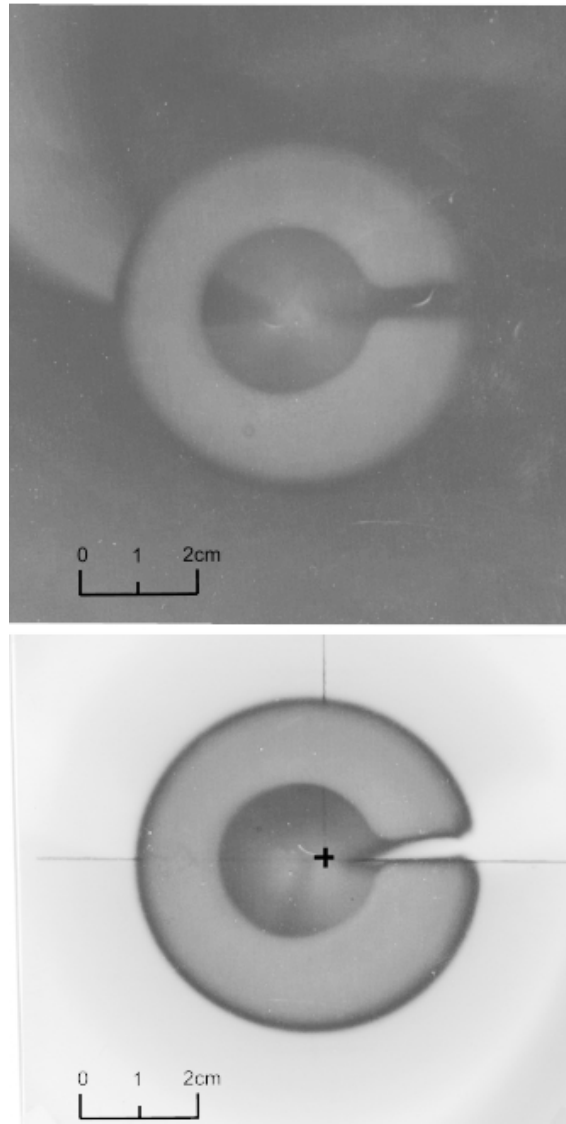


Figure 6.5: Images of RNBs with background ions obtained at chamber A indicated in Figure 6.1. Top: Image obtained on front film. Bottom: Image obtained on a film piece located after first film (top) where the latter acts as a ca. 137 micron plastic absorber (see text). The images of the off-focus background beams are overexposed in these films as the exposure times were set to optimize images of the less intense ^8Li ions. (The original colored images have been converted to grayscale for publication.)

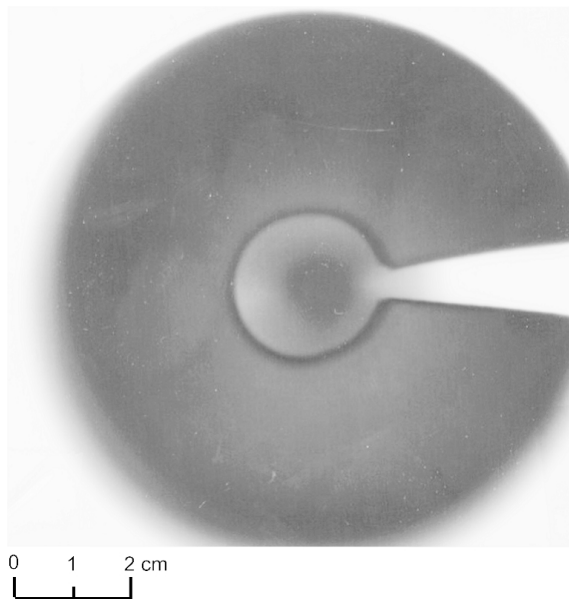


Figure 6.6: Image of RNBs, background ions, and radiation obtained at the cross-over chamber (B; Figure 6.1). The ions focused at the center of the image are the ${}^8\text{Li } q=3^+$ RNB and its analog ions. (The original colored images have been converted to grayscale for publication.)

images obtained at other locations (below) indicate a misalignment between the optical and ion-optical (magnetic) axes or a misalignment of the entrance aperture to the first solenoid. The latter is more likely as we observe a focused RNB image close the optical axis whereas the off-focus image is misaligned. This alignment information is critical for experiment design. As an example, at the cross-over focus location (B) a fast timing detector is planned for ToF operation and it is essential to minimize the count rate from any spurious ions at that location in order to utilize the full RNB intensity (up to $10^7/\text{sec}$ in some cases). The alignment and profile information also is needed to effectively implement a differential energy-loss absorber to compensate for the kinematic energy spread with production angle in the *TwinSol* secondary RNBs. In both cases these can help to minimize the energy spread inherent in the *TwinSol* RNBs [Voc08].

The film images just before and at the cross-over focus location (Figures 6.5

and 6.6) reveal a large background of unwanted i.e. out-of-focus ions and/or other radiation. At the forward location (A) we used two layers of film, where the front 137 micron thick EBT film (Figure 6.2) acts as an absorber for many of the low-energy ions, but not high-energy electrons, gamma rays or neutrons. The use of a film stack was done to help identify radiation in the images obtained as several types background sources were anticipated. At this location, any spurious ions or electrons present are nonetheless still constrained by the magnetic fields present and will show a distinct image (e.g. Figure 6.7). The radiation observed did not penetrate the aluminum film plate holder and hence produce any background radiation dose on the film behind the film being exposed. Thus the background likely is not due to x-rays, γ -rays and neutrons (which were expected sources of background radiation). We conclude, and the images obtained confirm, that the background of concern is primarily due to unwanted secondary ions made at the production target. The obvious candidates for the latter are the ca. 30 MeV scattered ions of the primary ${}^7\text{Li}$ beam in charge states $q = 1^+$, 2^+ and 3^+ , each of which will be on different trajectories than the ${}^8\text{Li}$ RNB of interest, as the latter is focused at the crossover due to its particular magnetic rigidity (Figure 6.6).

Analysis of the size of the images and location of the faraday cup support shadow seen i.e. its rotation angle (Figures 6.5 and 6.6), and thus the magnetic rigidity of the spurious ions, is consistent with this interpretation. Normally a beam block for the ${}^7\text{Li}$ $q = 3^+$ beam is located at that beam's focus location, but the new film data illustrate the need to also effectively block the $q = 1^+$ and 2^+ ${}^7\text{Li}$ scattered beams to minimize background ions downstream. Much of the spurious background is not directly seen with our primary silicon imaging detectors, which are limited in size (25 mm \times 25 mm) and thus cannot see large off-focus images. In fact the center

“hole” seen in some of the images (due to the beam stop) would overlap the silicon imaging detector at that location, yet the ions unseen in the silicon detector could still produce a large background of unwanted ions in downstream reaction-product detectors. As noted below in Sect. 6.3.4, there also may be some film darkening due to the presence of the beta (electron) and alpha particles emitted in the decay of ^8Li in flight or after stopping in the film or film paddle, a feature unique to RNB imaging.

RNB film images: Chamber C

Film holders placed within the smaller chamber (C) provide useful off-focus images at that location. These images which are several meters upstream of the ToF chamber(D) are shown in Figure 6.7. The off-focus image at the location of the small chamber(C) shows intense background ions near the magnetic axis, which were not directly seen in silicon imaging detectors previously placed at that location. The background is attributed to energetic electrons or very low-energy ions (i.e. ions easily bent in the magnets) spiraling down the solenoid axis and produced from various (unknown) sources along the beam line. A suitable block at that location will remove this background while permitting the secondary RNB of interest (comprising most of the intense ring image seen in Figure 6.6) to pass through. In Figure 6.7 and others, one also observes a significant source of background from ions scattered at very small angles, probably from the primary ^7Li beam scattered from the edge of the beam stop located at the front of the first solenoid. This indicates a misalignment of the beam stop and/or the *TwinSol* entrance aperture with the ion-optical (magnetic) axis. As discussed earlier this also is indicated in some of the other images (see Sect. 6.3.3.1).

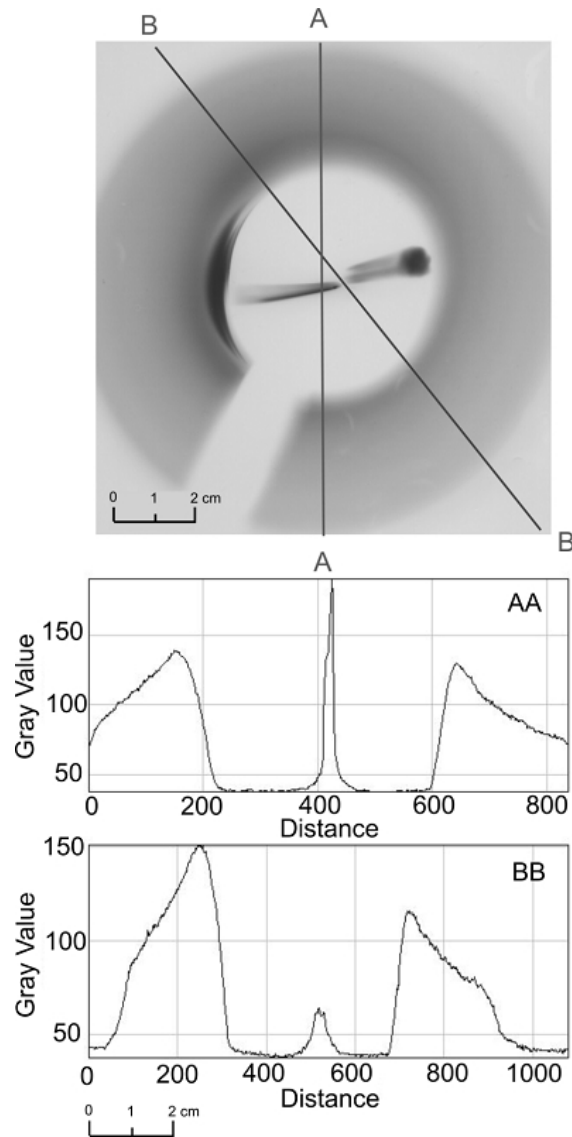


Figure 6.7: Off-focus image (top) and profiles (bottom) for cross sections indicated of the ^8Li RNB and background ions observed in the small chamber (C in Figure 6.1) upstream of the ToF chamber. The distance is relative to the film edge and corresponds to about 100 units/cm as indicated by the scale. (The original colored images have been converted to grayscale for publication.)

Using the film images, we can deduce the location and extent of the misalignments and hopefully either rectify them or alternatively use custom-made collimators to block out the unwanted ions. In the image shown in Figure 6.7 and as noted in similar images, we image the rotated “shadow” of the primary beam-block support shaft. The rotation angle from vertical is a measure of the magnetic rigidity of the ions being imaged owing to the spiraling motion of the ions in the solenoid fields [Mu02]. The rotation angle of this shadow as determined from suitable ray-trace calculations [Mu02] then can be used to confirm the identity of the ions (and analogs) in the image (see below). Using this image, any needed collimator or beam block support at this or other locations could be precisely aligned to correspond to this shadow and thus not intercept any of the useful RNB. Again, we are not primarily interested in the absolute dose e.g. the absolute intensity; that is known from the silicon position-sensitive imaging detectors that we typically use. It is the geometrical distribution of the RNB and the intensity relative to any background ions that are of primary interest here.

Figure 6.7 (bottom) shows two cross-sectional scans of the off-focus image shown in the figure. The image seen in Figure 6.7 (top), where the beam is not focused back to the axis, is an image of the secondary ^8Li and analog ions coming through the *TwinSol* entrance aperture (Figure 6.1). Thus the gray scale profiles shown in Figure 6.7 (bottom) are an indication of the ^8Li RNB production yield versus angle from 2° to 6° and in addition show the relative intensity of the spurious background ions near the axis. This can be very useful in selecting a suitable RNB production reaction and the corresponding optimal *TwinSol* entrance and cross-over apertures, as well as selecting suitable on-axis beam blocks.

RNB film images: New ToF chamber D

In addition to film images taken in chambers A, B and C, described above, images were obtained to determine the beam profile at the entrance, target position and exit locations of the new ToF chamber (D; Figure 6.1) . This again was done to determine possible sources of unwanted background and any misalignment of the new chamber with respect to the actual (i.e. ion-optical) beam axis (Figure 6.8). This information can then be used to design suitable collimators to minimize background and to determine the true beam axis to accurately calibrate RNB reaction scattering angles in that chamber. Alternately the information can be used to accurately adjust the alignment of the new chamber with respect to the true beam axis. This was particularly critical given the location of the new chamber on an extended beam line far downstream from the second solenoid where any upstream ion-optical misalignment would be magnified at the chamber target position. Fortunately slight adjustments of the available X-Y steerer(Figure 6.1) brought the ^8Li RNB back on line with the chamber center target position (Figure 6.8) without further chamber alignment as verified from the film EBT images (Figure 6.8)

6.3.4 Use in a typical ^8B and ^7Be low-energy RNB experiment

Shortly after the in-beam film tests with ^8Li described above were performed, a *TwinSol* experiment using ^8B and ^7Be secondary beams was scheduled with secondary reaction products detected in the small scattering chamber (C) located after the 2nd solenoid (Figure 6.1). This is a somewhat different ion-optical set up relative to transporting a beam to the back ToF chamber (D). Film images of the initial 24.6 MeV ^8B RNB together with other ions including analog ions were quickly obtained (Figure 6.9). Based on those images a suitable set of collimators was made

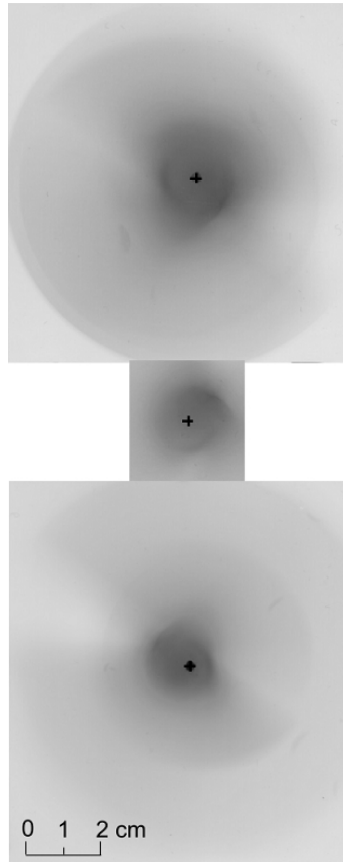


Figure 6.8: ^8Li RNB beam images (including contaminant ions) obtained in the new ToF chamber (D in Figure 6.1). Top: Image at entrance to the chamber. Middle: Image at the target location (center of chamber). Bottom: Image at exit of the chamber. (The original colored images have been converted to grayscale for publication.)

and suitably located to minimize unwanted ions for that specific experiment and the specific ion-optical setup used. This provided data with reduced background from contaminant ions and electrons. The results of this experiment recently have been published [Agu09].

6.4 Special Aspects of RNB Imaging

One interesting aspect of imaging RNBs alluded to previously is that RNBs decay in flight or when stopped with emission of a β -decay electron or other radiation. This radiation in principle can produce an additional darkening on the film if the beam is being stopped in the film or in the film paddle. In the case of the ^8Li beam used above, an electron with endpoint (i.e. maximum) energy of 13 MeV is emitted followed by the emission of two alpha particles of a few MeV from the ^8Be residual nucleus [NDE]. Fortunately, the relatively high magnetic fields present at most locations in the *TwinSol* system will confine any charged particles emitted to the beam magnetic axis and generally should not blur the images, but it could affect the RNB profiles deduced from the images. Hence in some applications using RNBs this added radiation may need to be considered. In certain cases an absorber might prove useful in selectively imaging the emitted radiation from the stopped RNB if it were very penetrating (e.g. a high-energy β -decay electron as in the case of ^8Li). It is planned to investigate this further.

6.5 Conclusions

The EBT film images confirm as expected, and now better quantify that there is a large background of scattered primary-beam ions (^7Li for the data shown) in various charge states at locations immediately downstream from the RNB production target. These travel slightly off axis relative to the optical and ion-optical axis at those

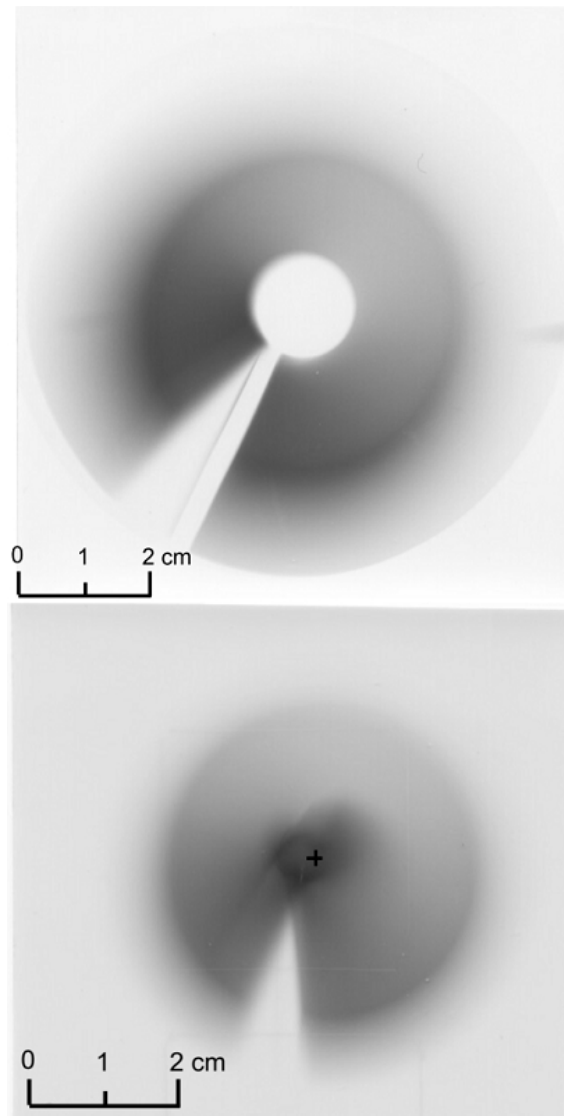


Figure 6.9: ^8B , ^7Be (analog) ions and background ions off focus (top) at the entrance to chamber C and on focus (bottom) at the target location in chamber C (Figure 6.1). Part of a low-energy ^8B and ^7Be RNB experiment to determine optimal collimation for that specific experiment. (The original colored images have been converted to grayscale for publication.)

locations. There is relatively less background from γ -rays and neutrons indicated, which is somewhat surprising but probably indicates the effectiveness of the extended tungsten-alloy beam block in place immediately after the faraday cup and beam stop [Mu02].

In other applications using high-sensitivity EBT film for ion-beam imaging where neutrons and photons (x-rays and γ -rays) could be a problem, it may be possible to use suitable absorbers among several sets of film to identify background not due to beam ions. This is being further investigated. In any event, the present film images obtained with the ^8Li RNB used here indicate the need for additional apertures, beam blocks and their alignment for specific RNB experiments. This is especially true for any cross-over fast-timing detector to be employed as planned for some future experiments using the new ToF chamber and beam line.

While the images discussed above are for a particular RNB apparatus, they should be representative of those possible using modified EBT film on other low-energy ion-optical systems used for RNB production or other applications.

Based on the above results, it is planned to routinely use the custom EBT film in most future *TwinSol* RNB experiments for efficiently designing and locating optimal apertures and beam blocks for specific RNB experiments. Likewise, as noted it is planned to further study the use of absorbers with the EBT film to provide differentiation between neutrons, γ -rays and low-energy ions produced near RNB production targets or elsewhere, and to exam the effects of radioactive decay products emitted from RNBs stopped in or near the imaging film.

A poster presented by the author on the custom EBT film-imaging project is displayed in Appendix F.

CHAPTER VII

Conclusions

7.1 Achievement of Project Goals

The absorber method for energy compensation in a solenoid was tested. The misalignment of the *TwinSol* optical and magnetic axis which limited the effectiveness of the technique was carefully investigated later using a custom-made version of Gafchromic[®] EBT medical X-ray film. The custom-made Gafchromic[®] high-sensitivity EBT film was found as a good way to image secondary RNBs in a solenoid-based apparatus especially at off-focus locations for the purpose of designing good beam blocks and collimators to improve beam purity. As part of these tests a first set of measurements of the energy and angular yield profile of a ⁷Be beam at an off focus position was carried out.

To facilitate testing various ToF detectors at UM, an oil-free vacuum test chamber was constructed along with development of a custom CAMAC-based USB2 Mac data acquisition and analysis system.

A new 32" vacuum chamber was designed and built as part of this thesis project for the purpose of facilitating the time-of-flight method to improve the energy resolution of *TwinSol*. Although delayed several months due to faulty vacuum welds, the complete installation of the ToF chamber was concluded in April, 2008 and several

tests and experiments using this chamber were carried out directly afterward.

Both intrinsic r.f. beam pulsing and cross-over timing detector ToF methods were investigated and improved energy resolution ($\times 2$) was obtained. The new MCP-ToF system and intrinsic beam pulsing were utilized in an experiment to measure the Coulomb excitation of ${}^8\text{Li}$ ($J^\pi=1+$, $E_x=0.98$ MeV). Using both thin and thick gold targets, a consistent set of data were obtained. The results are consistent with earlier *TwinSol* measurements without using ToF and indicate an unusually large $B(E2)\uparrow$ for ${}^8\text{Li}$ Coulomb excitation.

While the methods discussed above are for a particular RNB apparatus (*TwinSol*), they should be representative of improvements possible for other solenoid-based RNB production systems. Likewise the custom modified Gafchromic[®] EBT film should be suitable for use in other ion-optical systems used for RNB production and other applications.

7.2 Future of TwinSol ToF

TwinSol's ToF capabilities can be further developed. A steel magnetic-field shield box has been made and is planned to be put at the cross-over chamber position to reduce the effect of the *TwinSol* fringe fields on MCP signals. A detailed print of this steel shield box can be found in Appendix E. A first set of calculations has been done calculating the fringe magnetic field when using this magnetic shield. Figure 7.1 shows the magnetic field lines together with the flux density. After the shielding, the magnetic field at the MCP location should be less than a few gauss for an external fringe field of about 50 gauss (Chapter V).

A second MCP has been purchased and is available for use in the ToF chamber so one can achieve the MCP-to-MCP time-of-flight measurements. As discussed in

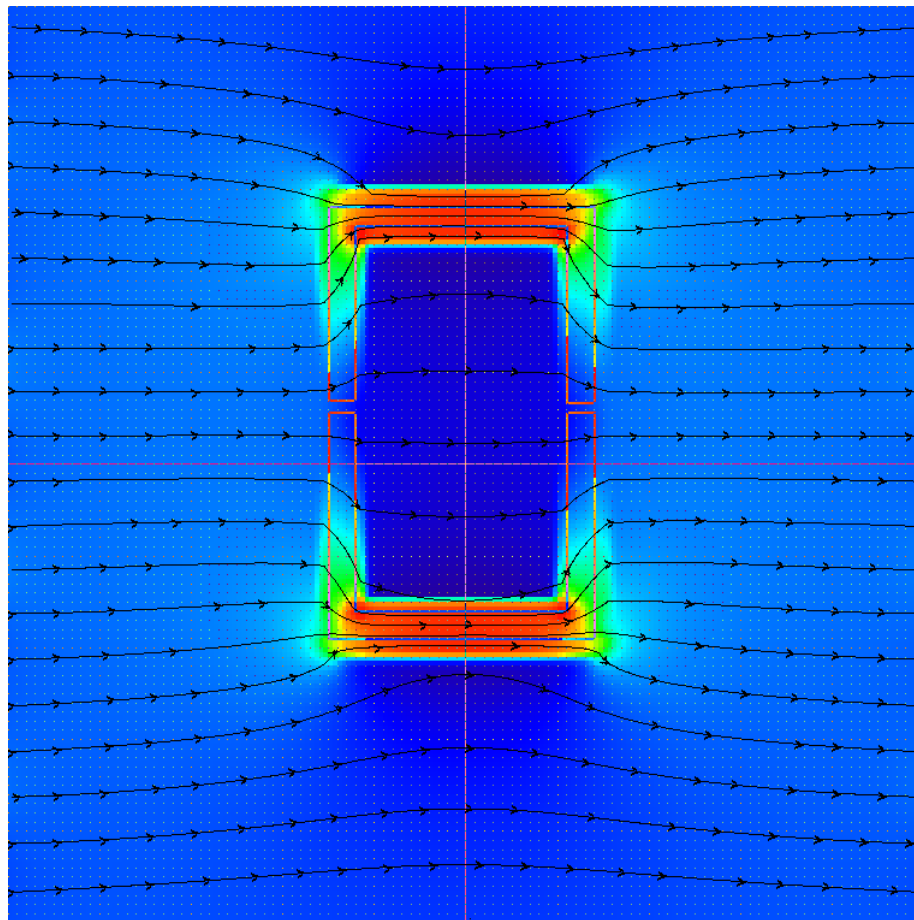


Figure 7.1: Fringe field calculation at the cross-over location when applying the magnetic shield.

Chapter V, the timing resolution so far has been dominated by the timing resolution of the Si detector for the case of MCP-to-Si timing since the MCP is much superior in timing resolution. With the insertion of another MCP in front of the reaction target located in the ToF chamber (Figure 7.2), an MCP-to-MCP ToF measurement will greatly improve the time resolution hence the energy resolution for the whole *TwinSol* system (e.g. perhaps $\delta E < 250$ keV). However, noticeable inelastic excitation of the beam in the foil (or grids) used in the MCP setup was observed (Figure 4.14). A thinner foil and more transparent grids are needed to reduce this for future experiments.

With the help of the custom-made Gafchromic[®] EBT film, it was possible to care-

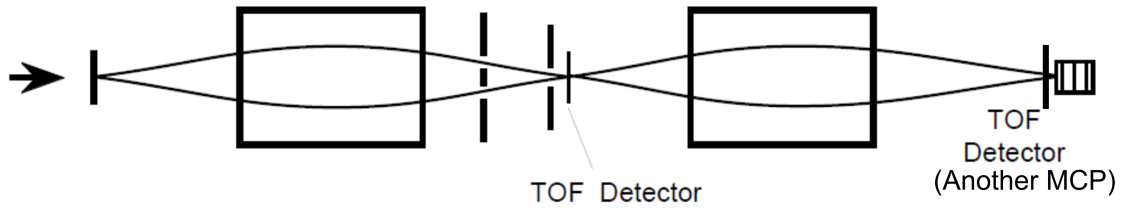


Figure 7.2: Schematic depiction of using two MCP detectors for ToF measurements.

fully investigate the optical and magnetic misalignment in *TwinSol* quantitatively and design suitable beam blocks together with a new energy absorber for use in the energy-compensation method. With the detailed knowledge of misalignment, one can expect much better energy resolution improvement when applying the new absorber, and in contrast to the MCP ToF system, this passive, non-electronic method can utilize the full RNB intensity ($>10^5/\text{s}$).

APPENDICES

APPENDIX A

Twinsol+ Program

A.1 Introduction

TwinSol+ program is a Visual C++ program written for calculating ray traces of charged particles in the *TwinSol* radioactive nuclear beam (RNB) apparatus. Part of the code is adapted from the previous Fortran program (“*TwinSol*”) written by Mu Lee as part of his PhD thesis work [Mu02].

There are several major improvements of the current *TwinSol+* program over the previous Fortran version “*TwinSol*”. First of all, the whole ray-tracing part is totally rewritten in standard C++ (ANSI C++) suitable to run on various platforms. Secondly, several new features are incorporated in the ray-tracing part, *e.g.* calculation of time of flight (ToF) information, calculation of magnetic field strength at a particular location and ray tracing for insertion of absorbers. Thirdly, a completely new graphical user interface (GUI) with easy configuration for the program is written on the Windows operating system. The previous *TwinSol* code doesn’t have the direct ability to draw ray traces on the screen and has to consort help of other plotting programs. New *TwinSol+* program has the plotting function built in and can draw ray traces directly which makes calculations more efficient.

A.2 *TwinSol+* Usage

As previously mentioned, the *TwinSol+* program implements a newly-developed GUI on the Windows XP or Vista operating system as shown in Figure A.1. (This GUI is developed under Visual C++ environment using Microsoft foundation class [MFC].)

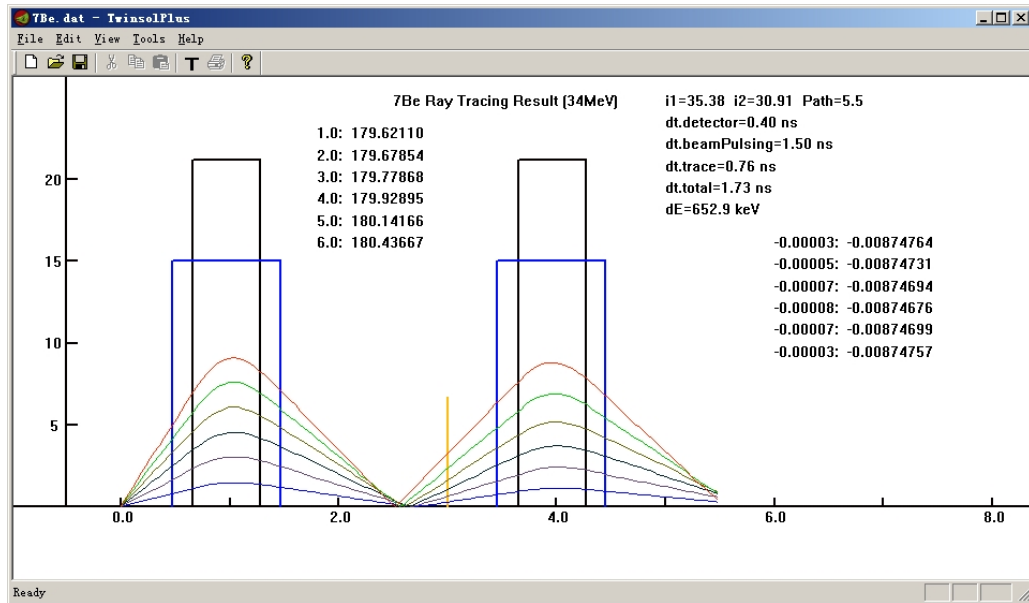


Figure A.1: Windows *TwinSol+* GUI.

As one can see, this program is similar to any other standard GUI Windows-based program with menus and toolbars for fast access of different tools and preferences in the program.



Figure A.2: *TwinSol+* menus and toolbars

Using menus and toolbars, one can create new, save current, or load previous ray trace calculations. Every new calculation shows a default ray trace result (34 MeV ${}^7\text{Be}$ from 1° to 6°). And once the previous calculation is loaded, the program will

automatically show the new ray-trace result in the plotting window.

One can configure the ray trace calculation by choosing Tools— >Preference.

Figure A.3 shows the preference property page:

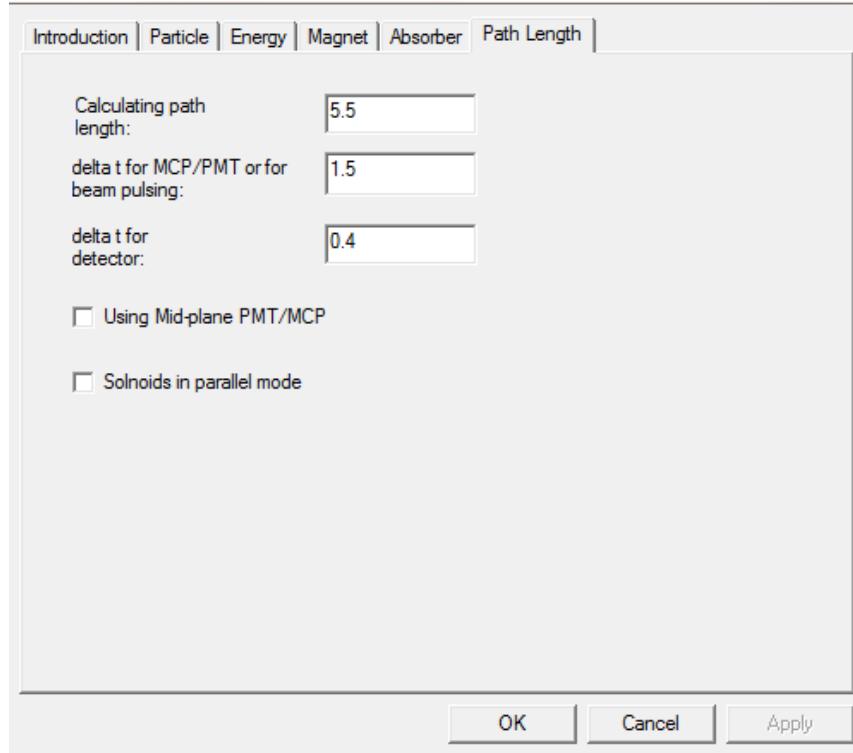


Figure A.3: *TwinSol+* preference property page

The property page has several clickable tabs on the top including “Introduction”, “Particle”, “Energy”, “Magnet”, “Absorber” and “Path length” settings. “Introduction” tab gives a brief review of all functions of the *TwinSol+* program. The “Particle” tab can set the particle’s atomic number, mass and charge. Figure A.4 shows the “Particle” tab.

The “Energy” tab (Figure A.5) is used to set the particle’s lab energy corresponding to different incoming angles. Due to the kinematic energy shift of the secondary RNB emitted from production target [Figure 1.2], the particles’ energy at different angles are slightly different. *TwinSol+* allows users to put in different energy at

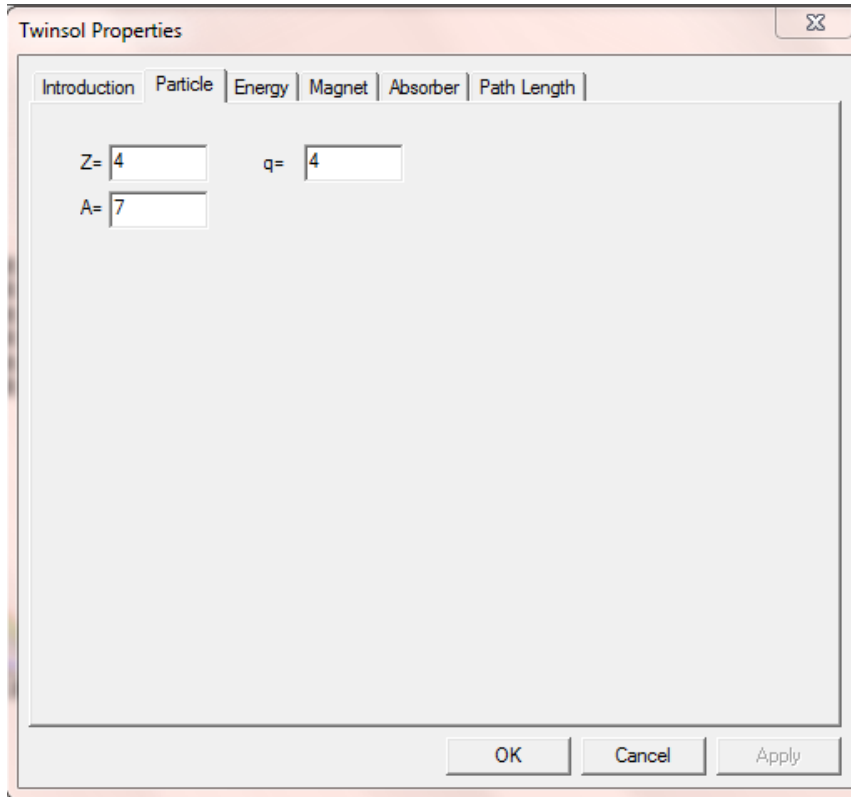


Figure A.4: “Particle” tab of *Twinsol+*.

different production angles.

The “Magnet” tab (Figure A.6) is the current setting for both solenoids in the UM-UND *Twinsol* RNB facility. The solenoid magnetic field along the axis can be calculated by using a finite, single-sheet current approximation [Mu02].

$$(A.1) \quad B(z) = 0.5 \times \mu_0 \times n \times I \times [\cos\theta_1 - \cos(180 - \theta_2)]$$

where n is the number of turns per unit length in solenoid. I is the solenoid current in amperes, and θ_1 and θ_2 are half of the vertex angles subtended by the two openings of the solenoid to the current sheet (Figure A.7). The radius of the current sheet R and L represents average of the solenoid coil dimension (here $R=17.8$ cm and $L=60$ cm).

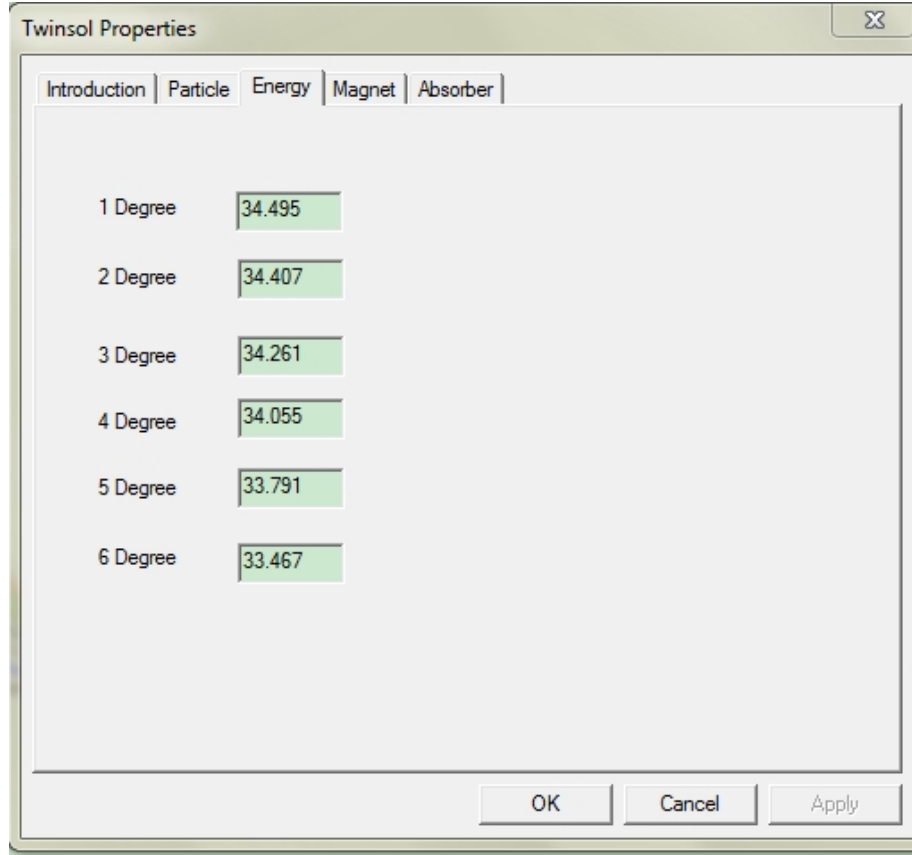


Figure A.5: “Energy” tab of *TwinSol+*.

The “Absorber” tab (Figure A.8) defines an inserted absorber’s atomic number, its mass, thickness and its location in *TwinSol* beam line. (Currently part of this tab’s code is still under construction and not fully functional.)

The “Path length” tab (Figure A.9) determines the path length for the calculation and, also, several important parameters for ToF calculation including uncertainty in the r.f. beam bunching, the timing resolution of the cross-over MCP or other detector and the timing resolution of the silicon detector in the back target chamber.

A.3 Sampled Calculations

Here we present several examples of *TwinSol+* calculations. The default calculation is a 34 MeV ^7Be beam in a cross-over mode (Figure A.10). It is assumed to use

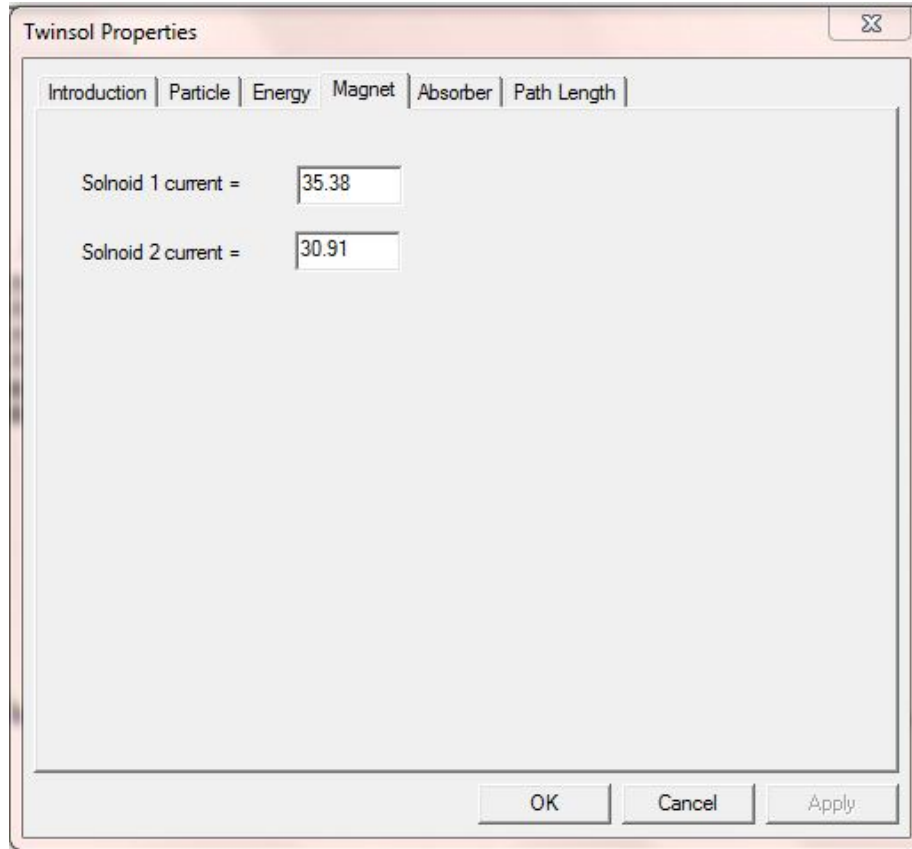


Figure A.6: “Magnet” tab of *TwinSol+*.

the original small target chamber at a 5.5 m flight path. The program shows the best energy resolution that can be achieved with a MCP cross-over ToF measurement is 332 keV FWHM.

Figure A.11 shows another example of 28 MeV ^8Li beam using a longer 8 m flight path. It is calculated using a MCP cross-over timing from the cross-over point to the center of the new ToF chamber. The calculation shows that with the longer flight path, the energy resolution can be improved to less than 200 keV FWHM.

Twinsol+ also can be used for calculation of ray traces using the parallel mode. Figure A.12 shows an example of 34 MeV ^7Be in parallel mode and with the longer flight path. Using the intrinsic beam r.f. bunching ToF (1.5 ns spread), the energy resolution would be about 415 keV FWHM. A listing of the *TwinSol+* code is given

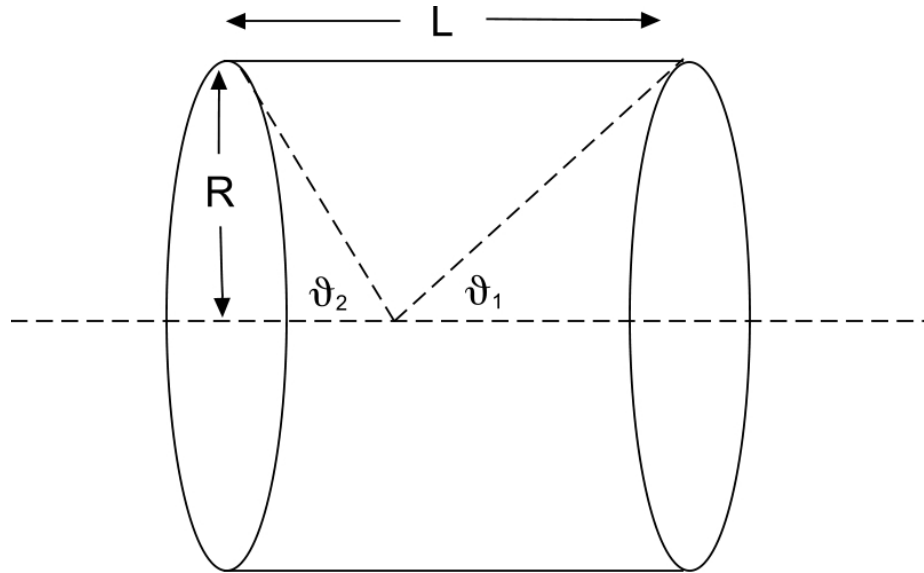
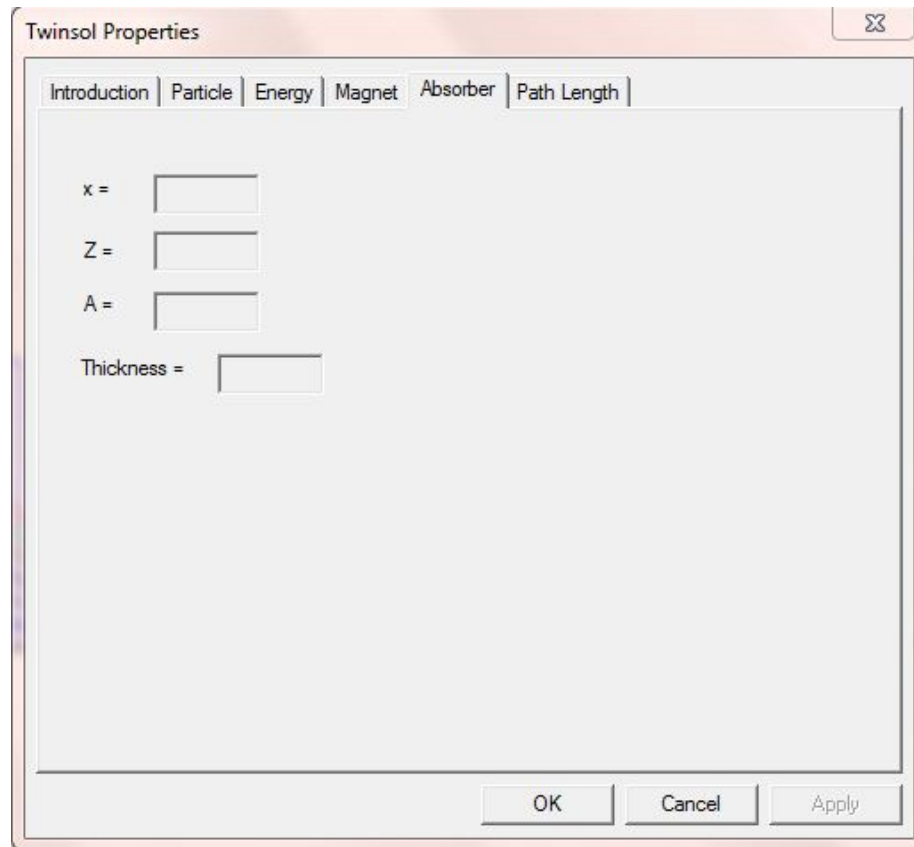


Figure A.7: Geometry for the on-axis magnetic field calculation from a solenoid current sheet approximation.

at A.4.

Figure A.8: “Absorber” tab of *TwinSol+*

A.4 Code for *Twinsol+* Program

```

#include "stdAfx.h"
#include "Twinsol.h"
#include <Cmath>
#include <stdio.h>
#include <iostream>
#include <fstream>

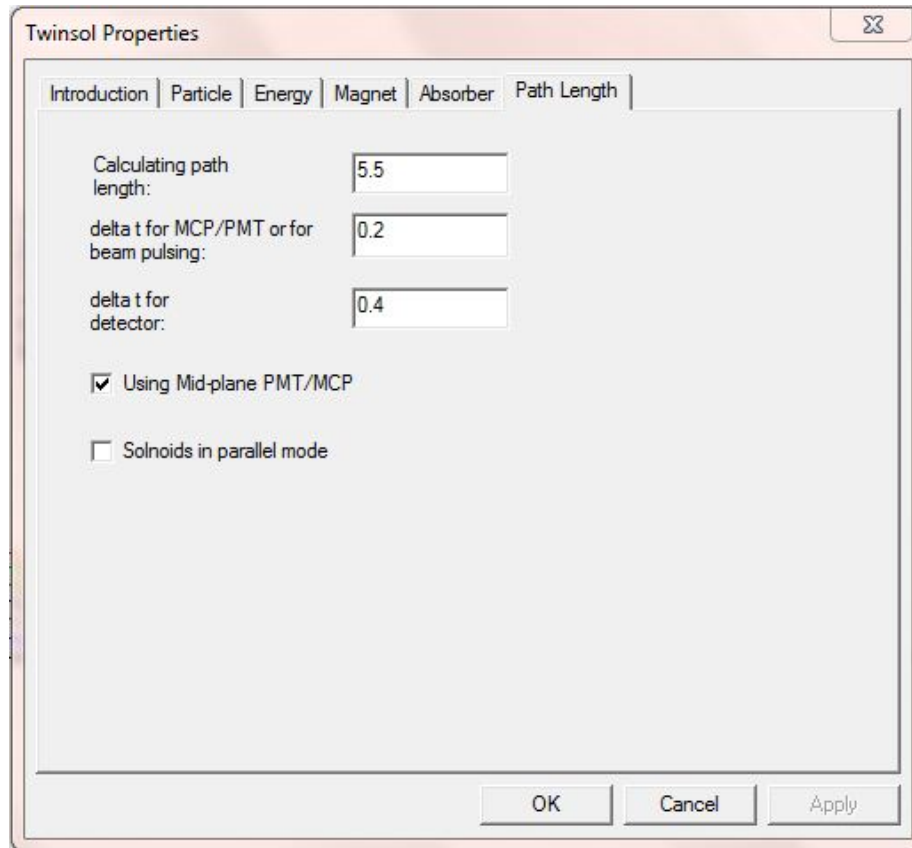
using namespace std;

#define PI 3.1415926
#define PI2 PI/2

void twinsol::b_cal(double &ma,double &ers,double &zz,double &cc,double &ll,double &rr,
double &bzsl,double &brsl,double &par_solenoid)
{
double maers,zc,zcs,zl,zls,scs,sc,sls,sl,sc3,sc5,sc7;
double sl3,sl5,sl7,hr,hrs,hr3,bzz,b1,b3,br;

maers=ma*ers;
zc=zz-cc;
zcs=zc*zc;
zl=zz-cc-ll;
zls=zl*zl;
scs=ers+zcs;
sc=sqrt(scs);
sls=ers+zls;
sl=sqrt(sls);
sc3=scs*sc;
    sc5=sc3*scs;
sc7=sc5*scs;
sl3=sls*sl;
sl5=sl3*sls;

```

Figure A.9: “Path length” tab of *TwinSol+*

```

s17=s15*s1s;
hr=rr/2;
hrs=hr*hr;
hr3=hrs*hr;
    bzz=ma*(zc/sc-z1/s1)-hrs*3*maers*(-zc/sc5+z1/s15);
b1=-hr*maers*(1/sc3-1/s13);
b3=hr3/2*3*maers*((4*zcs-ers)/sc7-(4*zls-ers)/s17);
brr=b1+b3;
bzsl+=par_solenoid*bzz;
brsl+=par_solenoid*brr;
}

double twinsol::twinsol_cal(CDC* pDC,int amu,int zo,int qo,double e0[6],double theta[6],double i1,double i2,
double CalPath, double mcptime,double dettime,bool usingmcp,bool parallel)
{
ofstream output1("output1.txt");
ofstream output2("output2.txt");
ofstream output3("output3.txt");
ofstream output4("output4.txt");
ofstream output5("output5.txt");
ofstream output6("output6.txt");
double time[6];
double tot_time=0;
double tot_energy=0;
for (int i=0;i<6;i++){tot_energy+=e0[i];}
tot_energy=tot_energy/6;

v0=hdz=ex=ey=ez=e_field=0.0;
char* filename="6li.dat";
rn=3;
nr=(int)rn;
    for (int i=0;i<6;i++)
    {
index[i]=0;

```

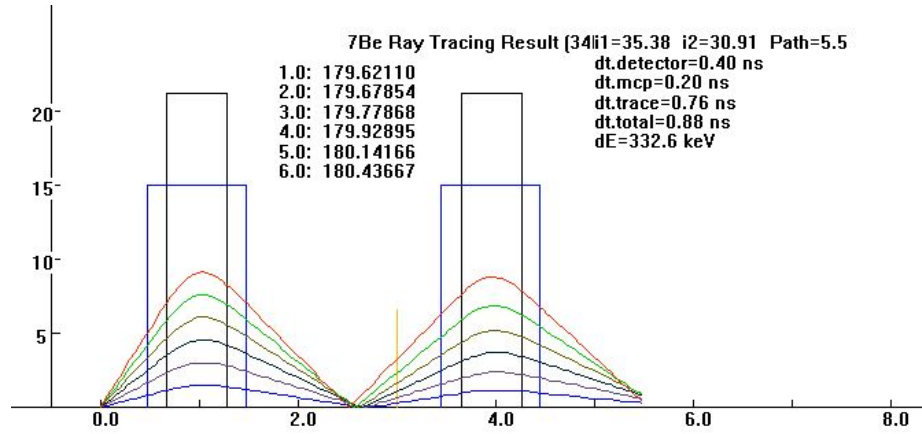


Figure A.10: Ray-trace calculation of 34 MeV ${}^7\text{Be}$ beam in *TwinSol* with a short flight path (5.5 m).

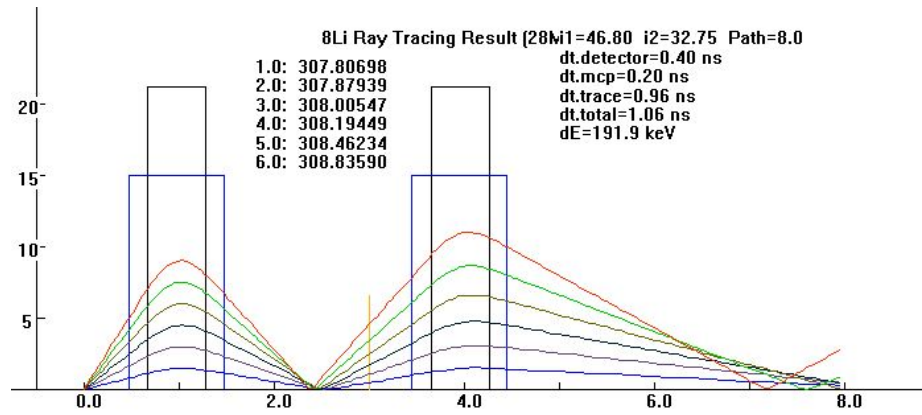


Figure A.11: Ray-trace calculation of a 28 MeV ${}^8\text{Li}$ beam in *TwinSol* with a long flight path (8 m).

```

}

ztgt=0.977;
dz=0.002;hdz=0.001;

znd=CalPath; //7.4
double stepnom=znd/dz;
int stepnum=(int)stepnom;
solname1=2;

separ=2.984; s1=0.62; er=0.2123; length=1.0; bore=0.15;
ma1=3.636*i1/100;
ma2=3.636*i2/100;

if (parallel==true)
par_solenoid=1.0;
else
par_solenoid=-1.0;

z1=ztgt-0.5*s1; z2=ztgt+separ-0.5*s1;

ll=s1;cc=z1;ccc=z2;lls=ll*ll;ers=er*er;
bm1=ma1*ll/sqrt(ers+lls/4); bm2=ma2*ll/sqrt(ers+lls/4);

drawmagnet(pDC,z1,er,s1,ztgt,length,bore,z2,separ);

CPen PenTwinSol[6];

```

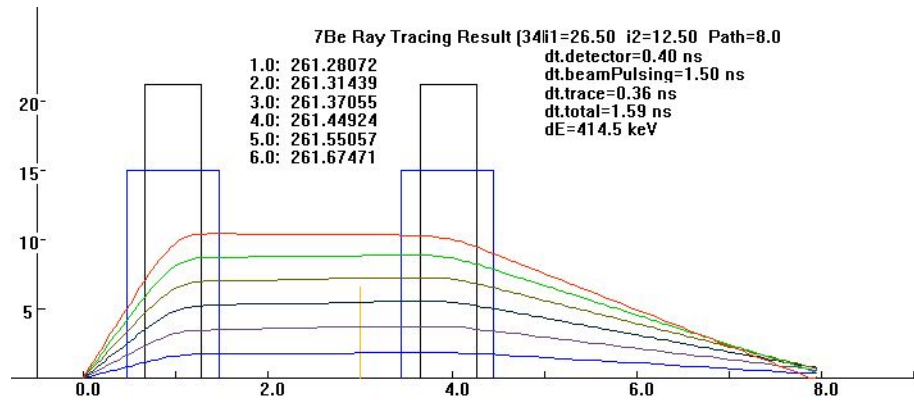


Figure A.12: Ray-trace calculation of 34 MeV ${}^7\text{Be}$ in parallel mode (8 m flight path).

```

PenTwinsol[0].CreatePen(PS_SOLID, 1, RGB(0,0,255));
PenTwinsol[1].CreatePen(PS_SOLID, 1, RGB(100,72,121));
PenTwinsol[2].CreatePen(PS_SOLID, 1, RGB(0,34,47));
PenTwinsol[3].CreatePen(PS_SOLID, 1, RGB(100,100,0));
PenTwinsol[4].CreatePen(PS_SOLID, 1, RGB(0,200,0));
PenTwinsol[5].CreatePen(PS_SOLID, 1, RGB(255,45,0));

pDC->MoveTo(0,0);

CString element;

switch(zo){
case 1:
element="H";
break;
case 2:
element="He";
break;
case 3:
element="Li";
break;
case 4:
element="Be";
break;
case 5:
element="B";
break;
case 13:
element="Si";
}
CString title;
title.Format("%d%s %s%.0f%s",amu,element,"Ray Tracing Result (",tot_energy,"MeV)");
tot_energy=0;

pDC->TextOut(250,380,title);

CString setting;
setting.Format("%s%.02f %s%.02f %s%.01f", "i1=",i1,"i2=",i2,"Path=",CalPath);
pDC->TextOut(500,380,setting);

setting.Format("%s%.02f %s", "dt.detector=",detttime,"ns");
pDC->TextOut(500,360,setting);
if (usingmcp==true)
{
setting.Format("%s%.02f %s", "dt.mcp=",mcptime,"ns");
pDC->TextOut(500,340,setting);
}
else
{
setting.Format("%s%.02f %s", "dt.beamPulsing=",mcptime,"ns");
pDC->TextOut(500,340,setting);
}

for (int i=0;i<6;i++)
{
time[i] = 0;
}

```

```

pDC->SelectObject(&PenTwinsol[i]);
pDC->MoveTo(0,0);

e1=zo;n=qo;m=amu;ang3=theta[i];e=e0[i];
t=ang3/57.3;
v0=1.389e+07*sqrt(e/m);
x0=y0=z0=t0=0;
x=x0;y=y0;z=z0;
vx=v0*sin(t); vy=0.0; vz=v0*cos(t);
gx=gy=gz=0.0;
hgx=hgy=hgz=0.0;
f7=f8=f9=0.0;
hf7=hf8=hf9=0.0;

for (int step=1;step<stepnum;step++)
{
v1=vx+hf7; v2=vy+hf8; v3=vz+hf9;
dt=dz/v3; dts=dt*dt;
xx=x+hgx; yy=y+hgy; zz=z+hgz;
xxs=xx*xx; yys=yy*yy; rrs=xxs+yys; rr=sqrt(rrs);
inrrs=1/(rrs+0.00000001); inrr=1/(rr+0.00000001);

bzsl=0; brsl=0; double temp=1;
b_cal(ma1,ers,zz,cc,ll,rr,bzsl,brsl,temp);
b_cal(ma2,ers,zz,ccc,ll,rr,bzsl,brsl,par_solenoid);

br=brsl; bz=bzsl;
bx=br*inrr*xx; by=br*inrr*yy;

cqm=9.648e+7*(n/m);

ax=cqm*(v2*bz-v3*by+ex);
ay=cqm*(v3*bx-v1*bz+ey);
az=cqm*(v1*by-v2*bx+ez);

gx=v1*dt+0.5*ax*dts;
gy=v2*dt+0.5*ay*dts;
gz=v3*dt+0.5*az*dts;
x=x+gx; y=y+gy;
//z=dz*(step);
z=z+gz;

double distance=sqrt(gx*gx+gy*gy+dz*dz);
double velocity=sqrt(vx*vx+vy*vy+vz*vz)*pow(10.,-9);
if (usingmcp==true) {
if (z==2.5) time[i]=0;
}

time[i]+=distance/velocity;

t0+=sqrt(gx*gx+gy*gy+dz*dz)/(1.0e-9*v0);

f7=ax*dt; f8=ay*dt; f9=az*dt; hf7=0.5*f7; hf8=0.5*f8; hf9=0.5*f9;
vx=vx+f7; vy=vy+f8; vz=vz+f9;

if (step%20==0){
xp=z*100;
yp=sqrt(x*x+y*y)*1500;
pDC->LineTo((int)xp,(int)yp);

switch (i){
case 0:
output1<<z<<" ";
output1<<sqrt(x*x+y*y)<<" ";
output1<<x<<" ";
output1<<y<<"\n";
break;
case 1:
output2<<z<<" ";
output2<<sqrt(x*x+y*y)<<" ";
output2<<x<<" ";
output2<<y<<"\n";
break;
case 2:
output3<<z<<" ";
output3<<sqrt(x*x+y*y)<<" ";
output3<<x<<" ";
output3<<y<<"\n";
}
}
}

```

```

break;
case 3:
output4<<z<<" ";
output4<<sqrt(x*x+y*y)<<" ";
output4<<x<<" ";
output4<<y<<"\n";
break;
case 4:
output5<<z<<" ";
output5<<sqrt(x*x+y*y)<<" ";
output5<<x<<" ";
output5<<y<<"\n";
break;
case 5:
output6<<z<<" ";
output6<<sqrt(x*x+y*y)<<" ";
output6<<x<<" ";
output6<<y<<"\n";
break;
}
}

if ((z-8.5)<0.01){
CString s;
s.Format("%.5f%s %.8f",br," ",bz);
}

double absorbthickness=10;
double absorber=2;
double m2=4;
double atrho=0.01;
double ion=e1;
double m1=amu;

double mm1=0,rho=0,vfermi=0,lfctr=0,pcoef [8];

getcoeff(ion,mm1,m1,absorber,m2,rho,atrho,vfermi,lfctr,pcoef);

CString s;
s.Format("%.5f",vx);

}
CString s_time;
s_time.Format("%.1f%s %.5f",ang3," ",time[i]);
pDC->TextOut(180,350-i*20,s_time);
}
double time_difference=time[5]-time[1];
setting.Format("%.2f %s",dt.trace=",time_difference,"ns");
pDC->TextOut(500,320,setting);
time_difference=sqrt(time_difference*time_difference+mcptime*mcptime+detttime*detttime);
setting.Format("%.2f %s",dt.total=",time_difference,"ns");
pDC->TextOut(500,300,setting);

CString s_time;

for (int i=0;i<6;i++){tot_time+=time[i];tot_energy+=e0[i];}
tot_time=tot_time/6;tot_energy=tot_energy/6;

tot_time=time_difference/tot_time;
tot_energy=2*tot_energy*tot_time;

s_time.Format("%.1f %s","dE=",tot_energy*1000,"keV");
pDC->TextOut(500,280,s_time);

return e;
}

void twinsol::drawmagnet(CDC *pDC,double z1,double er,double sl,double ztgt,double length,double bore,double z2,double separ)
{
static int x_factor=100,
y_factor=1500;
UINT m_z1=(int)(z1*x_factor);
UINT m_er=(int)(er*y_factor);
UINT m_sl=(int)(sl*x_factor);
UINT m_ztgt=(int)(ztgt*x_factor);
UINT m_length=(int)(length*x_factor);
UINT m_bore=(int)(bore*y_factor);
UINT m_z2=(int)(z2*x_factor);
UINT m_separ=(int)(separ*x_factor);

```



```

CPen PenBlue, PenBlack, PenAbsorber;
PenBlue.CreatePen(PS_SOLID, 2, RGB(0, 12, 255));
PenBlack.CreatePen(PS_SOLID, 2, BLACK_PEN);
PenAbsorber.CreatePen(PS_SOLID, 2, RGB(255, 185, 15));

pDC->SetViewportOrg(100, 400);
pDC->SetMapMode(MM_LOENGLISH);

pDC->MoveTo(-400, 0);
pDC->LineTo(1500, 0);

CString s;
pDC->MoveTo(-50, 0);
pDC->LineTo(-50, 500);

pDC->MoveTo(-50, 150);
pDC->LineTo(-40, 150);
s.Format("%0i", 10);
pDC->TextOut(-70, 157, s);

pDC->MoveTo(-50, 75);
pDC->LineTo(-40, 75);
s.Format("%0i", 5);
pDC->TextOut(-65, 82, s);

pDC->MoveTo(-50, 225);
pDC->LineTo(-40, 225);
s.Format("%0i", 15);
pDC->TextOut(-70, 232, s);

pDC->MoveTo(-50, 300);
pDC->LineTo(-40, 300);
s.Format("%0i", 20);
pDC->TextOut(-70, 307, s);

s.Format("%.1f", 0.0);
pDC->TextOut(0-8, -2, s);
pDC->MoveTo(0, 0);
pDC->LineTo(0, 8);
s.Format("%.1f", 1.0);

pDC->MoveTo(100, 0);
pDC->LineTo(100, 8);
s.Format("%.1f", 2.0);
pDC->TextOut(200-8, -2, s);
pDC->MoveTo(200, 0);
pDC->LineTo(200, 8);
s.Format("%.1f", 3.0);

pDC->MoveTo(300, 0);
pDC->LineTo(300, 8);
s.Format("%.1f", 4.0);
pDC->TextOut(400-8, -2, s);
pDC->MoveTo(400, 0);
pDC->LineTo(400, 8);
s.Format("%.1f", 5.0);

pDC->MoveTo(500, 0);
pDC->LineTo(500, 8);
s.Format("%.1f", 6.0);
pDC->TextOut(600-8, -2, s);
pDC->MoveTo(600, 0);
pDC->LineTo(600, 8);
s.Format("%.1f", 7.0);

pDC->MoveTo(700, 0);
pDC->LineTo(700, 8);
s.Format("%.1f", 8.0);
pDC->TextOut(800-8, -2, s);
pDC->MoveTo(800, 0);
pDC->LineTo(800, 8);
s.Format("%.1f", 8.0);

pDC->MoveTo(900, 0);
pDC->LineTo(900, 9.0);

pDC->MoveTo(m_z1, 0);
pDC->LineTo(m_z1, m_er);
pDC->LineTo(m_z1+m_s1, m_er);

```

```

pDC->LineTo(m_z1+m_sl,0);

pDC->SelectObject(&PenBlue);

pDC->MoveTo(m_ztgt-m_length/2,0);
pDC->LineTo(m_ztgt-m_length/2,m_bore);
pDC->LineTo(m_ztgt+m_length/2,m_bore);
pDC->LineTo(m_ztgt+m_length/2,0);

pDC->SelectObject(&PenBlack);

pDC->MoveTo(m_z2,0);
pDC->LineTo(m_z2,m_er);
pDC->LineTo(m_z2+m_sl,m_er);
pDC->LineTo(m_z2+m_sl,0);

pDC->SelectObject(&PenBlue);

pDC->MoveTo(m_ztgt+m_separ-m_length/2,0);
pDC->LineTo(m_ztgt+m_separ-m_length/2,m_bore);
pDC->LineTo(m_ztgt+m_separ+m_length/2,m_bore);
pDC->LineTo(m_ztgt+m_separ+m_length/2,0);

int absorb_pos=300;

pDC->SelectObject(&PenAbsorber);
drawAbsorber(pDC,absorb_pos);

}

double twinsol::pstop(double &ion,double m1,int &absorber,double &m2,double &velsqr,double pcoef[8],double &se)
{
double pe,sl,sh,velpwr;
pe=max(25,velsqr);
sl=(pcoef[1]*pow(pe,pcoef[6]))+(pcoef[3]*pow(pe,pcoef[4]));
sh=(pcoef[5]/pow(pe,pcoef[6]))*log((pcoef[7]/pe)+pcoef[8]*pe);
se=sl*sh/(sl+sh);
if (velsqr < 25){
velpwr=0.45;
if (absorber <= 6) velpwr=0.25;
se = pow(se*(velsqr/25),velpwr);
}
return se;
}

void twinsol::hstop(double &ion,double m1,int &absorber,double m2,double &velsqr,double pcoef[8],double &se)
{
double a,b,he,heh,sp;
he=max(1.,velsqr);
b=log(he);
a=0.2865+0.1266*b-0.001429*b*b+0.02402*b*b*b-0.01135*pow(b,4)+0.001475*pow(b,5);
heh=1-exp(-min(30,a));
a=(1+(0.007+0.00005*absorber)*exp(-pow((7.6-max(0,log(he))),2)));
heh=a*a*heh;
pstop(ion,m1,absorber,m2,he,pcoef,sp);
se=sp*heh*ion*ion;
if (velsqr<1) se=se*sqrt(velsqr/1);
}

void twinsol::histop(double ion,double m1,int absorber,double m2,
double velsqr,double e,double vfermi,
double lcfctr,double pcoef[8],double se)
{
double vrmin,yrmin,vvvv,vr,yr,eee,power,vmin,sp;
double aaaa,bbbb,qqqq,qqq1,1111,1110,1111,zeta;
yrmin=0.13;
vrmin=1.0;
vvvv=sqrt(velsqr/25)/vfermi;
if (vvvv >= 1) vr=vvvv*vfermi*(1+1/(5*vvvv*vvvv));

yr=max(yrmin,vr/pow(ion,0.6667));
yr=max(yr,vrmin/pow(ion,0.6667));
aaaa=-0.803*pow(yr,0.3)+1.3167*pow(yr,0.6)+0.38157*yr+0.008983*yr*yr;
qqqq=min(1,max(0,1-exp(-min(aaaa,50))));
bbbb=(min(0.43,max(0.32,0.12+0.025*ion)))/pow(ion,0.3333);
1110=(0.8-qqqq*(min(1.2,0.6+ion/30)))/pow(ion,0.3333);
1111=bbbb*(1-qqqq)/(0.025*min(16,1*ion));
if (qqqq < 0.2) 1111=0;
if (qqqq < (max(0,9-0.025*ion))){
qqq1=0.2;
}
}

```

```

1111=bbbb*(qqqq-0.2)/abs(max(0,0.9-0.025*ion)-0.200001);
}
if (qqqq < (max(0,1-0.025*min(16,1*ion)))) 1111=bbbb;
1111=max(1111,1110*1cfctr);
zeta=qqqq+(1/(2*pow(vfermi,2)))*(1-qqqq)*log(1+pow((4*1111*vfermi/1.919),2));
aaaa=-(7.6-max(0,log(velsqr)));
aaaa=aaaa*aaaa;
zeta=zeta*(1+(1/ion/ion)*(0.18+0.0015*absorber)*exp(aaaa));
if (yr<=max(yrmin,vrmin/pow(ion,0.6667))) {
vrmin=max(vrmin,yrmin*pow(ion,9.6667));
vmin=0.5*(vrmin+sqrt(max(0,vrmin*vrmin-0.8*vfermi*vfermi)));
eee=25*vmin*vmin;
pstop(ion,m1,absorber,m2,eee,pcoef,sp);
power=0.5;
if ((absorber==6) || ((absorber==14) || (absorber==32) && (ion<=19))) power=0.375;
se=sp*(zeta*ion)*(zeta*ion)*pow(velsqr/eee,power);
}
else{
pstop(ion,m1,absorber,m2,velsqr,pcoef,sp);
se=sp*(zeta*ion)*(zeta*ion);
}
}

void twinsol::absorbloss(double &vx,double &vy,double &vz,double &absorbthickness,
int &qo, double &m1,double &m2, double &e,double &atrho,
double &ion, double &absorber, double pcoef[8])
{
double se;
double sn;
double temp=(sqrt(vx*vx+vy*vy+vz*vz)/vz)*absorbthickness;
double j_max=temp/.001; int n=qo;
double vfermi=0,1fctr=0;

double e0=e;

j_max=100;

for (int j=1;j<=j_max;j++)
{
double velsqr=e*1000/m1;

double epsil=32.53*m2*e*1000/(n*absorber*(m1+m2)*(pow(static_cast<double>(n),0.23)+pow(absorber,0.23)));

if (epsil >= 30)
sn=log(epsil)/(2*epsil);
else
{
temp=0.01321*pow(epsil,0.21226)+0.19593*pow(epsil,0.5);
sn=0.5*log(1+1.1383*epsil)/(epsil+temp);
}

sn=sn*n*absorber*m1*8.462/((m1+m2)*(pow(static_cast<double>(n),0.23)+pow(absorber,0.23)));
sn=sn*atrho*0.001;

se=se*atrho*0.001;
e=e-se-sn;
if (e<0.000002) e=0.000002;
}
temp=sqrt(e/e0);
vx=temp*vx;vy=temp*vy;vz=temp*vz;v0=temp*v0;
}

void twinsol::drawAbsorber(CDC *pDC, int absorb_pos)
{
CPen PenBlue;
PenBlue.CreatePen(PS_SOLID, 2, RGB(0, 12, 255));

pDC->MoveTo(absorb_pos,0);
pDC->LineTo(absorb_pos,100);
}

void twinsol::getcoeff(double &ion,double &mm1, double &m1,double &absorber,double &m2,double &rho,
double &atrho,double &vfermi, double &1fctr, double pcoef[8])
{
double aaaa,bbbb;
int iiii;
double cccc,dddd,eeee,ffff,gggg,hhhh;
for (iiii=1;iiii<=6;iiii++){

```

```

switch(iiii){
case 1: aaaa=1;bbbb=1;cccc=1.0078;dddd=1.008;eeee=0.071486;ffff=4.271;gggg=1.0309;hhhh=1;
case 2: aaaa=2;bbbb=4;cccc=4.0026;dddd=4.0026;eeee=0.12588;ffff=1.894;gggg=0.15976;hhhh=1;
case 3: aaaa=3;bbbb=7;cccc=7.016;dddd=6.939;eeee=0.52969;ffff=4.597;gggg=0.59782;hhhh=1.1;
case 4: aaaa=4;bbbb=9;cccc=9.012;dddd=9.0122;eeee=1.8024;ffff=12.046;gggg=1.0781;hhhh=1.06;
case 5: aaaa=5;bbbb=11;cccc=11.009;dddd=10.811;eeee=2.3502;ffff=13.093;gggg=1.0486;hhhh=1.01;
case 6: aaaa=6;bbbb=12;cccc=12;dddd=12.011;eeee=2.2662;ffff=11.364;gggg=1;hhhh=1.03;
}
if (iiii==ion) lfctr=hhhh;
if (iiii==absorber){
m2=dddd;
rho=eeee;
atrho=ffff;
vfermi=gggg;
pcoef[1]=bbbb;pcoef[2]=cccc;pcoef[3]=dddd;pcoef[4]=ffff;pcoef[5]=gggg;pcoef[6]=hhhh;
}
}
}

void twinsol::drawEnergy(CDC *pDC, double e0[6])
{
CPen PenBlue, PenBlue1;
PenBlue.CreatePen(PS_SOLID, 2, BLACK_PEN);
pDC->SelectObject(PenBlue);

pDC->MoveTo(0, -50);
pDC->LineTo(0, -250);
pDC->LineTo(300, -250);

PenBlue1.CreatePen(PS_SOLID, 1, BLACK_PEN);
pDC->SelectObject(PenBlue1);

pDC->MoveTo(50+(e0[0]-33)*100, -200+20);
}

```

A.5 Code for *Electron Trajectory* Program

As mentioned in Section 4.3.3, a Monte-Carlo simulation program for calculating secondary electron trajectory in *TwinSol* fringe field was developed. The code for this program is listed here.

```

#include <Cmath>
#include <iostream>
#include <fstream>
#include <iomanip>
#include <ctime>

#define PI 3.1415926
#define PI2 PI/2

using namespace std;

void b_cal(double &ma, double &ers, double &zz, double &cc, double &ll, double &rr,
double &bzsl, double &brsl, double &par_solenoid)
{
double maers, zc, zcs, zl, zls, scs, sc, sls, sl, sc3, sc5, sc7;
double sl3, sl5, sl7, hr, hrs, hr3, bzz, b1, b3, brr;

maers=ma*ers;
zc=zz-cc;
zcs=zc*zc;
zl=zz-cc-ll;
zls=zl*zl;
scs=ers+zcs;
sc=sqrt(scs);
sls=ers+zls;
sl=sqrt(sls);

```

```

sc3=scs*sc;
sc5=sc3*scs;
sc7=sc5*scs;
sl3=s1s*sl;
sl5=sl3*s1s;
sl7=sl5*s1s;
hr=rr/2;
hrs=hr*hr;
hr3=hrs*hr;
bzz=ma*(zc/sc-zl/s1)-hrs*3*maers*(-zc/sc5+z1/s15);
b1=-hr*maers*(1/sc3-1/s13);
b3=hr3/2*3*maers*((4*zc5-ers)/sc7-(4*z1s-ers)/s17);
brr=b1+b3;
bzsl=par_solenoid*bzz;
brsl=par_solenoid*brr;
}

int main()
{
ofstream output("output.txt");
ofstream output2("output2.txt");
ofstream output3("energy.txt");
double times[6];
double tot_time=0;
double tot_energy=0;
double e0[1000];
for (int i=0;i<6;i++){e0[i]=34;}
for (i=0;i<6;i++){tot_energy+=e0[i];}
tot_energy=tot_energy/6;
double v0,hdz,ex,ey,ez,e_field;
v0=hdz=ex=ey=ez=e_field=0.0;

ex=1e5;ey=0;ez=-1e5;

double rn=3;
int nr=(int)rn;
int index[6];
for (i=0;i<6;i++)
{
index[i]=0;
}

double ztgt=1.021;
double dz=0.001;hdz=0.001;

double CalPath=0.2;
double znd=CalPath;
double stepnom=znd/dz;
int stepnum=(int)stepnom;
int solname=2;

double i1=35.38;
double i2=30.91;

double separ=2.984; double s1=0.62; double er=0.2123; double length=1.0; double bore=0.15;
double ma1=3.636*i1/100;
double ma2=3.636*i2/100;

bool parallel=false;
double par_solenoid;
if (parallel==true)
par_solenoid=1.0;
else
par_solenoid=-1.0;

double z1=ztgt-0.5*s1; double z2=ztgt+separ-0.5*s1;

double ll=s1;double cc=z1;double ccc=z2;double lls=ll*s1;double ers=er*er;
double bm1=ma1*ll/sqrt(ers+lls/4); double bm2=ma2*ll/sqrt(ers+lls/4);

double zo=4;
double qo=4;
double amu=7;
double theta[1000];

double el=1;double n=1;double m=5.45e-4;
double tmax=0.010;
double pmax=sqrt(2*m*tmax);

```

```

static int imax=600;

srand(time(NULL));

for (i=0;i<imax;i++) {
int x=rand()%100;
double p=(double)x/100;
e0[i]=1/(1-p*4/5)/1000;
output3<<e0[i]*1000<<" ";

if(i%8==0) theta[i]=(p*30+60)/180*3.14;
else if (i%3==0) theta[i]=(p*30+30)/180*3.14;
else theta[i]=(p*30)/180*3.14;

output3<<theta[i]/3.14*180<<endl;
}

double data[700][50];
double data2[700][50];

for (i=0;i<imax;i++)
{
times[i] = 0;

double ang3=theta[i];double e=e0[i];
double t=ang3;
v0=1.389e+07*sqrt(e/m);
double x0,y0,z0,t0;
x0=y0=t0=0;
z0=2.5;
double x,y,z;
x=x0;y=y0;z=z0;
double vx,vy,vz;
vx=v0*sin(t); vy=0.0; vz=v0*cos(t);
double gx,gy,gz;
gx=gy=gz=0.0;
double hgx,hgy,hgz;
hgx=hgy=hgz=0.0;
double f7,f8,f9;
f7=f8=f9=0.0;
double hf7,hf8,hf9;
hf7=hf8=hf9=0.0;

double v1,v2,v3,dt,dts,xx,yy,zz,xxs,yyys,rrs,rr,inrrs,inrr,bzsl,brsl,br,bz,bx,by,cqm,ax,ay,az;

stepnum=120;

for (int step=0;step<stepnum;step++)
{
v1=vx+hf7; v2=vy+hf8; v3=vz+hf9;
dt=dz/v3; dts=dt*dt;
xx=x+hgx; yy=y+hgy; zz=z+hz;
xxs=xx*xx; yyys=yy*yy; rrs=xxs+yyys; rr=sqrt(rrs);
inrrs=1/(rrs+0.00000001); inrr=1/(rr+0.00000001);

bzsl=0; brsl=0; double temp=1;
b_cal(ma1,ers,zz,cc,ll,rr,bzsl,brsl,temp);
b_cal(ma2,ers,zz,ccc,ll,rr,bzsl,brsl,par_solenoid);

br=brsl; bz=bzsl;
bx=br*inrr*xx; by=br*inrr*yy;

cqm=9.648e+7*(n/m);

ax=cqm*(v2*bz-v3*by+ex);
ay=cqm*(v3*bx-v1*bz+ey);
az=cqm*(v1*by-v2*bx+ez);

double b_field=sqrt(bx*bx+by*by+bz*bz);

gx=v1*dt+0.5*ax*dts;
gy=v2*dt+0.5*ay*dts;
gz=v3*dt+0.5*az*dts;
x=x+gx; y=y+gy;
z=z+gz;

data[i][step]=z;
data2[i][step]=x;

{

```

```

output<<z;
output2<<-sqrt(x*x+y*y);
}

double distance=sqrt(gx*gx+gy*gy+dz*dz);
double velocity=sqrt(vx*vx+vy*vy+vz*vz)*pow(10,-9);

times[i]+=distance/velocity;

t0+=sqrt(gx*gx+gy*gy+dz*dz)/(1.0e-9*v0);

f7=ax*dt; f8=ay*dt; f9=az*dt; hf7=0.5*f7; hf8=0.5*f8; hf9=0.5*f9;
vx=vx+f7; vy=vy+f8; vz=vz+f9;

}
}

for (i=0;i<imax;i++)
{
output<<2.5<<",";
output2<<0<<",";
for (int j=0;j<30;j++)
{
output<<data[i][j]<<",";
output2<<setprecision(3)<<data2[i][j]<<",";
}
output<<endl;
output2<<endl;
}

double time_difference=times[5]-times[1];

for (i=0;i<6;i++) {tot_time+=times[i];tot_energy+=e0[i];}
tot_time=tot_time/6;tot_energy=tot_energy/6;

tot_time=time_difference/tot_time;
tot_energy=2*tot_energy*tot_time;

return 0;
}

```

APPENDIX B

Time-of-Flight Chamber Design and Construction

B.1 Time-of-Flight Chamber Design

The previous small *TwinSol* target chamber (Figure 1.2) limited many experiments which could be done using the *TwinSol* facility due to its small dimension and shorter time-of-flight path. As part of this thesis project, it was decided to design and build a new bigger vacuum chamber to eliminate these limitations and locate it at a longer time-of-flight location.

The assembly layout and construction picture of this new ToF vacuum chamber are shown in Figure B.1. It consists of eight side plates with 250 mm (ISO-250) ports, a top lid, a bottom lid with various ISO ports, and two adapter rings with O-ring grooves. Each side plate was made from 6061 Aluminum and is 18.4" by 14.5" (467.36mm \times 368.3 mm; Figure B.2). Eight of these were then welded internally together forming the main frame of the new chamber 2" (812.8 mm) in diameter as shown in Figure B.3. (The 3D model of chamber was done using Google Sketchup [GSU]). Two adapter rings (Figure B.4) with o-ring grooves were then bolted and then welded onto the main frame of the new chamber. The welding was done by an outside contractor.

The bottom plate has two ISO-150 and one ISO-100 ports. One ISO-150 port

is used to connect with the main turbo molecular pump (model Pfeiffer) to the chamber. The ISO-100 port is used for insertion of the sliding target ladder shaft (Figure B.8).

B.2 Leak Testing and Vacuum Tests of the ToF Chamber

Due to extreme difficulty of aluminum vacuum welding, the chamber when initially tested could only be pumped to several microns in vacuum. Because welds were done at the inside of each side plate, it was hard to find the location of leaks from the outside. We used a helium leak chaser and found several leaks. Both epoxy and vacuum sealant were used inside the chamber and the vacuum of the chamber finally, as required, reach the 10^{-6} torr level with the turbo pump. Unfortunately the initial batch of vacuum epoxy (model Loctite 1C) was flawed and delayed successful sealing of the chamber leaks for several weeks until new epoxy was obtained.

The pumping of the ToF chamber is done in two stages. In the first stage, a three-stage sorption pump (Varian) is used to pump the vacuum from atmosphere down to less than 200 microns. Then the turbo pump is turned on and continues pumping the vacuum from 200 micron to the 10^{-6} torr level (about 1 hour) .

Figure B.7 shows the ToF chamber used in the beam line together with the sorption pump.

B.3 Construction of Other Components

Several vacuum components also were constructed in conjunction with the ToF chamber. Here we simply described these components.

The target ladder is part of this chamber system and it was designed to hold three 3" by 3" (7.62 mm \times 7.62 mm) target frames.

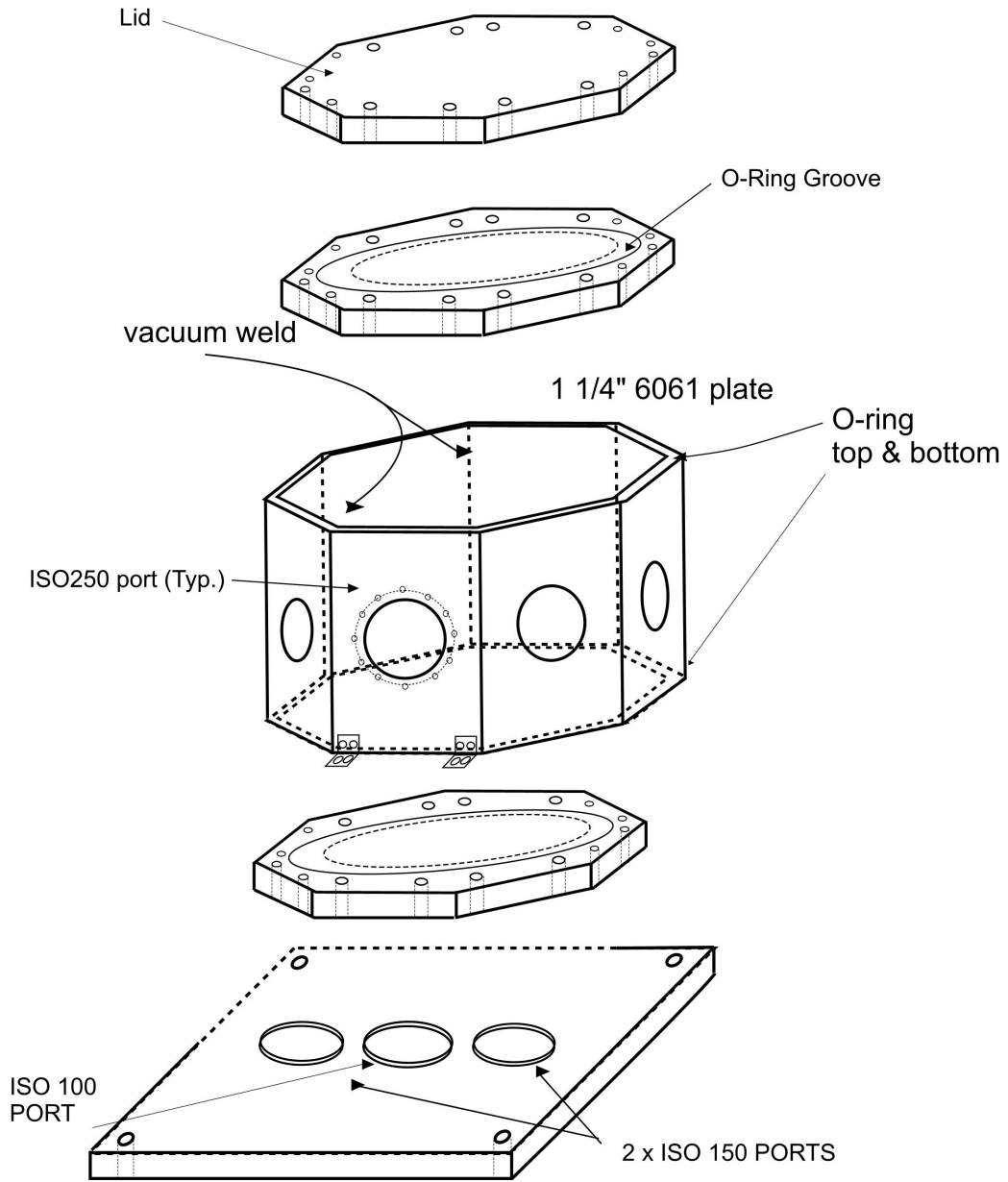


Figure B.1: Assembly layout of the new ToF chamber.

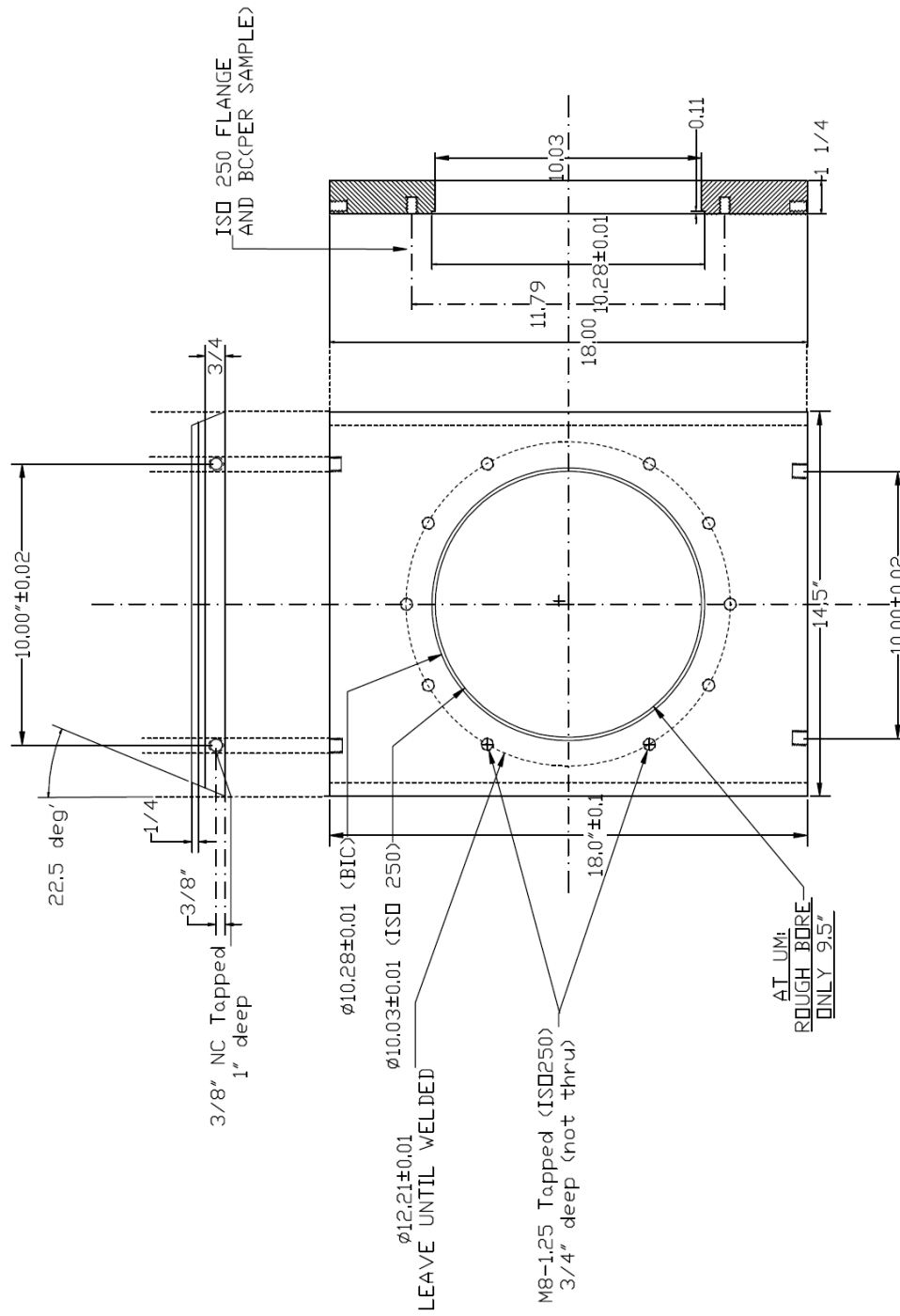


Figure B.2: ISO-250 side plate dimension for the ToF chamber.

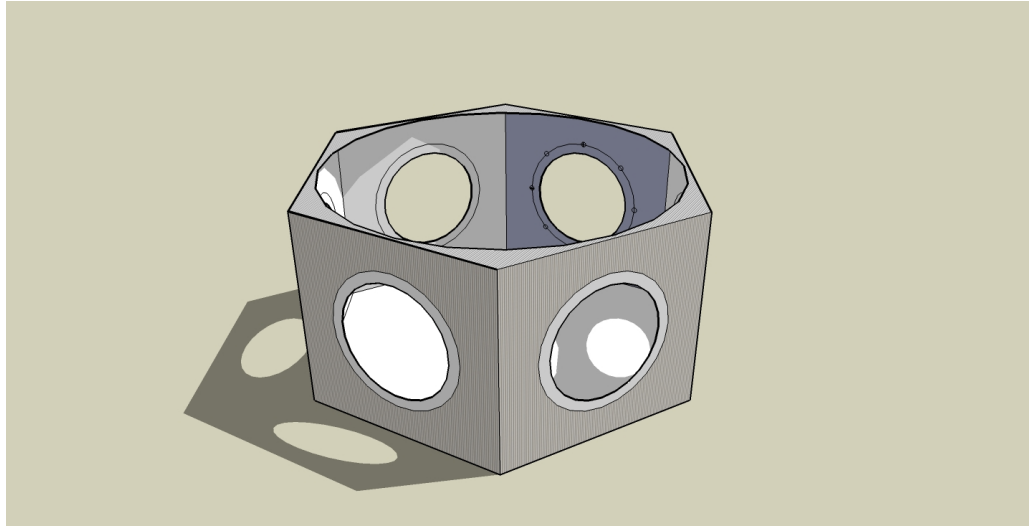
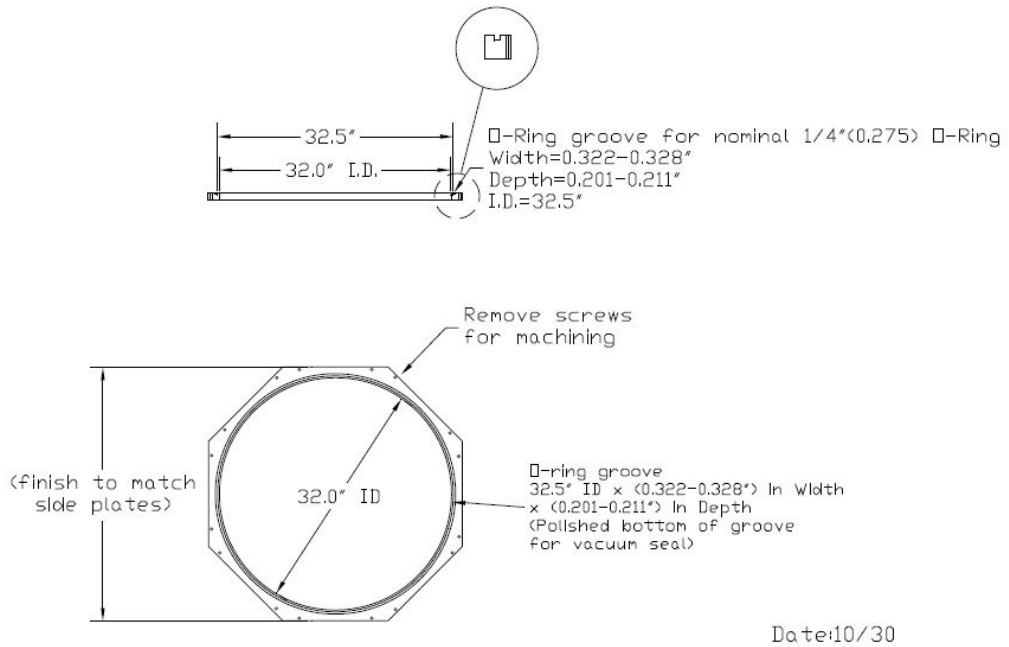


Figure B.3: ToF chamber frame 3D model.



Date:10/30

Figure B.4: Top adapter ring print.

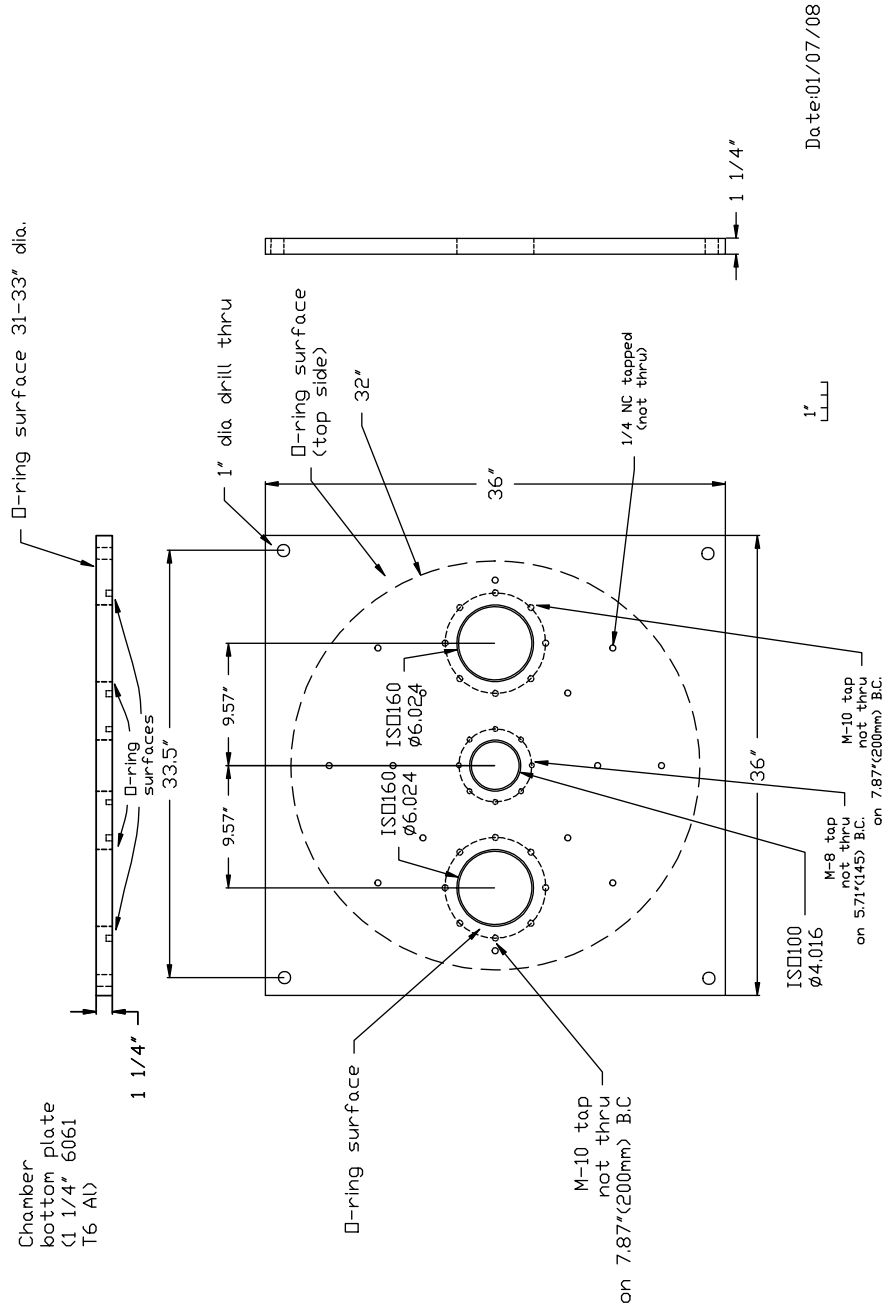
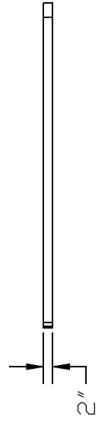
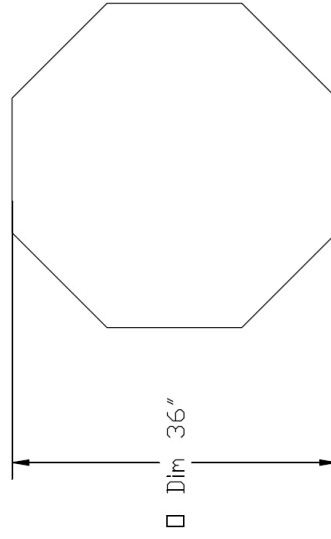


Figure B.5: The bottom plate for the ToF chamber.

Vacuum Chamber Lid
Option B (2" thick)*



Material: Non-anodized
aluminum honeycomb
*(to support vacuum
load over 32"
diameter vacuum
chamber opening)



Date: 12/18/07

Figure B.6: Print of top lid for *TwinSol* ToF chamber.

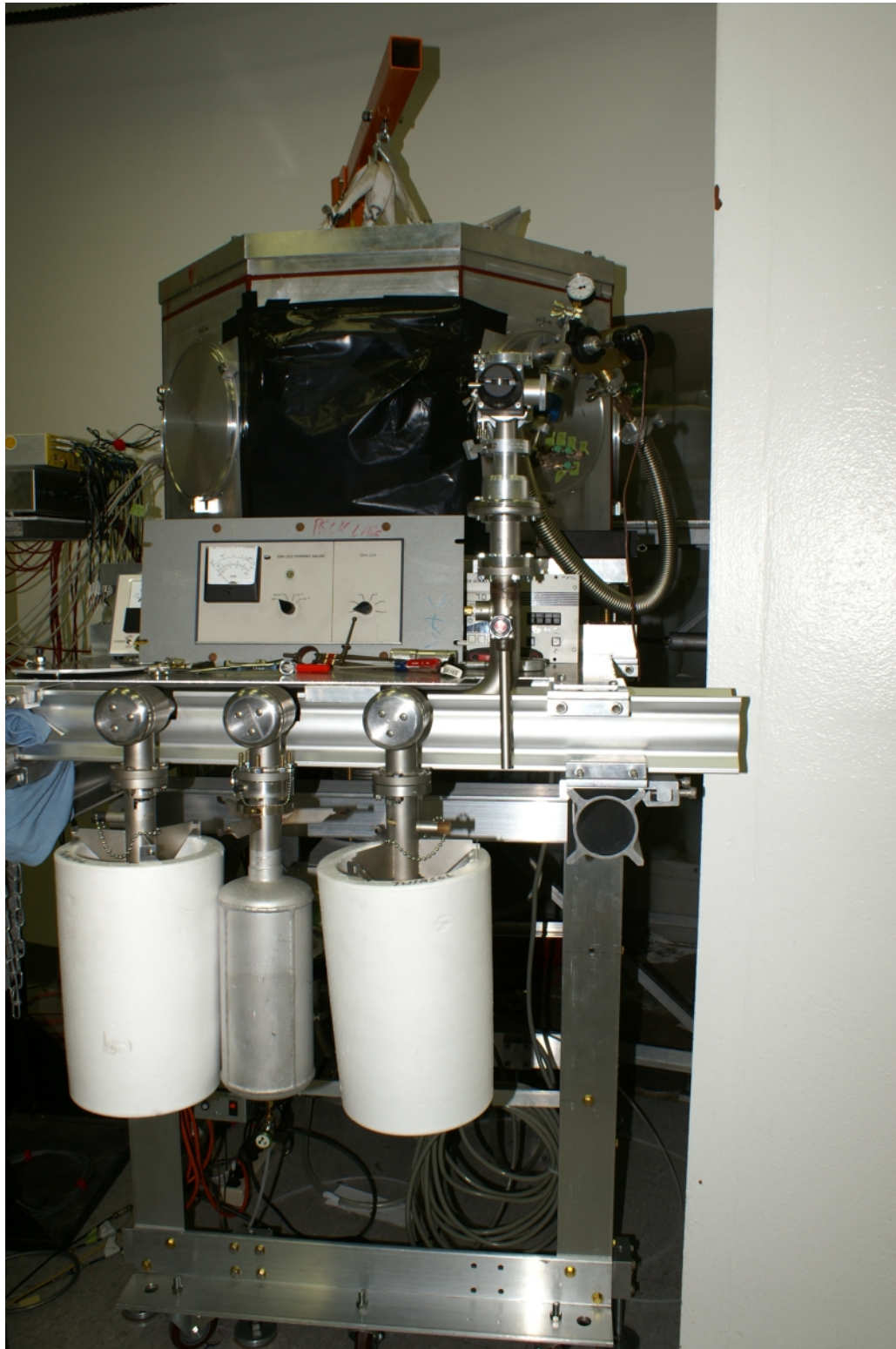


Figure B.7: The current configuration of the ToF chamber.

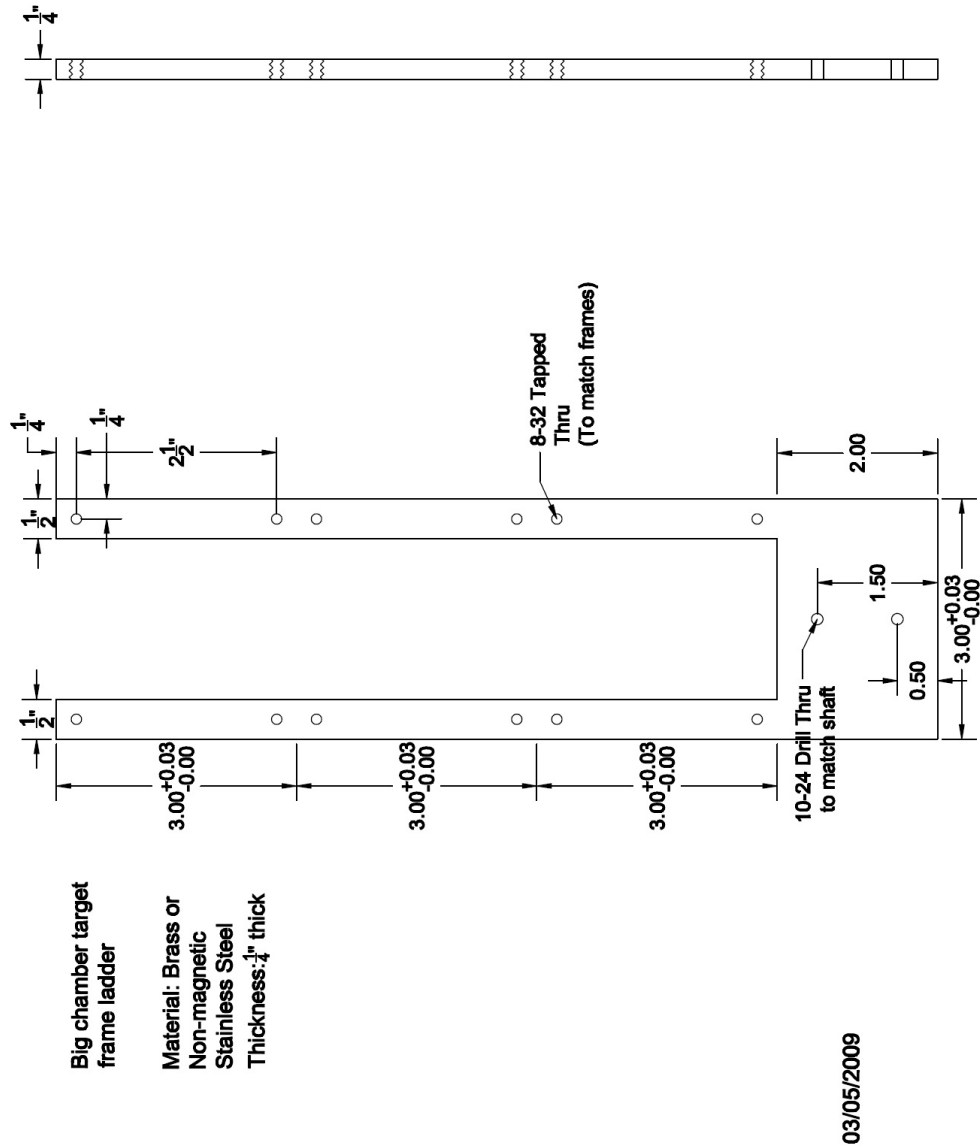


Figure B.8: Print of the ToF chamber target ladder.

A 28" rotating detector table also was designed, built and put inside the ToF chamber. A Teflon hub (Figure B.10) was made to support the rotational table and also provide access for the target ladder. This table (Figure B.9) was used to place standard UM-UND detector holders at specific spaced mounting locations. With its angle markings, the detector angles easily can be determined. An aluminum frame

(Figure B.11, related prints in Appendix E) was constructed to support the ToF chamber and adjust the height of the chamber to match the UND beamline. An hoist arm also was attached to this frame so the top lid could be lifted.

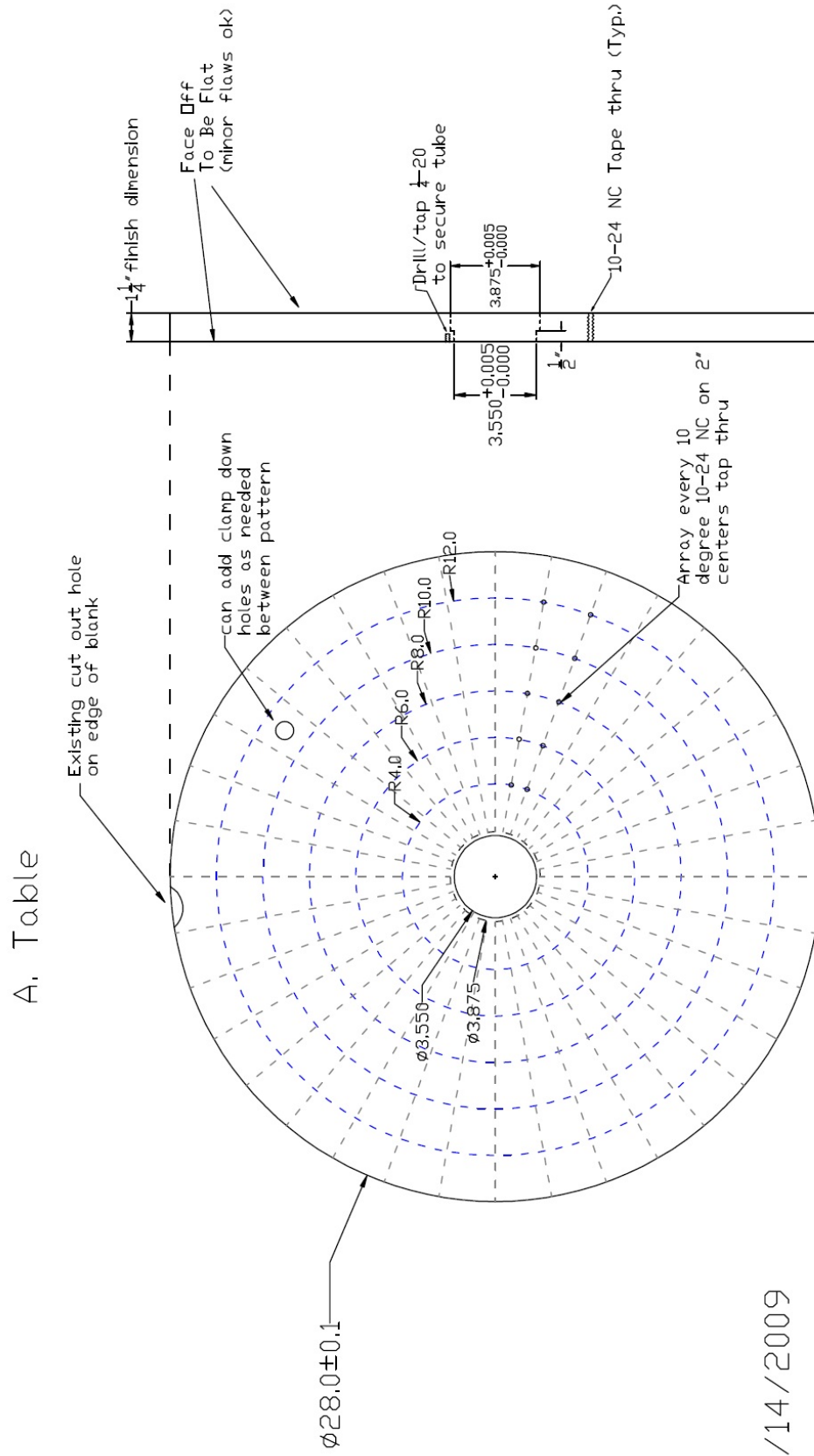


Figure B.9: ToF chamber rotating detector table.

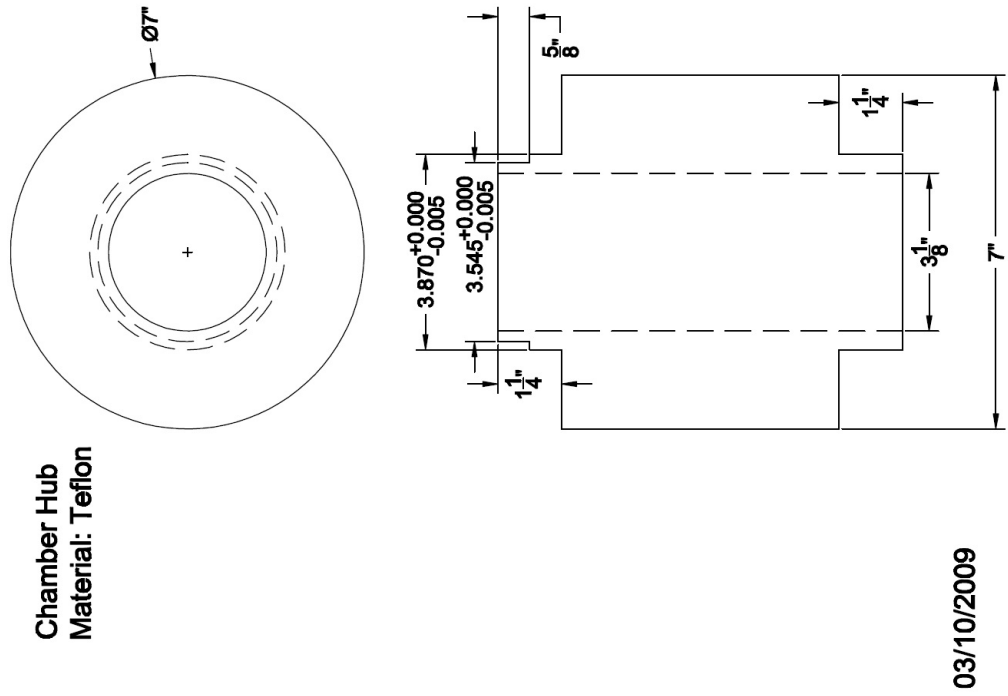


Figure B.10: Print of hub between the rotating table and the bottom plate of the ToF chamber.

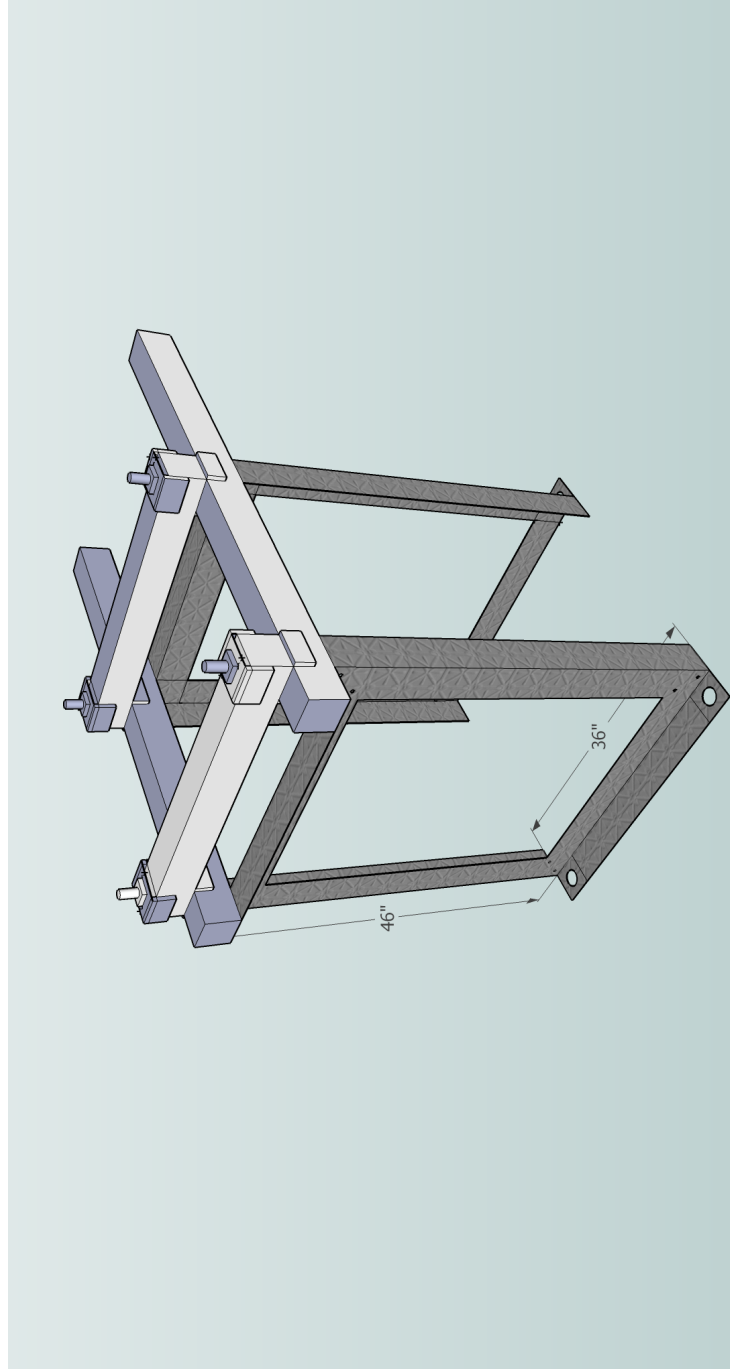


Figure B.11: The 3D model of the ToF chamber supporting frame.

APPENDIX C

Kmax CAMAC Data Acquisition System

C.1 Introduction

Computer automated measurement and control (CAMAC) is a standard bus for data acquisition and control used in nuclear and particle physics experiments as well as industry. The bus allows data exchange between plug-in modules (up to 24 in a single crate) and a crate controller, which then interfaces to a computer (in our case a Mac) or to a VME-CAMAC interface. The CAMAC standard differs from the NIM standard in two important ways [ORTEC]. First, the CAMAC crate has a built-in, digital data bus to provide computer communications with the modules. Second, the narrowest CAMAC modules are exactly half the width of the minimum NIM module width and allow a high density of signal inputs.

Kmax is a commercial CAMAC-interface program that provides a complete environment for data acquisition and instrument control with advanced features for data management, visualization, and reporting [Sparrow]. It supports single- and dual-parameter data displays, provides a variety of formatting options and allows the user to configure control panels directly on the computer display. The core environment can be expanded by adding user-defined controls, external commands and external functions.

C.2 Kmax-CAMAC System Developed for γ - γ Coincident Measurements

While the new ToF was under construction (Appendix B), a CAMAC-based data acquisition system was developed which eventually was used at UM to test ToF and other detectors needed for this thesis project. The system also proved valuable for other related work, and at the request of Prof. H. Griffin (UM Chemistry department) a CAMAC-based system for high speed γ - γ coincidence measurements using a radioactive source (^{228}Th) was developed and will be discussed here.

C.2.1 CMC100 controller¹

A complete data acquisition system for high-speed γ - γ coincidence measurements was set up with NIM and CAMAC modules and custom-written Kmax software. This system used a CMC100 FastCamac USB crate controller with a fast USB 2.0 interface [CMC100].

The CMC100 contains two host interfaces, USB 2.0 and RS232 [Figure C.1]. Incoming commands and data from either source are assembled into 32 bit words and sent to the command interpreter via a FIFO buffer. The total buffer space available is about 1000 words. Commands for the crate controller are executed immediately and the result is sent to the response buffer memory, also organized as a FIFO. Commands for the dataway are executed by the dataway interface and the response sent to the response buffer. Commands and instructions intended for the program store are sent to the list processor and stored. The list processor program memory is 512 words, and can contain multiple short programs. There are two registers, a 20 bit counter and a 32 bit accumulator. Programs can be executed in 3 ways: a LAM, an external NIM pulse, or a command from the host computer. The response buffer

¹Partly adapted from CMC100 operating manual

memory is organized as a FIFO and can contain about 1,048,000 CAMAC words. The CMC100 can read data from CAMAC modules at up to 40 Mbytes/sec. The 24 bit data words are expanded to 32 bits (adding a byte containing X, Q, LAM and crate number) and sent to the FIFO buffer [CMC100]. The rate into the USB interface is 40 Mbytes/sec. The USB host must pull the data from the controller. The USB 2.0 interface transmits data to and from the host in 512 byte blocks, at about 11 microseconds per block.

The USB buffers are normally available to be read by the host only when full (they are automatically committed to the USB when full). The flush (or commit to USB) command will cause a partially full buffer to be committed to the USB and available for transmission to the host.

C.2.2 NIM electronics setup

In $\gamma - \gamma$ coincidence measurements, two high-performance germanium detectors (HPGe) were used to detect gamma rays from a radioactive source (^{228}Th) in opposing directions. The detectors and source setup is shown in Figure C.2.

Two timing signals from CANBERRA 2002C pre-amplifiers were sent through ORTEC 454 timing filter amplifiers (TFA) and ORTEC 463 constant fraction discriminators (CFD) into the inputs of a TENNELEC TC 404A multipurpose coincidence module. One output from the TC 404A coincidence module went through a LECROY 222 dual-gate generator and generated the strobe for a CAMAC ORTEC 811 ADC. Another output from the coincidence module went through an ORTEC 427A delay amplifier and generated the pulser signal (which also was fed into the 811 ADC). Two separate outputs from the ORTEC 463 CFDs went through an ORTEC 416A gate & delay generator into the start and stop inputs of an ORTEC 437

time-to-pulse-height converter (TAC). Together with another output of the coincidence module sent to the gate input, the ORTEC 437 generated the TAC signal sent into the 811 ADC. The energy outputs from the pre-amplifiers went through CANNBERA 2026 amplifiers and created E1 and E2 signal in the ORTEC 811 ADC. A diagram of the electronic setup is shown in Figure C.3.

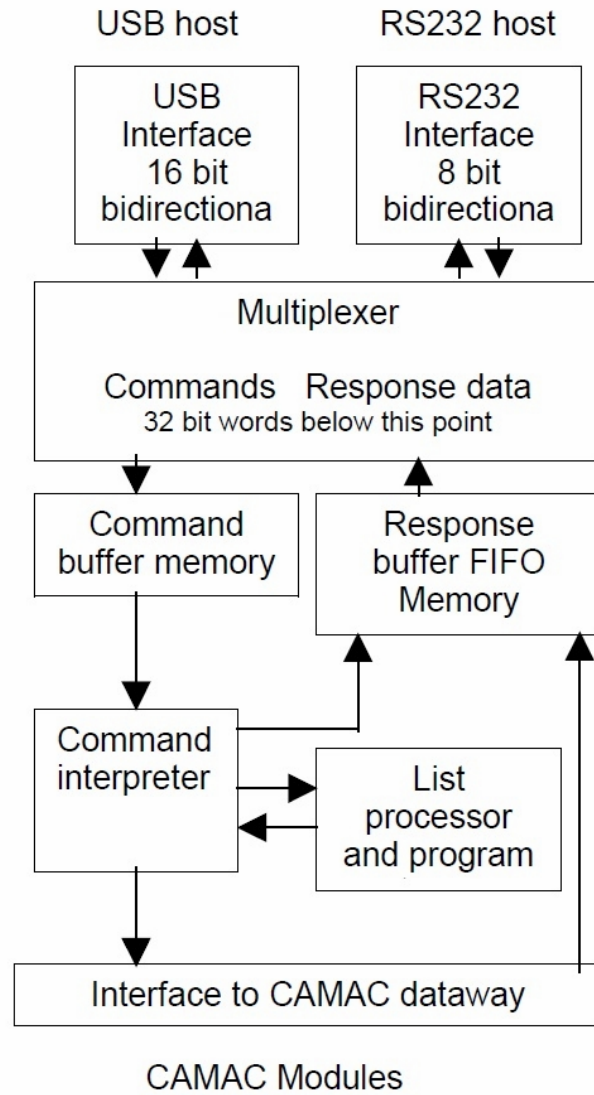


Figure C.1: CMC100 FastCamac USB Crate Controller [CMC100]

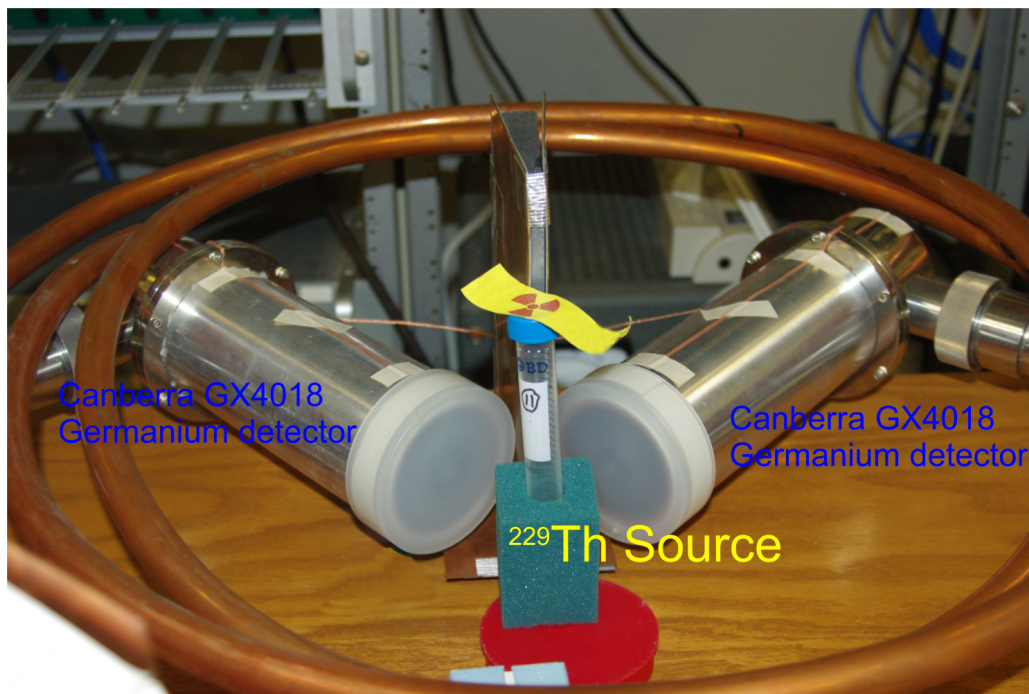


Figure C.2: CANBERRA GX4018 germanium detector positions relative to the ^{229}Th source.

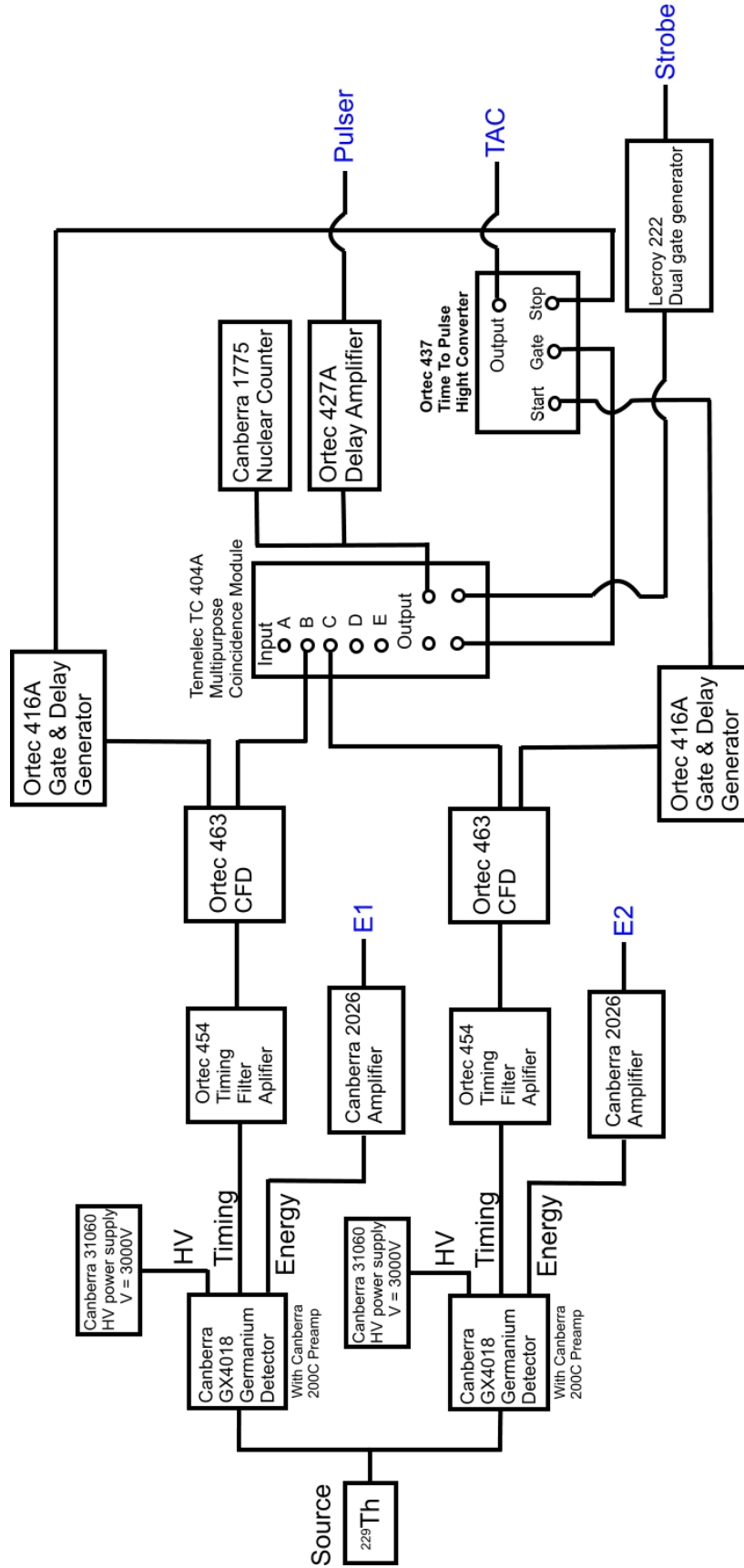


Figure C.3: NIM electronic setup for gamma-gamma coincidence measurements.

Then following the NIM electronics, two energy signals (E1 and E2), one TAC signal and one pulser signal were sent into the CAMAC ORTEC 811 ADC and onto the computer.

C.2.3 Data process in CAMAC

The two γ energy signals, called E1 and E2, were sent into the first two channels of the 811 ADC. The TAC signal was sent into the third channel and the pulser signal to the fourth channel of the 811 ADC. The CMC100 internal buffer was used for the realization of fast data acquisition. A set of program commands were stored in the CMC100 list processor. Upon execution, each channel of the 811 ADC was read accordingly and one data block including E1, E2, TAC and pulser signal was formed.



Figure C.4: Data block from ORTEC 811 ADC (5 bytes each).

Because the USB buffers of the CMC100 can only be read when full, the controller keeps reading data from the ORTEC 811 ADC when the gate is open. This yields very fast data processing speed. When the USB buffer is full, the controller sends a service request (SRQ) notice to the host computer and Kmax software processes this SRQ notice.

CAMAC internal commands sent into the CMC100 list processor are organized into 24 bits binary format. All command blocks begin with a 2-word header, `&hFFFFFFFF` followed by `&h00000000`, and end with a 1-word trailer, `&h0E000000` [this is the flush (or commit to USB) command]. In between the header and trailer are the commands executed by the CMC100 list processor. The Kmax commands in

this experiment are as follows (in JAVA code):

```
int[] data=new int[10];
data[0]=0;
dev.writeInt(99,0,4,data,0,1);
data[0]=0x08000002;
data[1]=0x08000002;
data[2]=(3<<9)+(0<<4)+0;
data[3]=(3<<9)+(0<<4)+1;
data[4]=(3<<9)+(0<<4)+2;
data[5]=(3<<9)+(0<<4)+3;
data[6]=(3<<9)+(11<<4)+12;
data[7]=0x1F000000;
data[8]=0x0E000000;
data[9]=0x1F000000;
dev.writeInt(27,0,16,data,0,10);
```

“*data[]*” is the array with all commands stored. *data[0][1]* is the header for the command. *data[2][3][4][5]* are commands reading 1-4 channel of 811 ADC, *data[6]* is the command to clear the register for the next data readout. *data[7][8][9]* tells the CMC100 list processor to end this readout process. Command “*dev.writeInt(27,0,16,data,0,10);*” sends this command list into the list processor.

When the primary buffer of the CMC100 is full, the controller sends a notification to Kmax, and Kmax then executes the `SRQ()` routine. In our case, 52429 data blocks constructed as in Figure C.4 were read in.

C.2.4 Kmax user interface

Kmax constructs corresponding 1D and 2D histograms of E1, E2 and TAC after data blocks were read in and stored in the buffer. Kmax software provides a set of JAVA utilities to build a graphical user interface (GUI) for data acquisition (DAQ). We built our GUI (Figure C.5) based on these JAVA utilities. We provide GUI buttons to start and stop the DAQ, save or open the events data file, and also create several histograms for 1D E1, E2 or TAC, and 2D histogram for E1 vs. E2 for identifying gamma-gamma coincident events. This GUI also supports the ability to gate on the 2D histogram and project coincidence-gated γ -energy spectra onto either the E1 or E2 axis.

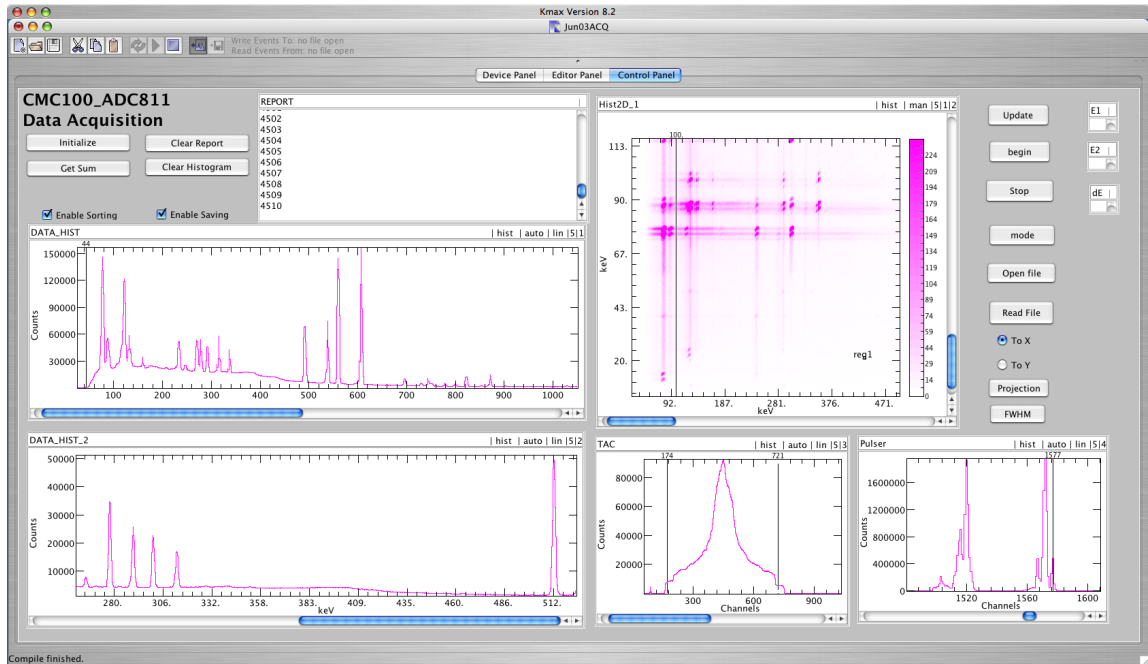


Figure C.5: Typical gamma-gamma coincidence measurements with Kmax GUI.

Together with several research tools mentioned in Appendix 5, HPGe gamma-gamma measurements are able to give extremely good resolution results and we are able to compare them with predictions from the literature. Figure C.6 shows a typical gamma spectrum obtained from this Kmax DAQ system with the ^{228}Th source.

C.3 System for γ -neutron Pulse Shape Discrimination (PSD) Measurements

Another application of the Kmax-CAMAC data acquisition system was a 2nd system using a JORWAY 73A model CAMAC controller with a SCSI to Firewire converter for a series of measurements using a new type of fast neutron detector [Mo09].

C.3.1 γ neutron PSD

In most neutron measurements, there are accompanying random gamma ray events. Instead of using the time-of-flight method, a means of uniquely identifying

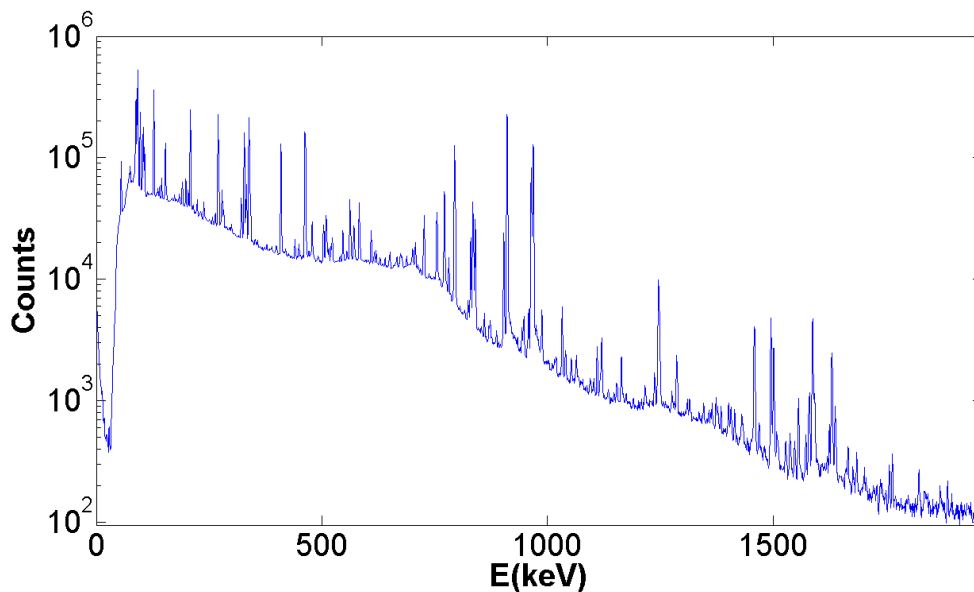


Figure C.6: Typical coincidence-gated gamma spectrum obtained from the CAMAC-Kmax DAQ system.

and separating neutron events from gamma events by using the pulse-shape difference of these two signals often is used [Marrone02][Brooks79][McBeth71]. Organic liquid scintillators such as C_6H_6 and C_6D_6 exhibit different responses to different types of incident radiation and particles. The recoiling particle from neutron scattering produce signals with slow decay times as compared with signals of recoiling energetic electrons from γ -rays. The pulses produced by Compton electrons from gamma events are found to contain most of their total emitted light in the leading edge, with relatively little light in the tail of the pulse. On the other hand, proton or deuteron recoils due to neutrons or heavier particles are found to have a larger fraction of the total light in the tail, and less in the leading edge. By integrating the signal tail and comparing it with the integral for the total pulse, we can achieve PSD between high energy neutrons and gammas (Figure C.7).

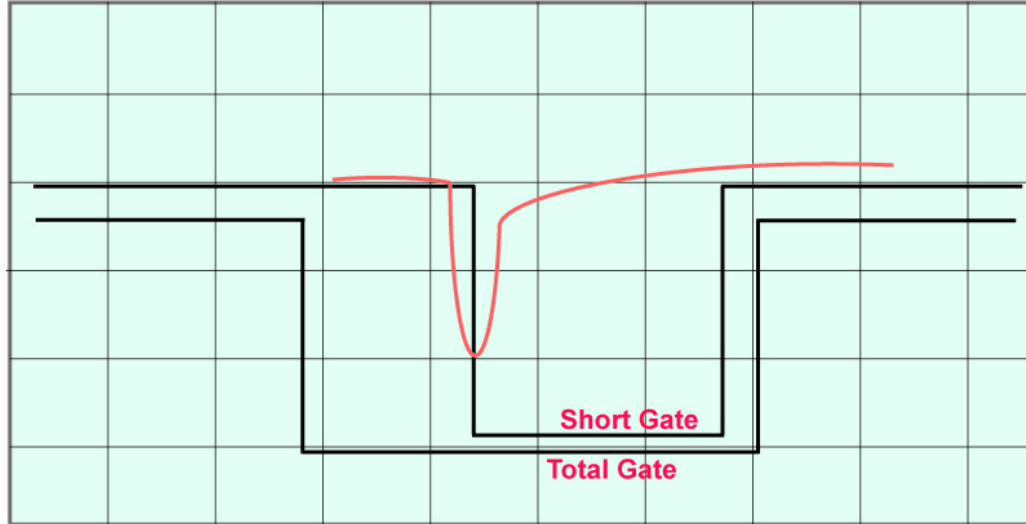


Figure C.7: Pulse-shape discrimination by applying two different time gates on anode PMT QDC signals (10 nsec/ch).

C.3.2 C_6D_6 neutron detector data acquisition

The above was used as part of another UM thesis project [Mo09], where a C_6D_6 liquid scintillator was coupled with a photomultiplier (PMT) to detect neutrons. The anode signals from the PMT were obtained from an ORTEC-265 base and put into a LeCroy 428F analog fan out. The signal was then sent from the fan out into a constant-fraction discriminator (CFD) where two gates were generated and sent to a LeCroy 2249A charge-to-pulse-height converter (QDC) before Kmax received the data. The schematic describing this data acquisition process is shown in Figure C.8 [MO09].

C.3.3 Kmax program for neutron-gamma PSD experiment

The CAMAC controller used in the neutron- γ PSD experiment was a Jorway model 73A SCSI bus crate controller. It is connected using a SCSI cable with a SCSI to Firewire (1394) adapter to the host Mac computer. Due to a limited built-in list processor, the Jorway controller [Jorway] acts event-by-event for every data read-out

process. The SRQ() routine in Kmax controls all read and write process instead of the list processor as in the CMC100 controller.

The Kmax GUI is similar to the one in Figure C.5 and a typical neutron-gamma 2D histogram obtained using this CAMAC-Kmax system is shown in Figure C.9.

C.4 Kmax Code Listings

C.4.1 Gamma-gamma coincidence measurement Kmax Java code

```

import kmax.ext.*;
import java.lang.*;

public class Runtime implements KmaxRuntime {
KmaxToolsheet tlsh;
KmaxDevice dev;
KmaxWidget report;
KmaxHist dataHist;
KmaxHist dataHist2;
KmaxHist Hist2D;
KmaxHist TAC;
KmaxHist pulser;
KmaxHist project1;
KmaxWidget toX;
KmaxWidget toY;
KmaxWidget E1,E2,dE;

int slotADC = 3;
int numEvents = 0;
int[] rData=new int[262145];

boolean isReady = false;
boolean isRunning = false;

public void init(KmaxToolsheet toolsheet) {
tlsh = toolsheet;
dev = tlsh.getKmaxDevice("DEV1");
report = tlsh.getKmaxWidget("REPORT");
dataHist=tlsh.getKmaxHist("DATA_HIST");
dataHist2=tlsh.getKmaxHist("DATA_HIST_2");
TAC=tlsh.getKmaxHist("TAC");
pulser=tlsh.getKmaxHist("pulser");
Hist2D=tlsh.getKmaxHist("Hist2D_1");
project1=tlsh.getKmaxHist("project1");
toX=tlsh.getKmaxWidget("ToX");
toY=tlsh.getKmaxWidget("ToY");
tlsh.setProperty("FILESIZE","655360000");
E1=tlsh.getKmaxWidget("E1");
E2=tlsh.getKmaxWidget("E2");
dE=tlsh.getKmaxWidget("dE");
}

public void GO(KmaxToolsheet toolsheet) {
isReady = false;
isRunning = false;
}

public void initDAQ(KmaxWidget widget) {
int[] datArray = new int[1];

report.setProperty("TEXT", "");
disableList();

int[] data = {1};
int error = dev.writeInt(99, 0, 2, data, 0, 1);

dev.writeInt(28, 8, 26, null, 0, 0);
dev.writeInt(28, 9, 26, null, 0, 0);

datArray[0] = 1 << ( 3 - 1);
dev.writeInt (30, 0, 16, datArray, 0, 1);

writeList5();

disableList();

dataHist.setValueAxisMode(2);
dataHist.clear();
int[] range={1,1023,1,1023};
dataHist.setRanges(range);
dataHist.update();
dataHist2.clear();
dataHist2.setRanges(range);
}

```

```

dataHist2.update();
dataHist2.setValueAxisMode(2);

Hist2D.clear();
Hist2D.update();
TAC.clear();
TAC.update();
pulser.clear();
pulser.update();

isReady = true;

dev.writeInt(slotADC, 12, 26, null, 0, 0) ;

}

public void fileopen(KmaxWidget widget){

System.out.println ("In newEventFile - before showFileChooser.");

String filePath = tlsh.showFileChooser("Create new event file", "evnt", "New");

System.out.println ("In newEventFile - after showFileChooser.");

if (filePath ==null) {
tlsh.setProperty("STATUSSTR", "The file choolser returned null.");
return;
}
int error = tlsh.newEventFile(filePath);
tlsh.setProperty("STATUSSTR", "error = " + error);
}

public void summation(KmaxWidget widget)
{
int count1=dataHist.getTotal();
int count2=dataHist2.getTotal();
int TACcount=TAC.getTotal();
report.setProperty("INSERT","Total # for E1 = "+count1+"\n");
report.setProperty("INSERT","Total # for E2 = "+count2+"\n");
report.setProperty("INSERT","Total # for TAC = "+TACcount+"\n");
}

public void fileread(KmaxWidget widget) {
int[] blkinfo = new int[3];
String lastName = "";
int totalEvents = 0;
int i;
int n=0;
int[] rData=new int[262144];
tlsh.setProperty("BUFSIZE","262144");

while (true) {
n++;
String fileName = tlsh.getEventFile(tlsh.EV_READ_FILE).getName();
if ( !fileName.equals(lastName)) {
report.setProperty("INSERT", "----- "
+ fileName + " -----" + "\n");
lastName = fileName;
}

tlsh.clearEventBuffer(tlsh.PRIMARY_BUFFER);
int result = tlsh.readNextBlockHeader(blkinfo);

if (result != tlsh.NO_ERROR) {
tlsh.setProperty("STATUSSTR", "End of file sequence. result = " + result);
report.setProperty("INSERT", "This is the end of file!\n");
break;
}
report.setProperty("INSERT", "<< TYPE, SIZE, COUNT >>= "
+ blkinfo[0] + ", " + blkinfo[1] + ", " + blkinfo[2] + "\n" );
totalEvents += blkinfo[2];

tlsh.loadEventBuffer(tlsh.PRIMARY_BUFFER);

rData=tlsh.getEventBuffer(tlsh.PRIMARY_BUFFER);

```

```

tlsh.sortEventBuffer(tlsh.PRIMARY_BUFFER);

report.setProperty("INSERT", n + "blocks read \t");

}

report.setProperty("INSERT", "Total Events = " + totalEvents + "\n" );
report.setProperty("INSERT", "# of blocks = " + (n-1) + "\n");
dataHist.update();
dataHist2.update();
Hist2D.update();
}

public void mode(KmaxWidget widget){
int axismode=dataHist.getValueAxisMode();
if (axismode==KmaxHist.LINEAR_MODE){
dataHist.setValueAxisMode(1);}
else if (axismode==KmaxHist.LOG_MODE){
dataHist.setValueAxisMode(0);}
}

double[] datapoint=new double[6];

public void SRQ(KmaxDevice device) {

tlsh.setProperty("BUFSIZE","270000");

int srqData=dev.getSRQData();

if ((srqData & 3)==0){
tlsh.setProperty("STATUSSTR","Ignoring SRQ event!");
return;
}

numEvents++;

report.setProperty("INSERT",numEvents+"\n");

disableList();
//dev.readInt(27,1,0,rData,0,262144);
dev.readInt(27,1,0,rData,0,262145);
enableList();

tlsh.clearEventBuffer(tlsh.PRIMARY_BUFFER);
int error=tlsh.addEventBlock(tlsh.PRIMARY_BUFFER,5,5,52429,rData);

tlsh.saveEventBuffer(tlsh.PRIMARY_BUFFER);
tlsh.sortEventBuffer(tlsh.PRIMARY_BUFFER);

dataHist.update();
dataHist2.update();
TAC.update();
pulser.update();

Hist2D.update();

}

public void HALT(KmaxToolsheet toolsheet) {
dev.writeInt(28, 8, 26, null, 0, 0);
dev.writeInt(28, 9, 26, null, 0, 0);

}

public void reStart() {
dev.writeInt(slotADC, 12, 26, null, 0, 0) ;
}

public void START_STOP(KmaxWidget widget) {

if (isRunning) {

```

```

        numEvents=0;
dev.writeInt(30, 9, 26, null, 0, 0);

widget.setProperty("LABEL", "Start");
isRunning = false;
return;
}

if (isReady) {

widget.setProperty("LABEL", "Stop");
isRunning = true;
tlsh.setProperty("STATUSSTR", "The DAC is running.");
}

}

```

```

public void zero(KmaxWidget widget){
disableList();
disableList();
flush();
}

```

```

public void flush(){
int[] data={7};
dev.writeInt(27,2,16,data,0,1);
}

```

```

public void writeList(){
int error=0;
int[] data=new int[7];

data[0]=0;
dev.writeInt(99,0,4,data,0,1);

data[0]=0x08000002;
data[1]=0x08000002;
data[5]=0x1F000000;
data[6]=0x0D000000;
dev.writeInt(27,0,16,data,0,7);

}

```

```

public void writeList5(){
int[] data=new int[10];
data[0]=0;
dev.writeInt(99,0,4,data,0,1);
data[0]=0x08000002;
data[1]=0x08000002;
data[2]=(3<<9)+(0<<4)+0;
data[3]=(3<<9)+(0<<4)+1;
data[4]=(3<<9)+(0<<4)+2;
data[5]=(3<<9)+(0<<4)+3;
data[6]=(3<<9)+(11<<4)+12;
data[7]=0x1F000000;
data[8]=0x0E000000;
data[9]=0x1F000000;
dev.writeInt(27,0,16,data,0,10);
}

```

```

public void begin(KmaxWidget widget){
flush();
enableList();
}

```

```

public void trigger(KmaxWidget widget){
int[] rData=new int[262145];
tlsh.setProperty("BUFSIZE", "270000");

disableList();

dev.readInt(27,1,0,rData,0,262145);
flush();

enableList();
}

```

```

int j=0;

tlsh.clearEventBuffer(tlsh.PRIMARY_BUFFER);

int error=tlsh.addEventBlock(tlsh.PRIMARY_BUFFER,5,5,52429,rData);
if (error==KmaxToolsheet.BUFFER_FULL){
report.setProperty("INSERT","BUFFER_FULL\n");
}
tlsh.saveEventBuffer(tlsh.PRIMARY_BUFFER);
tlsh.sortEventBuffer(tlsh.PRIMARY_BUFFER);

dataHist.update();
dataHist2.update();
Hist2D.update();
TAC.update();
pulser.update();
}

public void readList(KmaxWidget widget){
int[] data={0};
dev.readInt(30,0,1,data,0,1);

data[0]=0;
dev.writeInt(99,0,4,data,0,1);
data=new int[6];
int dataCount=data.length;
dev.readInt(27,0,0,data,0,dataCount);
int i;
for (i=0;i<dataCount;i++){
}
}

public void readStatus(){
int[] data={0};
dev.readInt(27,15,0,data,0,1);
}

public void disableList(){
int[] data={0};
dev.writeInt(27,1,16,data,0,1);
}

public void enableList(){
int[] data={4+8};
dev.writeInt(27,1,16,data,0,1);
}

public void triggerList(){
int[] data={2};
dev.writeInt(27,2,16,data,0,1);
}

public void readBuf(){
disableList();
int[] data=new int[512];
dev.readInt(27,2,0,data,0,512);
enableList();
}

public void UPDATE_HIST(KmaxWidget widget){
dataHist.update();
}

public void project(KmaxWidget widget){
String selectedName = Hist2D.getSelectedRegion();
if (selectedName == null)
tlsh.setProperty("STATUSSTR", "No region selected");
else
tlsh.setProperty("STATUSSTR", selectedName + " is selected");

int total=Hist2D.getRegionSum(selectedName);
report.setProperty("INSERT",total + "\n");
}

public void ToX(KmaxWidget widget) {
toY.setProperty("VALUE", "0");
}

```

```

public void ToY(KmaxWidget widget) {
toX.setProperty("VALUE", "0");
}

public void getFWHM(KmaxWidget widget) {
String selectedName = project1.getSelectedRegion();
if (selectedName == null)
tlsh.setProperty("STATUSSTR", "No region selected");
else
tlsh.setProperty("STATUSSTR", selectedName + " is selected");

double[] centroid=project1.getRegionCentroid(selectedName);
double[] fwhm=project1.getRegionFWHM(selectedName);
tlsh.setProperty("STATUSSTR", "Centroid="+round(centroid[0])+";FWHM="+round(fwhm[0]));
}

public double round(double number) {

int places = 3;
double fact = Math.pow(10,places);

double doub = Math rint(number*fact);
return (doub/fact);
}
}

```

C.4.2 Neutron-gamma PSD experiment Kmax Java code

```

/*
-----
Hawk_M4 Toolsheet Version 3.0
Uses a single AD413 to do event-by-event data acquisition.
Buffering should be added for highspeed requirements
Changing the LLD could be automated
-----
*/

import kmax.ext.*;
import java.lang.*;
import java.math.*;

public class Runtime implements KmaxRuntime {
KmaxToolsheet tlsh; // Store a reference to the toolsheet environment
KmaxDevice dev;
KmaxWidget report;
KmaxWidget startStop;
KmaxWidget doSort;
KmaxWidget doSave;

KmaxHist dataHist;
KmaxHist dataHist2;
KmaxHist dataHist2D;
KmaxHist dataHist2D_1;

KmaxHist project1;

int count = 0;
int slotADC = 2; // The toolsheet has one CAMAC ADc 2249SG 114 in this slot
int slotADC2 = 3;
int numEvents = 0;

//Change these values to change the LLD in the ADC, value[mVolts] = 2* LLDn
int LLD = 25;
int ULD = 255;

boolean isReady = false;
boolean isRunning = false;

/**
 * The 'init' method is executed at compile time.
 */
public void init(KmaxToolsheet toolsheet) {
tlsh = toolsheet; // Save this reference for use in the toolsheet
dev = tlsh.getKmaxDevice("DEV1");
startStop = tlsh.getKmaxWidget("START_STOP");
}
}

```

```

report = tlsh.getKmaxWidget("REPORT");

dataHist = tlsh.getKmaxHist("DATA_HIST");
dataHist2 = tlsh.getKmaxHist("DATA_HIST2");
dataHist2D = tlsh.getKmaxHist("HIST2D");
dataHist2D_1 = tlsh.getKmaxHist("HIST2D_1");

doSort = tlsh.getKmaxWidget("DO_SORT");
doSave = tlsh.getKmaxWidget("DO_SAVE");

project1=tlsh.getKmaxHist("project1");

dataHist.setEventID(5);
dataHist2.setEventID(5);
} // init

/**
 * The 'GO' method is executed when the GO button is clicked.
 */
public void GO(KmaxToolsheet toolsheet) {
startStop.setProperty("LABEL", "Start");
isReady = false;
isRunning = false;
tlsh.setProperty("STATUSSTR", "SCM301_AD114.VERSION 1.0");
} // GO

/**
 * The 'initDAQ' method is executed when the initDAQ button is clicked.
 */
public void initDAQ(KmaxWidget widget) {
int[] datArray = new int[1];
int devErr = 0;

if (isRunning) {
tlsh.showWarning("You must stop Aquisition before Re-initializing.");
return;
}

// Clear the REPORT text widget
report.setProperty("TEXT", "");

report.setProperty("INSERT", "Initializint the controller ...\\n");

count = 0;
// Init the controller
devErr = dev.writeInt(28, 8, 26, null, 0, 0); // SCM 301: CAMAC Initialize.
if (devErr != 0) {
report.setProperty("INSERT", "device error = " + devErr + "\\n");
return;
}

dev.writeInt(28, 9, 26, null, 0, 0); // SCM 301: CAMAC Clear.
dev.writeInt(30, 9, 26, null, 0, 0); // SCM 301: Set CAMAC Inhibit.
dev.writeInt(30, 10, 24, null, 0, 0); // SCM 301: Disable BD Output.

// Calculate and write the LAM mask
datArray[0] = 1 << (slotADC - 1);
dev.writeInt(30, 0, 16, datArray, 0, 1); // SCM 301: Load LAM Mask.

setMode(2);

// Initialize the ADC: Coincidence Mode; CAMAC Random Access; disable Zero Suppression
// Disable Overflow suppression; Disable channel gates; Enable Master Gate
// devErr = dev.writeInt(slotADC, 0, 9, null, 0, 0); // AD 114 ADC: Clear module.
devErr = dev.writeInt(slotADC, 0, 9, null, 0, 0);
devErr = dev.writeInt(slotADC2, 0, 9, null, 0, 0);
if (devErr != 0) {
report.setProperty("INSERT", "device error = " + devErr + "\\n");
return;
}

isReady = true;
tlsh.setProperty("STATUSSTR", "Toolsheet initialized");
} // initDAQ

```



```

/**
 * The 'SRQ' method is executed when a device requests service.
 */
int status;
int[] tempData = new int[3]; // a temp array for the reads.
int[] tempData2 = new int[1];
double PSD;
int result;
public void SRQ(KmaxDevice device) {
    count++;
    tlsh.setProperty("STATUSSTR", "SRQ event " + count);
    // report.setProperty("INSERT", "event="+count+"\n");

    int[] statArray = new int[1];

    setMode(2);

    int error = dev.writeInt(30, 9, 26, null, 0, 0); // SCM 301: Set CAMAC Inhibit.

    numEvents ++;
    // This is the actual readout

    error = dev.readInt(slotADC, 11, 2, tempData, 0, 1); // AD 114 ADC:READ DATA.
    error = dev.readInt(slotADC2, 11, 2, tempData2, 0, 1);
    //report.setProperty("INSERT",tempData[0]+"\n");
    error = dev.readInt(0, 0, 1, statArray, 0, 1); // get the status.
    if (statArray[0] != 0 ) { // We had an IO error
        tlsh.setProperty("STATUSSTR", "IO error while reading ADC in SRQ, restart required.");
        return;
    }

    tempData[1]=tempData2[0];

    tempData[2]=(tempData[1]-tempData[0]);

    result = tlsh.addEventRecord(tlsh.PRIMARY_BUFFER, 5, 3, tempData);

    if (result == KmaxToolsheet.BUFFER_FULL) {

        result = tlsh.saveEventBuffer(tlsh.PRIMARY_BUFFER);

        result = tlsh.sortEventBuffer(tlsh.PRIMARY_BUFFER);

        result = tlsh.clearEventBuffer(tlsh.PRIMARY_BUFFER);
        tlsh.addEventRecord(tlsh.PRIMARY_BUFFER, 5, 3, tempData);

        tlsh.setProperty("STATUSSTR", "numEvents = " + numEvents);

        UPDATE_HIST(null);

        report.setProperty("INSERT", "Block read\n");
    }
    else if (result != 0 ) { // We had a buffer error
        tlsh.setProperty("STATUSSTR", "Buffer error while adding event record, restart required.");
        return;
    }

    dev.writeInt(30, 9, 24, null, 0, 0); // SCM 301: Remove CAMAC Inhibit.

} // end SRQ

/**
 * The 'HALT' method is executed when the HALT button is clicked.
 */
public void HALT(KmaxToolsheet toolsheet) {
    tlsh.setProperty("STATUSSTR", "HALT event!");
} // HALT

public void reStart() {
    dev.writeInt (slotADC, 0, 26, null, 0, 0) ; // AD 114 ADC:Enable ADC.
    dev.writeInt (slotADC2, 0, 26, null, 0, 0);
    dev.writeInt(slotADC, 0, 9, null, 0, 0); // AD 114 ADC: Clear module.
    dev.writeInt(slotADC2, 0, 9, null, 0, 0);
    dev.writeInt(30, 9, 24, null, 0, 0); // SCM301: Remove CAMAC Inhibit.
} // reStart

```

```

/**
 * The 'START_STOP' method is executed when the START_STOP button is clicked.
 */
public void START_STOP(KmaxWidget widget) {

    if (isRunning) { // We need to stop the process

        dev.writeInt(30, 9, 26, null, 0, 0); // SCM301: Set CAMAC Inhibit.
        dev.writeInt(28, 9, 26, null, 0, 0); // SCM 301: CAMAC Clear.
        //dev.writeInt(30, 10, 24, null, 0, 0); // SCM 301: Disable BD Output.

        int result = 0;
        if (doSave.getProperty("VALUE").equals("1"))
            result = tlsh.saveEventBuffer(tlsh.PRIMARY_BUFFER);

        if (doSort.getProperty("VALUE").equals("1")) {
            result = tlsh.sortEventBuffer(tlsh.PRIMARY_BUFFER);
            report.setProperty("INSERT", "sortEvents returned - " + result + "\n");
        }
        result = tlsh.clearEventBuffer(tlsh.PRIMARY_BUFFER);

        widget.setProperty("LABEL", "Start");
        isRunning = false;
        tlsh.setProperty("STATUSSTR", "The DAC is stopped. count = " + count);
        return;
    } // The if isRunning scope

    if (isReady) { // Then we can start the DAC
        reStart();
        widget.setProperty("LABEL", "Stop");
        isRunning = true;
        tlsh.setProperty("STATUSSTR", "The DAC is running.");
    }
    else {
        tlsh.showWarning("The system is not initialized. Initialize before starting.");
    }

} // START_STOP

/**
 * The 'CLEAR_REPORT' method is executed when the CLEAR_REPORT button is clicked.
 */
public void CLEAR_REPORT(KmaxWidget widget) {
    report.setProperty("TEXT", "");
} // CLEAR_REPORT

/**
 * The 'CLEAR_HISTS' method is executed when the CLEAR_HISTS button is clicked.
 */
public void CLEAR_HIST(KmaxWidget widget) {
    dataHist.clear();
    dataHist2.clear();
    dataHist2D.clear();
    dataHist2D_i.clear();
    UPDATE_HIST(null);
} // CLEAR_HIST

/**
 * The 'UPDATE_HISTS' method is executed when the UPDATE_HISTS button is clicked.
 */
public void UPDATE_HIST(KmaxWidget widget) {
    dataHist.update();
    dataHist2.update();
    dataHist2D.update();
    dataHist2D_i.update();
} // UPDATE_HISTS

/**
 * The 'GET_PROPS' method is executed when the GET_PROPS button is clicked.
 * It returns all the available properties of the CAMAC system
 */
public void GET_PROPS(KmaxWidget widget) {

```

```

int[] data = new int[1];
int error = 0;

setMode(2);

error = dev.readInt(slotADC, 0, 0, data, 0, 1); // AD 114 ADC:Read Control Register
if (error != 0) {
    t1sh.setProperty("STATUSSTR", "In GET_PROPS:: readInt1, error :: "
+ dev.getErrorMessage(error));
    return;
}
report.setProperty("INSERT", "Control Register = " + data[0] + "\n");

// Get the CAMAC Status
int status = getCAMACStatus();
report.setProperty("INSERT", "CAMAC Status = " + status + "\n");

// Now test the ADC LAM
error = dev.writeInt(slotADC, 0, 8, null, 0, 0); // D 413 ADC: Test LAM.
if (error != 0) {
    t1sh.setProperty("STATUSSTR", "In GET_PROPS:: readInt3, error :: "
+ dev.getErrorMessage(error));
    return;
}
status = getCAMACStatus();
if (status == 0)
    report.setProperty("INSERT", "ADC LAM = True\n");
else
    report.setProperty("INSERT", "ADC LAM = False\n");

} // GET_PROPS

/**
 * The getCAMACStatus method is used to get the last status returned.
 * Status is implemented in the driver as a pseudo register
 */
public int getCAMACStatus() {
    int[] status = new int[1];
    int error = dev.readInt( 0, 0, 1, status, 0, 1); // read the status register
    if (error != 0) {
        t1sh.setProperty("STATUSSTR", "In getCAMACStatus:: readInt, error :: "
+ dev.getErrorMessage(error));
        return -1;
    }
    return status[0];
}

/**
 * The setMode method is used to set the transfer mode in the controller
 * Mode is implemented in the driver as a pseudo register
 */
public void setMode( int mode) {
    int[] modeArray = new int[1];
    modeArray[0] = mode;
    int error = dev.writeInt( 0, 0, 2, modeArray, 0, 1); // read the status register
    if (error != 0) {
        t1sh.setProperty("STATUSSTR", "In setMode:: readInt, error :: "
+ dev.getErrorMessage(error));
    }
}

} // setMode

public void trigger(KmaxWidget widget){

    t1sh.saveEventBuffer(t1sh.PRIMARY_BUFFER);
    t1sh.sortEventBuffer(t1sh.PRIMARY_BUFFER);
    //dataHist.update();
    //dataHist2.update();
    UPDATE_HIST(null);
    t1sh.clearEventBuffer(t1sh.PRIMARY_BUFFER);
    report.setProperty("INSERT", "Update OK\n");
}

```

```

public void resolution(KmaxWidget widget){
    double[] res=new double[1];
    res=dataHist.getRegionFWHM("reg1");
    report.setProperty("INSERT","FWHM of reg1="+res[0)+"\n");
}

public void fileread(KmaxWidget widget) {
    int[] blkinfo = new int[3];
    String lastName = "";
    int totalEvents = 0;
    int i;
    int n=0;

    while (true) {
        n++;
        String fileName = tlsh.getEventFile(tlsh.EV_READ_FILE).getName();
        if ( !fileName.equals(lastName)) {
            report.setProperty("INSERT", "----- "
                + fileName + " -----" + "\n");
            lastName = fileName;
        }

        tlsh.clearEventBuffer(tlsh.PRIMARY_BUFFER);
        int result = tlsh.readNextBlockHeader(blkinfo);

        if (result != tlsh.NO_ERROR) {
            tlsh.setProperty("STATUSSTR", "End of file sequence. result = " + result);
            report.setProperty("INSERT", "This is the end of file!\n");
            break;
        }
        report.setProperty("INSERT", "<< TYPE, SIZE, COUNT >>= "
            + blkinfo[0] + ", " + blkinfo[1] + ", " + blkinfo[2] + "\n" );
        totalEvents += blkinfo[2];

        tlsh.loadEventBuffer(tlsh.PRIMARY_BUFFER);

        tlsh.sortEventBuffer(tlsh.PRIMARY_BUFFER);

        report.setProperty("INSERT", n + " blocks read \t");

    }
    report.setProperty("INSERT", "Total Events = " + totalEvents + "\n" );
    report.setProperty("INSERT", "# of blocks = " + (n-1) + "\n");
    UPDATE_HIST(null);
}

public void project(KmaxWidget widget){
    project1.clear();
    String selectedName = dataHist2D_1.getSelectedRegion();
    if (selectedName == null)
        tlsh.setProperty("STATUSSTR", "No region selected");
    else
        tlsh.setProperty("STATUSSTR", selectedName + " is selected");

    int result = dataHist2D_1.projectRegion(selectedName, "project1", KmaxHist.ALONG_Y);
    if (result != 0) { tlsh.setProperty("STATUSSTR", "error:" + result); return;}
    project1.update();
    int totalnumber=project1.getTotal();

    int total=dataHist2D_1.getRegionSum(selectedName);
    report.setProperty("INSERT",total + "\n");
}

} // End of the runtime object

```

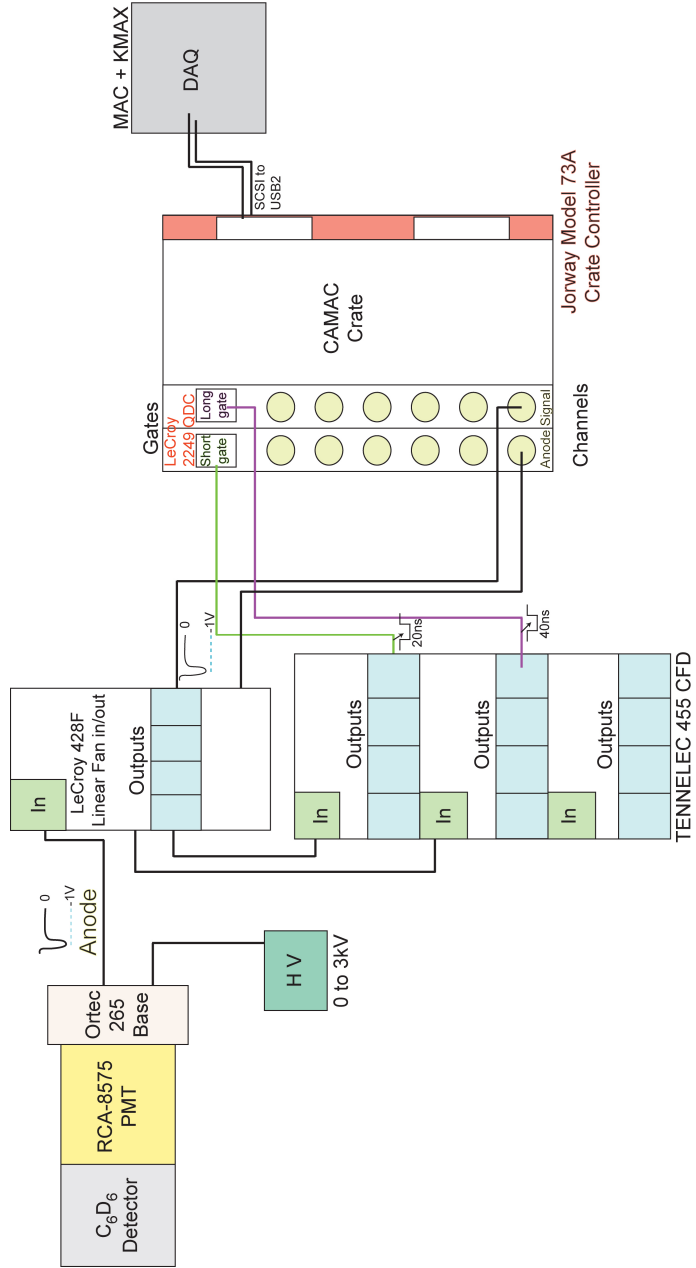


Figure C.8: Neutron detector data acquisition schematic [Mo09].

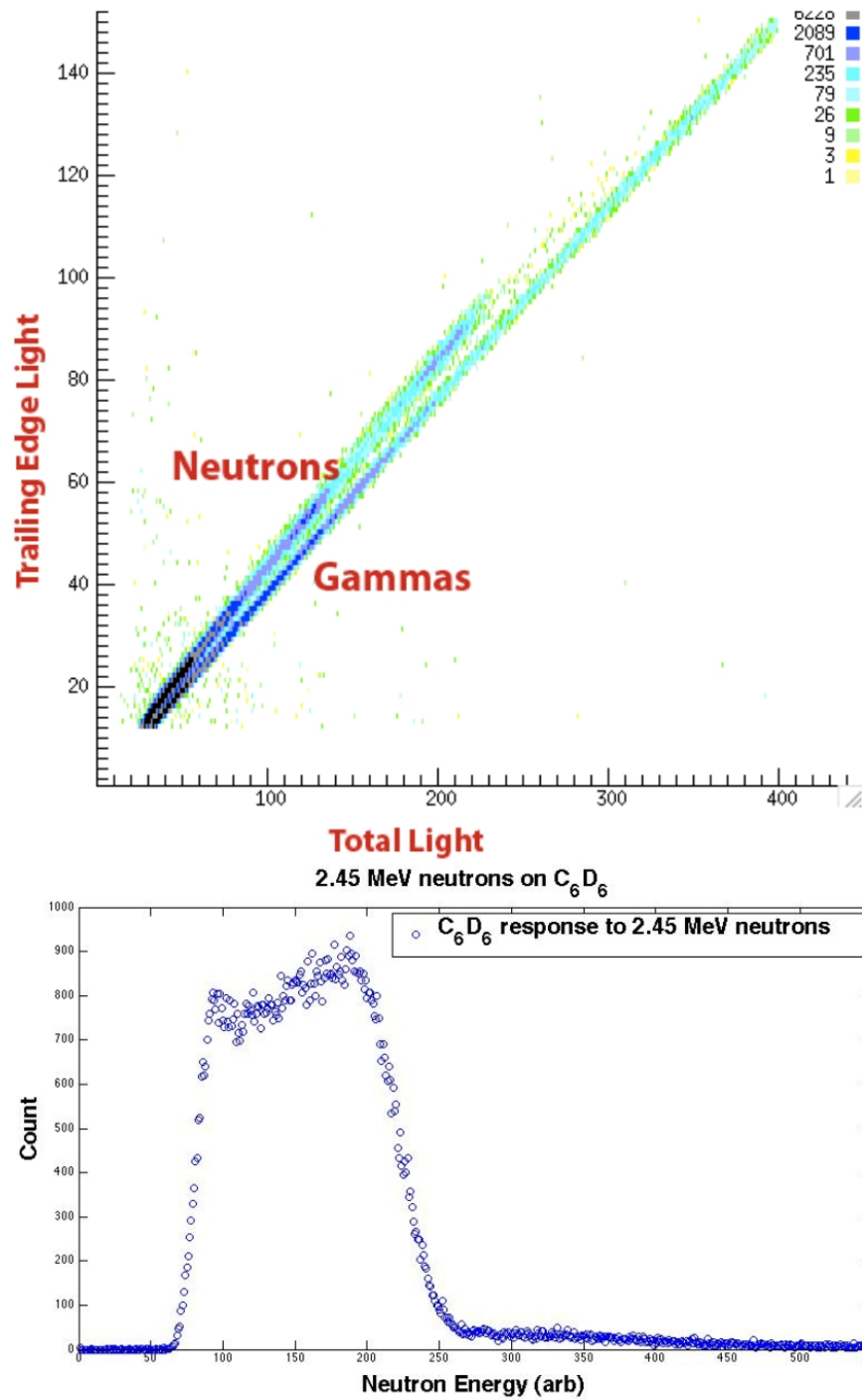


Figure C.9: Top: 2-dimensional histogram obtained using the Kmax DAQ system showing the PSD between neutrons and γ s [Mo09]. Bottom: Projected neutron spectrum after gating on the neutron group in the 2D PSD histogram.

APPENDIX D

Tutorial: KMAX Program for Gamma-gamma Coincidence Experiments

This chapter gives detailed illustration of the design and use of several custom KMAX-based data acquisition and analysis programs developed over two years of gamma-gamma coincident measurements done in conjunction with Prof. H. Griffin (UM Chemistry department). These were developed to provide a better understanding of the KMAX program so it could be modified and used for testing ToF system and analyzing ToF data at UM. The results of γ - γ coincidence of ^{228}Ac are also discussed.

D.1 Several Utilities Developed for γ - γ Coincidence Analysis

D.1.1 Data acquisition software Kmax and its limitations

As discussed in Appendix C Kmax [Sparrow] is a complete environment for CAMAC-based data acquisition and instrument control with advanced features for data management, visualization, and reporting. It is a self-consistent, fully integrated application, inter-operating with native OS's and other compatible application programs. We're using NIM electronics together with CAMAC modules for collecting and transferring data for a set of gamma-gamma coincidence measurement. Kmax supports high-level communications with the CAMAC electronic modules. The latest version of Kmax 8 uses a Java interface to communicate with native drivers for

the CAMAC modules. We designed a corresponding Graphical User Interface (GUI) to show both 1D and 2D gamma-gamma coincidence histograms.

As shown in Figure. C.5, this program can control the start and stop of the data acquisition system and display histograms in both 1D and 2D fashion. The high-speed CAMAC controller CMC100 [CMC100] has a built-in buffer for fast reading and the data reading process is processed only when the built-in buffer is full. The program registers corresponding pulse height information for every gamma-gamma coincidence from 2 different channels of the CAMAC ADC together with a readout from the ADC corresponding to input from a NIM time to amplitude converter (TAC). When the CMC100's buffer is full, Kmax reads a series of energy from two different detectors together with time information. Then these data are sent into the histogram and recorded on disk files in binary format.

We are able to use Kmax's gating facility to generate gates manually on 2D histogram and then project data onto one specific axis e.g. energy. However if we have several hundred gamma gates, this manual process becomes very tedious. So we developed a program that can automatically generate corresponding projections based on an input gate file. Kmax also is able to read the previous saved binary data file and regenerate histograms in GUI. However when the data file is very big, the reading process can be very time-consuming.

Although Kmax is a good DAQ program, with all the above limitations for data gating and analysis, we decided to develop another set of data transfer and analysis tools.

D.1.2 Binary data compressing program - Compact

Since there is one extra byte not being used in the original Kmax binary data file, and we also want to do some preliminary operations on the binary file, we first developed a program ‘Compact’ to further compress the binary data and remove spurious unwanted information.

Originally Kmax records every number in 4 bytes as default, but since we only need 2 bytes for each number in our case, we can compress the binary data by throwing away unused bytes but in some cases, the Ortec 811 CAMAC ADC could generate numbers bigger than 2048, out of our interested channel range. We would like to set a gate on both energy channels and time channels to remove such events.

Sometime due to electronic deviation coming from temperature change or noise, the energy signal from the ADC can shift slightly, and we would like to remove this shift in our final data. One method is feeding a precision pulser signal into the ADC and watch the deviation event-by-event then later correct it when compressing the binary data. To do this we built a automatical shifting mechanism based on the pulser output in an custom analysis program.

This program saved substantial disk space for storing data from the original Kmax data files. For example, a typical Kmax data file usually takes 600 Mbytes, after compressing using Compact, the new compressed binary file takes less than 150 Mbytes in size.

The use of ‘Compact’ is as follows:

```
compact [event file]
```

The original version of ‘Compact’ is a console program and the user has to type in the required information via prompts. This could get very tedious when processing a

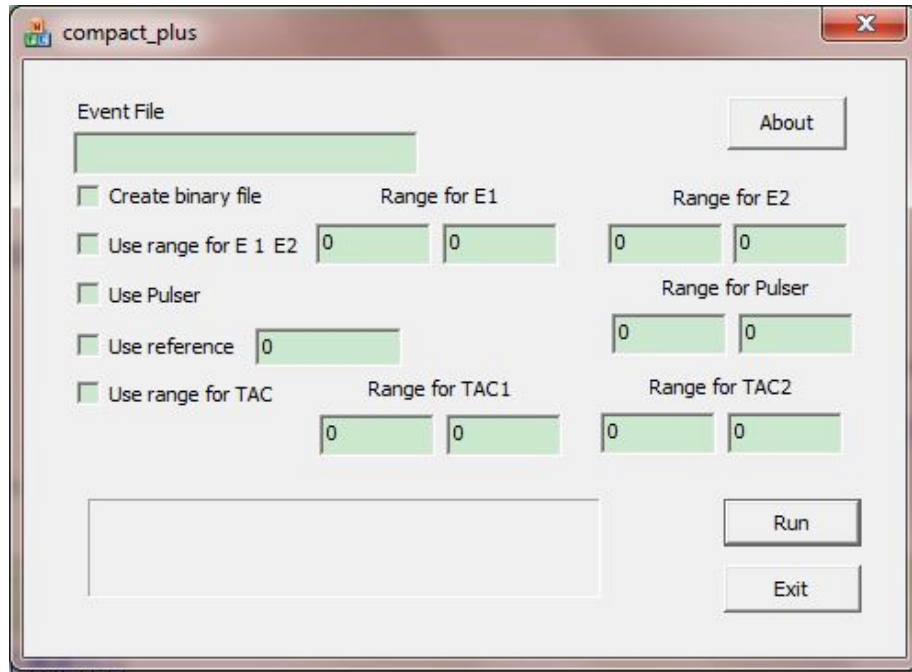


Figure D.1: Program Layout of Compact plus

lot of files. Later we developed a GUI version called ‘Compact Plus’ and it can easily input and change numbers graphically. As shown in Figure. D.1, the user can easily define the gates on either of the energy signals and determine if to use the pulser information to fix the random ADC shifts. The progress bar on the bottom of the user interface is very convenient for showing the progress of the data compression.

D.1.3 2D-array generating program - Transfer

The first set of the analysis codes are all written based on use of the compressed binary data file. We found the analysis programs getting slower and slower with more and more gates applied, sometimes taking hours to finish analyzing one set of gates. Hence we decided to generate a 2 dimensional 2048×2048 array to store energy information and develop new analysis code. This 2D array is also stored in compressed binary mode. The typical file size for this 2D array file is about 8 Mbytes. Using this new variation of the analysis code, one can finish the same analysis process

in seconds instead of hours.

The usage of ‘Transfer’ program is as follows:

```
transfer [compressed binary file] [output 2D array file]
```

D.1.4 Program for histogram projection - Projection

One useful tool we developed is called ‘Projection’. This code can read an ascii text file for a set of gates. The typical gates file looks like this:

```
1,30,100,300
```

```
2,60,300,500
```

Each line is a gate definition. The first parameter specifies which histogram the gate is applied on (can be either 1 or 2). The second parameter is a notation for the energy which also serves as the name for projection result file. The third and fourth parameter is the definition of begin the and end of the gate spectrum.

The use of this program is as follows:

```
projection [compressed binary file] [gates definition file]
```

After running Projection, in the above example, 2 files named as ‘1_30.tka’ and ‘2_60.tka’ are created which are projected histograms according to these two gates. Every projected histogram file is named by the histogram gate applied on it and the energy of the gate.

The original version of Projection works with compressed binary data file. We also have developed a new version working with the 2D array data file. The new version runs faster.

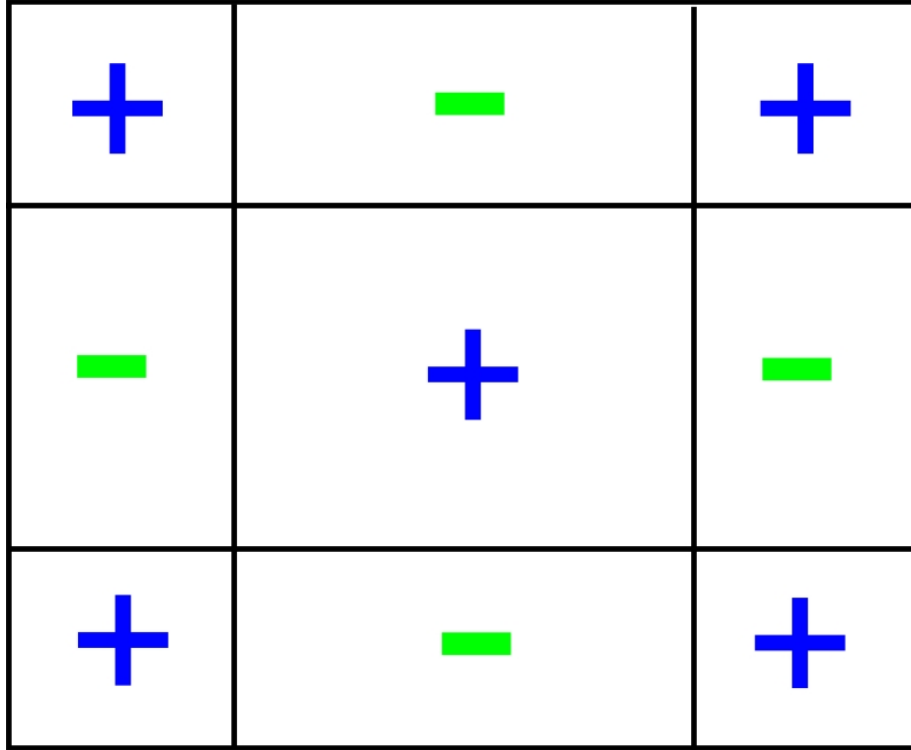


Figure D.2: Scheme of the program Analyze is using to get the net and the error.

D.1.5 Calculation of coincidence intensity - Analyze

One major program for our coincidence analysis we created is ‘Analyze’, it reads two separate gates files with energy peaks and background information from both detectors, then calculates the corresponding net sum and its error for every coincident peak. Then we can use this intensity to compare with theoretical predictions.

The format of a typical gate file for Analyze consists of the definition of peak region and the background region. Each line in the gate file is as follows:

```
peak energy, maximum channel for peak, minimum channel for peak,
maximum channel for background 1, minimum channel for background 1,
maximum channel for background 2, minimum channel for background 2
```

With two peaks in coincidence, we can define both a ‘+’ zone and a ‘-’ zone. If a number falls in peak zones or background zones of both energies, we call it in the

‘+’ zone. If it falls in one peak zone and one background zone, we assign it in the ‘-’ zone. These ‘+’ and ‘-’ zones are shown in Figure. D.2. Then the net and its error are defined as following for each coincidence:

$$(D.1) \quad net = plus - minus$$

$$(D.2) \quad error = \sqrt{plus + minus}$$

The net (after corrected for chance coincidence) is the intensities for the coincidence peaks. After running this program, two files ‘net.txt’ and ‘error.txt’ are created. The format for running ‘Analyze’ is as follows:

```
analyze [compressed binary file] [gates file of E1] [gates file of E2]
```

The original version of Analyze reads the compressed binary data file, then determine event-by-event whether the number falls in one of the peak coincidence’s ‘+’ or ‘-’ zone. This process involves much looping and file reading operations hence makes the program run slow especially when we have many gates set in both spectra. In some cases, one calculation can last several hours. With the new version of ‘Analyze’ utilizing the 2D 2048×2048 array, we can read all data at once and calculate net and error directly without doing it event-by-event. It’s much faster and can finish the same job in seconds instead of hours.

D.1.6 Matlab subroutine - Readnet

To easily compare calculated net and theoretical predictions, we also developed a subroutine called ‘Readnet’. Using this subroutine, we read net.txt, error.txt files and predictions generated by a separate program [TKA] into Matlab. Then, intensities

are sorted together with corresponding gates and peak energies. After that, this subroutine searches predicted values corresponding closest to the observed coincidence peak energies in the prediction file. The output file format is:

```
net, error, 1st gate number, 2nd gate number, E1, E2, prediction
```

With this output, we can easily compare predictions and measured energies and intensities for any specific coincidence.

D.2 Data Analysis and Results

With the help of above programs, the data of ^{228}Th nuclear states fed in ^{228}Ac decay were analyzed. A set of ^{228}Ac coincidence data were taken through a 10-day period using Kmax DAQ system. The corresponding data event file was then sorted out using ‘Compat+’ into a compact binary format file. A 2048×2048 2-dimensional array was constructed using the program ‘Transfer’ and then analyzed by program ‘Projection’ and ‘Analyze’. The ‘Projection’ created projected histogram from gates either on E1 and E2 (Figure D.3 and D.4). And the ‘Analyze’ calculated the ‘net’ and ‘error’ for corresponding coincidence peak for later comparison with theoretical predictions.

One of the challenges for accurately calculating the coincidence intensities is determining the chance coincidence rates. Since the chance coincidence only depends on the intensity of the source, its rate can be determined by setting a gate on a region in the histogram where there is definitely no strong coincidence present. We did this by setting a gate on the first channel of the histogram. Figure D.3 shows the chance coincidence histogram obtained by gating on the first channel of E1. In this histogram, one prominent chance-coincidence peak is 911 keV peak, which only coincidence with itself. By using this peak as a reference, we could deduce the ra-

tio of chance-coincidence correction in the ‘net’ obtained by ‘Analyze’ program for comparison with predictions. For example, for correction of (209 keV, 129 keV) coincidence, we took a look at the E1 histogram gated by E2 at 129 keV peak (Figure D.4). The 911 keV peak is beside a strong 903 keV coincidence peak but resolved due to superior energy resolution of HPGe detectors. The intensity of this peak was measured and compared with the intensity of 911 keV peak measured in the E1 chance coincidence spectrum. The ratio of two intensities was used for the correction of the ‘net’. The same method was then applied on E2 chance coincidence to get another ratio for E2. Through this process, the final ‘net’ can be written as

$$(D.3) \quad Net_{corrected} = (Net - r1 \times sum1 - r \times sum2) \times P_{eff}$$

$r1$ and $r2$ are the corresponding intensities ratios for E1 and E2. $sum1$ and $sum2$ are the sum of corresponding gates in both E1 and E2 chance-coincidence histograms. P_{eff} is the detection efficiency. $Net_{corrected}$ is the corrected ‘net’ as the result for comparing with theoretical predictions [TKA]. For example, for the above (209 keV, 129 keV) coincidence, the total ‘net’ after chance coincidence correction is 8553 counts where theoretical prediction gives 8087 counts. However in some cases, since the ^{228}Ac we used was a mixed source, and the predictions were derived based on a single source, some results were reasonably off the predictions, but a new set of predictions with considerations of relative abundance of mixed source will be calculated and used in the future research.

A list of the most recent report for coincidence relationships [Dal87] for ^{228}Ac are shown in Figure D.5. However it does not agree with the accepted decay scheme. For example the 328.0 keV and 270.2 keV γ rays deexcite the same level and should have exactly the same coincidences. Similarly the intensities of 338.3 keV γ peak

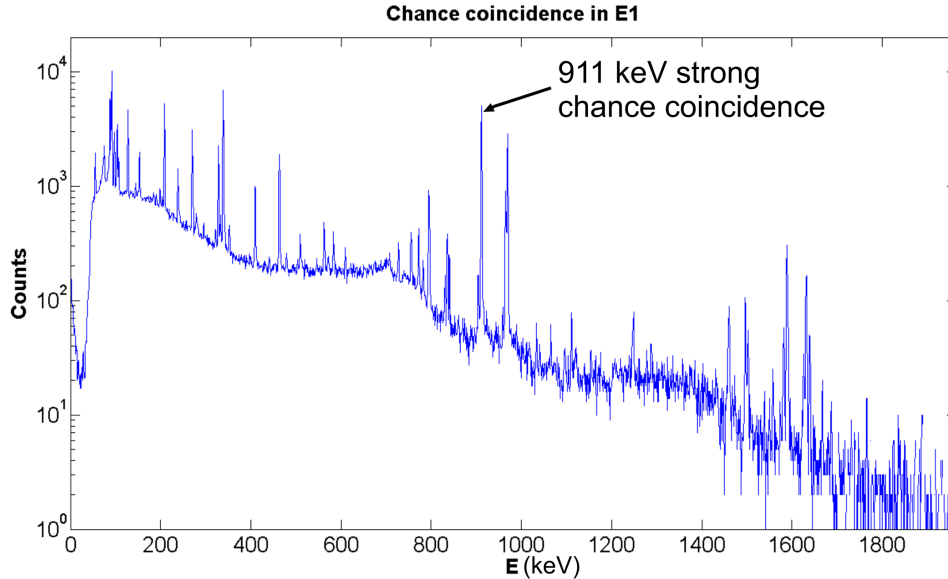


Figure D.3: The chance coincidence of E1 obtained by gating on the first channel of E1 histogram using the program ‘Projection’.

and 209.3 keV γ peak should be the same. The table from [Dal87], which doesn’t show these similarities, must not be right. So we decided to use our system to investigate. We went through these previous measured coincidence relationships. Not only our measurements can confirm their correct relationships, but also we could see coincidence beyond their range. For coincidence with gate 129 keV, we get the same spectrum as [Dal87] but with more coverage in ranges. We are able to see coincidence until 1872 keV while the previous measurements only went up to 1573.4 keV. At low energies, our measurements went less than previous lowest energy (141 keV) and included K and L x-rays. As expected, our measurements correctly show the same intensity for γ rays of 328 keV, 270 keV couple and 338 keV, 209 keV couple.

D.3 Code Lists

D.3.1 Compact code

```
// compact_plusDlg.cpp : implementation file
//
```

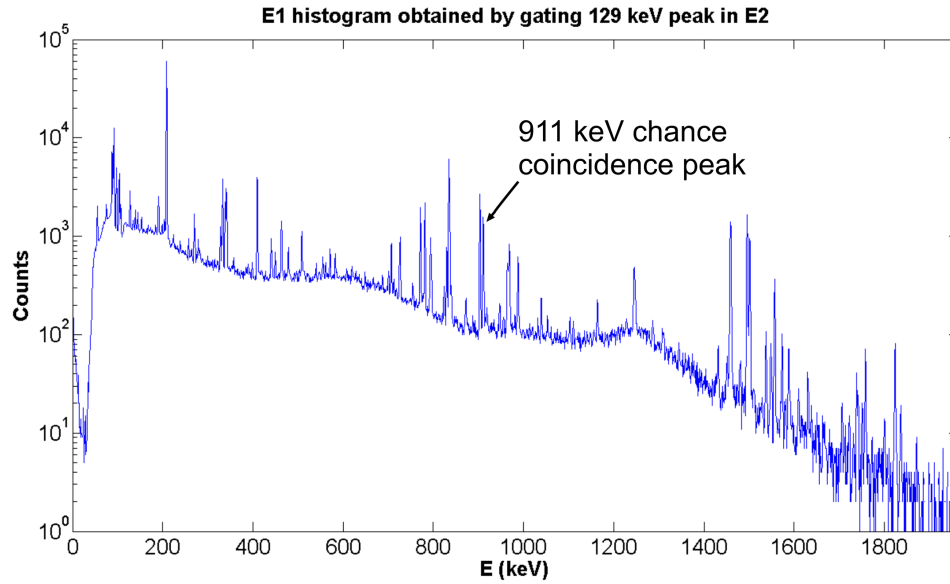



Figure D.4: The E1 histogram obtained by gating a 129 keV peak on E2 using the program ‘Projection’.

```
#include "stdafx.h"
#include "compact_plus.h"
#include "compact_plusDlg.h"

short swapbit(short x);

#ifdef _DEBUG
#define new DEBUG_NEW
#endif

// CAboutDlg dialog used for App About

class CAboutDlg : public CDialog
{
public:
    CAboutDlg();

    // Dialog Data
    enum { IDD = IDD_ABOUTBOX };

protected:
    virtual void DoDataExchange(CDataExchange* pDX);    // DDX/DDV support

    // Implementation
protected:
    DECLARE_MESSAGE_MAP()
};

CAboutDlg::CAboutDlg() : CDialog(CAboutDlg::IDD)
{
}

void CAboutDlg::DoDataExchange(CDataExchange* pDX)
{
    CDialog::DoDataExchange(pDX);
}

```

Gate (keV)	Coincident transitions (keV)
99+3	263.6, 341.0, 409.4, 463.0, 835.7, 911.2, 964.8, 969.0, 1245.0, 1374.2
129±4	141.0, 145.8, 191.3, 209.2, 332.4, 341.0, 357.0, 409.4, 440.4, 449.2, 463.0, 478.3, 509.0, 555.1, 562.5, 572.3, 583.4, 688.1, 701.7, 707.4, 726.9, 772.3, 782.1, 792.8*, 830.5, 835.7, 873.2, 904.2, 919.0, 987.7, 988.6, 1039.6, 1245.0, 1247.04, 1430.9, 1459.1, 1495.8, 1501.6, 1537.9, 1548.6, 1557.0, 1573.4
209±4	281.9, 321.6, 503.8, 520.2, 523.1, 546.5, 610.6, 616.3, 640.4, 651.4, 794.9, 840.3
270±4	129.1, 278.9, 478.3, 572.3, 620.4, 663.8, 726.9, 772.3, 830.5, 901.2, 947.9, 1019.9, 1247.0, 1249.7, 1287.7
328±3	321.6, 503.8, 546.5, 616.3, 640.4, 794.9, 840.3
338±3	478.3, 572.3, 620.4, 726.9, 772.3, 830.5, 947.9, 1247.0, 1249.7, 1287.5
772±4	129.1, 209.2, 263.6, 281.9, 321.6, 338.3
911±7	77.3, 99.5, 129.1, 154.0, 184.5, 199.4, 341.0, 378.0, 440.4, 463.0, 555.1, 562.5, 570.9, 674.6, 677.1, 755.3, 791.5, 853.2, 919.0, 976.0, 1040.9

Figure D.5: Summary of γ - γ coincidence relationships. An asterisk denotes only seen in coincidence experiments [Dal87].

```

BEGIN_MESSAGE_MAP(CAboutDlg, CDialog)
END_MESSAGE_MAP()

// Ccompact_plusDlg dialog

Ccompact_plusDlg::Ccompact_plusDlg(CWnd* pParent /*=NULL*/)
: CDialog(Ccompact_plusDlg::IDD, pParent)
, m_FileName(_T(""))
, m_CreateBinary(FALSE)
, m_UseRange(FALSE)
, m_UsePulser(FALSE)
, m_UseTac(FALSE)
, m_UseReference(FALSE)
, m_E1min(0)
, m_E1max(0)
, m_E2min(0)
, m_E2max(0)
, m_Reference(0)
, m_PulserMin(0)
, m_PulserMax(0)
, m_tac1Min(0)

```

```

, m_tac1Max(0)
, m_tac2Min(0)
, m_tac2Max(0)
{
m_hIcon = AfxGetApp()->LoadIcon(IDR_MAINFRAME);
}

void Ccompact_plusDlg::DoDataExchange(CDataExchange* pDX)
{
CDialog::DoDataExchange(pDX);
DDX_Text(pDX, IDC_FILENAME, m_FileName);
DDX_Check(pDX, IDC_BIN, m_CreateBinary);
DDX_Check(pDX, IDC_USERANGE, m_UseRange);
DDX_Check(pDX, IDC_USEPULSE, m_UsePulser);
DDX_Check(pDX, IDC_USETAC, m_UseTac);
DDX_Check(pDX, IDC_USEREFERENCE, m_UseReference);
DDX_Text(pDX, IDC_E1MIN, m_E1min);
DDX_Text(pDX, IDC_E1MAX, m_E1max);
DDX_Text(pDX, IDC_E2MIN, m_E2min);
DDX_Text(pDX, IDC_E2MAX, m_E2max);
DDX_Text(pDX, IDC_REFERENCE, m_Reference);
DDX_Text(pDX, IDC_PULSEMIN, m_PulserMin);
DDX_Text(pDX, IDC_PULSEMAX, m_PulserMax);
DDX_Text(pDX, IDC_TAC1MIN, m_tac1Min);
DDX_Text(pDX, IDC_TAC1MAX, m_tac1Max);
DDX_Text(pDX, IDC_TAC2MIN, m_tac2Min);
DDX_Text(pDX, IDC_TAC2MAX, m_tac2Max);
DDX_Control(pDX, IDC_BIN, m_CheckBoxBin);
DDX_Control(pDX, IDC_PROGRESS, m_progress);
DDX_Control(pDX, IDC_USERANGE, m_CheckBoxRange);
DDX_Control(pDX, IDC_USEPULSE, m_CheckBoxPulse);
DDX_Control(pDX, IDC_USEREFERENCE, m_CheckBoxReference);
DDX_Control(pDX, IDC_USETAC, m_CheckBoxTac);
}

BEGIN_MESSAGE_MAP(Ccompact_plusDlg, CDialog)
ON_WM_SYSCOMMAND()
ON_WM_PAINT()
ON_WM_QUERYDRAGICON()
//}}AFX_MSG_MAP
ON_BN_CLICKED(IDCANCEL, &Ccompact_plusDlg::OnBnClickedCancel)
ON_BN_CLICKED(IDOK, &Ccompact_plusDlg::OnBnClickedOk)
ON_BN_CLICKED(IDC_BIN, &Ccompact_plusDlg::OnBnClickedBin)
ON_NOTIFY(NM_CUSTOMDRAW, IDC_PROGRESS, &Ccompact_plusDlg::OnNMCustodrawProgress)
ON_BN_CLICKED(IDC_ABOUT, &Ccompact_plusDlg::OnBnClickedAbout)
END_MESSAGE_MAP()

// Ccompact_plusDlg message handlers

BOOL Ccompact_plusDlg::OnInitDialog()
{
CDialog::OnInitDialog();

// Add "About..." menu item to system menu.

// IDM_ABOUTBOX must be in the system command range.
ASSERT((IDM_ABOUTBOX & 0xFFF0) == IDM_ABOUTBOX);
ASSERT(IDM_ABOUTBOX < 0xF000);

CMenu* pSysMenu = GetSystemMenu(FALSE);
if (pSysMenu != NULL)
{
CString strAboutMenu;
strAboutMenu.LoadString(IDS_ABOUTBOX);
if (!strAboutMenu.IsEmpty())
{
pSysMenu->AppendMenu(MF_SEPARATOR);
pSysMenu->AppendMenu(MF_STRING, IDM_ABOUTBOX, strAboutMenu);
}
}

// Set the icon for this dialog. The framework does this automatically
// when the application's main window is not a dialog
SetIcon(m_hIcon, TRUE); // Set big icon
SetIcon(m_hIcon, FALSE); // Set small icon

// TODO: Add extra initialization here

return TRUE; // return TRUE unless you set the focus to a control

```

```

}

void Ccompact_plusDlg::OnSysCommand(UINT nID, LPARAM lParam)
{
if ((nID & 0xFFFF) == IDM_ABOUTBOX)
{
CAboutDlg dlgAbout;
dlgAbout.DoModal();
}
else
{
CDialog::OnSysCommand(nID, lParam);
}
}

// If you add a minimize button to your dialog, you will need the code below
// to draw the icon. For MFC applications using the document/view model,
// this is automatically done for you by the framework.

void Ccompact_plusDlg::OnPaint()
{
if (IsIconic())
{
CPaintDC dc(this); // device context for painting

SendMessage(WM_ICONERASEBKGD, reinterpret_cast<WPARAM>(dc.GetSafeHdc()), 0);

// Center icon in client rectangle
int cxIcon = GetSystemMetrics(SM_CXICON);
int cyIcon = GetSystemMetrics(SM_CYICON);
CRect rect;
GetClientRect(&rect);
int x = (rect.Width() - cxIcon + 1) / 2;
int y = (rect.Height() - cyIcon + 1) / 2;

// Draw the icon
dc.DrawIcon(x, y, m_hIcon);
}
else
{
CDialog::OnPaint();
}
}

// The system calls this function to obtain the cursor to display while the user drags
// the minimized window.
HCURSOR Ccompact_plusDlg::OnQueryDragIcon()
{
return static_cast<HCURSOR>(m_hIcon);
}

void Ccompact_plusDlg::OnBnClickedCheck1()
{
// TODO: Add your control notification handler code here
}

void Ccompact_plusDlg::OnEnChangeEdit1()
{
// TODO: If this is a RICHEDIT control, the control will not
// send this notification unless you override the CDialog::OnInitDialog()
// function and call CRichEditCtrl().SetEventMask()
// with the ENM_CHANGE flag ORed into the mask.

// TODO: Add your control notification handler code here
}

void Ccompact_plusDlg::OnBnClickedCancel()
{
// TODO: Add your control notification handler code here
OnCancel();
}

short swapbit(short x)
{
short temp1=(x>>8)&0x00ff;
short temp2=x<<8;
return temp1+temp2;
}

```

```

#define WRITEDATA ++histE1[E1];++histE2[E2];++histPulse[pulse];++histTAC[TAC];if (useBinary==1){myfile2.write(reinterpret_cast<char *>(p

void Ccompact_plusDlg::OnBnClickedOk()
{
// TODO: Add your control notification handler code here
//OnOK();
//int nIndex;
//CString par;
//int E1min,E1max,E1min,E2max,pulseMin,pulseMax,reference,tac1Min,tac1Max,tac2Min,tac2Max;
//bool bin,range,pulse,tac,useReference;
//nIndex = GetDlgItemText(IDC_FILENAME, par);
CString output;
int useBinary = m_CheckBoxBin.GetCheck();
int useRange = m_CheckBoxRange.GetCheck();
//output.Format("%d",useRange);
//MessageBox(output);
int usePulse = m_CheckBoxPulse.GetCheck();
int useReference = m_CheckBoxReference.GetCheck();
int useTac=m_CheckBoxTac.GetCheck();
//output.Format("%d",useRange);
//MessageBox(output);
int nIndex;
CString fileName;

int E1min,E1max,E2min,E2max,pulseMin,pulseMax,reference,tac1min,tac1max,tac2min,tac2max;
nIndex = GetDlgItemText(IDC_FILENAME,fileName);

GetDlgItemText(IDC_E1MIN,output);
E1min=atoi(output)-1;
GetDlgItemText(IDC_E1MAX,output);
E1max=atoi(output)-1;
GetDlgItemText(IDC_E2MIN,output);
E2min=atoi(output)-1;
GetDlgItemText(IDC_E2MAX,output);
E2max=atoi(output)-1;
GetDlgItemText(IDC_PULSEMIN,output);
pulseMin=atoi(output)-1;
GetDlgItemText(IDC_PULSEMAX,output);
pulseMax=atoi(output)-1;
GetDlgItemText(IDC_REFERENCE,output);
reference=atoi(output)-1;
GetDlgItemText(IDC_TAC1MIN,output);
tac1min=atoi(output)-1;
GetDlgItemText(IDC_TAC1MAX,output);
tac1max=atoi(output)-1;
GetDlgItemText(IDC_TAC2MIN,output);
tac2min=atoi(output)-1;
GetDlgItemText(IDC_TAC2MAX,output);
tac2max=atoi(output)-1;

//output.Format("%d",E1min);
//MessageBox(output);

m_progress.SetStep(1);

//MessageBox(fileName);

//strBinaryVal.Format("The Check Box Value is : %d",val);
//MessageBox(strBinaryVal);

class Data{
public:
unsigned int E1;
unsigned int E2;
unsigned int TAC;
unsigned int pulse;
unsigned int zero;
};

unsigned int histE1[2048];
unsigned int histE2[2048];
unsigned long histPulse[2048];
unsigned int histTAC[2048];

for(int j=0;j<2048;++j)
{
histE1[j]=0;
histE2[j]=0;
histPulse[j]=0;
}

```

```

histTAC[j]=0;
}

int length;

Data *y = new Data[52429];
char *x = new char[16];

ifstream myfile (fileName,ios::binary);
//ofstream myfile2;
//output.Format("The Check Box Value is : %d",myfile.is_open());
//MessageBox(output);
//if (useBinary==1){
CString outputName=fileName.Left(fileName.Find('.')+".bin";
ofstream myfile2(outputName, ios::out|ios::binary);
//}

if (myfile.is_open())
{
myfile.seekg (0, ios::end);
length = myfile.tellg();
//output.Format("The Check Box Value is : %d",length);
//MessageBox(output);

myfile.seekg (0, ios::beg);

myfile.seekg(513);

int total_block=length/(sizeof(Data)*52429);
//output.Format("The Check Box Value is : %d",total_block);
//MessageBox(output);

m_progress.SetRange(0,total_block);

int block=0;
int pos=myfile.tellg();
int progress=0;

//m_progress.SetPos(50);

//MessageBox("test");

while (! myfile.eof())
{
progress=pos/length;
m_progress.SetPos(block);
//UpdateData();
++block;
myfile.seekg(8,ios::cur);
pos=myfile.tellg();

if ((length-pos)<100) break;
myfile.read((char*)y,sizeof(Data)*52429);
for (int i=0;i<52429;i++){

int E1=swapbit(((y+i)->E1>>8));
int E2=swapbit(((y+i)->E2>>8));
int TAC=swapbit(((y+i)->TAC>>8));
int pulse=swapbit(((y+i)->pulse>>8));

if (E1>2047) E1=2047;
if (E2>2047) E2=2047;
if (TAC>2047) TAC=2047;
if (pulse>2047) pulse=2047;

if (useReference==1){
E1=E1-(pulse-reference);
E2=E2-(pulse-reference);
TAC=TAC-(pulse-reference);
}

int* p1=&E1;
int* p2=&E2;
int* p3=&TAC;;

//++histPulse[pulse];
//++histTAC[TAC];
if (usePulse==1 && pulse>=pulseMin && pulse<=pulseMax){

```

```

if (useRange==1 && E1>=E1min && E1<=E1max && E2>=E2min && E2<=E2max){
if (useTac==1 && ((TAC>=tac1min && TAC<=tac1max) || (TAC>=tac2min && TAC<=tac2max)) )
{
WRITEDATA
}
else if (useTac==0){WRITEDATA}
}
else if (useRange==0){
if (useTac==1 && ((TAC>=tac1min && TAC<=tac1max) || (TAC>=tac2min && TAC<=tac2max)) )
{
WRITEDATA
}
else if (useTac==0){WRITEDATA}
}
}
else if (usePulse==0) {
if (useRange==1 && E1>=E1min && E1<=E1max && E2>=E2min && E2<=E2max){
if (useTac==1 && ((TAC>=tac1min && TAC<=tac1max) || (TAC>=tac2min && TAC<=tac2max)) )
{
WRITEDATA
}
else if (useTac==0){WRITEDATA}
}
else if (useRange==0){
if (useTac==1 && ((TAC>=tac1min && TAC<=tac1max) || (TAC>=tac2min && TAC<=tac2max)) )
{
WRITEDATA
}
else if (useTac==0){WRITEDATA}
}
}
}
}

CString E1_name="E1"+fileName.Left(fileName.Find('.')+".tka";
CString E2_name="E2"+fileName.Left(fileName.Find('.')+".tka";
histE1[0]=1000;
histE1[1]=1010;
histE2[0]=1000;
histE2[1]=1010;

myfile.close();
myfile2.close();

ofstream E1File(E1_name);
ofstream E2File(E2_name);
ofstream PulseFile("pulse.txt");
ofstream TacFile("tac.txt");
for (int i=0;i<2048;i++)
{
E1File<<histE1[i]<<"\n";
E2File<<histE2[i]<<"\n";
PulseFile<<histPulse[i]<<endl;
TacFile<<histTAC[i]<<endl;
}

MessageBox("Finish");
}
else
MessageBox("Event file not open!");
}

void Ccompact_plusDlg::OnBnClickedBin()
{
// TODO: Add your control notification handler code here
//CString strBinaryVal;

//int val = m_CheckBoxBin.GetCheck();

//strBinaryVal.Format("The Check Box Value is : %d",val);

//MessageBox(strBinaryVal);
}

void Ccompact_plusDlg::OnNMCustomdrawProgress(NMHDR *pNMHDR, LRESULT *pResult)
{
LPNMCUSTOMDRAW pNMCD = reinterpret_cast<LPNMCUSTOMDRAW>(pNMHDR);
// TODO: Add your control notification handler code here
*pResult = 0;
}

```

```

}

void Ccompact_plusDlg::OnBnClickedAbout()
{
// TODO: Add your control notification handler code here
CAboutDlg dlgAbout;
dlgAbout.DoModal();
}

```

D.3.2 Transfer code

```

#include <iostream>
#include <vector>
#include <fstream>
#include <string>
#include "console.h"
using namespace std;

namespace con = JadedHoboConsole;

int main (int argc, char *argv[]) {
// cout<<"test";

int length;
class Data{
public:
unsigned short E1;
unsigned short E2;
unsigned short TAC;
};

Data *y = new Data[1];

if (!argv[1])
{
cout<<con::fg_green<<"\t\tKmax 8.x binary output file projection program v0.1 \n"
<<"\t\t\tCopyright <c> 2007 \n"
<<"\t\tHao Jiang , Henry Griffin\tDec.2007\n"
<<"\n"
<<con::fg_white<<"Usage: projection [file] [gates] \n";
exit(1);
}

vector<vector<int>> > hist ( 2048, vector<int> ( 2048 ) );

ifstream myfile (argv[1],ios::binary);
string filename=argv[2];
ofstream outfile (filename.c_str(), ios::out|ios::binary|ios::app);

if (myfile.is_open())
{
int n=0;
myfile.seekg (0, ios::end);
length = myfile.tellg();
cout<<"File length="<<length<<endl<<endl;
myfile.seekg (0, ios::beg);
while (! myfile.eof())
{
++n;
myfile.read((char*)y,sizeof(Data));
short E_1=y->E1,E_2=y->E2;
++hist[E_1][E_2];
}
}

for (int i=0;i<2048;i++) {
for (int j=0;j<2048;++j){
int* temp=&hist[i][j];
outfile.write(reinterpret_cast<char *>(temp),2);
}
}
return 0;
}

```



```
}

```

D.3.3 Projection code

```
#include <iostream>
#include <fstream>
#include <string>
#include <bitset>
#include <algorithm>
#include <vector>
#include <math.h>
#include <sstream>
#include "console.h"
using namespace std;

namespace con = JadedHoboConsole;
string int2string(int i);

void Tokenize(const string& str,
              vector<string>& tokens,
              const string& delimiters = " ");

struct Energy{
int spectrum,E,Emin,Emax;
};

int main (int argc, char *argv[]) {
int length;

unsigned short* y=new unsigned short;

;vector<int> Ehist(2048);

int histE[100][2048];

if (!argv[1])
{
cout<<con::fg_green<<"\t\tKmax 8.x binary output file projection program v0.1 \n"
<<"\t\t\tCopyright <c> 2007 \n"
<<"\t\tHao Jiang , Henry Griffin\tDec.2007\n"
<<"\n"
<<con::fg_white<<"Usage: projection [file] [gates] \n";
exit(1);
}

ifstream myfile (argv[1],ios::binary);

vector<Energy> E;

if (argv[2]) {

ifstream eventfile(argv[2]);

if (eventfile.is_open())
{
while (!eventfile.eof())
{

vector<string> vecString;
vecString.clear();
string temp;
getline(eventfile,temp);
Tokenize(temp, vecString, ",");

Energy E_temp;

E_temp.spectrum=atoi(vecString[0].c_str());
E_temp.E=atoi(vecString[1].c_str());
E_temp.Emin=atoi(vecString[2].c_str())-1;
E_temp.Emax=atoi(vecString[3].c_str())-1;

E.push_back(E_temp);

}
}
}

```

```

vector<vector<int>> hist ( 2048, vector<int> ( 2048 ) );
    if (myfile.is_open())
    {
myfile.seekg (0, ios::end);
length = myfile.tellg();
cout<<"File length="<<length<<endl<<endl;
myfile.seekg (0, ios::beg);
for (int i=0;i<2048;i++) {
for (int j=0;j<2048;j++)
{
    myfile.read((char*)y,2);
hist[i][j]=*y;
}
}
}

for (int i=0;i<E.size();i++)
{
if (E[i].spectrum==1)
{
for (int k=E[i].Emin;k<=E[i].Emax;k++)
{
for (int m=0;m<2048;m++)
{
histE[i][m]+=hist[k][m];
}
}
}
if (E[i].spectrum==2)
{
for (int k=E[i].Emin;k<=E[i].Emax;k++)
{
for (int m=0;m<2048;m++)
{
histE[i][m]+=hist[m][k];
}
}
}
}

for (int i=0;i<E.size();++i) {
string f=int2string(E[i].spectrum)+"_"+int2string(E[i].E)+"_tka";
ofstream outfile(f.c_str());
if (E[i].spectrum==1)
for (int j=0;j<2048;++j)
outfile<<histE[i][j]<<endl;
if (E[i].spectrum==2)
for (int j=0;j<2048;++j)
outfile<<histE[i][j]<<endl;
}

return 0;
}

void Tokenize(const string& str,
vector<string>& tokens,
const string& delimiters)
{
string::size_type lastPos = str.find_first_not_of(delimiters, 0);
string::size_type pos      = str.find_first_of(delimiters, lastPos);
while (string::npos != pos || string::npos != lastPos)
{
tokens.push_back(str.substr(lastPos, pos - lastPos));
lastPos = str.find_first_not_of(delimiters, pos);
pos = str.find_first_of(delimiters, lastPos);
}
}

string int2string(int i)
{
string str;
stringstream out;
out << i;
str = out.str();
return str;
}

```

D.3.4 Analyze code

```

#include <iostream>
#include <fstream>
#include <string>
#include <bitset>
#include <algorithm>
#include <vector>
#include <math.h>
#include "console.h"
using namespace std;

namespace con = JadedHoboConsole;

void Tokenize(const string& str,
              vector<string>& tokens,
              const string& delimiters = " ");

struct Energy{
int plusmin,plusmax,minus1min,minus1max,minus2min,minus2max;
};

int main (int argc, char *argv[]) {
int length;
unsigned short* y=new unsigned short;

// vector<short> E1,E2;

if (!argv[1])
{
cout<<con::fg_green<<"\t\tKmax 8.x binary output file analyzing program v0.6 \n"
<<"\t\t\tCopyright <c> 2008 \n"
<<"\t\tHao Jiang , Henry Griffin\tDec.2008\n"
<<"\n"
<<con::fg_white<<"Usage: analyze3 [file] [gates] \n";
exit(1);
}

ofstream Myfile1("E1.txt");
ofstream Myfile2("E2.txt");

int histE1[2048];
int histE2[2048];

for(int j=0;j<2048;++j)
{
histE1[j]=0;
histE2[j]=0;
}

ifstream myfile (argv[1],ios::binary);

vector<Energy> E1,E2;

const int dim=200;
int sum[dim][dim],sum2[dim][dim];
for (int i=0;i<dim;++i)
for (int j=0;j<dim;++j){
sum[i][j]=0;
sum2[i][j]=0;
}

if (argv[2] && argv[3]) {

ifstream eventfile2(argv[3]);
ifstream eventfile(argv[2]);

if (eventfile.is_open())
{
while (!eventfile.eof())
{

vector<string> vecString;
vecString.clear();
string temp;
getline(eventfile,temp);

```

```

Tokenize(temp, vecString, ",");

Energy E_temp;

E_temp.plusmin=atoi(vecString[1].c_str())-1;
//cout<<E_temp.plusmin<<endl;
E_temp.plusmax=atoi(vecString[2].c_str())-1;
E_temp.minus1min=atoi(vecString[3].c_str())-1;
E_temp.minus1max=atoi(vecString[4].c_str())-1;
E_temp.minus2min=atoi(vecString[5].c_str())-1;
E_temp.minus2max=atoi(vecString[6].c_str())-1;

E1.push_back(E_temp);
}
}

if (eventfile2.is_open())
{
while(!eventfile2.eof())
{
vector<string> vecString;
vecString.clear();
string temp;
getline(eventfile2,temp);
Tokenize(temp, vecString, ",");

Energy E_temp;

E_temp.plusmin=atoi(vecString[1].c_str())-1;

E_temp.plusmax=atoi(vecString[2].c_str())-1;
E_temp.minus1min=atoi(vecString[3].c_str())-1;
E_temp.minus1max=atoi(vecString[4].c_str())-1;
E_temp.minus2min=atoi(vecString[5].c_str())-1;
E_temp.minus2max=atoi(vecString[6].c_str())-1;

E2.push_back(E_temp);
}
}

//cout<<E1.size()<<endl;
//cout<<E2.size()<<endl;

ofstream output("temp.txt");

vector<vector<int>> > hist ( 2048, vector<int> ( 2048 ) );

if (myfile.is_open())
{
myfile.seekg (0, ios::end);
length = myfile.tellg();
cout<<"File length="<<length<<endl<<endl;
myfile.seekg (0, ios::beg);
//while (! myfile.eof())
for (int i=0;i<2048;i++) {
for (int j=0;j<2048;j++)
{
myfile.read((char*)y,2);
hist[i][j]=*y;
}
}
}

vector<vector<int>> > net ( E1.size(), vector<int> ( E2.size() ) );
vector<vector<double>> > error ( E1.size(), vector<double> ( E2.size() ) );

for (unsigned int gate1=0;gate1<E1.size();gate1++)
for (unsigned int gate2=0; gate2<E2.size(); gate2++)
{

int plus=0;
int minus=0;
for (int i=E1[gate1].plusmin;i<=E1[gate1].plusmax;i++)
for (int j=E2[gate2].plusmin;j<=E2[gate2].plusmax;j++)
plus +=hist[i][j];
for (int i=E1[gate1].minus1min;i<=E1[gate1].minus1max;i++)
for (int j=E2[gate2].minus1min;j<=E2[gate2].minus1max;j++)

```

```

plus +=hist[i][j];
for (int i=E1[gate1].minus1min;i<=E1[gate1].minus1max;i++)
for (int j=E2[gate2].minus2min;j<=E2[gate2].minus2max;j++)
plus +=hist[i][j];
for (int i=E1[gate1].minus2min;i<=E1[gate1].minus2max;i++)
for (int j=E2[gate2].minus1min;j<=E2[gate2].minus1max;j++)
plus +=hist[i][j];
for (int i=E1[gate1].minus2min;i<=E1[gate1].minus2max;i++)
for (int j=E2[gate2].minus2min;j<=E2[gate2].minus2max;j++)
plus +=hist[i][j];
for (int i=E1[gate1].minus1min;i<=E1[gate1].minus1max;i++)
for (int j=E2[gate2].plusmin;j<=E2[gate2].plusmax;j++)
minus +=hist[i][j];
for (int i=E1[gate1].minus2min;i<=E1[gate1].minus2max;i++)
for (int j=E2[gate2].plusmin;j<=E2[gate2].plusmax;j++)
minus +=hist[i][j];
for (int i=E1[gate1].plusmin;i<=E1[gate1].plusmax;i++)
for (int j=E2[gate2].minus1min;j<=E2[gate2].minus1max;j++)
minus +=hist[i][j];
for (int i=E1[gate1].plusmin;i<=E1[gate1].plusmax;i++)
for (int j=E2[gate2].minus2min;j<=E2[gate2].minus2max;j++)
minus +=hist[i][j];

net[gate1][gate2]=plus-minus;
error[gate1][gate2]=sqrt(static_cast<double>(plus+minus));
//error[gate1][gate2]=sqrt((plus+minus));
//cout<<net[gate1][gate2]<<","<<error[gate1][gate2]<<endl;
}

cout<<E1.size()<<endl;
cout<<E2.size()<<endl;

/* for(i=0;i<2048;++i)
{
Myfile1<<histE1[i]<<"\n";
Myfile2<<histE2[i]<<"\n";
} */

ofstream Myfile3("net.txt");
ofstream Myfile4("error.txt");

for (i=0;i<E1.size();i++) {
for (int j=0;j<E2.size();j++){
Myfile3<<net[i][j]<<',';
Myfile4<<setprecision(4)<<error[i][j]<<',';
//cout<<sqrt(static_cast<double>(sum[i][j]+sum2[i][j]));
}
Myfile3<<"\n";
Myfile4<<"\n";
}

Myfile3.close();
Myfile4.close();

return 0;
}
}

void Tokenize(const string& str,
vector<string>& tokens,
const string& delimiters)
{
string::size_type lastPos = str.find_first_not_of(delimiters, 0);
string::size_type pos      = str.find_first_of(delimiters, lastPos);
while (string::npos != pos || string::npos != lastPos)
{
tokens.push_back(str.substr(lastPos, pos - lastPos));
lastPos = str.find_first_not_of(delimiters, pos);
pos = str.find_first_of(delimiters, lastPos);
}
}
}

```

D.3.5 ReadNet Matlab code

```

clear all;
net=load('net.txt');
error=load('error.txt');
e1input=load('e1inputout');
e2input=load('e2inputout');
prediction=load('list5c.txt');
e1chance=load('2_1.tka');
e2chance=load('1_1.tka');
net2=mat2vec(net);
netSort=sort(net2,'descend');
E1gate=zeros(16443,1);
E1=zeros(16443,1);
E2gate=zeros(16443,1);
E2=zeros(16443,1);
predict=zeros(16443,1);
errorSort=zeros(16443,1);
E1gatemin=zeros(16443,1);
E1gatemax=zeros(16443,1);
E2gatemin=zeros(16443,1);
E2gatemax=zeros(16443,1);
rest=1;
for i=1:length(net2)
    if rest>1
        rest=rest-1;
        continue
    end
    [k,l]=find(net==netSort(i));
    rest=length(k);
    if size(k)==1
        E1gate(i)=k;
        E2gate(i)=l;
        E1gatemin(i)=e1input(k,2);
        E1gatemax(i)=e1input(k,3);
        E2gatemin(i)=e2input(l,2);
        E2gatemax(i)=e2input(l,3);
        E1(i)=e1input(k,1);
        E2(i)=e2input(l,1);
        errorSort(i)=error(E1gate(i),E2gate(i));
    else
        for j=1:length(k)
            E1gate(i+j-1)=k(j);
            E2gate(i+j-1)=l(j);
            E1gatemin(i+j-1)=e1input(k(j),2);
            E1gatemax(i+j-1)=e1input(k(j),3);
            E2gatemin(i+j-1)=e2input(l(j),2);
            E2gatemax(i+j-1)=e2input(l(j),3);
            E1(i+j-1)=e1input(k(j),1);
            E2(i+j-1)=e2input(l(j),1);
            errorSort(i+j-1)=error(E1gate(i+j-1),E2gate(i+j-1));
        end
        continue
    end
end
for i=1:length(net2)
    a=find(abs(prediction(:,1))-E1(i))<3);
    b=find(abs(prediction(:,2))-E2(i))<3);
    c=common(a,b);
    if c>0
        predict(i)=prediction(c,3);
    end
end
result=[netSort,errorSort,E1gate,E1gatemin,E1gatemax,E2gate,E2gatemin,E2gatemax,E1,E2,predict];

```

APPENDIX E**Other Prints for *TwinSol* Project**

During this thesis project, there were several vacuum components made and in this Appendix, prints for these are listed.

ISO 250 - ISO 100 Adapter
 Plate
 Modifications to existing ISO
 250 Blank plate(Provided)
 Quantity:2

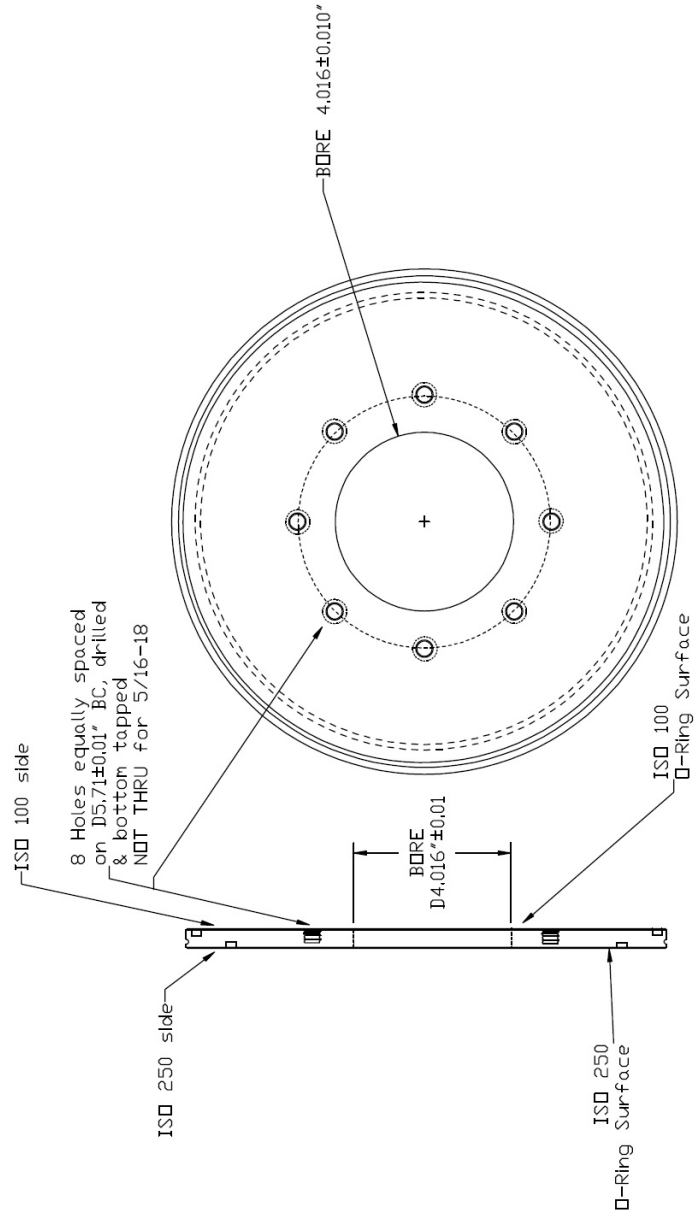


Figure E.1: Print for ISO 250 to ISO 160 adapter plate (material: aluminum).

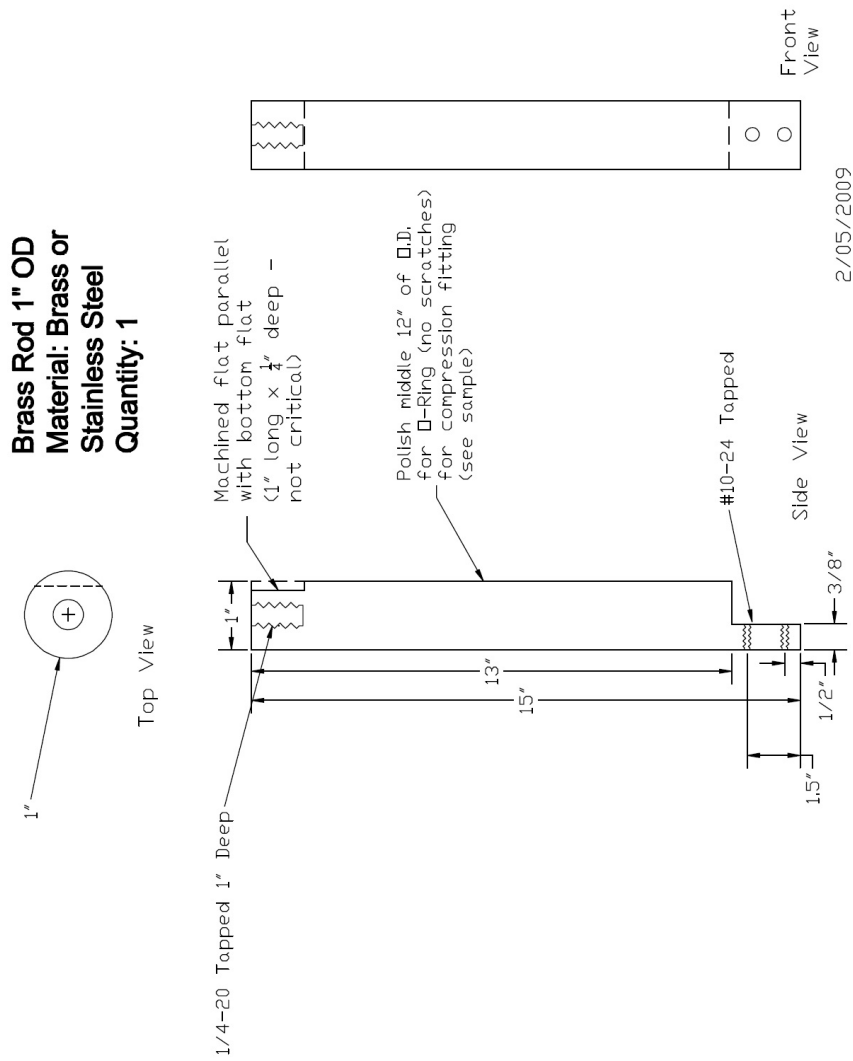


Figure E.2: Print of brass rod for holding MCP support plate.

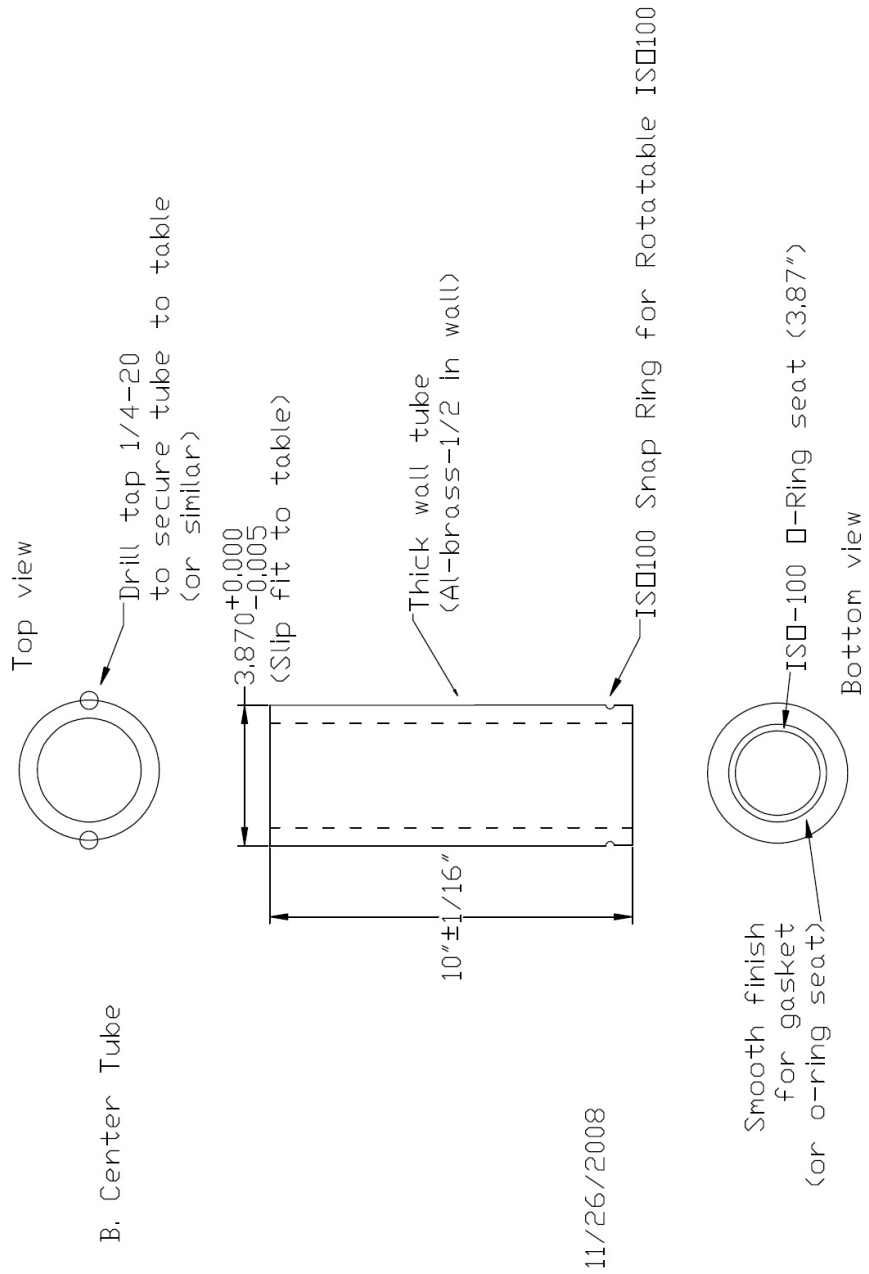


Figure E.3: Print of center tube (material: aluminum).

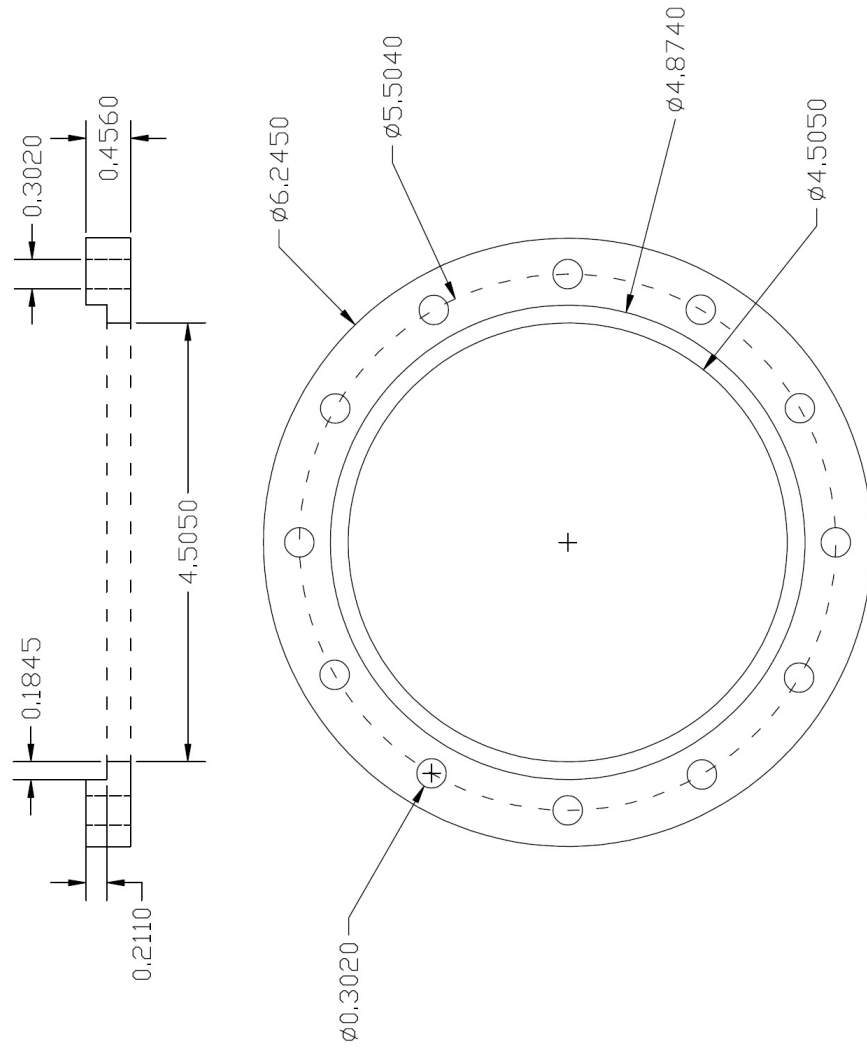


Figure E.4: Print of collar (material: aluminum).

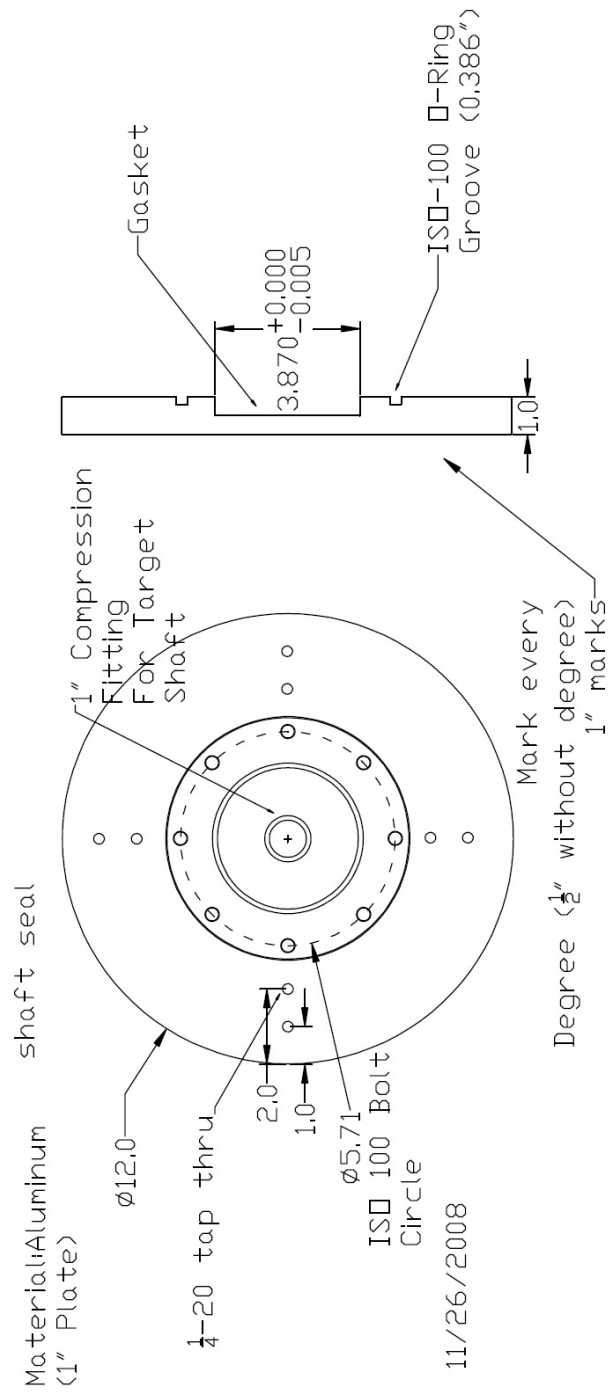


Figure E.5: Print of custom ISO 100 plate (material: aluminum).

Film Paddle
Material: Aluminum or Brass
1/8 inch thick

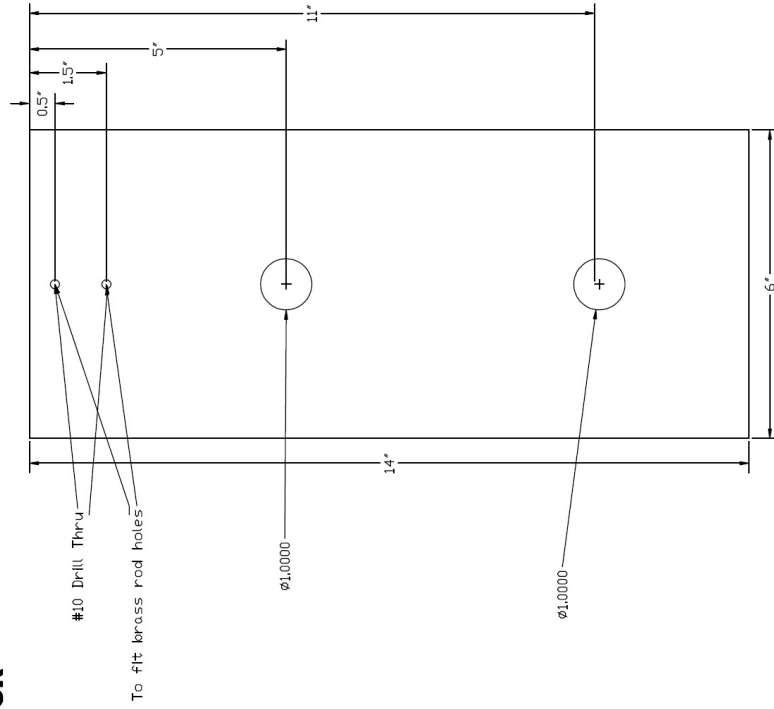


Figure E.6: Print of EBT film paddle (material: aluminum).

ISO100 Plate with BNC and Vacuum LEMO feedthrus

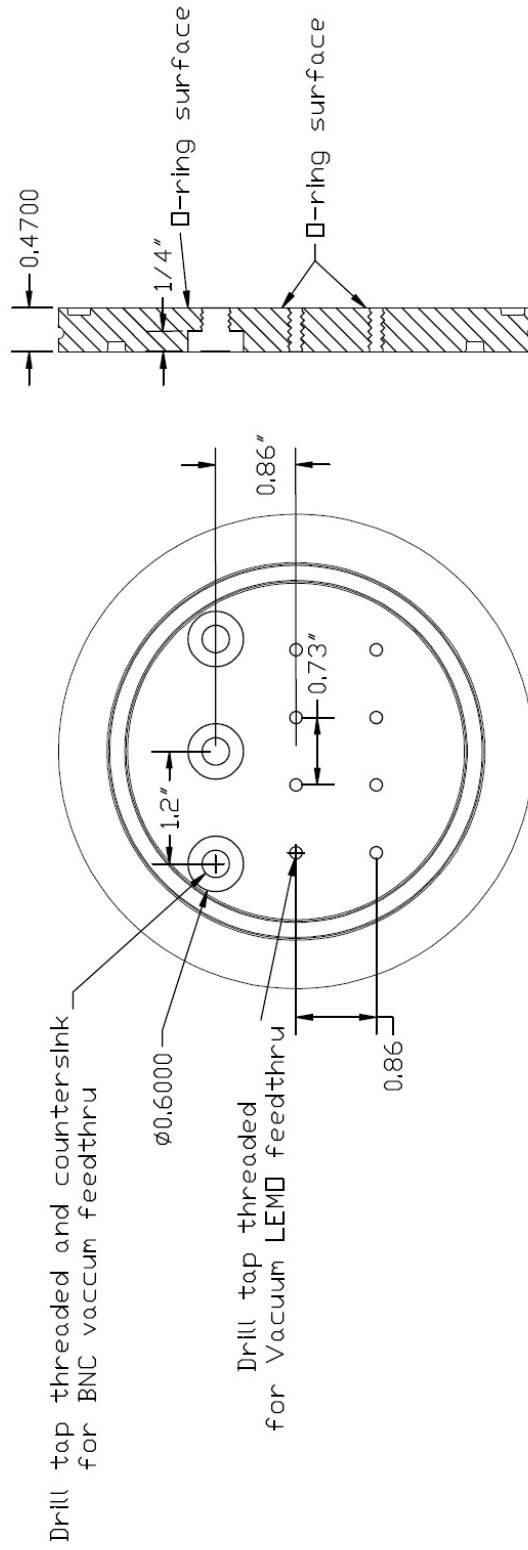


Figure E.7: Print of modified ISO 100 plate with vacuum and LEMO feedthroughs (material: aluminum).

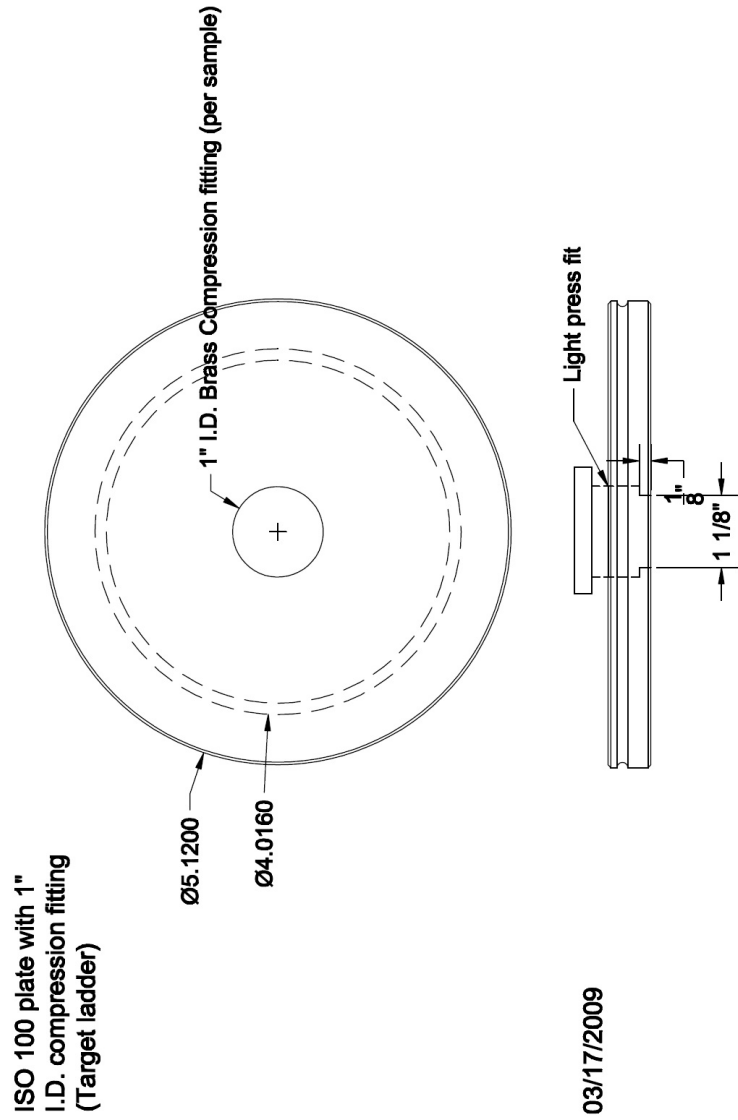


Figure E.8: Print of modified ISO 100 plate with compression fitting (material: aluminum).

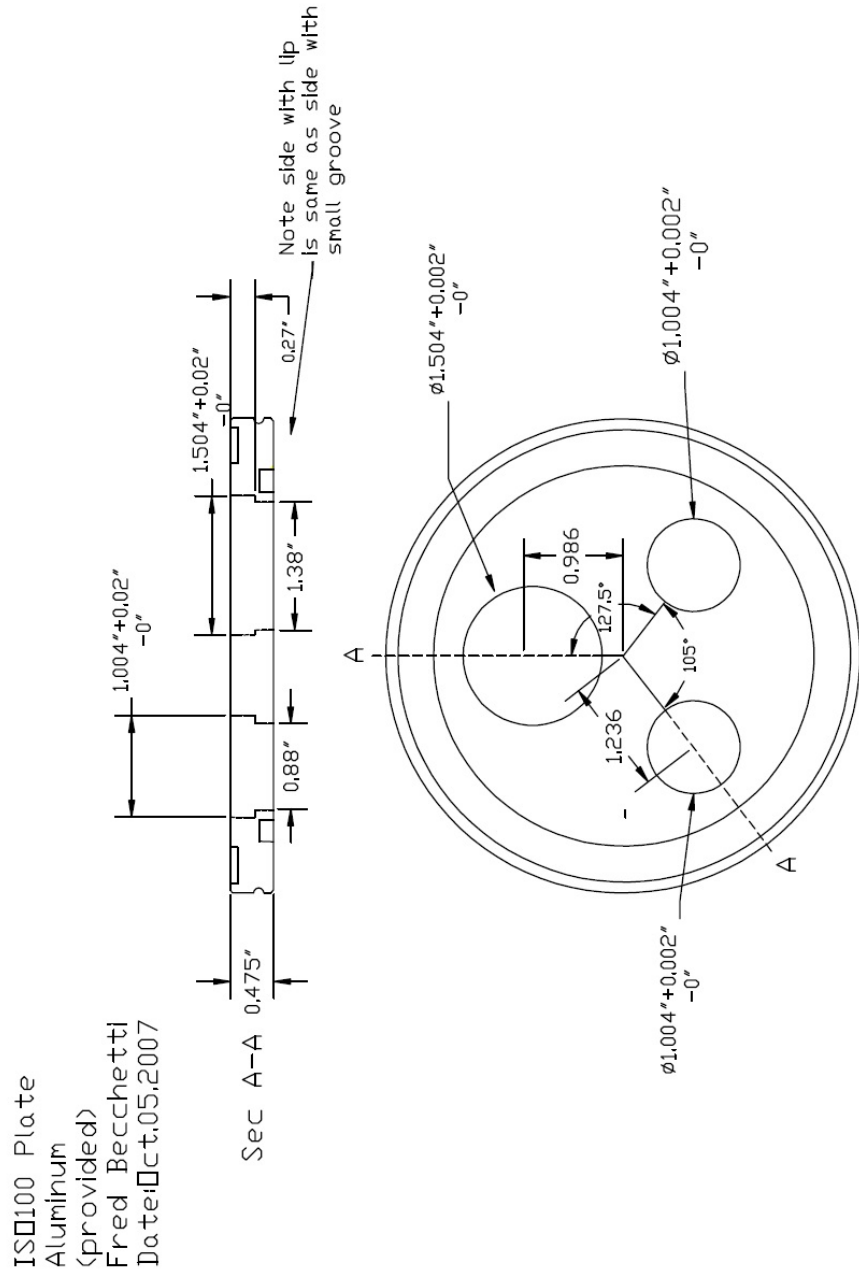


Figure E.10: Print of modified ISO 100 plate (material: aluminum).

4" Dependex to ISO 160 Adapter

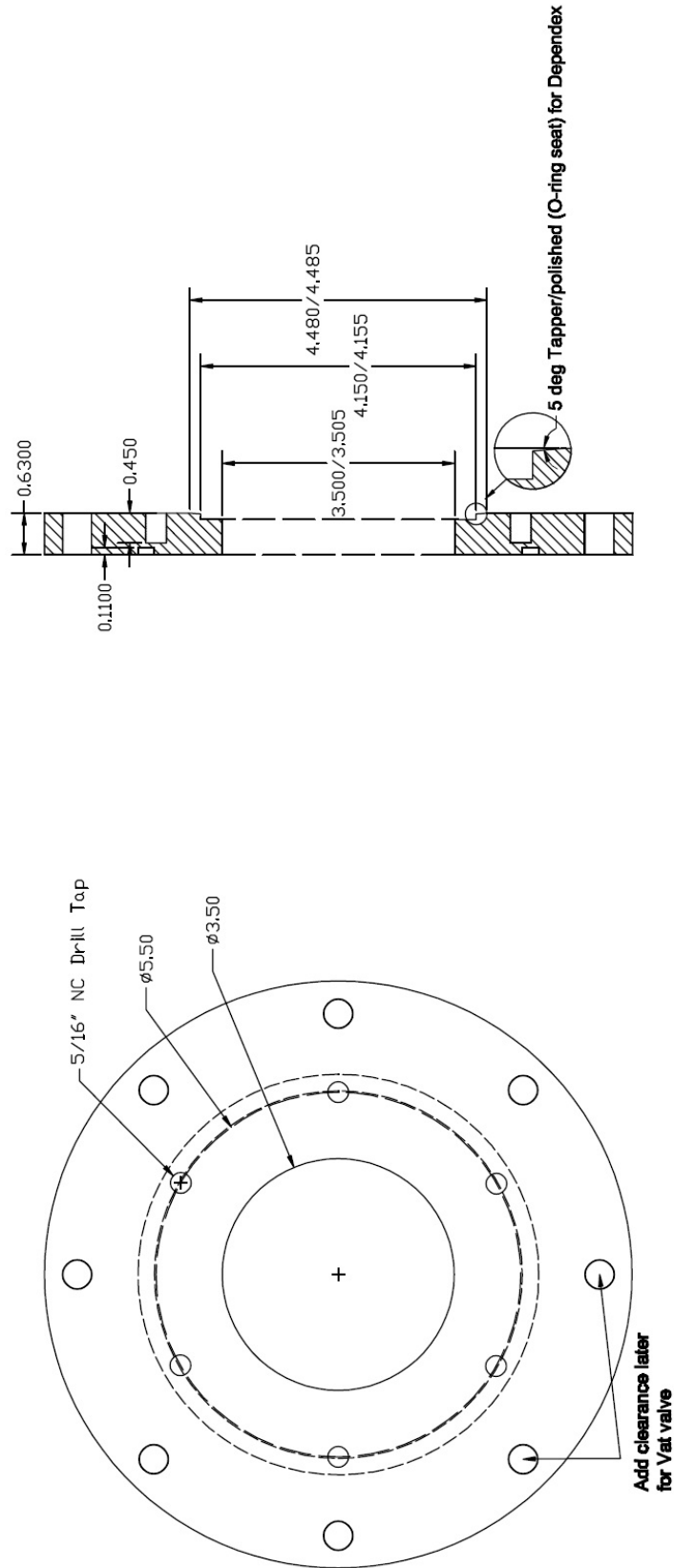


Figure E.11: Print of ISO 160 to Dependex plate adapter (material: aluminum).

ISO 250 to ISO 160 Adapter

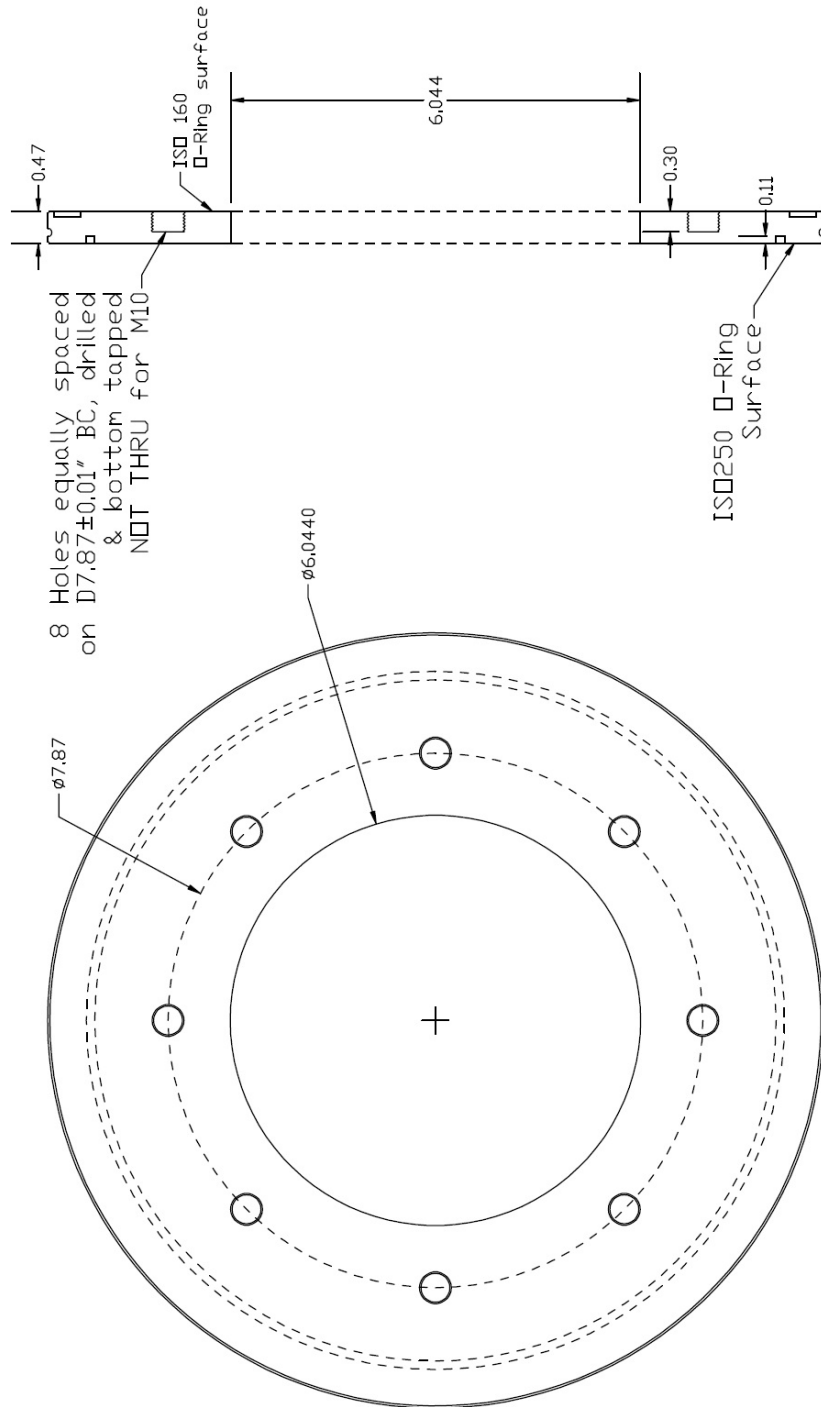


Figure E.12: Print of ISO 250 to ISO 160 adapter (material: aluminum).

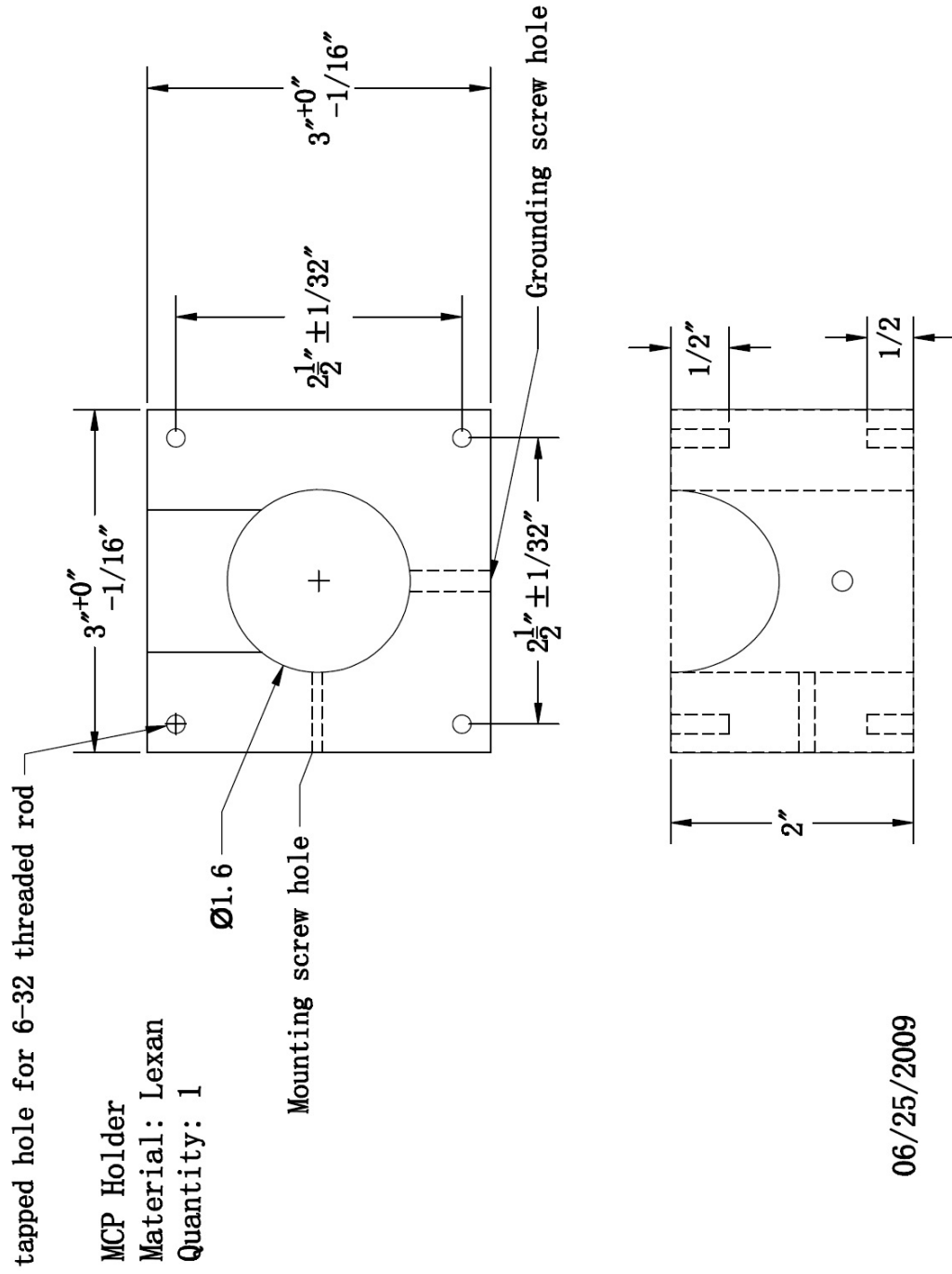


Figure E.13: Print of Lexan MCP holder.

06/25/2009

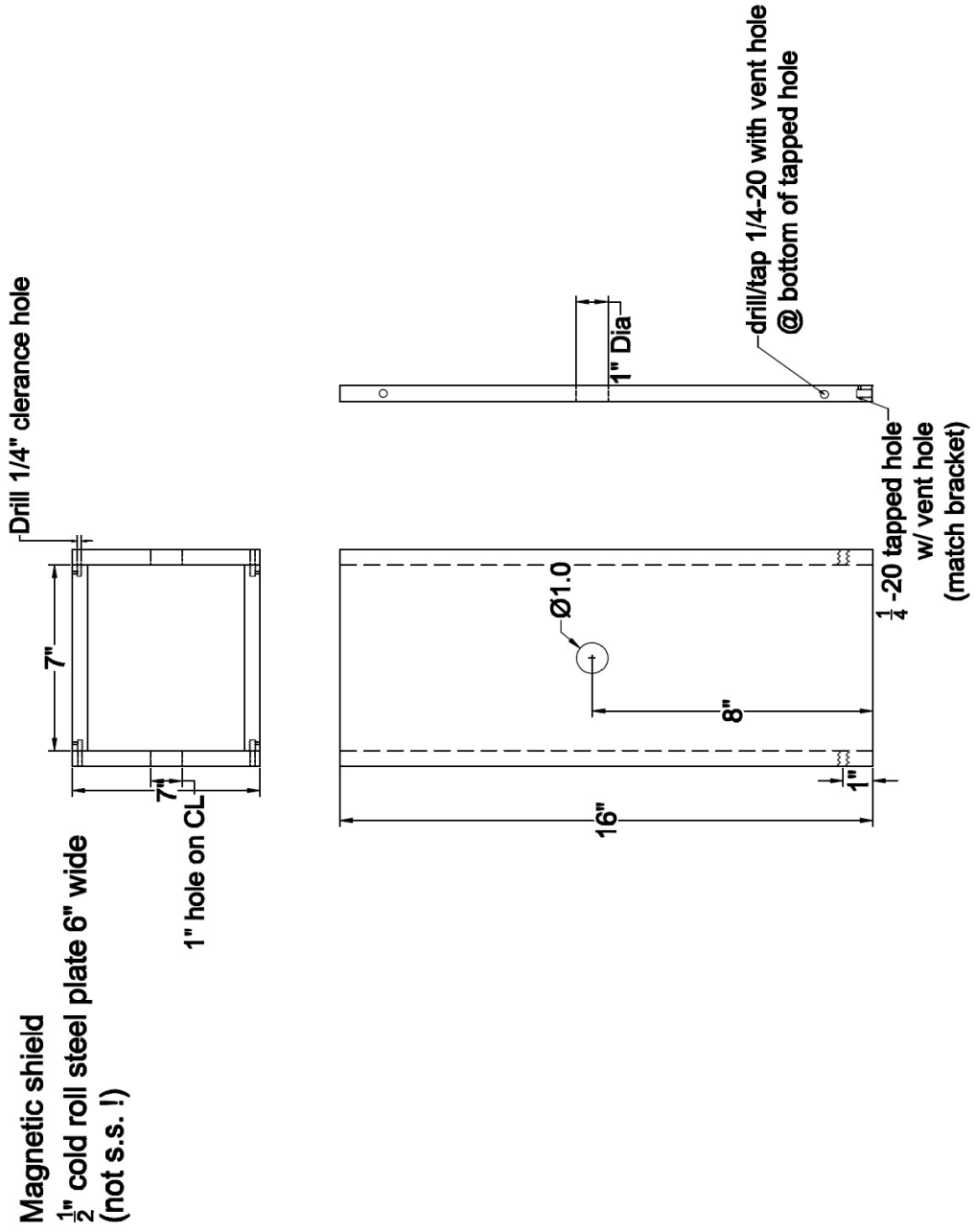


Figure E.14: Print of magnetic field shielding box for MCP (material: steel).

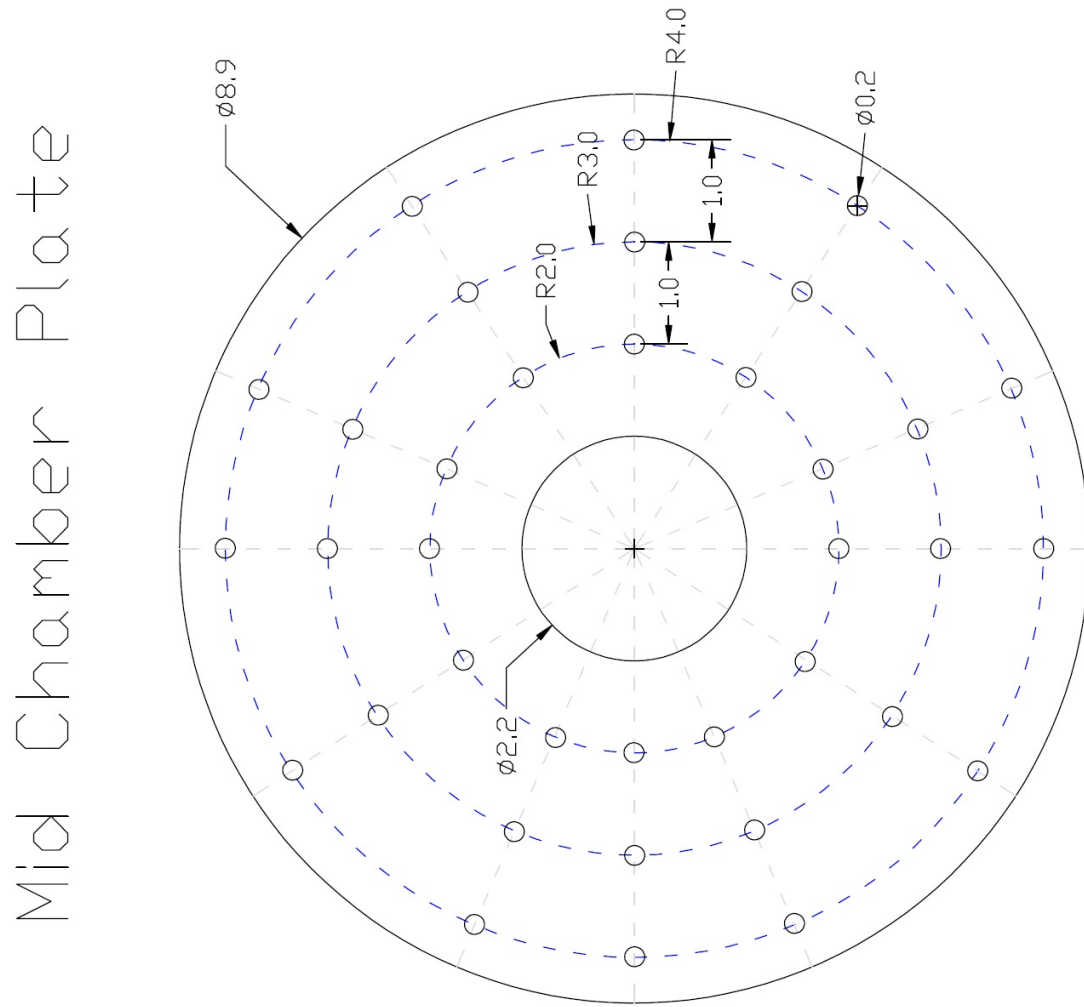


Figure E.15: Print of mid chamber supporting plate (material: aluminum).

Lexan ISO100 Plate

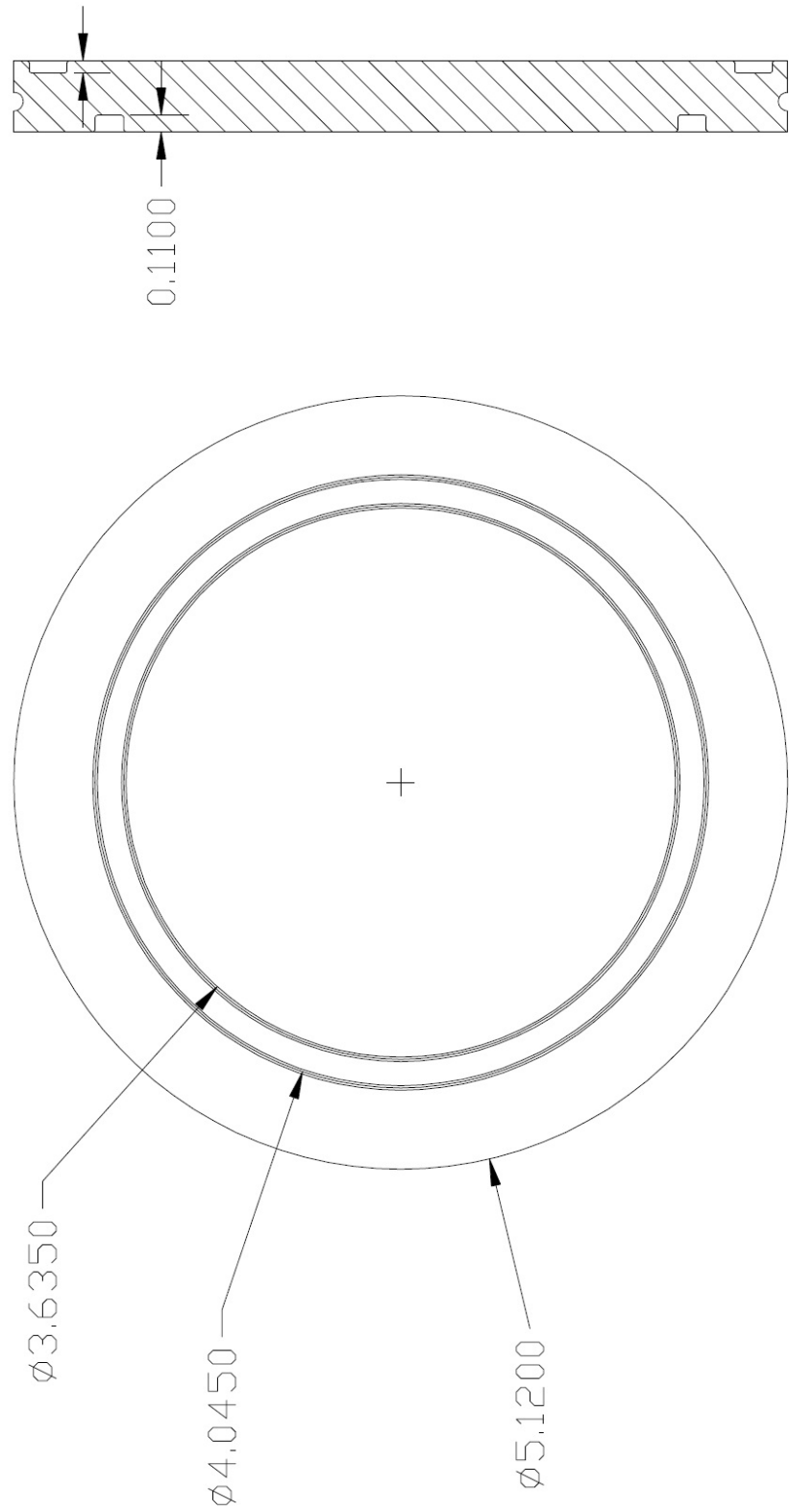


Figure E.16: Print of ISO 100 Lexan viewing plate.

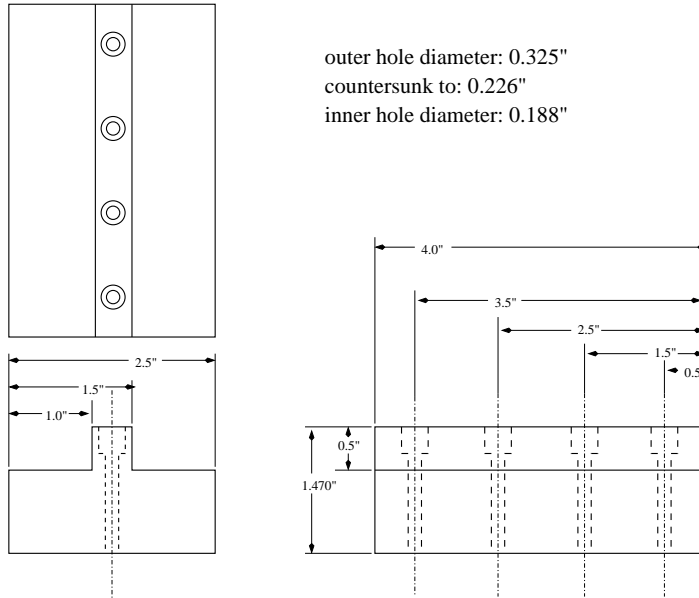


Figure E.17: Print of detector holder (material: aluminum).

TwinSol ToF Target Frame Design (a)

Material: $\frac{1}{16}$ " Aluminum
 Quantity: 4

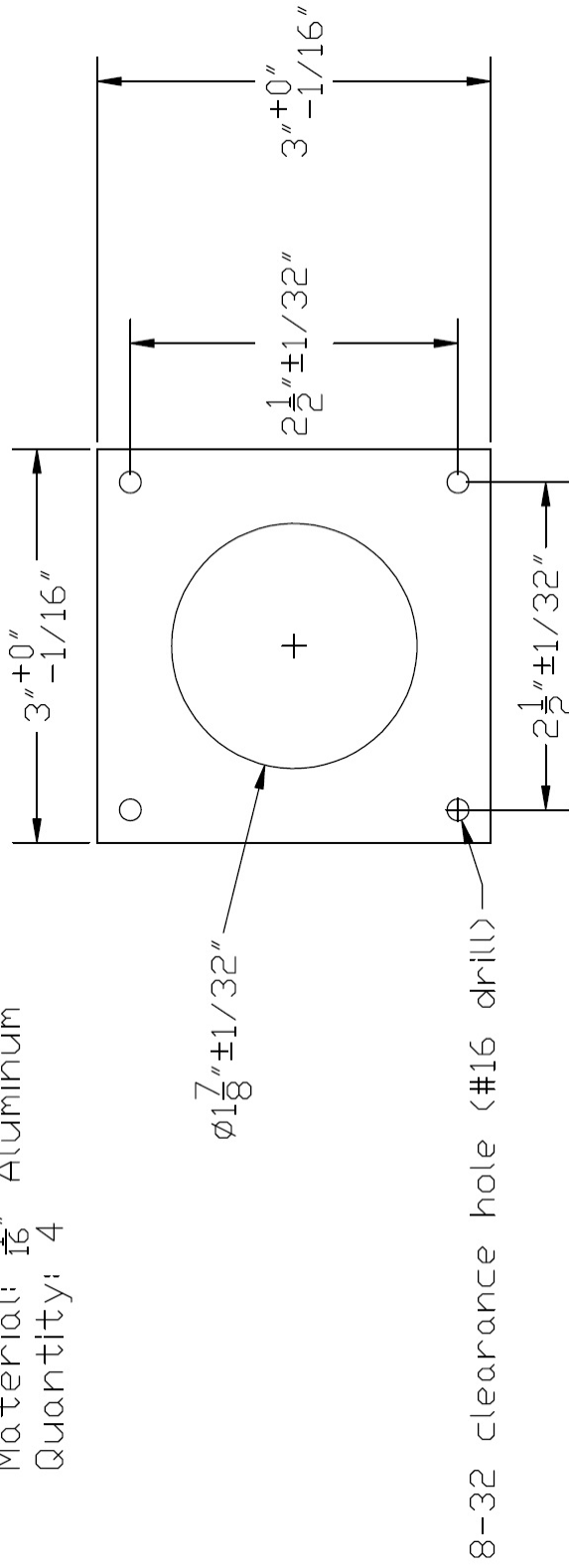


Figure E.18: Print of target frame for *TwinSol* ToF chamber.

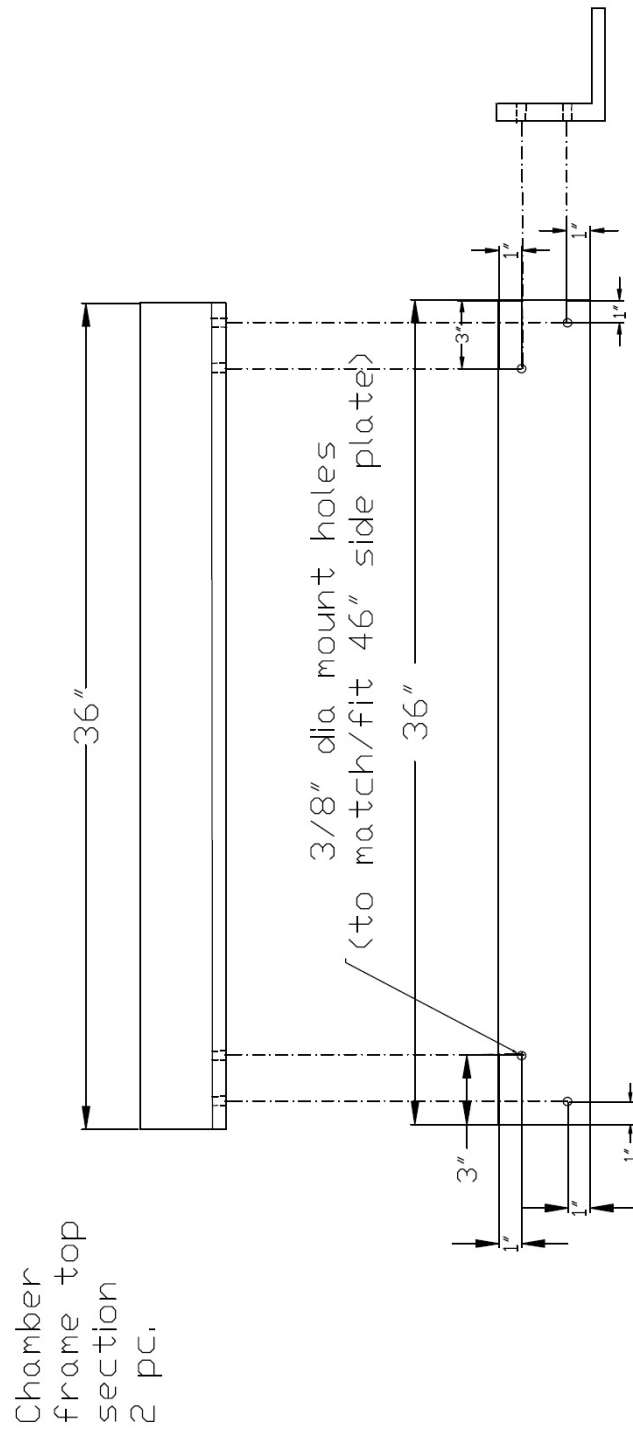


Figure E.19: Print of ToF chamber frame top piece (material: aluminum).

Chamber Frame
 Levelling Screw
 Block (6)
 Material: T6061 Al

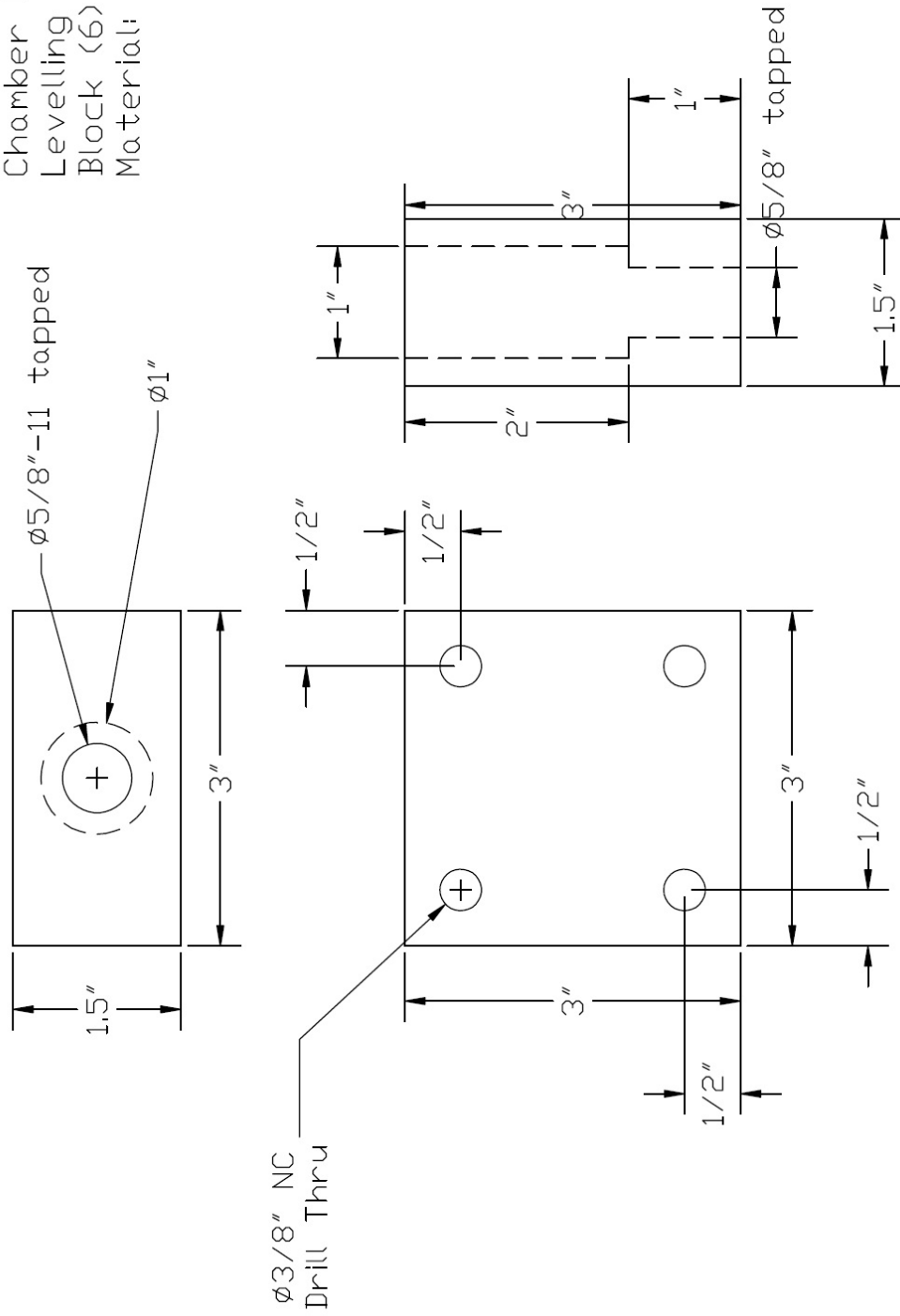


Figure E.22: Print of leveling block for ToF chamber frame (material: aluminum).

APPENDIX F

Poster SORMA-WEST 2008

Paper presented at SORMA West Conf. 2008

Quantitative Low-Energy Ion Beam Profile Measurement with Gafchromic Film (a)

Hao Jiang, F.Becchetti, A.Villano, M.Ojaruega, A.Rose^(b), R.Raymond, R.Torres-Isea
 Department of Physics, University of Michigan - Ann Arbor, MI
 J. Kolata, A.Roberts
 Department of Physics, University of Notre Dame

Abstract
 Light-insensitive Gafchromic films are used in low energy secondary radioactive nuclear beam (RNB) profile imaging in a solenoid based system. Initial tests with an alpha source are examined. The ⁸Li beam profile imaging results are reported. They are part of a project to develop an extended time-of-flight beam line at UM-UND low energy radioactive beam facility *TwinSol* operated at the University of Notre Dame FN Tandem accelerator (A.Villano, et al. this conference).

Gafchromic(c) EBT film features

- Sensitive to doses ranging from about 1cGy to 800cGy
- Self developing in real time
- Uniform and consistent
- Energy-independent dose response from KeV to MeV
- Near tissue-equivalent
- High spatial resolution
- Insensitive to light
- Water resistant - usable in water phantoms
- Digitized with Vidar, Epson and Microtek scanners

Configuration of Gafchromic EBT Dosimetry Film (modified with laminate on one side removed for low energy ion imaging)

ACTIVE LAYER - 17 microns
EXPOSURE LAYER - 1 microns
ACTIVE LAYER - 17 microns
CLEAR POLYESTER - 97 microns

⁸Li beam profile imaging

Ray trace calculation result

Film on the target frame in the ToF chamber

28.5MeV 8Li Beam profiling test result

Image taken at the center of ToF chamber Image taken at the back of ToF chamber Image taken at the front of ToF chamber

Image profile

Surface profile of the image

Image taken at the off-focus small chamber (Image will be used to insert a precise aperture to block unwanted secondary ions and electrons.)

Exposures used: 0.5 - 2hrs at 10⁵ 8Li/sec

Alpha (Cm243 source test)

Alpha source image tests are taken both in vacuum and in air.

Image test setup Exposed film

Image profile

Surface profile of the image

UM-UND TwinSol Group Members

F. Becchetti
 J. Kolata
 R. Raymond
 A. Villano
 Hao Jiang
 M. Ojaruega
 A. Roberts

Conclusion
 Modified Gafchromic EBT film appears to be an ideal medium for precise quantitative imaging of low energy ion beams including low-intensity secondary radioactive beams.

(a) Supported by NSF grants PHY- 0601243 & PHY-0652591
 (b) Summer NSF REU Student (U. of Arizona)
 (c) International Specialty Products (ISP)

Figure F.1: Film poster presented in SORMA west conference.

BIBLIOGRAPHY

BIBLIOGRAPHY

- [Ald66] K. Alder and A. Winther, "Coulomb Excitation" (Academic, New York, 1966).
- [Ald75] K. Alder and A. Winther, "Electromagnetic Excitation" (North-Holland, New York, 1975).
- [Agu09] "Reaction cross sections for ^8B , ^7Be , and $^6\text{Li}+^{58}\text{Ni}$ near the Coulomb barrier: Proton-halo effects", E. F. Aguilera et al. *Physical Review C* 79 (2009) 021601(R).
- [Amr07] " ^7Be -induced α -transfer reaction on ^{12}C ," H. Amro, F.D. Becchetti, Y. Chen, H. Jiang, M. Ojaruega, M.J. Golobish, H.C. Griffin, J.J. Kolata, B. Skorodumov, G. Peaslee, P.A. DeYoung, P. Mears, D. Denby, J. Brown, J.D. Hinfefeld, A.M. Moro, *Eur. Phys. J. Special Topics*, 150, (2007) 1-7.
- [Bas81] "Scattering and charge-exchange reactions with polarized ^3He on lithium isotopes", A.K. Basak, O. Karban, S. Roman, G.C. Morrison, C.O. Blyth, J.M. Nelson, *Nucl. Phys. A* 368 (1981) 74.
- [Baz02] "The program LISE: a simulation of fragment separators", D. Bazin, O. Tarasov, *Nucl. Instrum. and Meth. A* 482 (2002) 307-327.
- [Bec89] "Design of a 7T solenoid magnetic lens system for radioactive beam", F.D. Becchetti, W.Z. Liu, *Rev. Sci. Instrum.* 60 (7) (1989) 1228.
- [Bec91] "Production and use of ^6He , ^7Be , ^8Li , ^{12}B and metastable nuclear beams", F.D. Becchetti, J.A. Brown, K. Ashktorab, J.W. Jänecke, W.Z. Liu, D.A. Roberts, R.J. Smith, J.J. Kolata, K. Larrikin, A. Morsad and R.E. Warner, *Nucl. Instrum. and Meth.*, B56/57 (1991) 554-558.
- [Bec97] "Low-Energy radioactive beam experiments using the UM-UND solenoid RNB apparatus at the UND tandem: past, present and future," F.D. Becchetti and J.J. Kolata, *Proc. 14th Int'l. Conf. on the Application of Accelerators in Research and Industry*, Denton, Texas, November 1996, J.L. Duggan and I.L. Morgan, editors, *AIP Conference Proceedings* 392 pp 369-375 (AIP Press, Woodbury, New York, November 1997).
- [Bec03] "The TwinSol low-energy radioactive nuclear beam apparatus: Status and Recent Results," F.D. Becchetti, M.Y. Lee, T.W. O'Donnell, D.A. Roberts, J.J. Kolata, L.O. Lamm, G. Rogachev, V. Guimarães, P.A. DeYoung, S. Vincent, *Nucl. Instrum. Meth. A* 505 (2003) 377-380.
- [Bro91] "Coulomb excitation of ^8Li ", J.A. Brown, F.D. Becchetti, J.W. Janěcke, K. Ashktorab, D.A. Roberts, J.J. Kolata, R.J. Smith, K. Lamkin, R.E. Warner, *Physical Review Letters* 66 (1991) 2452-2455.
- [Bus80] "A position-sensitive transmission time detector", F. Busch, W. Pfeffer, B. Kohlmeyer, D. Schull and F. Puhlhofer, *Nucl. Instrum. and Meth.* 171 (1980) 71-74.
- [Brooks79] "Development of Organic Scintillators," F.D. Brooks, *Nucl. Instrum. Meth.* 162 (1979) pp. 477-505.

- [Cas99] “New physics with radioactive beams: exotic structures in loosely bound systems”, R.F. Casten, *Journal of Physics G*25, no.4, (1999) 747-753.
- [Cmc100] “CMC100 FastCamac USB Crate Controller”, CMC CAMAC user manual <http://www.cmcamac.com/>.
- [Cyb03] “Updated nucleosynthesis constraints on unstable relic particles”, R. Cybutt et al. *Physical Review D* 67 (2003) 103521.
- [Dal87] “ ^{228}Th nuclear states fed in ^{228}Ac decay”, J. Dalmasso, H. Maria, and G. Ardisson, *Physical Review C* 36 (1987) 2510-2526.
- [Fan07] “A time detector design for MeV particles using secondary electron emission and microchannel plates”, Z. Fang and D.J. O’Connor, *Rev. Sci. Instrum.* 68 (11) (1997) 4027-4034.
- [Gre75] “Fast-timing measurements using a Chevron microchannel plate electron multiplier”, M. I. Green, P. F. Kenealy and G. B. Beard, *Nucl. Instrum. and Meth.* 126 (1975) 175.
- [Hao07] “Energy-spread compensation in a solenoid-based secondary radioactive beam apparatus”, Hao Jiang, H. Amro, M. Ojaruega, F.D. Becchetti, J.J. Kolata, *Nucl. Instrum. and Meth. in Physics Research A* 579 (2007) 461-465.
- [Hen08] “FAIR - recent developments and status”, W.F.Henning, *Nuclear Physics A*805 (2008) 502c-510c.
- [ISP] International Specialty Products, 1361 Alps Road, Wayne, New Jersey, 07470, USA (<http://www.ispcorp.com>).
- [Joe79] “Microchannel plate detectors”, J. Wiza, *Nucl. Instrum. and Meth.* 162 (1979) 587-601.
- [Kol89] “A radioactive beam facility using a large superconducting solenoid,” J.J. Kolata, F.D. Becchetti, W.Z. Liu, D.A. Roberts, and J.W. Jänecke, *Nucl. Instrum. and Meth.* B40/41 (1989) 503-506.
- [Kra09] “Michigan State wins contest to host DOE’s rare isotope beam lab”, D. Kramer, *Physics Today* (Feb. 2009) 25-26.
- [Kum88] “Ultrafast microchannel plate photomultipliers”, H. Kume, K. Koyama, K. Nakatsugawa, S. Suzuki and David Fatlowitz, *Applied Optics*, Vol. 27, No. 6 (1988) 1170-1178.
- [Kunz] DWBA code DWUCK4 by P.D. Kunz, University of Colorado.
- [Lew08] “The SPIRAL 2 project”, M. Lewitowicz, *Nuclear Physics A* 805 (2008) 519c-525c.
- [Liu90] “Production and Use of Radioactive Ion Beams for Measurements of Nuclear Reactions”, W. Liu, Ph.D Thesis, University of Michigan, 1990.
- [Marrone02] “Pulse shape analysis of liquid scintillators for neutron studies”, S. Marrone et al. *Nucl Instrum. Meth. A* 490 (2002) pp. 299-307.
- [McBeth71] “Pulse shape discrimination in inorganic and organic scintillators” G. W. McBeth, R. A. Winyard and J.E. Lutkin. *Nucl. Instrum. Meth.* 95 (1971) pp. 141-153.
- [Mo09] “Fast Neutron Measurements using Deuterated Liquid Scintillators”, Mitaire Ojaruega (Ph.D. Thesis, University of Michigan 2009).
- [Mor98] “Radioactive Nuclear Beam Facilities Based on Projectile Fragmentation”, D.J. Morrissey and B.M. Sherrill, *Proc. Royal Soc. A* 356 (1998) 1985-2006.
- [Mor03] “Neutron-Rich Isotopes from ^{208}Pb at 86 MeV/u”, D.J. Morrissey, B.M. Sherrill, *Nucl. Instrum. and Meth.* B204 (2003) 90-96.

- [Mu02] “Twinsol: A Dual Superconducting Solenoid Ion-Optical System for the Production and Study of Low-Energy Radioactive Nuclear Beam Reactions,” M.-Y. Lee (Ph.D. Thesis, University of Michigan 2002).
- [Mu99] “Study of nuclear reactions with intense, high-Purity, low-energy radioactive ion beams using a versatile multi-configuration dual superconducting-solenoid system”, M.-Y. Lee, et al., Nucl. Instrum. and Meth. A 422 (1999) 536-540.
- [NDE] Nuclear Data Evaluation (<http://atom.kaeri.re.kr/>).
- [NIH] NIH Image (<http://rsb.info.nih.gov/nih-image/>).
- [Odo94] “A mass separator using a large solenoid “lens” with time-of-flight and position sensitive detectors”, T.W. O’Donnell, et al., Nucl. Instrum. and Meth. A 353 (1994) 215-216.
- [ORNL] Data acquisition and analysis software package developed at the Holifield Heavy-Ion Research Facility, Oak Ridge National Laboratory, Oak Ridge, Tennessee, USA.
- [Ptol] Ptolemy: Nuclear Reaction Code, by Steven Pieper, Argonne National Lab (ANL) (unpublished).
- [Rol88] “Cauldrons in the Cosmos”, C.E. Rolfs and W.S. Sydney, (University of Chicago Press, Chicago, USA 1988).
- [Ros52] “High Energy Particles”, B. Rossi, (Prentice-Hall, Inc., Englewood Cliffs, NJ, 1952).
- [Sat80] “Introduction to Nuclear Reactions”, G.R. Satchler, (Oxford University Press, New York 1980).
- [Sch98] “Big-bang nucleosynthesis enters the precision era, Reviews of Modern Physics 70”, G.R. Satchler, 1 (1998) 303-318.
- [Sha00] “A fast and accurate position-sensitive timing detector based on secondary electron emission”, D. Shapira, T.A. Lewis and L.D. Hulett, Nucl. Instrum. and Meth. in Physics Research A 454 (2000) 409-420.
- [She99] “Charge-exchange reactions with a secondary triton beam”, B.M. Sherrill, et al., Nucl. Instrum. and Meth. A 432 (1999) 299-304.
- [Sparrow] Sparrow Corporation, <http://www.sparrowcorp.com/>.
- [TKA] Gamma intensity prediction program from Prof. Henry Griffin (unpublished).
- [Voc08] “Improvements of the DRAGON recoil separator at ISAC”, C. Vockenhuber et al. Nucl. Instrum. and Meth. in Phys. Res. B 266 (2008) 4167-4170.